



Advanced Technology Composite Fuselage—Materials and Processes

*D. B. Scholz, E. F. Dost, B. W. Flynn, L. B. Ilcewicz, K. M. Nelson, A. J. Sawicki,
and T. H. Walker*
The Boeing Company • Seattle, Washington

R. S. Lakes
The University of Iowa • Iowa City, Iowa

NOTICE

FOR EARLY DOMESTIC DISSEMINATION

Because of its significant early commercial potential, this information, which has been developed under a U.S. Government program, is being disseminated within the United States in advance of general publication. This information may be duplicated and used by the recipient with the express limitation that it not be published. Release of this information to other domestic parties by the recipient shall be made subject to these limitations.

Foreign release may be made only with prior NASA approval and appropriate export licenses. This legend shall be marked on any reproduction of this information in whole or in part.

Date for general release April 30, 1999

Printed copies available from the following:

NASA Center for AeroSpace Information
800 Elkridge Landing Road
Linthicum Heights, MD 21090-2934
(301) 621-0390

FOREWORD

This document is one of nine complementary final technical reports on the development of advanced composite transport fuselage concepts. The work described was performed by the Boeing Commercial Airplane Group, Seattle, Washington, from May 1989 through December 1995 under contracts NAS1-18889 and NAS1-20013, Task 2. The contracts were sponsored by the National Aeronautics and Space Administration, Langley Research Center (NASA-LaRC) as part of the Advanced Composite Technology (ACT) program. Direction from NASA-LaRC was provided by M.J. Shuart, J.G. Davis, W.T. Freeman, and J.B. Nelson.

The nine documents comprising the final documentation for the NASA/Boeing ATCAS program include:

Advanced Technology Composite Fuselage

- **Program Overview (CR-4734).** *Synopsis of program approach, timeline and significant findings. Design synthesis considering manufacturing, materials, processes, structural performance, maintenance, and cost.*
- **Manufacturing (CR-4735).** *Baseline manufacturing and assembly approaches. Process and tooling developments, and manufacturing demonstration activities to address critical manufacturing issues.*
- **Materials and Processes (CR-4731).** *Baseline and alternative materials and processes. Material and process developments. Material performance.*
- **Structural Performance (CR-4732).** *Methods used for design sizing. Analysis and test activities supporting assessment of design development methodologies for critical performance issues.*
- **Repair and Damage Assessment Supporting Maintenance (CR-4733).** *Maintenance considerations in design. Detailed repair concepts for quadrant design. Fabrication, inspection, and analytical developments.*

Cost Optimization Software for Transport Aircraft Design Evaluation (COSTADE)

- **Overview (CR-4736).** *Synopsis of COSTADE initiative, including integration of cost, weight, manufacturing, design, structural analysis, load redistribution, optimization, and blending.*
- **Design Cost Methods (CR-4737).** *Components of cost analysis and their interactions. Theoretical framework for process-time prediction. Methods for developing and maintaining cost equations. Applications to ATCAS quadrant designs.*
- **User's Manual (CR-4738).** *COSTADE user instructions, including hardware requirements and installation procedures. Program structure, capabilities, and limitations. Basis of cost model and structural analysis routines. Example problems.*
- **Process Cost Analysis Database (CR-4739).** *Rationale for database framework. Database user's guide, including capabilities and limitations. ATCAS process step equations.*

Use of commercial products or names of manufacturers in this report does not constitute official endorsement of such products or manufacturers, either expressed or implied, by the Boeing Company or the National Aeronautics and Space Administration.

At completion of these contracts, Boeing program management included Bjorn Backman as Program Manager, Peter Smith as Technical Manager, and Larry Ilcewicz as Principal Investigator. Authors listed for this contractor report prepared portions of the document. The members (past and present) of the Boeing ACT contract team who contributed to the work described in this document include:

Program Management:

Phil Whalley
Ron Johnson
Ray Horton
Jordan Olson
Bjorn Backman

Technical Management:

Peter Smith

Principal Investigators:

Randy Coggeshall
Larry Ilcewicz

Structural Design:

George Truslove
Chris Hanson
Ken Griess
Mike Schram
Stephen Metschan
Mike Morris
Tuan Le

Computing Support:

Bob Lundquist
Bill Koch
Sterling Johnston

Structural Analysis:

Tom Walker
Ernie Dost
Gary Swanson
Blake Flynn
Gerald Mabson
David Carbery
Scott Finn
Dan Murphy
Bernhard Dopker
David Polland
William Avery
Jerry Bodine
Doug Graesser
Andre Williams
Mark Fedro
Peter Grant
Adam Sawicki
Pierre Minguet

Technical Aide:

Bill Waltari

Materials and Processes:

Dodd Grande
David Scholz
Karl Nelson
Tony Falcone
Brian Perkins

Manufacturing Technology:

Tom May
Kurtis Willden
Val Starkey
Tim Davies
Mark Gessel
Joe Hafenrichter
Bob Matetich
Ken Goodno
Dick Curran
Ken Dull
Rob Biornstad
Peter Lohr
Stan Stawski
Chris Harris
Greg Bell
Jan Koontz
Rob Synder
Tom Cundiff
Gary Moon

Cost Estimating:

Kent Venters
Will Gaylord
Cal Pfahl
David Tervo
Len Witonsky
Odo Bormke
Robert Humphrey
Mike Proctor
Hans Fredrikson
Dennis Stogin

Fire Worthiness:

Jim Peterson
Thomas Murray

Developmental Manufacturing:

Jose Valdez
Ponci Puzon
Bonnie Luck

Test Laboratories:

Ron Slaminko
John Schneider
Carl Preuss
Joan Dufresne
Tony Phillips
Dan Moreillon
Bill Hardrath

Business Management:

Jeff Heineman
Marge Apeles
Kyra Gorelich

QC and NDE Development:

Ken Mackey
Brian Lempriere
Bill Fortig
John Linn

Weights:

Glenn Parkan

Repair Development:

Bert Bannink
Mike Evens
Sherry Marrese

Customer Support:

Dave Berg
Jeff Kollgaard

Materiel:

Maureen Hughes
Mark Jones
Steve Ruth
Doug Wood
Christal Tyson-Winston
Howard Lanie
Mark McConnell
Tom Hesketh

Industry And University Design-Build-Team Members

University of Washington: Kuen Y. Lin James Seferis Zelda Zabinsky Mark Tuttle	Sikorsky Aircraft: Christos Kassapoglou	United Airlines: Bob Bernicchi John Player
Stanford University: Fu-Kuo Chang	Northrop/Grumman: Ravi Deo Steve Russell Bob Ley Ram Vastava Ram Ramkumar	Cherry Textron: Howard Gapp
Oregon State University: Tim Kennedy	McDonnell Douglas: Benson Black	Sunstrand: Glen Smith Hossein Saatchi Bill Durako
M.I.T.: Paul Lagace Tim Gutowski David Hoult Greg Dillon Hugh McManus	Lockheed Aero. Systems: Tony Jackson Ron Barrie Bob Chu Dan Skolnik Jay Shukla Bharat Shah Lowell Adams Lisa Ott	ICI Fiberite: Erinann Corrigan Russ Holthe
Drexel University: Jonathan Awerbuch Albert Wang Alan Lau Frank Ko	Fiber Innovations: Steve Goodwin Garrett Sharpless	G.M.I.: Roland Chemana
University of Iowa: Roderic Lakes	Hercules Materials Co.: Doug Cairns David Cohen Roger Stirling Lynn Muir Will McCarvill Yas Tokita	Intec: Brian Coxon Chris Eastland Rod Wishart Shreeram Raj Don Stobbe
University of Utah: William Bascom John Nairn	Alliant Techsystems: Carroll Grant George Walker Tammy Harris Todd Brown Mark Wheeler Jon Poesch Vern Benson	Zetec: Chuck Fitch Gregg Colvin
University of Wyoming: Donald Adams Rhonda Coguill Scott Coguill	American Airlines: Jim Epperson Marcus Peter	Draper Laboratory: Ed Bernardon
U. of Cal. Santa Barbara: Keith Kedward	Northwest Airlines: Jim Oberg Erik Restad Mark Wolf	Hexcel: Stacy Biel Julaine Nichols Kevin Marshal
Univ. of British Columbia: Anoush Poursartip		E. I. Du Pont De Nemours: Jim Pratte Hal Loken Ginger Gupton
Brigham Young University: Ken Chase		Materials Science Corp.: Walt Rosen Anthony Caiazzo
San Jose State University: Robert Anderson		Structural Consultant: John McCarty
Dow-UT: Rich Andelman Douglas Hoon		EBCO Tooling: Rich Roberts

TABLE OF CONTENTS

1.0	SUMMARY	1-1
2.0	INTRODUCTION	2-1
3.0	BASELINE AND ALTERNATIVE MATERIALS AND PROCESSES	3-1
3.1	FUSELAGE CROWN QUADRANT	3-1
3.1.1	Crown Panel Skins	3-2
3.1.2	Crown Panel Stringers	3-3
3.1.3	Circumferential Frames	3-3
3.2	FUSELAGE KEEL QUADRANT	3-4
3.2.1	Keel Panel Skins	3-5
3.2.2	Circumferential Frames	3-8
3.2.3	Intercostals and Bonded Attachment Chords	3-9
3.2.4	Cargo Floor Beams and Stanchions	3-9
3.3	FUSELAGE SIDE QUADRANT	3-9
3.3.1	Side Panel Skins	3-10
3.3.2	Circumferential Frames	3-11
3.3.3	Window Frames	3-11
3.3.4	Passenger Door Reinforcing Elements	3-11
3.3.5	Passenger Floor Beams and Stanchions	3-11
4.0	MATERIAL AND PROCESS DEVELOPMENTS	4-1
4.1	AUTOMATED FIBER PLACEMENT	4-1
4.1.1	Prepreg Tow Materials	4-1
4.1.2	Fiber Placement	4-4
4.2	SANDWICH CORE MATERIALS	4-8
4.2.1	Cellular Core Materials	4-8
4.2.2	In-Situ Processing Foam Core	4-9
4.2.3	Foam-Filled Honeycomb	4-10
4.3	HEAT FORMING OF HONEYCOMB CORE MATERIALS	4-10
4.4	SANDWICH CORE CLOSE-OUTS	4-15
4.4.1	Longitudinal Panel Splices	4-15
4.4.2	Circumferential Panel Splices	4-19
4.4.3	Window Cutouts	4-19
4.5	BRAIDING AND RESIN TRANSFER MOLDING	4-22

4.6	AUTOCLAVE CURE	4-25
4.6.1	Stiffened Skin Structure	4-25
4.6.2	Thick Laminate/Sandwich Structure	4-25
5.0	MECHANICAL PERFORMANCE OF SELECTED MATERIALS	5-1
5.1	FUSELAGE SKIN MATERIALS	5-1
5.1.1	Stiffness	5-1
5.1.2	Strength and Notch Sensitivity	5-4
5.1.3	Bearing/Bypass	5-17
5.2	SANDWICH CORE MATERIALS	5-21
5.3	SANDWICH CORE CLOSE-OUTS	5-21
5.3.1	Longitudinal Panel Splices	5-22
5.3.2	Circumferential Panel Splices	5-22
5.3.3	Window Cutouts	5-22
5.4	BRAIDED TEXTILE ELEMENTS	5-23
5.4.1	Textile Composites Analysis Model (TECA)	5-23
5.4.2	Stiffness and Strength	5-24
5.4.3	Bearing/Bypass	5-25
5.5	BONDED JOINTS	5-25
6.0	DURABILITY	6-1
6.1	IMPACT DAMAGE RESISTANCE AND TOLERANCE	6-1
6.1.1	Laminate Structure	6-2
6.1.2	Sandwich Structure	6-6
6.2	ENVIRONMENTAL DURABILITY	6-12
6.2.1	Moisture Sorption by Diffusion	6-12
6.2.2	Sandwich Structure Fluid Ingress	6-14
6.2.3	Sandwich Structure Internal Fluid Migration	6-16
6.2.4	Material Degradation by Absorbed Fluids	6-23
7.0	FIRE WORTHINESS	7-1
8.0	CONCLUDING REMARKS	8-1
9.0	REFERENCES	9-1

APPENDICES

- APPENDIX A** **Quality Assurance Test Result for Prepreg Tow Materials**
- APPENDIX B** **Summary of Work Performed with Cellular Solids at the University of Iowa**
- APPENDIX C** **Mechanical Splices for Commercial Transport Fuselage Utilizing Tow-Placed and Textile Composites Revision A (November 1995)**
- APPENDIX D** **MDOC Joint Coupon Material Database**
- APPENDIX E** **MDOC Sandwich Panel Close-Out Evaluation**
- APPENDIX F** **Impact Damage Resistance and Tolerance of Sandwich Structures with Various Core Materials**
- APPENDIX G** **The Influence of Material, Structural, and Extrinsic Variables on the Impact Damage Resistance and Tolerance of Composite Sandwich Structure**

1.0 SUMMARY

The goal of Boeing's Advanced Technology Composite Aircraft Structures (ATCAS) program was to develop the technology required for cost and weight efficient use of composite materials in transport fuselage structure. This contractor report describes results of material and process selection, development, and characterization activities performed in support of the ATCAS program.

A design build team (DBT) approach was used in identification of materials and processes appropriate for use in fuselage applications. Carbon fiber reinforced epoxy was chosen for fuselage skins and stiffening elements and for passenger and cargo floor structures. The automated fiber placement (AFP) process was selected for fabrication of monolithic and sandwich skin panels. Circumferential frames and window frames were braided and resin transfer molded (RTM'd). Pultrusion was selected for fabrication of floor beams and constant section stiffening elements. Drape forming was chosen for stringers and other stiffening elements.

Development of selected materials and processes was pursued with the aid of industry and university associates. Significant efforts were expended on the development of the AFP, braiding, and RTM processes. Innovative sandwich core materials and core edge close-out design concepts were evaluated for use in fuselage applications. Autoclave cure processes were developed for stiffened skin and sandwich structures representative of ATCAS design concepts.

The performance of selected materials in fuselage applications was investigated. The stiffness, strength, notch sensitivity, and bearing/bypass properties of fiber-placed skin materials and braided/RTM'd circumferential frame materials were characterized. The strength and durability of cocured and cobonded joints were evaluated. The impact damage resistance of stiffened skin and sandwich structures typical of fuselage panels were investigated. The mechanisms by which fluids may penetrate and migrate through sandwich panels were studied. Finally, a cursory evaluation of the fire worthiness of a composite fuselage was performed.

Materials and processes identified for repair of ATCAS design concepts are described in [1].

2.0 INTRODUCTION

Boeing's ATCAS program was initiated in May 1989 under NASA contract NAS1-18889 as part of the Advanced Composites Technology (ACT) initiative. The primary objective of the ATCAS program is to develop and demonstrate an integrated technology which enables the cost and weight effective use of composite materials in fuselage structures of future aircraft. Task 2 of the Materials Development Omnibus Contract (MDOC, contract NAS1-20013) was awarded in November, 1993 as an extension of this work. An additional contract (NAS1-20553) has been awarded to verify this technology at large scale beginning in October, 1995.

The fuselage section just aft of the wing-to-body intersection of a commercial wide body transport aircraft was chosen for study (Figure 2-1). This section contains many of the structural details found throughout the fuselage. The 'quadrant' configuration was adopted to minimize the number of longitudinal splices while maintaining design flexibility for regions with differing requirements [2, 3].

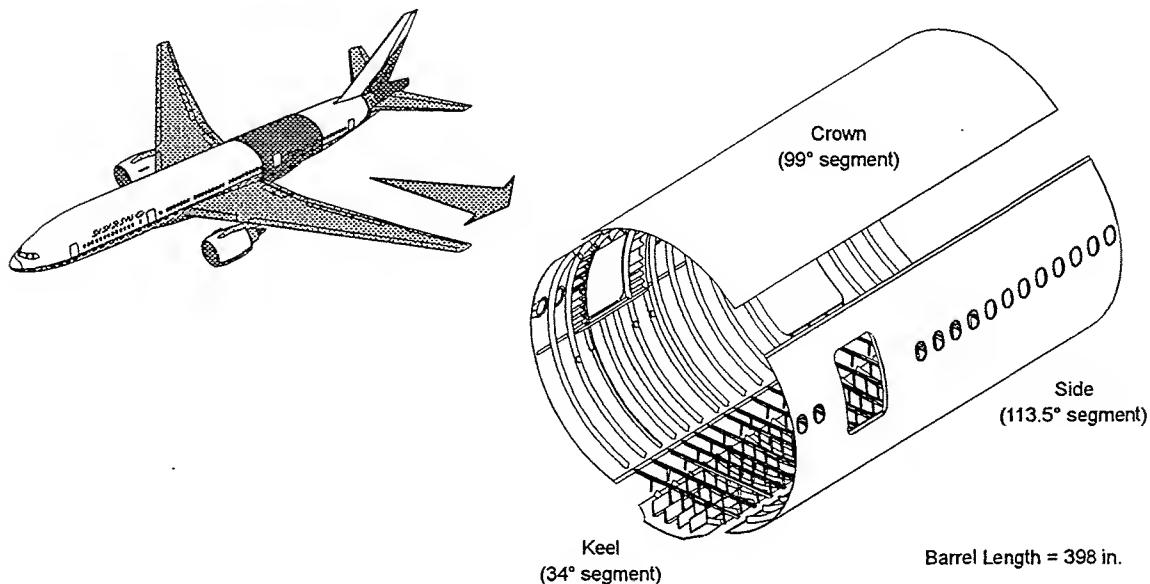


Figure 2-1. Baseline Vehicle and Study Section.

A three step process was employed by the ATCAS DBT for initial development of the fuselage design and manufacturing process [2, 3]. First, baseline concepts were selected for crown, keel, and side panels which had the greatest potential for cost and weight savings with an acceptable developmental risk. The second step was a "global evaluation" of selected baseline and alternative concepts in which detailed designs and manufacturing plans were developed for cost and weight estimates. A globally optimized design was generated from the most attractive features of baseline and alternative

concepts. The next step in design development, called "local optimization," involved detailed investigation and optimization of individual design elements.

Selection, development, and characterization of materials and manufacturing processes were performed in parallel with the design development to leverage trade study results in directing these efforts. This integrated approach also served to provide the DBT with more refined information as the program progressed. The design configurations, materials, and manufacturing processes selected for study by the DBT are described in Section 3 of this report. Section 4 provides a summary of material and process development efforts. Efforts to characterize material performance are summarized in the remainder of the report with emphasis on mechanical properties in Section 5, durability in Section 6, and fire worthiness in Section 7.

3.0 BASELINE AND ALTERNATIVE MATERIALS AND PROCESSES

3.1 Fuselage Crown Quadrant

The crown panel design concept chosen for local optimization is a stringer-stiffened skin configuration as illustrated in Figure 3-1 [2, 3]. The design features cocured longitudinal hat section stringers and cobonded J-section circumferential frames. Cut-outs in the frames allow continuous stringers, but necessitate the inclusion of fail-safe chords. No significant changes have been made to the baseline configuration during local optimization.

Design-constraining structural requirements for the baseline configuration include stability under axial compression loads, tension damage tolerance, minimum gage for impact damage resistance, and ultimate strength of panel splice joints [2, 3, 4]. The anticipated service environment includes a temperature range of -65° to 180°F and exposure to water and other fluids typically encountered in the aviation industry.

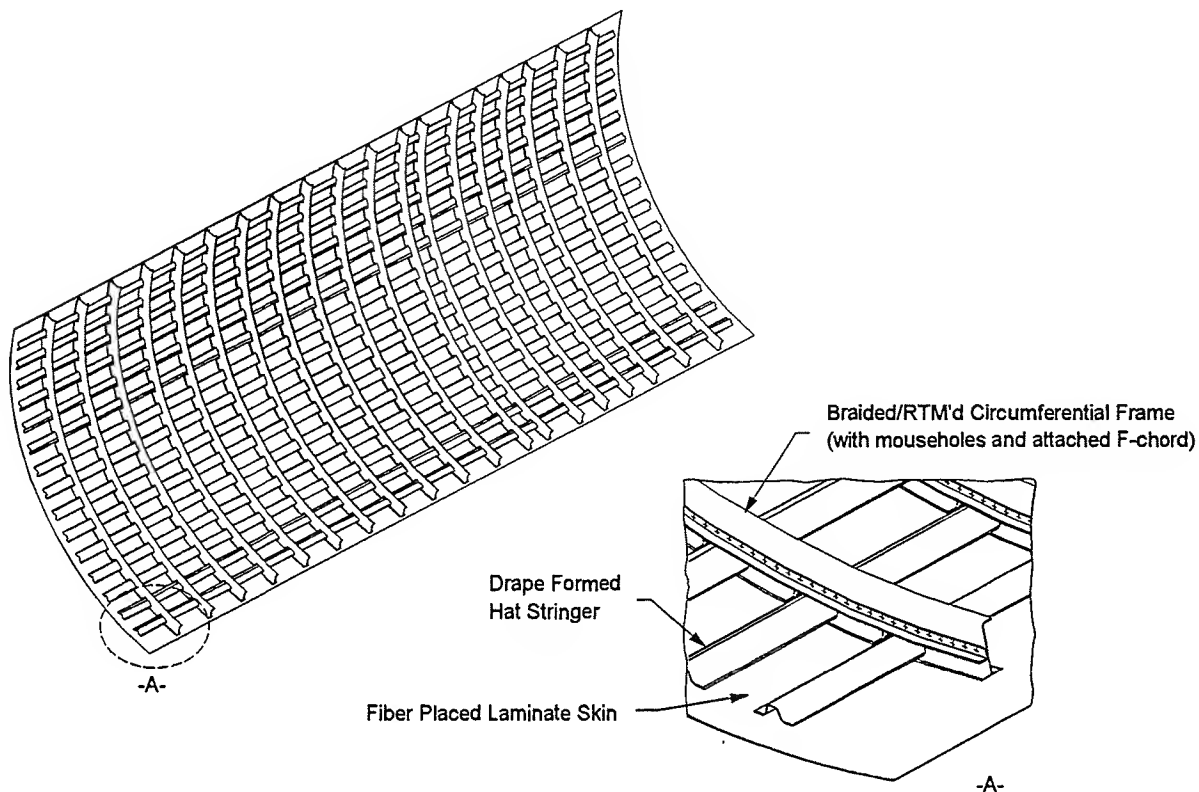


Figure 3-1. Baseline Crown Panel Design Concept.

Alternative design concepts considered during global evaluation included a similar stiffened skin panel with mechanically fastened Z-section frames and a sandwich panel

with cobonded J-section frames [2, 3]. Mechanically fastened frames offer a simplified bagging procedure which may offset the cost of frame installation. The increased flexibility of the bonded skin-stringer panel and the ability to adjust the location of circumferential frames would reduce pull-up forces and shimming requirements for assembly. The sandwich design concept offers commonality with the side and keel designs described below and the potential for reducing or eliminating circumferential frames.

3.1.1 Crown Panel Skins

Automated fiber placement was selected as the baseline process for fabricating fuselage skin panels because of the potential for reduced raw material cost relative to prepreg tape. The projected cost reductions were to be achieved through the elimination of backing paper. An even greater reduction in material cost through prepregging in-line with fiber carbonization was proposed by one supplier. The projected cost reductions have not yet been realized and may be offset by increased packaging requirements. The fiber placement process also offers the ability to lay up material on a compound contour (e.g. fuselage nose and tail sections).

Hercules' band-cut-and-add (BCA) fiber placement head was used for crown panel development work. The BCA head collimates and "ribbonizes" individual prepreg tows into a band of prepreg tape just prior to contact with the tool. A significant limitation of this process is the current requirement for band end cuts which are perpendicular to the fiber orientation. Furthermore, BCA head fiber placement process variations have been shown to have a significant influence on material performance (see Section 5.1.2) and process control has not been demonstrated. Alternative skin fabrication processes include fiber placement with a tow-cut-and-add (TCA) head and automated lay-up of prepreg tape. The TCA head, which places individual prepreg tows, offers greater ply drop/add capability. However, the TCA head is less tolerant of prepreg tow width variations and the increased complexity of the TCA head may result in more down time.

A standard modulus carbon fiber in an untoughened epoxy matrix (e.g. AS4/938) was selected for fabrication of crown panel skins with the following rationale. Results of cost/weight trade studies indicated that the improved performance of intermediate modulus fiber (e.g. IM6) did not justify the additional cost for skin applications [2, 3]. The untoughened matrix has since been found to provide improved tension fracture performance relative to toughened matrices as discussed in Section 5.1.2. The untoughened matrix is generally available for lower cost than toughened versions.

A promising alternative skin material is an intraply carbon/glass hybrid which provides excellent notched tension performance as discussed in Section 5.1.2. However, the use of glass results in reduced stiffness and increased density. The lower material cost may be offset by the complicated logistics of manufacture and inspection.

Fabric surface plies would likely be added to retard fiber breakout during machining operations. The addition of carbon fabric plies has been found to improve the tension fracture toughness of some laminated composite materials as discussed in Section 5.1.2.

Fabric surface plies may also improve the fire resistance properties of the material. Glass fabric surface plies may offer even greater improvements in tension fracture performance and fire resistance, and would provide inherent isolation from aluminum components for protection against galvanic corrosion. Glass fabric may be obtained for lower cost, but is heavier and more compliant than carbon. A potential liability of fabric surface plies is the tendency for stiffener disbonds to propagate between the fabric surface ply and stiffener instead of into the skin as discussed in [4]. A detailed cost/weight trade study would be required to identify the most efficient skin material system.

Alternative skin materials which are compatible with a sandwich design concept are Hexcel's T300/F584 and Hercules' AS4/8552. T300/F584 may offer the improved tension fracture properties of an untoughened matrix. AS4/8552 offers improved impact damage resistance and commonality with keel and side quadrant panels.

3.1.2 Crown Panel Stringers

Global evaluation indicated that hat section stringers should be drupe formed following lay-up with a tape laying machine [2, 3]. The stringers would then be cocured over elastomeric mandrels with the skin. An epoxy film adhesive would be used to provide improved toughness in the cocured joint. The durability of the elastomeric mandrels in a production environment has not been demonstrated. A method of inspecting the cocured hat stringers and underlying skin would be required.

The results of global evaluation indicated AS4/3501-6 was the most cost/weight efficient stringer material for the selected design configuration [2, 3]. However, the greater understanding of structural damage tolerance gained during local optimization suggests the increased stiffness and strength of an intermediate modulus fiber in a toughened matrix (e.g. IM7/8552) is desirable [2, 5]. Updated cost/weight trade studies will be required to identify the most efficient material.

Pultruded blade stringers were projected to be very costly during global evaluation because of the high cost of the prepreg charge required. Pultrusion with in-situ impregnation processes which have recently been developed may provide lower cost stringers. The requirement for a constant cross-section would result in increased weight although the impact of this requirement could be reduced by local trimming of the blade height and flange width. Pultruded stringers would be cobonded (instead of cocured) and would therefore require a surface preparation process. An alternative material system compatible with the pultrusion process has not been identified.

CYTEC's Metalbond 1515-3M (0.05 lbs/ft²) film adhesive was chosen for cocuring the stringers to the skin panel because of extensive Boeing experience with this material in similar applications.

3.1.3 Circumferential Frames

Globally optimized circumferential frames are braided with a two dimensional (2-D) triaxial architecture (see Section 4.5) and resin transfer molded. An innovative

manufacturing plan described in [6] results in an efficient process for fabricating the curved elements. Maintaining a near constant inner mold line for the skin allows the use of a minimal number of unique tools to produce a large number of frames. This fabrication process has been demonstrated for J-section frames by Fiber Innovations (Section 4.5). A manufacturing plan and tooling concepts for frames with an integral fail-safe chord have been developed, but the process has not been demonstrated.

AS4/RSL 1895 was initially chosen for development of the braiding and RTM processes. Although intermediate modulus fiber may be more structurally efficient, AS4 was deemed less likely to be damaged during the braiding process. Shell's RSL 1895 is no longer produced. An alternative matrix resin is 3M's PR-500 which has been used by Lockheed for development of keel and side panel circumferential frames under their ACT contract (NAS1-18888).

Alternative frame fabrication processes considered during global evaluation included compression molding of prepreg charges and stretch forming of long discontinuous fibers (LDF) in a thermoplastic matrix. Both alternative concepts were projected to be more costly than braiding/RTM for circumferential frames. Extruded and roll formed aluminum frames are a cost and weight efficient alternative, although an electrical isolation scheme would be required for protection from galvanic corrosion if used in a composite fuselage.

Metalbond 1515-3M was selected for cobonding circumferential frames to the skin in all quadrants. Although Boeing has gained extensive experience with this adhesive system, a reliable surface preparation process has not been developed for the precured frames.

3.2 Fuselage Keel Quadrant

Global evaluation resulted in selection of a sandwich configuration for fuselage keel panels [2, 7]. The traditional keel chords responsible for carrying high axial compression loads through the main landing gear wheel well area were replaced by a thick (approximately one inch) laminate at the forward end of the keel panel. The laminate transitioned into a sandwich structure toward the sides and aft end as axial line loads diminished. This transition provided a uniform inner mold line which reduced the number of unique circumferential frames required. The sandwich configuration also negated the need for stringers. Panned-down panel edges provided a solid laminate edge band for splicing to the adjoining side panels. Intercostals were used to stabilize the heavily loaded forward area of the panel. The cargo floor structure was constructed of discreet floor beam and stanchion elements.

Several changes to the baseline configuration have resulted in the locally optimized keel panel illustrated in Figure 3-2. The width of the solid laminate "tab-out" (which extends forward between the main landing gear wheel wells) was increased. Panned-down panel edges have been converted to a constant thickness sandwich construction to provide increased stability at the panel edges [2, 8]. The constant inner mold line also simplifies the circumferential frames and the skin-to-frame interface.

The arc length of the keel panel may be increased in future studies to move the longitudinal panel splice out of the areas of concentrated loads created by the wheel well cutouts and cargo door [2]. This change would also simplify assembly by encompassing the entire cargo floor structure within the keel panel.

Primary structural design drivers which influence keel material selection are stability under axial loads, axial compression strength and damage tolerance, and strength of panel splice joints [2, 4, 7]. Although the maximum service temperature may be lower than that expected for the crown, exposure to fluids will be greatest in the keel.

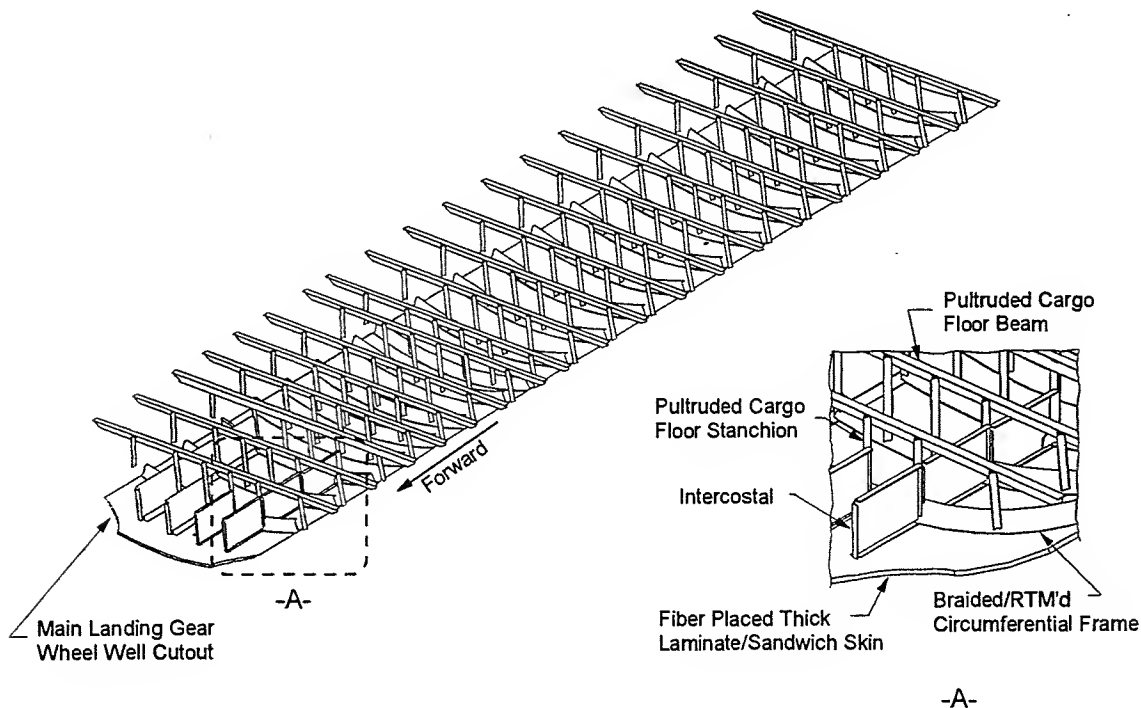


Figure 3-2. Baseline Keel Panel Design Concept.

3.2.1 Keel Panel Skins

Facesheets

The automated fiber placement process was chosen for fabrication of keel panel skins for reasons similar to those described in Section 3.1.1. The BCA head was again used for development. However, the TCA head may be required to provide a smooth transition in facesheet thickness in areas of multiple ply drops which is critical for cobonding circumferential frames to the keel panel.

Hercules' AS4/8552 was selected for keel sandwich facesheets [9]. Design trade studies again indicated standard modulus fiber would be most cost and weight efficient [2, 7]. A moderately toughened matrix was desired for the compression loaded structure to provide a balance of impact damage resistance, strength, and notch sensitivity [9]. The material

had previously been shown to be compatible with the automated fiber placement and sandwich cocure processes. The current and projected costs of 8552 prepregs were reasonable and competitive with other candidate systems. AS4/8552 plain weave fabric plies were added to the panel surfaces and against the core for the reasons described in Section 3.1.1.

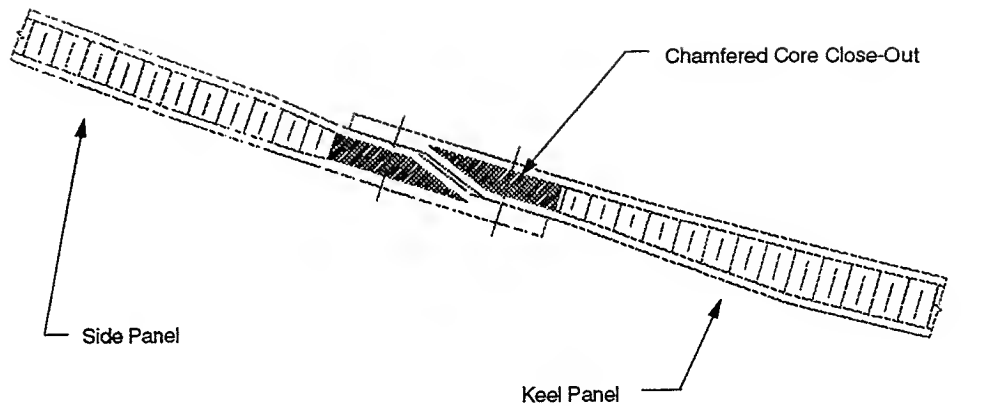
An alternative skin material, Hexcel's T300/F584, was used for much of the keel development work. T300/F584 prepreg tape is currently used in production by Boeing for fabrication of sandwich structure. However, the material was available in prepreg tow form only on the laboratory scale.

Core Materials

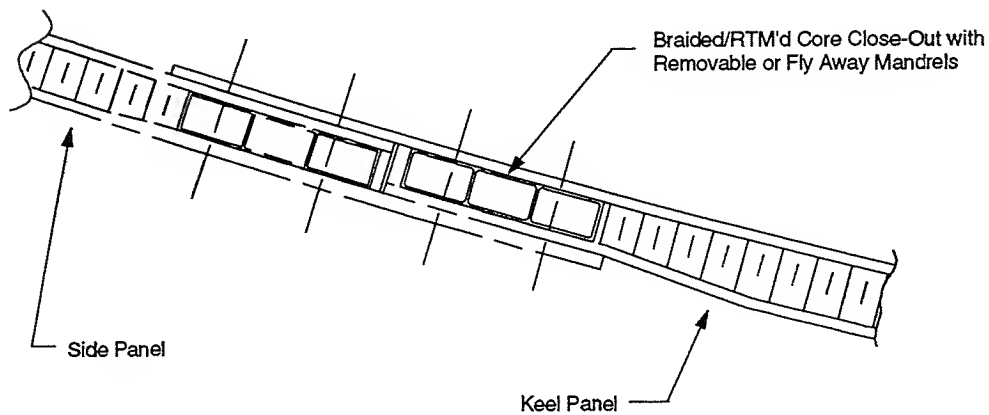
A variety of foams, honeycombs, and foam-filled honeycombs were considered for sandwich core materials. Hexcel's HRP (fiberglass reinforced phenolic) honeycomb was chosen as the baseline keel core material during local optimization because it exhibited the best combination of shear stiffness, impact damage resistance, cost, and weight [9]. Du Pont's Korex was later identified as a potential alternative which could provide reduced weight, improved impact damage resistance, and improved environmental durability at an acceptable cost penalty [9, 10].

Core Close-Outs

Core close-out configurations which were studied for longitudinal panel splices are illustrated in Figure 3-3 [8]. The close-outs are required to protect the core from the environment and to react fastener clamp-up loads. The chamfered close-out configuration may allow the use of only two rows of fasteners. However, a very stiff close-out may be required to aid load transfer through the eccentric load path. The baseline full-depth close-out is constructed of a series of braided/RTM'd tubes fabricated with removable or fly-away mandrels. The tubes are braided with carbon fiber and molded with an epoxy resin. Fly away mandrels could be made of dense foam, foam-filled honeycomb, or foam in combination with strips of solid laminate under the bolt lines. The full depth close-out reduces the risk of core crush during autoclave cure and provides a direct load path through the panel splice for both inner and outer facesheets. However, it would likely be more expensive and requires four rows of fasteners. The ability of the close-out to react fastener clamp-up loads must also be demonstrated.



a. Ramped Core Close-Out



b. Full Depth Core Close-Out

Figure 3-3. Longitudinal Panel Splice Core Close-out Design Concepts

An aft circumferential panel splice core close-out concept is illustrated in Figure 3-4 [8]. This design concept features ramped facesheets to accommodate splice plates. The close-outs could be made of solid laminate or an injection molded, chopped fiber composite. A variation with the honeycomb core extending through the ramp is more cost and weight efficient, but the strength and durability of the core to facesheet bond in the ramped area must be demonstrated. The results of preliminary tests are encouraging (see Section 5.3.2).

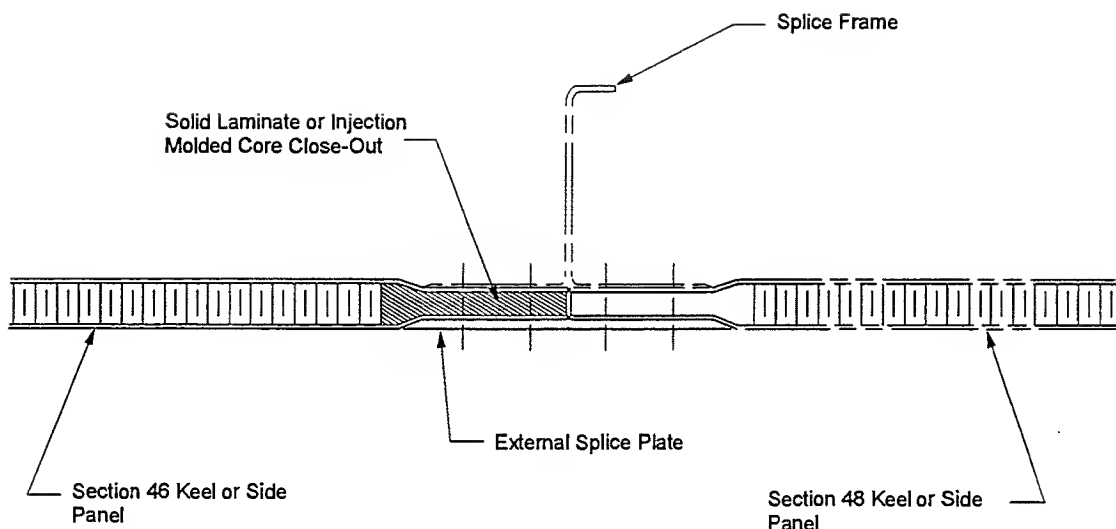


Figure 3-4. Circumferential Panel Splice Core Close-out Design Concepts

Attachments and Penetrations

Detail design concepts have also been developed for penetrations and attachments to the sandwich structure for drain holes, fairings, and antennae [11]. Bonded attachments which do not compromise the facesheet as a barrier to moisture ingress are preferred where feasible. Solid core inserts offer the greatest resistance to moisture ingress where penetration of the sandwich is required. Glass reinforced epoxy may be used for solid inserts to avoid creating structural hard points in the skin panel. Braided/RTM'd inserts similar to those described for longitudinal panel splice core close-outs have also been considered.

Adhesives

Metalbond 1515-3M film adhesive was chosen for cocuring the facesheets to the core and core close-outs because of extensive Boeing experience with this material in similar applications. Hysol's X9899 Synspand expanding syntactic foam is a promising candidate for splicing core materials and bonding core close-outs to core materials. The expanding syntactic foam should provide improved resistance to internal fluid migration relative to traditional foaming adhesives.

3.2.2 Circumferential Frames

Design and development of circumferential frames for the keel panel was performed by Lockheed under their ACT contract (NAS1-18888). The J-section frames are braided with a two dimensional (2-D) triaxial architecture (see Section 4.5) and resin transfer molded of AS4/PR-500.

3.2.3 Intercostals and Bonded Attachment Chords

Resin transfer molding of a woven preform and pressclave processing of a prepreg charge were considered for fabrication of intercostals. The pressclave process would intuitively be very cost efficient. A trade study has not been performed to determine whether standard or intermediate modulus carbon fiber should be used.

Intercostal attachment chords are constant section elements which are amenable to the pultrusion process. Standard modulus fiber would be adequate for this application because the design is constrained by the strength of the bolted joint with the intercostal. Development of the pultrusion process was not pursued and, therefore, a compatible resin system has not been identified. The chords are cobonded to the skin panel with film adhesive. A reliable surface preparation process is needed to ensure removal of release agent used in the pultrusion process from the surfaces to be bonded.

3.2.4 Cargo Floor Beams and Stanchions

Cargo floor beams and stanchions are also of constant cross-section and should be pultruded. Standard modulus fiber would likely be adequate for these elements. These elements are mechanically fastened to the circumferential frames.

3.3 Fuselage Side Quadrant

The left side panel containing a passenger door was selected for study by the DBT. Insufficient resources were available to study the right side panel which also contains a large cargo door. A sandwich configuration (Figure 3-5) was chosen for local optimization of fuselage side panels because of the greater potential for meeting ACT goals for cost and weight efficiency relative to a stringer stiffened skin design [2, 10]. The sandwich configuration provides a uniform inner mold line (by varying core height to account for changes in skin gage) which reduces the number of unique circumferential frames required. The potential for reducing or eliminating circumferential frames for the sandwich configuration has also been considered. The sandwich structure transitions into a solid laminate at the passenger door which allows mechanical fastening of the door cutout reinforcing structure. The door cutout area is reinforced with a system of edge frames, auxiliary frames, door sill chords, and intercostals as illustrated in the figure. Passenger floor beams (not shown) are supported by a pair of stanchions.

Design-constraining structural requirements for the sandwich configuration include stability and damage tolerance under combined loads, ultimate strength of panel splice joints, and ultimate strength of high stress concentration areas around windows and door cutouts [2, 4, 10]. The anticipated service environment for fuselage side panels is similar to that described for the crown.

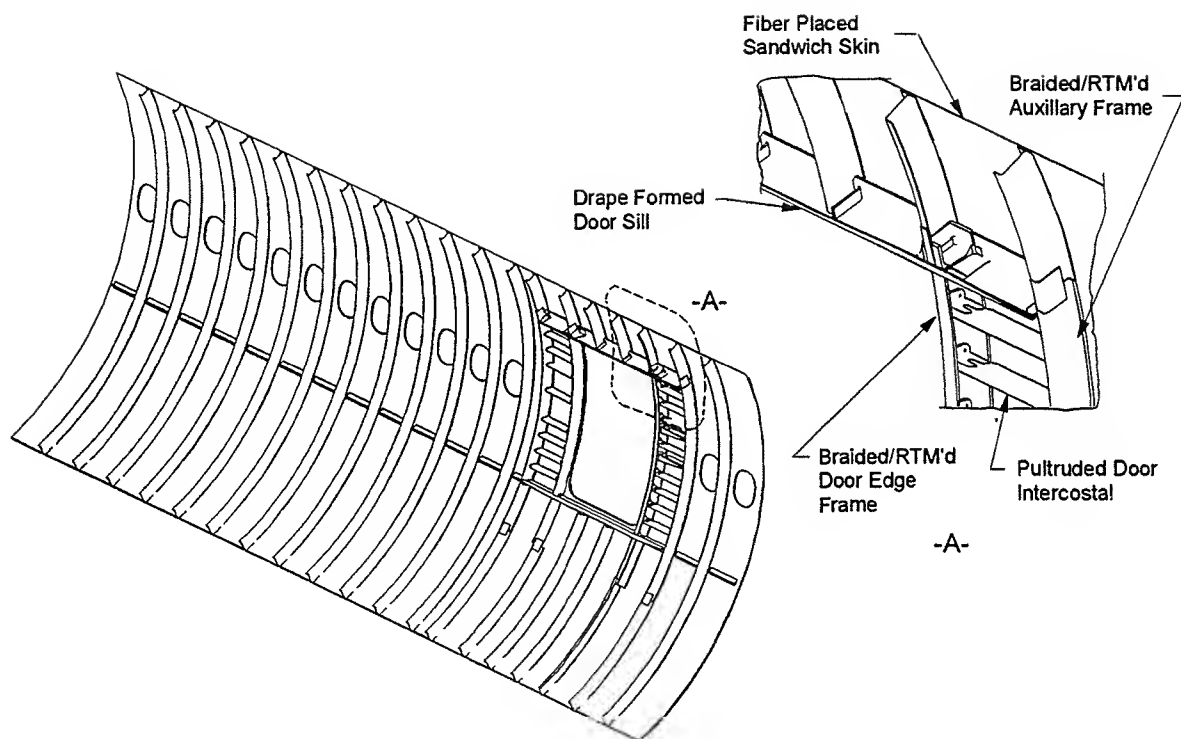


Figure 3-5. Baseline Side Panel Design Concept.

The alternative design configuration considered during global evaluation, a stringer stiffened skin panel, offers lower risks related to manufacture, performance, and maintenance [2, 10]. However, this design concept does not offer the cost savings potential relative to an aluminum airplane which was projected for the sandwich configuration.

3.3.1 Side Panel Skins

The automated fiber placement process was chosen for fabricating side panel skins for reasons similar to those described in Section 3.1.1. The TCA head was selected for development because preliminary Hercules' studies indicated it would be more efficient than the BCA head due to the number and complexity of ply drops in the panel.

Hercules' AS4/8552 prepreg tow and plain weave fabric and Du Pont's Korex honeycomb core material were selected for side panel sandwich skins for the reasons described in Section 3.2.1.

Sandwich core close-outs at the longitudinal and circumferential panel splices are similar to those described in Section 3.2.1 for the keel panel. A chamfered core with laminate edge band would be used for the upper longitudinal splice to the current stringer stiffened skin crown design concept.

Both full-depth core close-outs and chamfered core with laminate edge band concepts have been considered for window cutouts. Full depth braided and RTM'd glass/epoxy tubes with fly-away mandrels similar to those described in Section 3.2.1 for longitudinal panel splice close-outs are light weight, but a solid fiberglass/epoxy insert made from toroidal fabric (to reduce material scrap) offers better resistance to clamp-up loads and moisture ingress at lower cost. Chamfered core with laminate edge band concepts are being developed by Lockheed under their ACT contract[NAS1-18888].

3.3.2 Circumferential Frames

Design and development of circumferential frames for the side panel was performed by Lockheed under their ACT contract (NAS1-18888). The J-section frames are braided with a two dimensional (2-D) triaxial architecture (see Section 4.5) and resin transfer molded of AS4/PR-500.

3.3.3 Window Frames

Braiding and resin transfer molding of AS4/PR-500 has also been adopted for fabrication of window frames which were developed by Lockheed under their ACT contract [NAS1-18888]. The window frames are mechanically fastened to the skin panel. The use of full depth sandwich close-outs at window cutouts would eliminate the need for the upstanding flange featured in the Lockheed design because the skin would possess adequate inherent out-of-plane bending stiffness.

Forged aluminum window frames are a cost and weight efficient alternative, although an electrical isolation scheme would be required for protection from galvanic corrosion if used in a composite fuselage.

3.3.4 Passenger Door Reinforcing Elements

Passenger door edge frames and auxiliary frames are braided and RTM'd with AS4/PR-500 in a manner similar to that employed for circumferential frames [2, 10]. Fabrication of the edge frames was demonstrated by Northrop-Grumman Corporation under subcontract to Boeing. The auxiliary frames are cobonded to the skin panel while the edge frames are mechanically fastened following cure of the skin panel. Passenger door sill chords are drape formed from IM6/8552 tape and plain weave fabric, and are mechanically fastened to the cured skin panel. Passenger door intercostals are pultruded and installed with mechanical fasteners. Intermediate modulus fiber has also been identified for the intercostals

3.3.5 Passenger Floor Beams and Stanchions

Passenger floor beams are constant section, and are therefore amenable to pultrusion. Stanchions should be drape formed because of a joggle which is required in the web for assembly. Intermediate modulus fiber has been identified for these elements due to the desire for high stiffness. However, AS4 may be adequate for floor beams because the

same bending stiffness can be achieved with the addition of a small amount of material in the flanges.

4.0 MATERIAL AND PROCESS DEVELOPMENTS

4.1 Automated Fiber Placement

Automated fiber placement is a process in which yarns of preimpregnated fiber or slit prepreg tape are collimated and applied to a tool to fabricate composite structure with plies of unidirectional reinforcement as illustrated in Figure 4-1. The primary advantage of fiber placement over conventional tape lamination processes is the ability to lay up material on a compound contour. Two types of automated fiber placement were investigated for fabrication of fuselage skin panels. The fundamental difference between the two processes is contained within the fiber placement "head" and is related to the manner in which the prepreg tow is delivered to the part. Hercules' BCA (band-cut-and-add) head "ribbonizes" the prepreg tow into a band of prepreg tape just prior to contact with the part while the TCA (tow-cut-and-add) head places each prepreg tow onto the part independently. Aspects of automated fiber placement which are related to producibility and manufacturing cost are discussed in [2, 6, 12]. The following discussion is restricted to prepreg tow material developments and experiences with the influence of the AFP process on material performance.

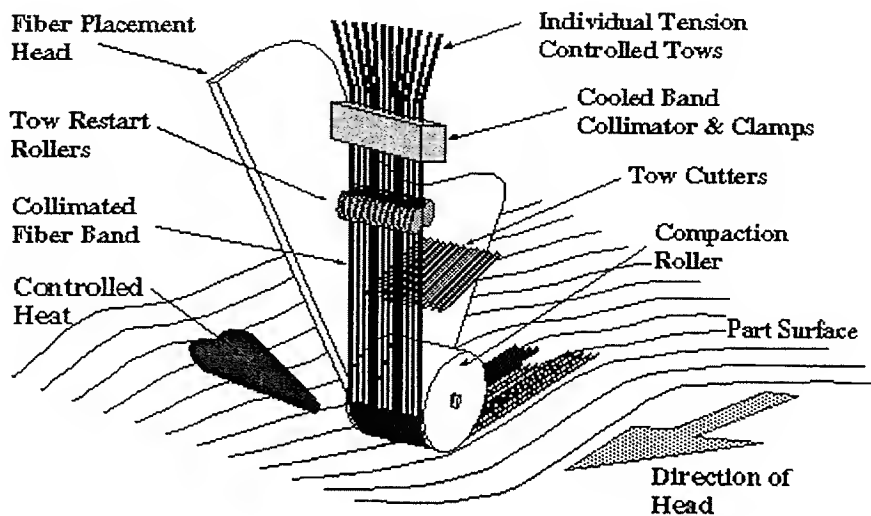


Figure 4-1. Schematic of the Automated Fiber Placement Process.

4.1.1 Prepreg Tow Materials

A variety of prepreg tow materials were procured from three suppliers as shown in Table 4-1. Prepreg tow was defined by the fiber type and tow size, type and amount of fiber sizing, resin type, and resin content. Resin content was generally specified to provide a nominal fiber volume of 57% with the following exceptions. Some materials were

ordered with high resin content so that the influence of resin content on performance could be evaluated. Higher resin content was defined for the AS4/8553-40 material because of the interlayer toughened nature of the material. The T300/F584 material was also ordered with a higher resin content so that it would be consistent with the tape form of the material used by Boeing in production applications. A solution prepregging process was employed by Fiberite and Hexcel while Hercules used a hot melt film process. Slit tape materials were not pursued under the ATCAS program due to the perceived higher cost of the raw material and the requirement for removal of backing paper during fiber placement. Slit tape materials were also expected to create more debris during fiber placement because of the potential for cut fibers on the edge of the tape.

Fiber sizing was employed to improve the handling characteristics of the tow materials during early prepregging efforts. The use of sizing was eventually abandoned because the unsized fiber was observed to spread more uniformly to the desired width during the prepregging process.

Physical properties of the prepreg tow which were monitored for quality assurance purposes included the fiber lineal weight, resin content and prepreg tow width. The density and glass transition temperature as well as several mechanical properties of a cured laminate were also monitored. Chemical characterization by high performance liquid chromatography (HPLC) and infrared analysis were performed by material suppliers to ensure consistent chemistry and level of advancement. The results of quality assurance testing are summarized in Appendix A and are discussed below.

Table 4-1: Prepreg Tow Materials Used in the ATCAS Program.

Supplier	Fiber Type	Tow Size	Fiber Sizing	Resin Type	Resin Content
Fiberite	AS4 carbon	6K	solvated epoxy	938	35.0
					44.8
				977-2	35.0
					36.7
		12K	solvated epoxy	977-2	35.0
	IM7 carbon	12K	emulsified epoxy	938	35.7
				977-2	43.9
	T1000G carbon	12K	solvated epoxy	938	34.7
Hercules	AS4 carbon	12K	emulsified epoxy	938	27.8
			emulsified epoxy	8553-40	40.0
	S-2 glass	20 end	unsized	8552	35.0
Hexcel	T300 carbon	12K	solvated epoxy	F584	38.0

Fiber lineal weight is considered a key characteristic of prepreg tow because of its direct influence on fiber areal weight in the finished part. Areal weight is controlled by placing prepreg tows at fixed intervals with the TCA head. Areal weight may be varied with the BCA head by varying the width of the ribbonized prepreg band. In both cases, the gross

fiber areal weight of a given ply is also dependent on the interval on which successive bands are placed. Once the manufacturing process is fixed, the areal weight is dictated solely by the lineal weight of the prepreg tow. The fiber areal weight in turn has a direct effect on the mechanical performance of the part. It also affects cured ply thickness which is of interest for downstream manufacturing processes. Only minor variation [coefficient of variation (c.o.v.) = 1 to 2%] was observed in the fiber lineal weight of prepreg tow materials, with the exception of one lot of IM7/977-2 which exhibited a c.o.v. of 4%. The source of variation in the IM7/977-2 material was not pursued.

Resin content has a significant influence on mechanical performance and a direct effect on cured ply thickness. Mean values of resin content were typically very close to nominal for all of the materials. The hot melt impregnation process employed by Hercules provided prepreg tow with little variation in resin content (c.o.v. = 1 to 2%). Greater variation (c.o.v. = 2 to 4%) was observed in the resin content of tow materials produced by Fiberite and Hexcel with the solution coating process.

The width of the prepreg tow influences the tow-to-tow overlap or gap conditions in parts fabricated with the TCA head. Tow materials which are too wide may be deformed by the fixed-width chutes through which they must travel. The BCA head is generally more tolerant of tow width variations because prepreg tows are not required to travel through individual chutes. The ribbonizing process acts to spread the tows, eliminating gaps and reducing the severity of overlap conditions. The amount of ribbonizing which can be performed, however, is dependent on resin flow. Mean values of tow width were again typically very close to nominal with several exceptions (see Appendix A). The best control over tow width variation was demonstrated with Hercules' hot melt process which provided AS4/8552 tow materials with a c.o.v. of 4%. The solution processes employed by Fiberite and Hexcel resulted in greater variation, with c.o.v.'s ranging from 6 to 17%.

Prepreg tow materials must exhibit appropriate tack for despooling and for adherence to the tool or part during fiber placement. The tow must also be capable of traveling through the fiber placement machine without deforming or leaving debris on the machine which would result in excessive cleaning requirements. The prepreg tow materials described above were found to be acceptable for use with the fiber placement process with the following exception. One lot of AS4/8552 which exhibited a dry surface resulted in a significant level of material scrap and associated AFP machine downtime because of low tack. The dry surface was attributed to a forming process which was intended to reduce variation in tow width, but which also tended to draw the fiber to the surface of the prepreg tow.

The tack and integrity of a particular type of prepreg tow may be influenced by altering the resin chemistry, level of advancement, and level of impregnation, and by controlling temperature during spooling, storage, and fiber placement. Resin chemistry and level of advancement also influence raw material stability in the manufacturing environment (i.e. out-time) and flow during cure. The amount of tension applied during prepregging and during fiber placement may influence despooling and adherence to the part. These

parameters must all be adjusted in concert to provide a robust process for cost efficient manufacturing.

4.1.2 Fiber Placement

The prepreg tow materials described above were used to fabricate unconfigured test panels and manufacturing demonstration articles which in turn served as configured test panels. Fiber placement was performed by Hercules with the fiber placement machine designated FPM2.

The AS4/938 material was used primarily in fabrication of fuselage crown test panels with a BCA head. The band width and band centerline spacing were adjusted to provide fiber areal weight of 190 g/m². A cross-section of a fiber-placed AS4/938 laminate is presented in Figure 4-2. The physical properties of some of the test panels were characterized by resin digestion. Fiber areal weight was found to be within 4% of nominal. However, significant variations in resin content and associated variations in thickness were observed in some panels. Resin content variations could not be traced to the prepreg tow and are attributed to resin flow during autoclave cure.



Figure 4-2. Microstructure of an AS4/938 Laminate Fabricated with the Automated Fiber Placement Process (BCA Head).

Reduced stiffness in some crown test panels has been attributed to fiber distortion [13] which may have resulted from the fiber placement process, or may have been a result of movement during cure.

Fiber placement of AS4/938 with the BCA head resulted in significant improvements in tension fracture performance over similar tape laminates [14, 15] as discussed in Section 5.1.2. The improved performance has been attributed to a non-homogeneous ply architecture resulting from the fiber placement process and from stacking (as opposed to staggering) of band edge splices in plies of like orientation. A quantitative evaluation of variations in ply thickness, fiber volume, and fiber distribution was attempted by Clarkson University through optical image analysis. A coefficient of variation in ply thickness of 13% was observed along with "a suggestion of periodicity...of about one inch" which correlates with the width of the prepreg band used in fiber placement of the part. Variations in fiber distribution across the AFP band were also reported. A detailed investigation into the dependence of tension fracture performance on microstructural

characteristics and a significant quality assurance effort would be required to exploit the improved performance in structural design.

AS4/938, AS4/977-2, IM7/938, and IM7/977-2 materials were used to fabricate stiffened skin panels for an impact damage resistance designed experiment described in [16]. The fiber placement process was found to influence the mechanisms by which damage is created during an impact event as discussed in Section 6.1.1.

The T1000G/938 and S-2/938 materials were used to fabricate intraply hybrids with AS4/938 as illustrated in Figure 4-3 [14]. Band width and centerline spacing were again adjusted to provide 190 g/m² fiber areal weight in the AS4 material and the same ply thickness (0.0074 inch) in the T1000G and S-2 materials. A cross-section of an AS4-S2/938 intraply hybrid is presented in Figure 4-4. Note the overlap of carbon and glass tows which is a result of the ribbonizing process. These materials were found to possess significantly improved tension fracture performance as discussed in Section 5.1.2 [14, 17].

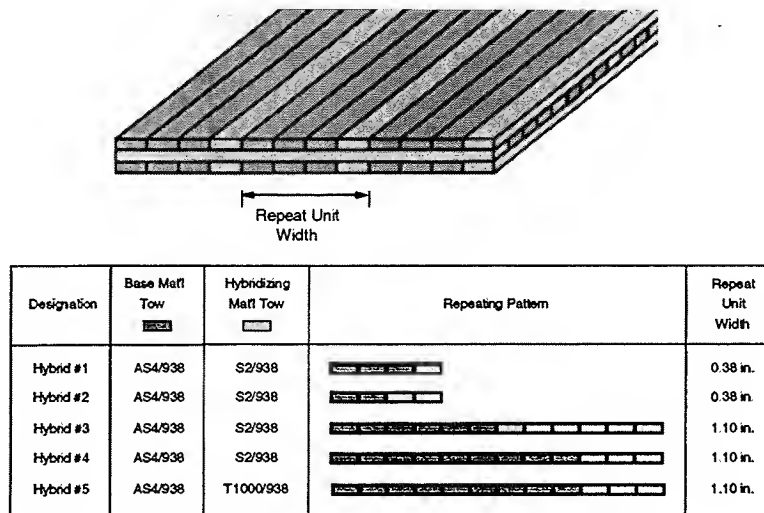


Figure 4-3. Intraply Hybrid Laminates Fabricated with the Automated Fiber Placement Process.

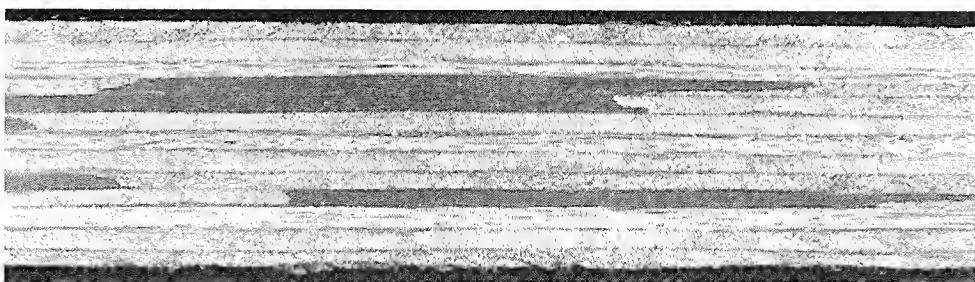


Figure 4-4. Microstructure of an Intraply Hybrid Laminate Fabricated with the Automated Fiber Placement Process (BCA Head).

The AS4/8553-40 was used in an attempt to fabricate an interlayer particulate-toughened material for the keel. The ribbonizing action of the BCA head resulted in dispersion of the toughening particles throughout the carbon plies as shown in Figure 4-5. The merits of this microstructure were not evaluated. Fiber placement of AS4/8553-40 was not pursued further because of reports of excessive wear in AFP machine components from the toughening particles.



Figure 4-5. Microstructure of an AS4/8553-40 Interlayer Particulate Toughened Laminate Fabricated with the Automated Fiber Placement Process (BCA Head).

Hexcel's T300/F584 was used in early keel panel development with the BCA head. The band width and band centerline spacing were again adjusted to provide fiber areal weight of 190 g/m². A cross-section of a fiber-placed T300/F584 sandwich facesheet is presented in Figure 4-6. Initial problems with despooling of T300/F584 were eliminated by adjusting the temperature of the creel to reduce tack. No significant differences in performance (compression notch sensitivity) were observed between T300/F584 sandwich panels with fiber-placed and laminated tape facesheets.

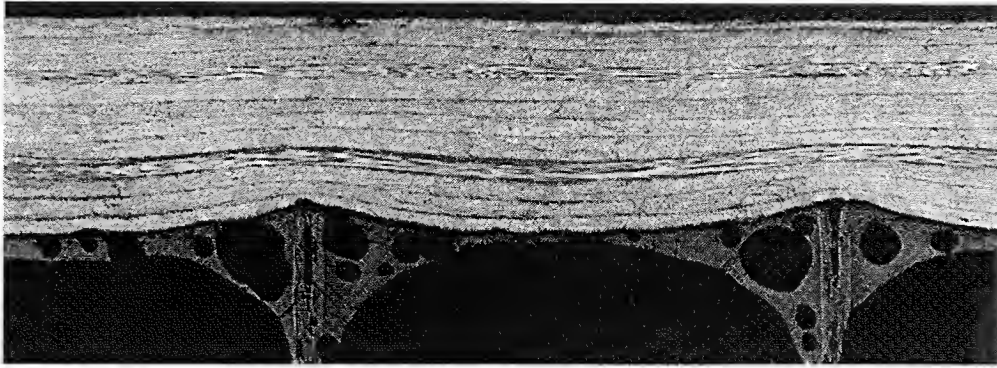


Figure 4-6. *Microstructure of a T300/F584 Sandwich Facesheet Fabricated with the Automated Fiber Placement Process (BCA Head).*

Hercules' AS4/8552 was used for local optimization of keel panels with the BCA head. The BCA head was again used to produce test panels with fiber areal weight of 190 g/m². No significant problems were encountered in fiber placement of the AS4/8552 material with the exception of a single lot of material which exhibited low tack, as discussed above. No significant differences in performance (compression notch sensitivity) were observed between panels which were fiber placed with the BCA head and panels which were made with tape.

A TCA head, which was built for the Great Lakes Composites Consortium, was used for fabrication of side quadrant test panels with AS4/8552. The 0.182-inch tow centerline spacing of this head provided a fiber areal weight of 185 g/m² when used for fiber placement of 12K AS4 tow. A cross-section of a fiber-placed AS4/8552 sandwich facesheet is presented in Figure 4-7. No direct comparisons could be made with the performance of panels made with the BCA head or with tape because plain weave fabric was included in the side quadrant panels.

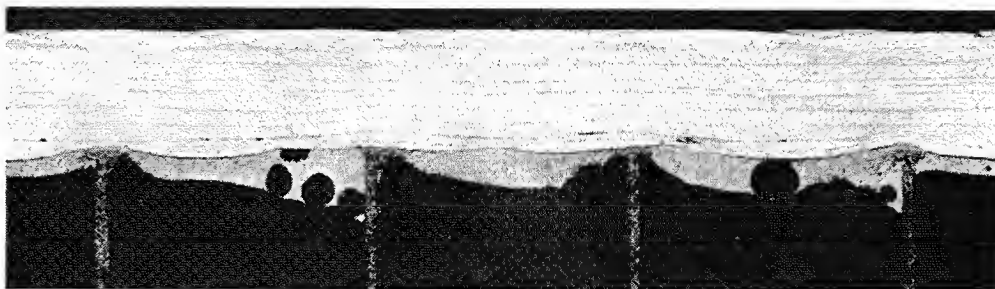


Figure 4-7. *Microstructure of an AS4/8552 Sandwich Facesheet Fabricated with the Automated Fiber Placement Process (TCA Head). Note the Use of Fabric Plies on the Part Surface and Against the Core.*

4.2 Sandwich Core Materials

A variety of honeycombs, foam-filled honeycombs, and foams were considered for sandwich core materials. Developmental and "off the shelf" products were considered. Cost/weight design trade studies resulted in identification of Hexcel's HRP honeycomb as the baseline core material for primary structural applications as discussed in Section 3.2.1. Du Pont's Korex honeycomb was later identified as a cost and weight efficient alternative which may also provide improved impact damage resistance and environmental durability. These products are readily available. Developmental core materials which were investigated are discussed below.

4.2.1 Cellular Core Materials

Cellular materials potentially having attributes (e.g., impact damage resistance and high shear modulus) attractive for the sandwich core of fuselage panels were considered. As with other materials, the microstructure of a cellular solid depends on the material constituents and fabrication processes. In turn, the mechanical properties of the foam material are strongly dependent on its microstructure. The optimum cellular microstructure for the desired sandwich core properties was evaluated using theoretical analyses, laboratory process trials, and mechanical tests. Although this work provided a fundamental basis for future efforts, significant manufacturing and structural developments are needed for use of an optimized cellular core material in transport aircraft panels.

Significant results from the studies performed with cellular solids include development of laboratory processes for making polymeric and metallic foams with re-entrant microstructure (Figure 4-8), yielding negative Poisson's ratio response. The unique material properties of foams with re-entrant microstructure were verified through analytical and empirical methods. Elongation, indentation and impact damage resistance, fracture toughness, and microbuckling instability were addressed. The influence of coupon size and boundary conditions were considered.

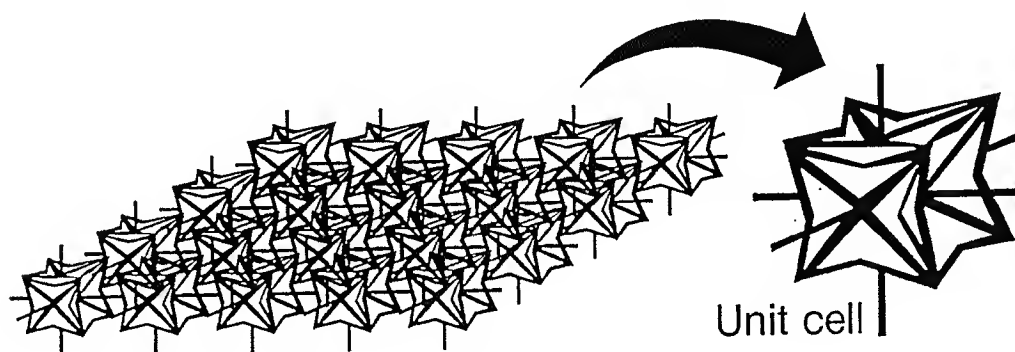


Figure 4-8. Cellular Core Material with Re-Entrant Microstructure.

Most of these studies, which were performed at the University of Iowa under the direction of Dr. Roderic Lakes, have been documented in the open literature. Summaries of the pertinent results and references are included in Appendix B.

4.2.2 In-Situ Processing Foam Core

A process for fabricating fuselage keel sandwich panels by concurrent cure of a thermoset foam core and the sandwich facesheets was investigated [18]. This process was of interest for its potential for producing low cost sandwich structure through elimination of manufacturing processes traditionally associated with machining and splicing other types of core material (e.g., honeycomb). The process was also expected to provide a strong, reliable bond between facesheet and core through cocure of the polymer matrices. Foam core sandwich test panels were fabricated with Sundstrand's FEF (Foam Expansion Fabrication) process (Figure 4-9). Both unfilled and chopped-carbon-fiber-filled foam cores were manufactured. The mechanical properties and impact damage resistance of the foam core materials were characterized. The development effort was discontinued due to the projected costs of process development and tooling for manufacturing scale-up. Initial tests indicated poor mechanical performance relative to honeycomb.

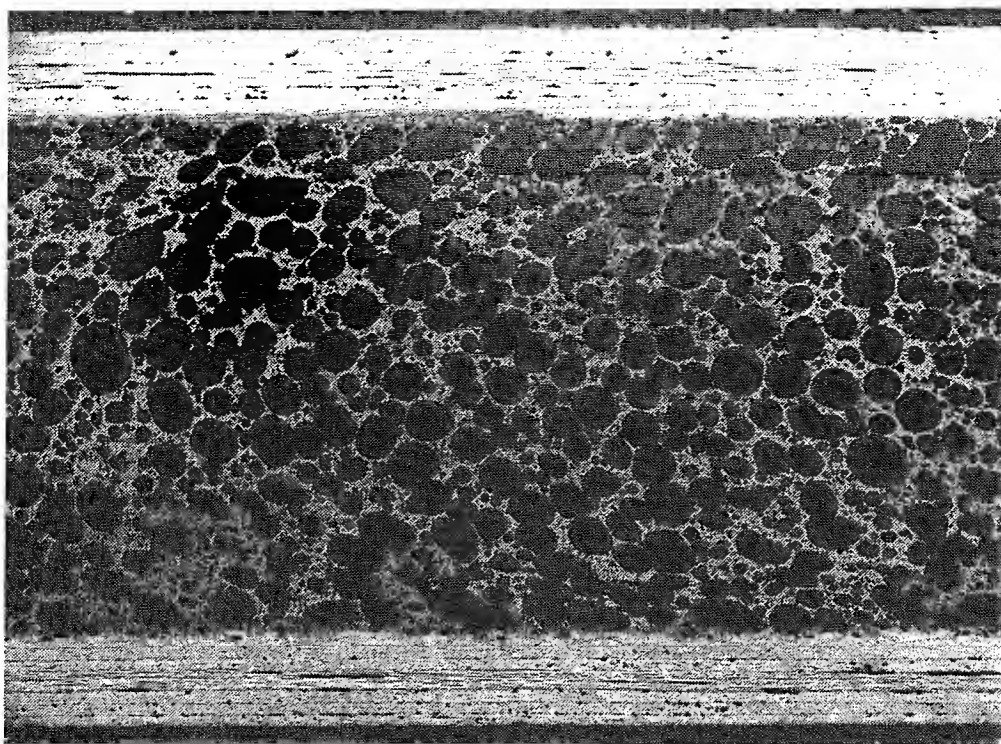


Figure 4-9. *Foam Core Sandwich Structure Fabricated with Sundstrand's Foam Expansion Fabrication Process.*

4.2.3 Foam-Filled Honeycomb

Foam-filled honeycombs (Figure 4-10) were investigated for use as keel sandwich core materials in an effort to enhance impact damage resistance. A cyanate-ester foam developed by Hexcel was of particular interest because of its resistance to moisture sorption [19]. A manufacturing process development effort was initiated and sandwich panels with foam filled HRP and HRH-10 (Nomex) core materials were fabricated. This effort was curtailed due to poor performance in impact damage resistance surveys as discussed in Section 6.1.2. However, foam filled honeycombs were used in development of sandwich core close-outs as discussed in Sections 4.4.1 and 4.4.3.

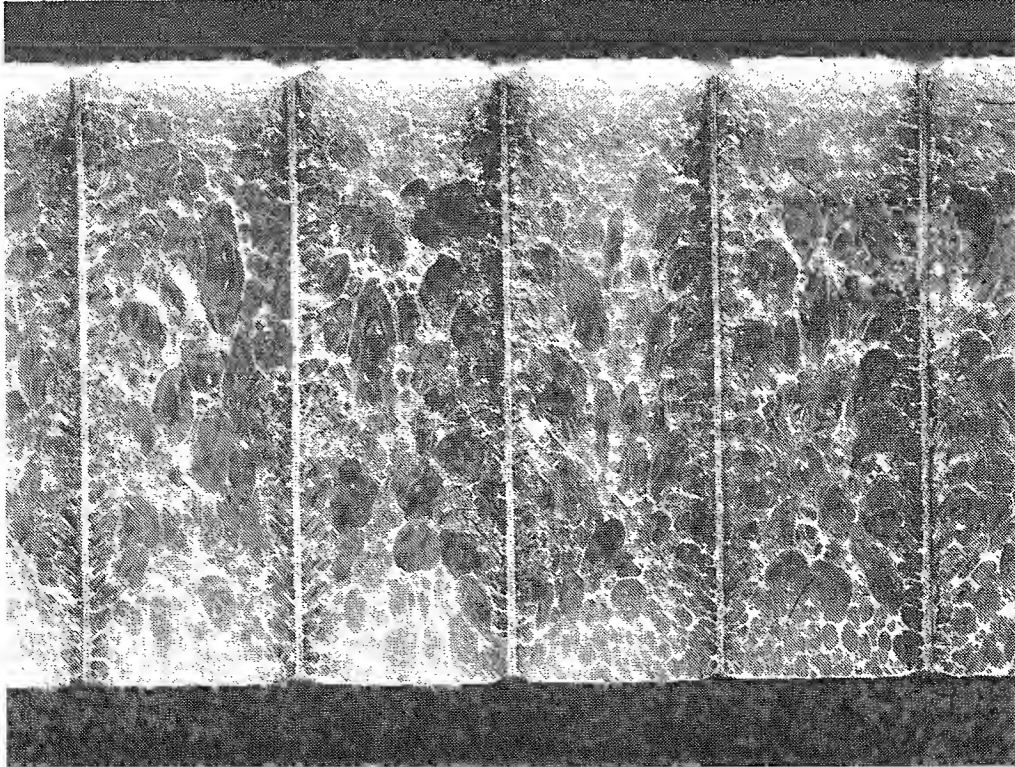


Figure 4-10. Foam-Filled Honeycomb Fabricated with Hexcel's Cyanate-Ester K Foam and HRH-10-1/8-5.0 Honeycomb.

4.3 Heat Forming of Honeycomb Core Materials

Honeycomb core materials often must be heat formed to contour. Cold drape forming trials of the HRP keel core detail indicated that heat forming would be required. Successful heat forming of phenolic matrix honeycomb materials such as HRP must be conducted at temperatures above the glass transition temperature (T_g) of the phenolic resin. Above the T_g , the honeycomb becomes soft and easily deformed. Forming at temperatures below the T_g may result in springback, buckled cell walls, and/or node bond failure. The T_g of incoming phenolic matrix honeycomb materials has been measured to range from 340 to 430°F. The material will likely continue to polymerize/cross link at typical forming temperatures, causing the T_g to rise to a maximum which is dependent on the processing temperature.

The temperature at which forming may be conducted should be limited by the temperature at which oxidation or pyrolyzation of the phenolic matrix occurs. The temperature may also be limited by pyrolyzation of the node bond adhesive (oxidation of the adhesive is not expected to occur because it is protected from the processing atmosphere). Processing at temperatures above that which cause thermal degradation would require an understanding of degradation kinetics and appropriate control over the time of exposure in production.

A process window was determined for heat forming HRP honeycomb core details without degrading the material [9]. The process window was defined to avoid oxidation/pyrolyzation of the phenolic resin matrix and node bond adhesive. The effect of additional polymerization caused by the heat forming process on mechanical properties was also evaluated. The rate of polymerization at typical heat forming temperatures was characterized to aid in definition of specific processes.

Thermogravimetric analysis (TGA) was used to identify temperatures at which oxidation and pyrolyzation may occur in the honeycomb and in the constituent materials. Weight loss was observed in three regimes (Figure 4-11) and was attributed to: volatilization of absorbed water, evolution of additional water as a byproduct of further polymerization, and thermal degradation of the phenolic matrix. The results indicate core forming operations should be conducted at temperatures below 500°F (260°C).

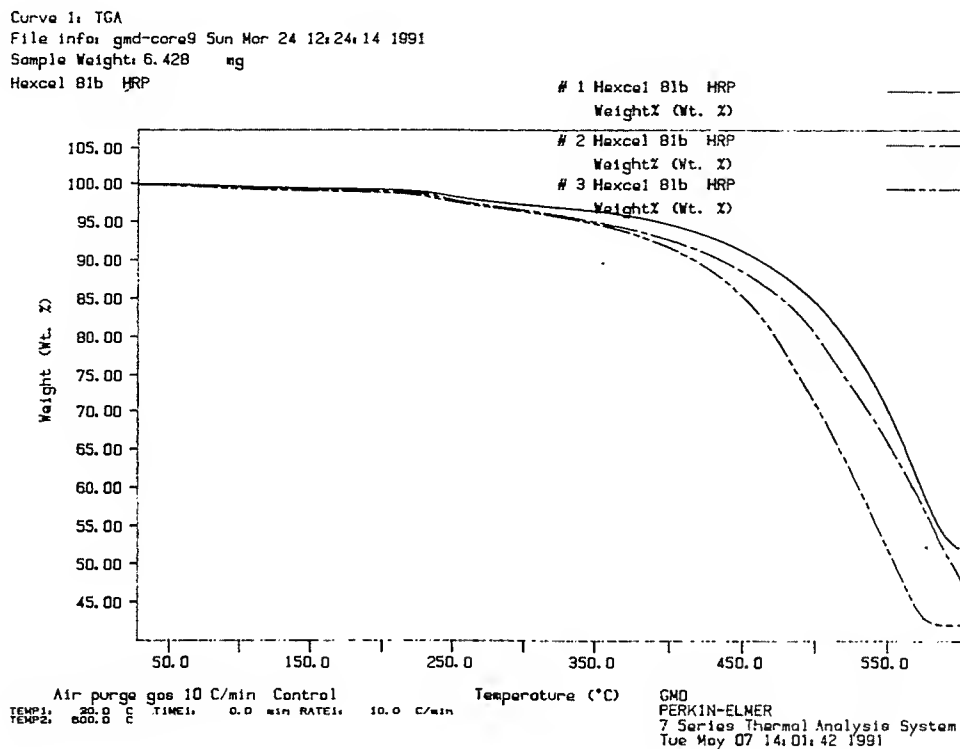


Figure 4-11. Thermogravimetric Analysis of Hexcel's HRP Honeycomb.

Dynamic mechanical analysis (DMA) was used to characterize the rate of polymerization at typical heat forming temperatures. The results of these tests were used to define thermal exposure times and temperatures for mechanical test panels (Figure 4-12).

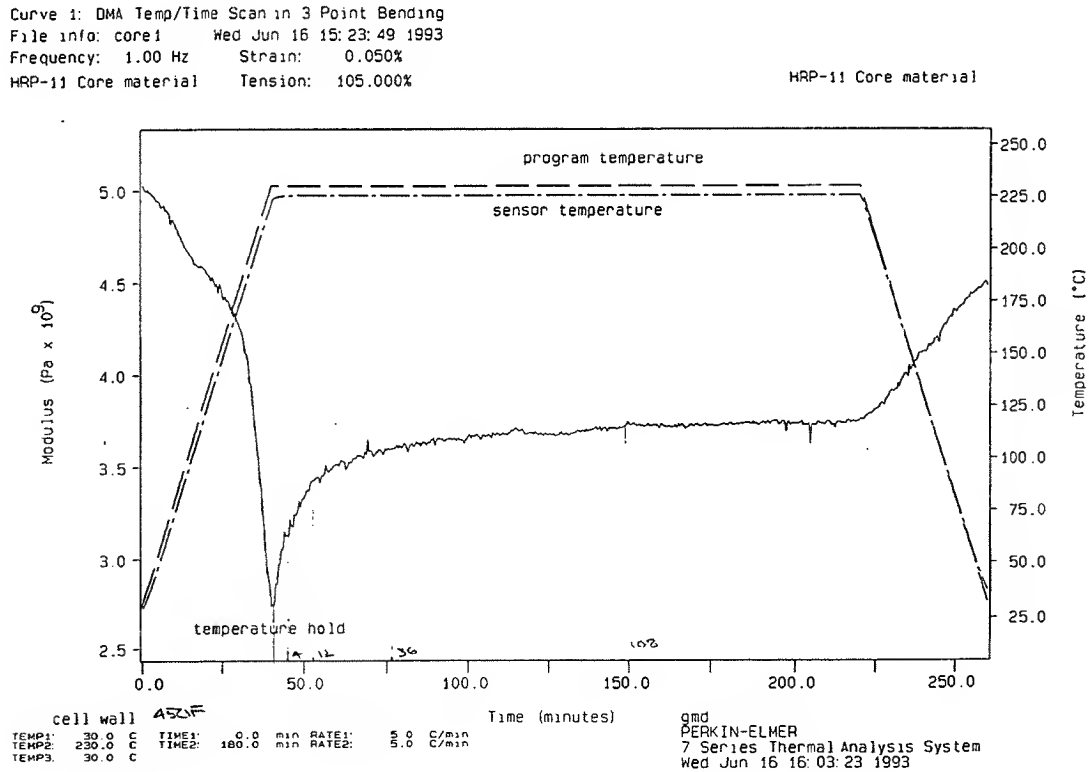


Figure 4-12. Dynamic Mechanical Analysis of Hexcel's HRP Honeycomb.

Test panels representative of the aft keel sandwich structure were fabricated with honeycomb details which had been subjected to various thermal exposures. The sandwich structures were tested for core shear strength as well as impact damage resistance. Shear strength test results were correlated with T_g as an indication of the level of polymerization. The shear strength was reduced only slightly by processing at 450°F as shown in Figure 4-13. Processing at 500°F caused a greater reduction in shear strength.

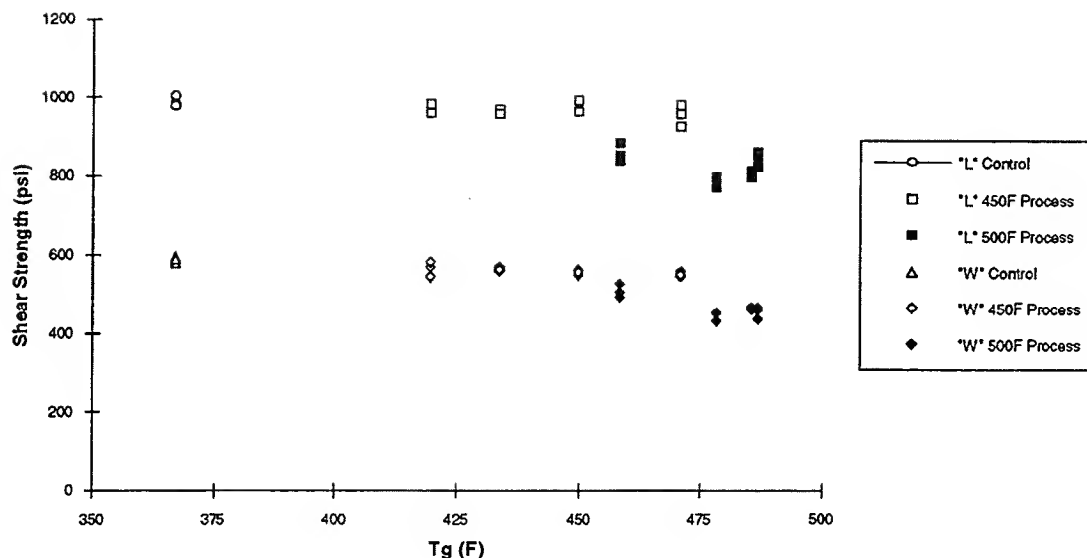


Figure 4-13. Through-Thickness Shear Strength of Hexcel's HRP Honeycomb Following Exposure to Elevated Temperatures. "L" and "W" Indicate Loading Parallel and Perpendicular to the Core Ribbon, Respectively.

Impact surveys were conducted to determine the effect of the thermal exposure on impact damage resistance. The panels were impacted at low velocity with a one inch diameter spherical steel tup at energy levels ranging from 100 to 500 inch-pounds. Through-transmission ultrasonic (TTU) inspection was used to determine the planar extent of impact damage. The reliability of TTU for detecting impact damage in sandwich structures was verified, as discussed in Section 6.1.2. Impact damage resistance was degraded only slightly for processing at 450°F and to a greater extent for processing at 500°F as shown in Figures 4-14 and 4-15. A significant amount of variation was observed in coupons processed at 500°F.

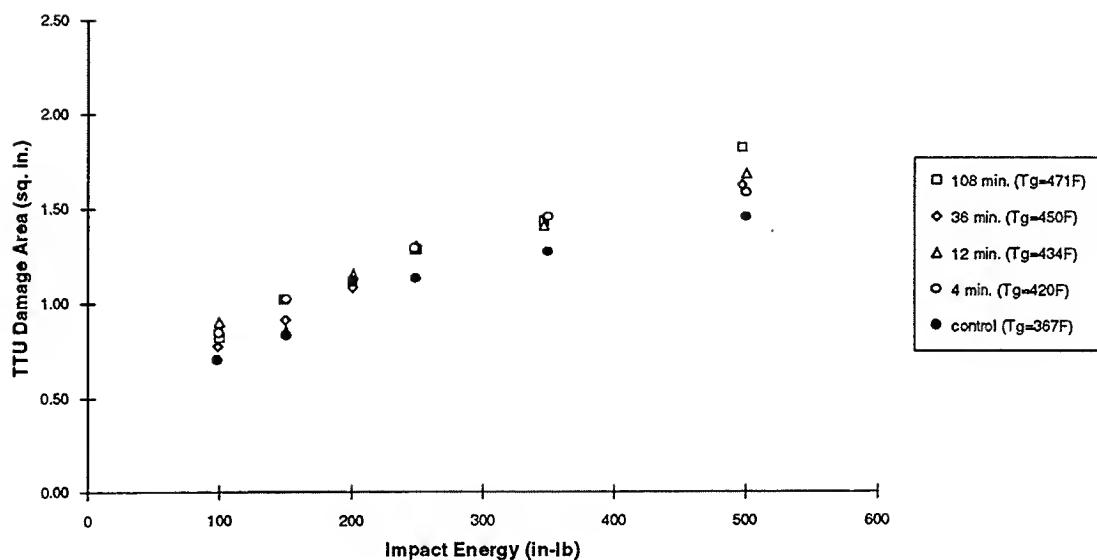


Figure 4-14. Impact Damage Resistance of Hexcel's HRP Honeycomb Following Exposure to 450°F.

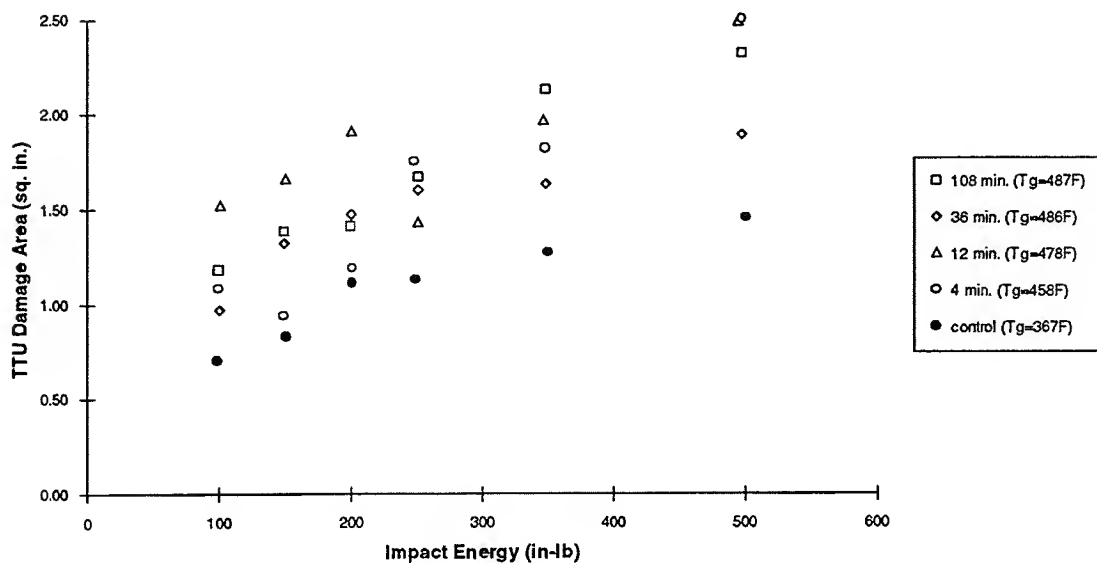


Figure 4-15. Impact Damage Resistance of Hexcel's HRP Honeycomb Following Exposure to 500°F.

Results of mechanical testing described above indicate that heat forming of HRP honeycomb may be conducted at 450°F with little effect on performance. Processing at 500°F should be expected to result in nominal degradation of shear strength and a significant reduction in impact damage resistance. The temperature at which thermal

degradation begins may have been over estimated from results of thermogravimetric analysis because of failure to account for the dynamic nature of the test.

A similar effort was initiated to determine a process envelope for Hexcel's TPC honeycomb. TMA results indicated a T_g of 365° to 390°F. Results of TGA indicated thermal degradation beginning at about 645°F. Results of this preliminary investigation indicate that a heat forming process for Hexcel's TPC honeycomb should be performed between 390° and 645°F. A more detailed study should be performed to confirm this conclusion, especially considering the failure of thermal analyses to accurately identify the temperature at onset of thermal degradation for HRP.

A process window has not been determined for Du Pont's Korex material. However, thermal degradation is expected to occur in the same temperature regime as for HRP because a phenolic matrix resin is used in fabrication of both materials.

4.4 Sandwich Core Close-Outs

The primary design requirements for sandwich core close-outs are to react fastener clamp-up loads and to protect the core from fluid ingress. Ramped core close-outs may also be required to aid load transfer through the eccentric load path imposed on the facesheet.

A variety of sandwich core close-out design concepts were investigated for use at longitudinal and circumferential panel splices and window cutouts. Core close-outs were incorporated into flat test panels and manufacturing demonstration articles which in turn served as configured test panels. All panels were inspected with TTU. The core close-out area was sectioned for optical microscopy, where appropriate, to document microstructure. Core close-out fabrication efforts and results of optical microscopy are described below. Results of fastener clamp-up, bearing/bypass and configured panel splice joint tests are discussed in Section 5. Core inserts for penetrations and attachments to sandwich structures were not pursued beyond development of the design concepts described in Section 3.2.1.

4.4.1 Longitudinal Panel Splices

Full depth and chamfered core close-out concepts were developed for longitudinal panel splices. Three types of full depth close-outs were fabricated. The first concept illustrated in Figure 4-16, consisted of a series of braided and resin transfer molded carbon/epoxy tubes. Individual tubes were braided with 3K and 6K AS4 fiber in a triaxial pattern. Three tubes were then combined and an additional ply braided over the assembly. Shell's RSL 1895 epoxy was used for resin transfer molding. The close-out was bonded to the honeycomb core detail with foaming adhesive prior to incorporation into the panel bond assembly. A cross-section of a core close-out in an aft keel manufacturing demonstration article is presented in Figure 4-17. Note the slight distortion of the horizontal cell walls (and facesheets) due to autoclave pressure.

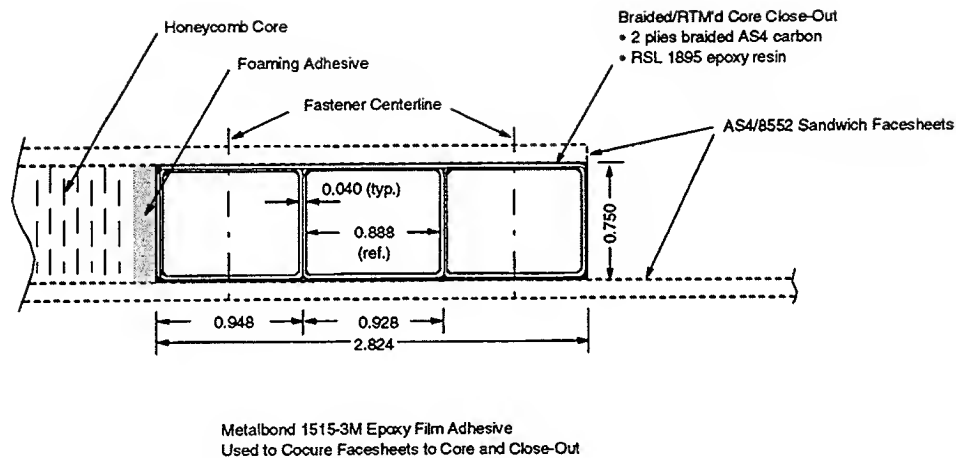


Figure 4-16. Longitudinal Panel Splice Core Close-out Constructed of Braided/RTM'd Carbon/Epoxy Tubes.

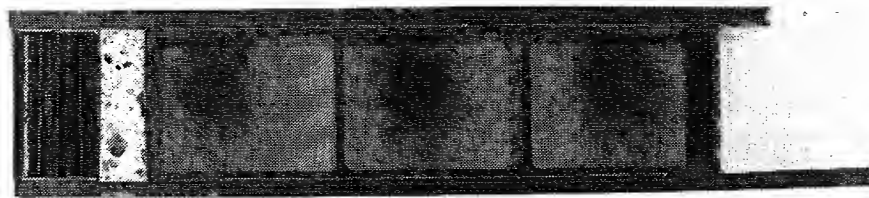


Figure 4-17. Longitudinal Panel Splice Core Close-out Manufacturing Demonstration (Braided/RTM'd Carbon/Epoxy Tubes).

A second design concept (Figure 4-18) consisted of a single braided and resin transfer molded carbon/epoxy tube with a core consisting of solid carbon/epoxy laminate and foam filled honeycomb strips. The solid laminate strips are located along fastener lines to react clamp-up loads. The assembled core serves as a braiding mandrel and fly away resin transfer molding tool. Hexcel's cyanate-ester K foam was used to fill the honeycomb for manufacturing demonstration articles. The K foam proved inadequate to resist RTM mold pressures and became infiltrated with resin. A more robust foam, such as that described below for window cutout core close-outs, would be required to pursue this concept further.

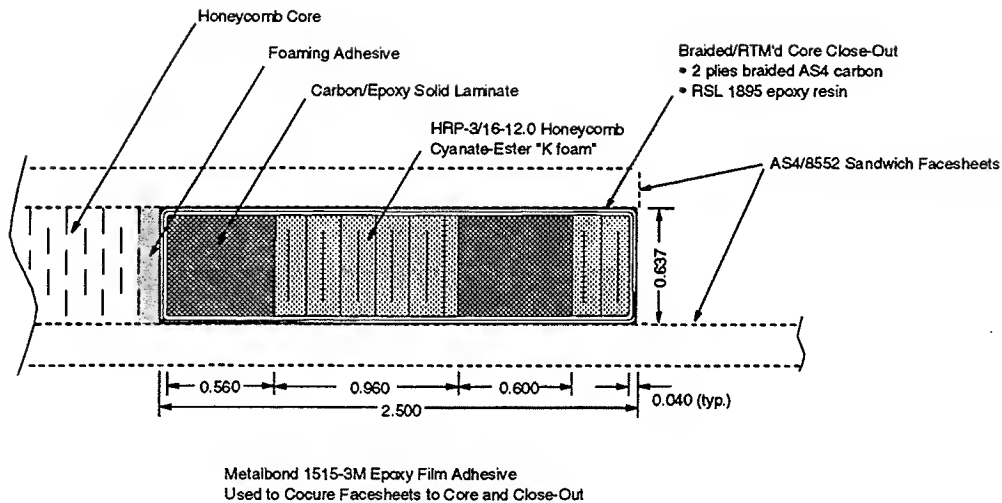


Figure 4-18. Longitudinal Panel Splice Core Close-out Constructed of a Braided/RTM'd Carbon/Epoxy Tube with Solid Carbon/Epoxy Laminate and Foam Filled Honeycomb Core.

Solid laminate and (unfilled) honeycomb strips were cobonded with glass fabric caps in a third full depth concept, illustrated in Figure 4-19. A cross-section of this close-out in a flat test panel is presented in Figure 4-20. Distortion of the facesheets resulted from mismatch of the close-out and core.

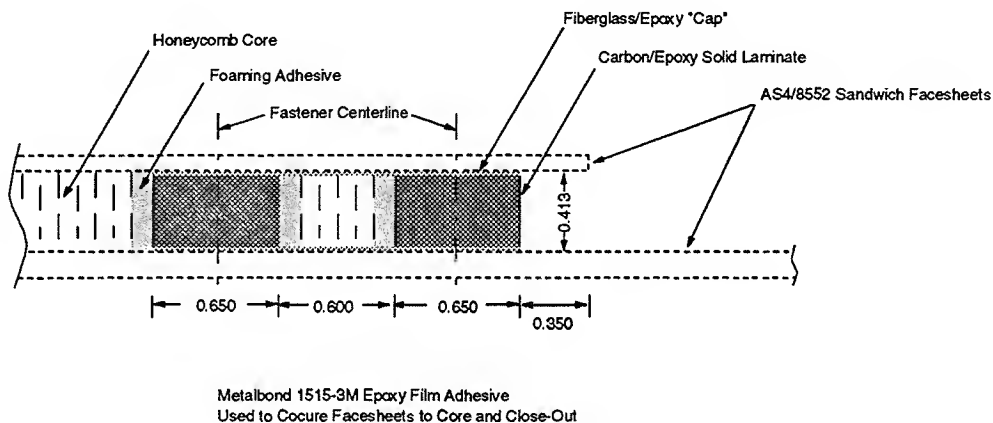


Figure 4-19. Longitudinal Panel Splice Core Close-out Constructed of Solid Carbon/Epoxy Laminate and Honeycomb with Fiberglass/Epoxy Caps.

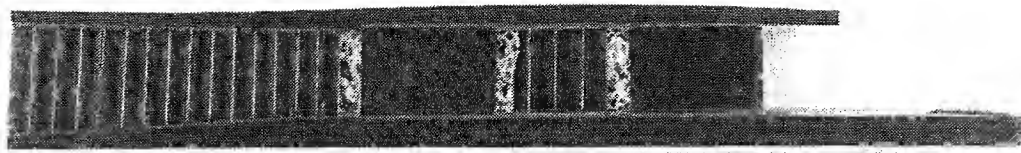


Figure 4-20. Longitudinal Panel Splice Core Close-out Manufacturing Demonstration (Solid Carbon/Epoxy Laminate and Honeycomb with Fiberglass/Epoxy Caps).

One chamfered core close-out concept with laminate edge band was pursued. The design consisted of syntactic foam filled honeycomb with a fiberglass overwrap as illustrated in Figure 4-21. The foam-filled honeycomb was used for improved fastener clamp-up resistance. The fiberglass overwrap was included to improve resistance to fluid ingress and could be fabricated with the braiding/RTM process. A cross-section of the core close-out in a longitudinal splice test panel is presented in Figure 4-22.

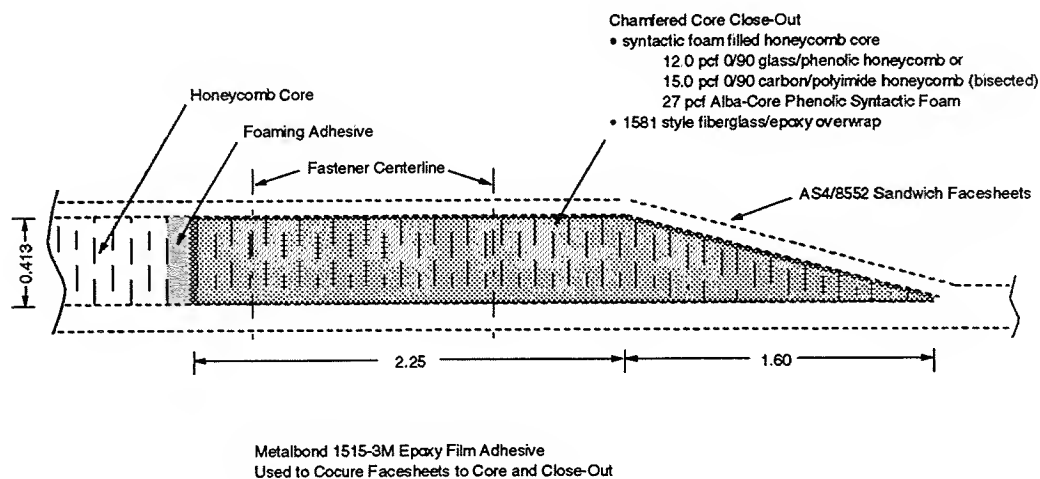


Figure 4-21. Longitudinal Panel Splice Core Close-out Constructed of Chamfered Foam Filled Honeycomb with Fiberglass/Epoxy Overwrap.

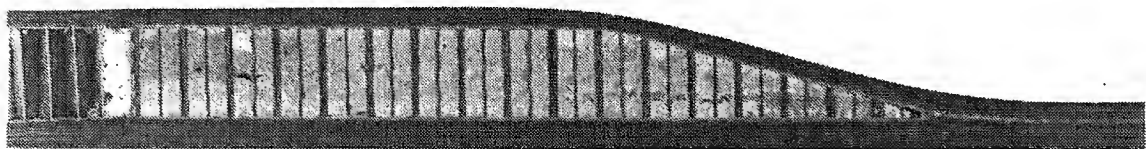


Figure 4-22. Longitudinal Panel Splice Core Close-out Manufacturing Demonstration (Chamfered Foam Filled Honeycomb with Fiberglass/Epoxy Overwrap).

4.4.2 Circumferential Panel Splices

Only full depth core close-out concepts were pursued for circumferential panel splices. All of the concepts exhibited small chamfers on each side of the panel to accommodate splice plates, as illustrated in Figure 4-23. The primary difference between various concepts lay in whether the honeycomb extended through the chamfered area or was replaced by solid laminate in this area. Minor differences in close-outs manufactured for keel and side panels were in the type of core material and in the depth of the core chamfer. A cross-section of a core close-out in a circumferential splice test panel is presented in Figure 4-24.

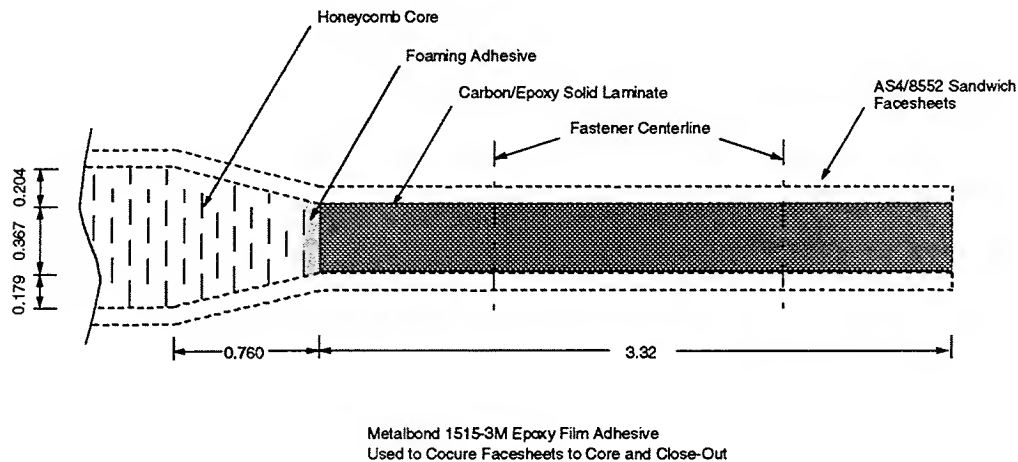


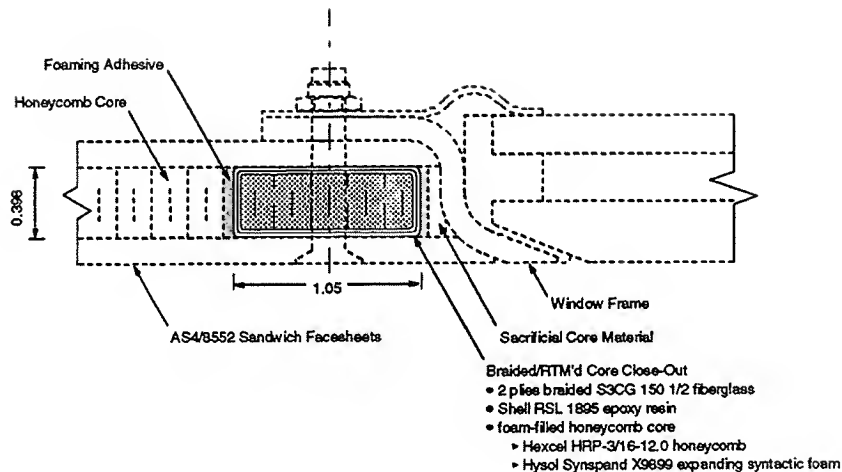
Figure 4-23. Circumferential Panel Splice Core Close-Out.



Figure 4-24. Aft Side Circumferential Panel Splice Core Close-Out Manufacturing Demonstration.

4.4.3 Window Cutouts

Full depth and chamfered core close-out concepts were pursued for window cutouts. Braided and resin transfer molded full depth core close-outs (Figure 4-25) were fabricated by Boeing's Defense and Space Group under Task 20 of task order contract NAS1-18954 [20]. S-2 glass and AS4 carbon fiber were braided in a 2-D triaxial architecture over syntactic foam filled honeycomb mandrels which also served as the close-out core. Shell's DPL 862 epoxy was used for resin transfer molding. A cross-section of a core close-out in a window belt test panel is presented in Figure 4-26.



Cytec Metabond 1515-3M Epoxy Film Adhesive
used for Cocuring the Facesheets to the Core end Close-Out

Figure 4-25. Window Cutout Core Close-Out Constructed of Braided and Resin Transfer Molded Tubes with Syntactic Foam Filled Honeycomb Core.

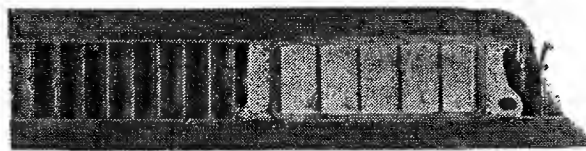


Figure 4-26. Window Cutout Core Close-Out Manufacturing Demonstration (Braided and Resin Transfer Molded Fiberglass/Epoxy Tubes with Syntactic Foam Filled Honeycomb Core).

Full depth solid fiberglass/epoxy laminate core close-outs (illustrated in Figure 4-27) were employed in one sub component test panel. Cross-sections of these close-outs are not available because the entire manufacturing demonstration article is being used for structural test.

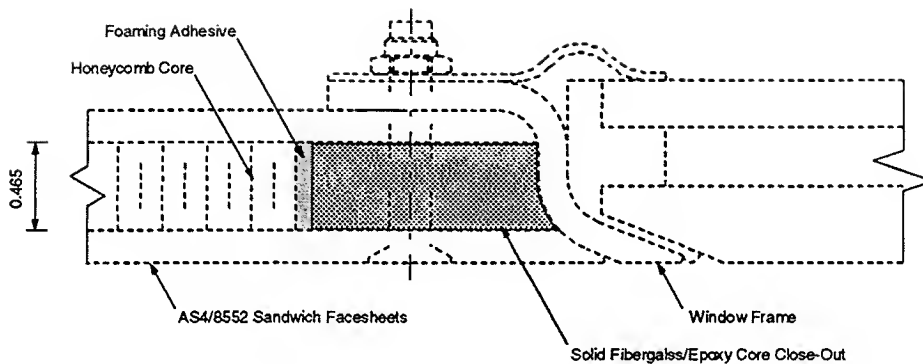


Figure 4-27. Window Cutout Core Close-Out Constructed of Solid Fiberglass/Epoxy.

One chamfered core close-out configuration was investigated for window cutouts. The facesheets are drape formed over a chamfered core detail to provide a laminate edge band as shown in Figure 4-28. A 30° chamfer is desired to provide adequate area for bonding of the circumferential frame to the sandwich structure between windows. Selective cutting of prepreg tows in the area of the core chamfer may allow drape forming around the elliptical detail without wrinkling the facesheet material as described in [6]. Staggering of prepreg tow cuts should result in little effect on the strength and durability of the facesheet material, although this must be verified. A manufacturing trial was performed with prepreg tape which was cut in a representative manner. A cross-section of the chamfered region is presented in Figure 4-29. The bagside facesheet was successfully drape formed over the core chamfer with no bridging or porosity. No wrinkles were observed in the facesheet.

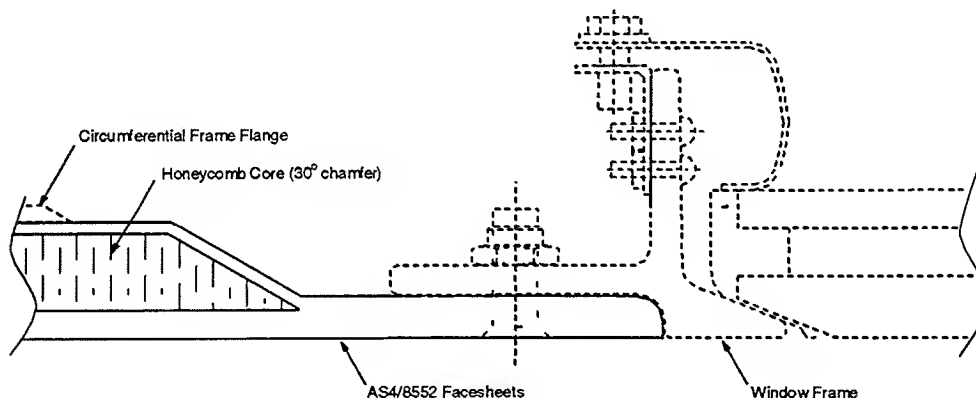


Figure 4-28. Ramped Core Close-Out Design Concept for Window Cutouts.

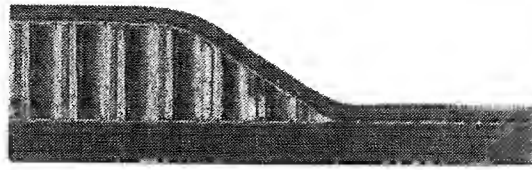


Figure 4-29. Ramped Core Close-Out Manufacturing Demonstration.

Additional ramped core/laminate edge band design concepts were pursued by Lockheed under their ACT contract [NAS1-18889].

4.5 Braiding and Resin Transfer Molding

Braiding and resin transfer molding were identified as the most cost efficient means of fabricating composite circumferential frames [2, 3] with a novel manufacturing plan described in [4]. Advancements in braiding and RTM technology were pursued through both analytical and experimental efforts [21]. Two dimensional (2-D), 2-D triaxial (illustrated in Figure 4-30), and three dimensional (3-D) braid patterns were investigated. Although intermediate modulus fiber may be more structurally efficient for stiffening elements, AS4 fiber was chosen for the development effort because it was deemed less likely to be damaged during the braiding process. Shell's DPL-862 epoxy resin was chosen for development of the molding process and for early mechanical property characterization because of its low cost and manufacturing properties (rheometrics). Shell's RSL 1895 epoxy resin was later adopted for development of circumferential frames because the DPL-862 was found to possess inadequate mechanical properties. RSL 1895 is no longer produced by Shell. 3M's PR-500 fluorinated epoxy is an attractive alternative resin which was selected by Lockheed for further development of circumferential frames under their ACT contract [NAS1-18888]. Braiding and consolidation of commingled AS4/PEEK yarn was also pursued as an alternative process [21].

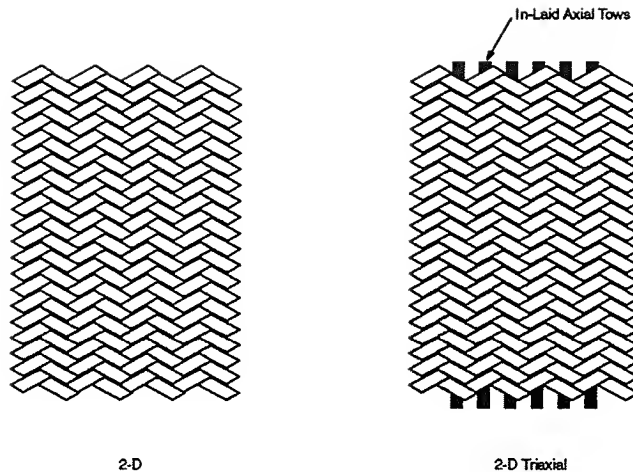


Figure 4-30. Braided Composite Fiber Architectures Investigated by the ATCAS Program.

Preliminary development of the braiding and resin transfer molding processes with the DPL-862 resin was accomplished through a series of processing trials [21]. The quality of processing trial panels were evaluated via non-destructive and destructive techniques. Fiber orientation in mechanical test panels was evaluated by surface measurements and radiographic inspection (x-ray opaque tracer yarns were included in fiber preforms). Ultrasonic inspection was found to be of marginal value for detecting porosity and voids in braided composites because of a large difference in attenuation between areas with high and low fiber volume, which are inherent to the fiber architecture. Optical microscopy and resin digestion tests were used to characterize fiber and void volume. Critical process parameters were adjusted until no further improvements in part quality could be achieved. The resulting process was used in fabrication of mechanical test panels with 2-D triaxial and 3-D braid architectures. Large variations in braid angle ($\pm 5^\circ$) were observed within and between mechanical test coupons. Fiber volume was found to vary by up to 9% from the nominal 60%. Void volumes of up to 3% in 2-D braided and up to 6% in the 3-D braided composites were measured.

The process was optimized for circumferential frames with Shell's RSL 1895 resin. Three 2-D triaxial braid architectures were pursued. A series of circumferential frames, three feet in arc length, were fabricated along with additional mechanical test panels. Improvements in the preform handling procedure reduced variations in braid angle to within $\pm 2.5^\circ$ in mechanical test panels. Fiber volume was found to be within 5% of the target value of 55%. Void volume was reduced to $\leq 0.5\%$ with the RSL 1895 resin (Figure 4-31). The quality of the frame manufacturing trials were found to be consistent with the flat mechanical test panels.

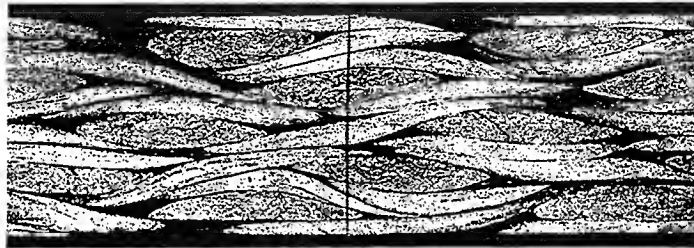


Figure 4-31. Microstructure of 3' Braided/RTM'd Circumferential Frame Manufacturing Process Development Article.

Circumferential frames of eight foot arc length were manufactured to address scale-up issues as discussed in [6], and for use in sub component panels. Surface porosity noted in one region of each frame during initial efforts was eliminated through minor process adjustments. Ultrasonic inspection indications running the length of some frames were found to be a result of stacking (instead of nesting) of axial tows in adjacent plies as shown in Figure 4-32 [6, 22]. The associated areas of high and low fiber volume resulted in large differences in ultrasonic attenuation as discussed above.

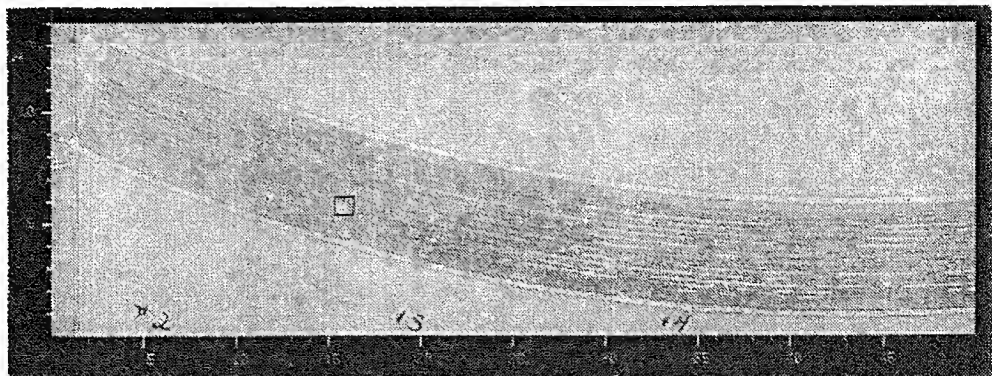
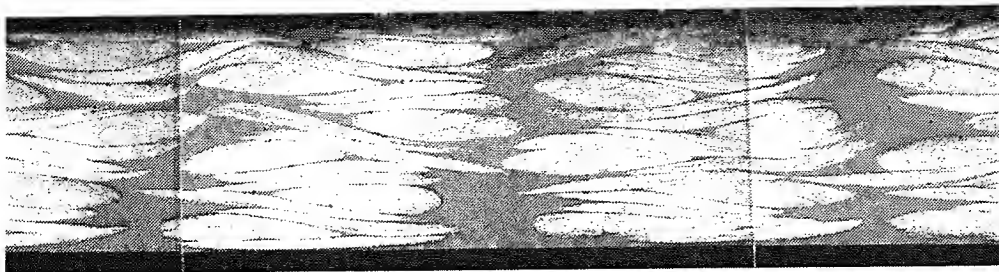


Figure 4-32. Microstructure of 8' Braided/RTM'd Circumferential Frame Manufacturing Demonstration Article. The Stacked Axial Tows Resulted in Variations in Ultrasonic Attenuation as Shown in the C-Scan.

Analytical methods which were developed to predict stiffness, stresses from environmental and mechanical loads, failure mechanisms, and the progressive failure history of braided composites [21] are described in Section 5.4.1. Results of mechanical test programs intended to characterize the performance of the braided composite panels described above are discussed in Sections 5.4.2 and 5.4.3.

Braiding and resin transfer molding were also employed in fabrication of sandwich core close-outs as discussed in Section 4.4.

4.6 Autoclave Cure

4.6.1 Stiffened Skin Structure

Little effort was expended in development of the autoclave cure cycle for stiffened skin structure with Fiberite's 938 matrix resin. A significant level of experience has been gained through production manufacture of parts with similar resin systems (e.g., Fiberite's 934). The manufacturer's recommended cure cycle was used by Hercules in fabrication of crown test articles. Minor surface porosity was eliminated through the use of peel ply on the part surface. Resin flow during cure resulted in resin content variations and resin flash around design details. Tooling modifications partially resolved this problem [6]. A more generalized solution may be achieved through alteration of the cure cycle and resin rheometrics to increase the minimum viscosity and reduce resin flow during cure.

4.6.2 Thick Laminate/Sandwich Structure

Keel and side panels exhibit thick laminates which transition into sandwich structure in areas of reduced loads. This structural configuration poses significant processing challenges. Cure of the epoxy matrix must be accomplished in a timely manner while avoiding uncontrolled exotherm. Low cycle time is desirable to limit capital expenditures for tooling and autoclaves while maintaining production rates. However, exotherm during the autoclave cure may result in damage to the part and tooling, and presents a safety hazard. The mechanical properties of epoxy resins are typically dependent on degree of cure. Competing reactions may even result in path dependent properties. An understanding of reaction rate kinetics and of the influence of the cure cycle on matrix properties is therefore required to define an efficient cycle which will avoid exotherm and provide uniform properties in the end item.

Concurrent consolidation of both thick laminate and sandwich facesheets must be accomplished while avoiding core crush or excess resin bleed from the part edges or into the core. Complete consolidation (i.e. no porosity) is desirable to achieve optimal mechanical performance and to provide a reliable barrier for moisture ingress into the core. Application of vacuum is typically used to draw air and volatiles from the system and compact the part. Autoclave pressure is then used to overcome the vapor pressure of remaining volatiles, and to force resin flow. The resin must exhibit a minimum viscosity which will allow flow for consolidation but inhibit excess resin bleed from the part. This

balance of rheology is intensified when cocuring sandwich structure where the autoclave pressure is reacted over a small portion of the part surface area and the resin may be pushed through the fiber bed into the core. Appropriate resin rheology and cure cycle thermal profile are therefore critical to proper consolidation of the keel and side panels.

A combined empirical and analytical approach was taken in development of a process for cocuring thick laminate/sandwich structure [9]. The reaction rate kinetics and rheology of 8552 epoxy were characterized. Results of dynamic differential scanning calorimetry (DSC) were used to confirm the ability to predict the reaction rate of the system. An auto catalytic kinetic model of the primary reaction adequately represents the data during the initial portion of the exotherm, as shown in Figure 4-33. The prediction diverges from experimental data as a second exothermic process begins at higher temperatures. Further refinement of the kinetic model to account for the second reaction were not pursued because the reaction progresses at a very slow rate at the cure temperature.

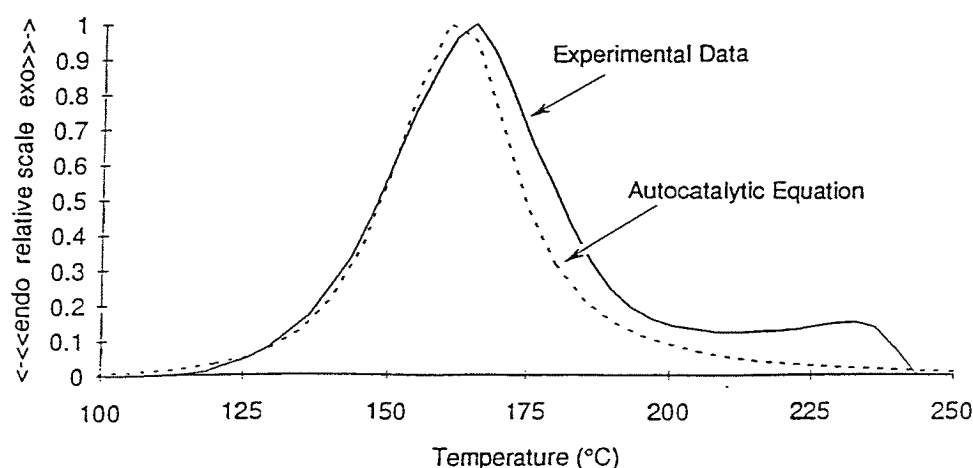


Figure 4-33. Comparison of Reaction Rate Kinetics of the 8552 Resin System with the Prediction of an Auto Catalytic Model.

The influence of cure cycle variations and extended time at cure temperatures on the performance of 8552 composites were evaluated by measurement of in-plane lamina shear modulus and modes I and II interlaminar fracture toughness. Mode I fracture toughness exhibited the greatest sensitivity to variations in the cure cycle. Mode I fracture toughness decreased by 14% from nominal under the most severe cure cycle tested (24 hours at 365°F), but is expected to vary by only 5% in a typical production environment. A good correlation of fracture toughness with residual heat of reaction for various cure cycles (Figure 4-34) indicates a path independent relationship between level of cure and mechanical performance.

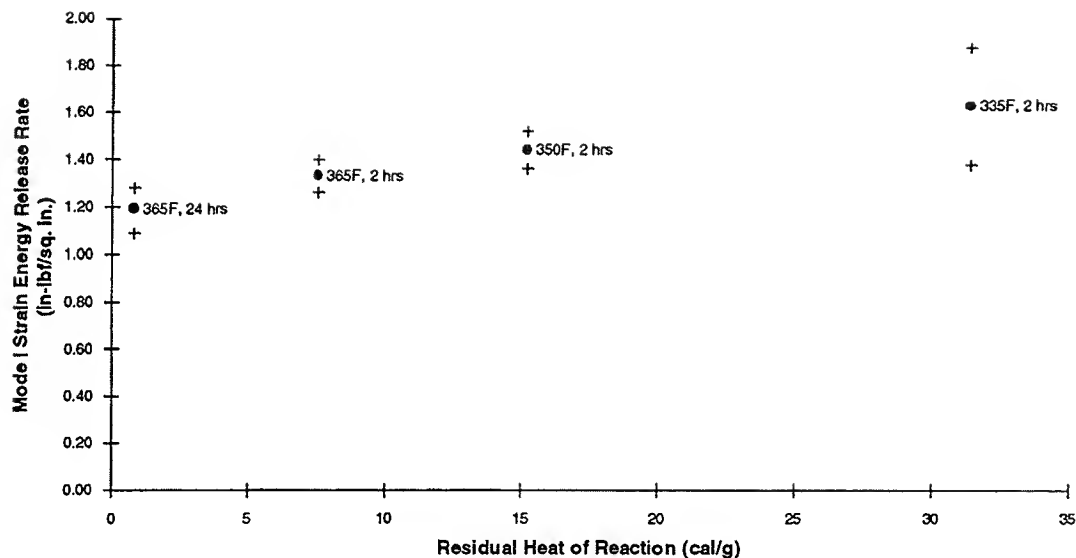


Figure 4-34. AS4/8552 Mode I Strain Energy Release Rate as a Function of Residual Heat of Reaction for Various Cure Cycles.

An instrumented sub component processing trial (Figure 4-35) was performed to verify heat transfer analyses and evaluate the quality of structure cured with a step cure process recommended by Hercules. Temperature data compiled during the process trial verified the prediction of an exotherm during a 300°F dwell as shown in Figure 4-36. The results provided confidence in the ability to predict the thermal profile of a large part during autoclave cure. Subsequent modeling efforts and processing trials showed that the use of heavy Invar tooling (typical of production) inhibits exotherm by acting as a heat sink. The baseline cure cycle has been simplified by elimination of the 300°F dwell which was originally intended to bleed energy from the system and avoid exotherm.

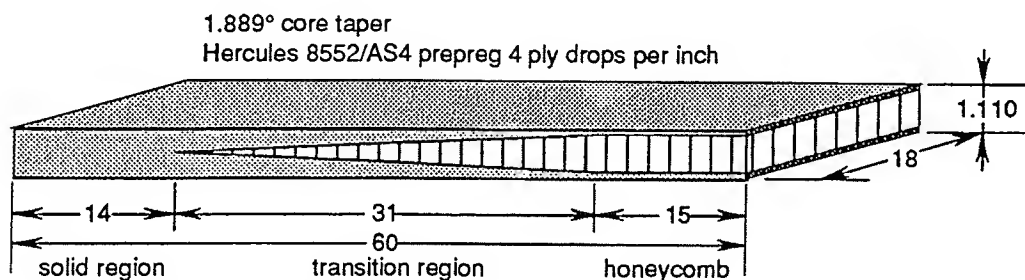


Figure 4-35. AS4/8552 Thick Laminate/Sandwich Process Trial Panel

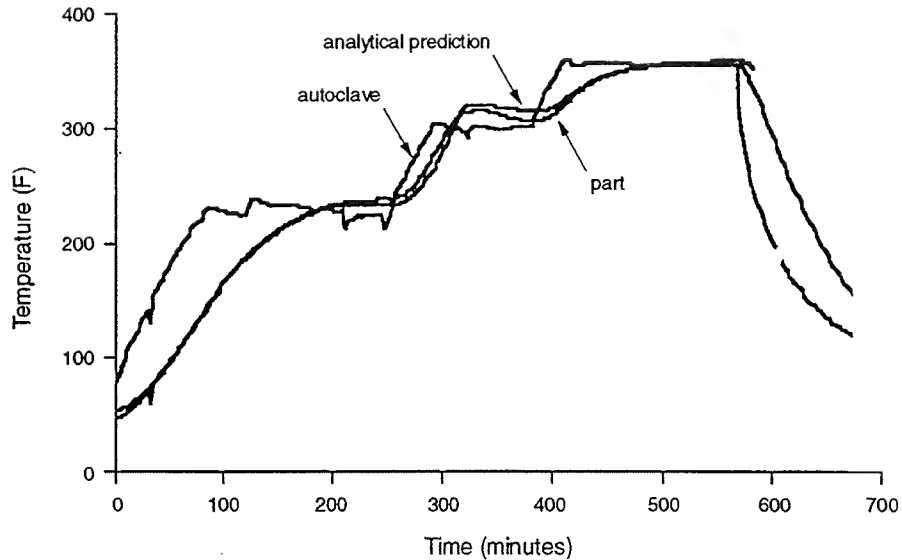


Figure 4-36. Comparison of Analytical and Experimental Results for the Thermal Response of the Process Trial Panel.

Sectioning and optical microscopy revealed good consolidation in both thick laminate and sandwich facesheet regions of the panel. Excess resin bleed was not observed from the part edges or into the core. Poor filleting of the film adhesive to the honeycomb cell walls was the sole anomaly noted in the panel. The significance of the poor adhesive fillets has not been determined.

Modification of the level of advancement of the prepreg tow to support efficient fiber placement resulted in minor porosity in some sandwich panels cured with the modified baseline cure cycle. Further modification of the prepreg tow resin chemistry and level of advancement to provide adequate out-time may amplify this problem. Additional process development work will be required to define a robust cure cycle for the final material form.

5.0 MECHANICAL PERFORMANCE OF SELECTED MATERIALS

The mechanical performance of selected materials were characterized to aid in material selection, and to provide the engineering community with the material properties of interest for the design and analysis of composite fuselage structures.

5.1 Fuselage Skin Materials

The stiffness, strength, notch sensitivity, and bearing/bypass properties of candidate skin materials were characterized. Efforts were focused on the baseline materials selected for the crown (AS4/938) and for the keel and side (AS4/8552). Other materials and material forms, including intermediate modulus fiber, interlayer toughened systems, and intraply hybrids (see Section 4.1.2), were considered. Plain weave fabric plies were incorporated on the surfaces of some laminates and sandwich facesheets. The influence of manufacturing process and process variations were investigated. Laminates fabricated with the fiber placement and tape lamination processes were tested. Both BCA and TCA fiber placement heads were employed.

5.1.1 Stiffness

Lamina moduli of candidate fuselage skin material systems are presented in Table 5-1. Lamina moduli were initially determined from unidirectional test data obtained from the literature and material suppliers. Micromechanics [23] were used to normalize test data to the appropriate fiber volume and to estimate values for which data was not available. The use of lamina modulus values obtained from unidirectional test coupons for predicting laminate modulus with classical laminated plate theory was found to be inaccurate. The compression modulus of AS4/938 coupons cut from configured test panels was measured to be 10 to 20% lower than predicted by laminated plate theory [13]. Results from coupon level tests of fiber placed and tape laminates were comparable. However, lower stiffness was observed in fiber placed panels during crippling tests. The lower stiffness of fiber placed panels may have been a result of fiber waviness which was not observed in tape laminates. The shear modulus of fiber placed laminates was also measured to be lower than expected and lower than that of tape laminates. The moduli of AS4/8552 laminates and sandwich structures were also measured to be lower than those predicted by laminated plate theory. No significant differences were observed between AS4/8552 laminates fabricated with the fiber placement and tape lamination processes nor between laminates and sandwich structures.

Table 5-1. Lamina Moduli of Candidate Material Systems as Determined from Unidirectional Test Data and Micromechanics. Values in Brackets were Derived from Multidirectional Laminates.

Form	Material	R.C. (%w/o)	V _f (%v/o)	E ₁ ^t (msi)	E ₁ ^c (msi)	E ₂ (msi)	G ₁₂ (msi)	ν ₁₂
Tape/Tow	AS4/938	35.0	56.8	19.6 [18.3]	18.8 [16.0]	1.36	0.72	0.32
	S-2/938	27.8	56.6	7.40	7.00	2.16	0.77	0.26
	T300/F584	38.0	55.4	17.5	15.9	1.28	0.66	0.34
	AS4/8552	35.0	57.4	18.8 [18.1]	17.8 [16.3]	1.36	0.76	0.32
	AS4/8553-40	40.0	53.3	17.9	16.3	1.31	0.65	0.34
	IM6/937	35.0	57.2	22.1	20.1	1.34	0.70	0.33
	IM7/8552	35.0	58.0	22.4	18.4	1.39	0.71	0.33
	IM7/8551-7	35.0	57.3	21.9	20.0	1.20	0.66	0.34
Plain Weave Fabric	AS4/938	38.0	53.6	9.5	8.6	*	0.68	0.044
	AS4/8552	38.0	54.2	9.2	8.7	*	0.72	0.046
	IM7/8552	38.0	54.7	11.2	9.7	*	0.70	0.041

* use values for E₁

Results from multidirectional laminate coupons were used to update lamina modulus values for AS4/8552 and AS4/938 tow materials. The axial lamina moduli required to accurately predict the measured modulus of each laminate was determined for tension and compression loading. The averages of these values are listed in the table in brackets. Other lamina moduli, which play a minor role in determination of laminate modulus, were not adjusted. The modulus of each laminate was then predicted with the updated lamina moduli to provide visibility of the error which may be expected from use of the updated values. A graphical comparison of predicted and measured laminate modulus for AS4/8552 is provided in Figures 5-1 through 5-3.

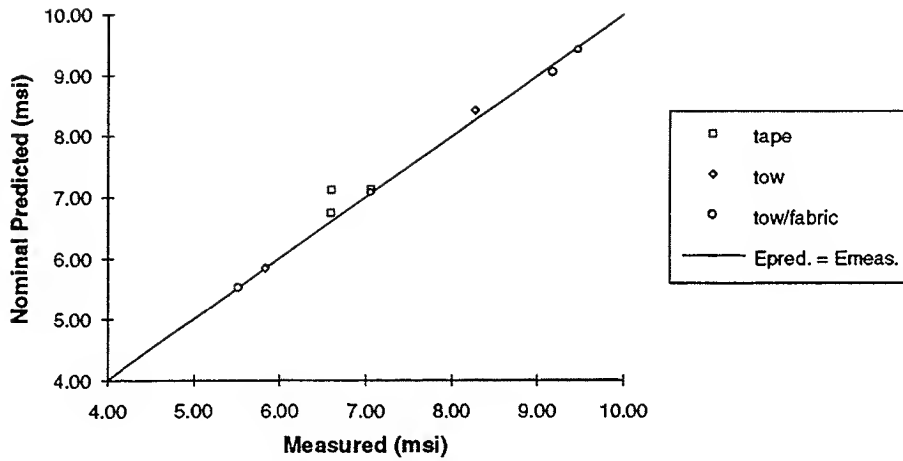


Figure 5-1. *Predicted and Measured Young's Moduli for Tensile Loading of AS4/8552 Laminates.*

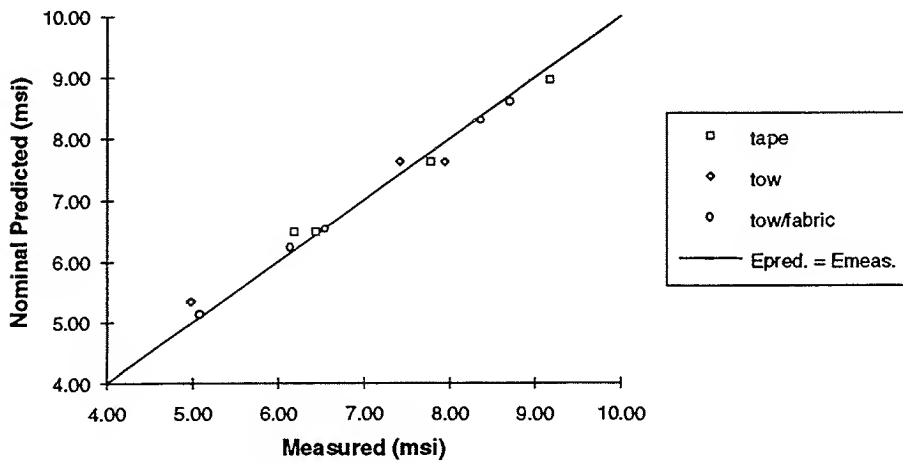


Figure 5-2. *Predicted and Measured Young's Moduli for Compression Loading of AS4/8552 Laminates.*

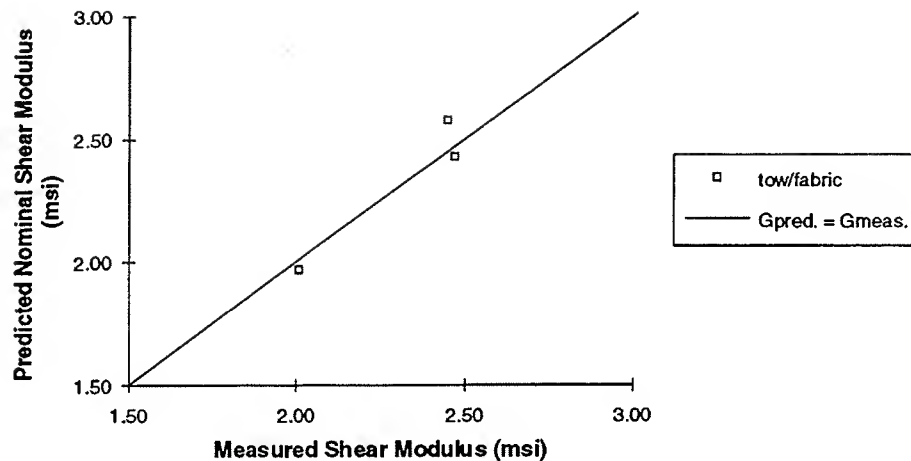


Figure 5-3. Predicted and Measured Shear Moduli of AS4/8552 Laminates.

The adjusted values of lamina axial moduli are 9 to 18% lower than those obtained from unidirectional test data with the greatest difference in values for compression modulus of AS4/938. This may be partially attributed to fiber distortion observed in some fiber placed laminates and is based on a relatively small number of coupons. However, the value is consistent with that used by McGowan [24] to accurately model the behavior of a five stringer crown compression test panel. The lamina modulus values for AS4/938 should be verified with attention to the amount of fiber distortion in the test coupons. Similar reductions in effective lamina moduli should be expected for the other materials.

The influence of extreme temperatures and of absorbed water on the modulus of a quasi-isotropic AS4/8552 laminate with fabric surface plies was investigated. Laminate modulus at -65°F was observed to be 5 to 6% higher than at room temperature for tension and compression loading. Hot/wet conditions had no significant effect on tension modulus but degraded compression modulus by 4%.

5.1.2 Strength and Notch Sensitivity

The strength and notch sensitivity of candidate fuselage skin materials were investigated to support ultimate strength and damage tolerance analyses. Unnotched and center-notched laminates and sandwich structures were tested in uniaxial tension and compression. Unnotched tests were performed primarily for material quality assurance purposes and for determination of laminate stiffnesses as discussed above. Unnotched strength data were also used to aid reduction of notched strength data and to support development of analytical methods. Machined slits were used to represent the range of less-defined damage states that can occur in service for damage tolerance analyses. The validity of representing through-penetrations with machined notches was investigated on a limited basis. The influence of test specimen geometry and strain rate were considered. Open and filled-hole tension and open-hole compression tests were also performed and are discussed in Section 5.1.3.

Tensile Strength and Notch Sensitivity

The tensile strength of coupons with through-penetrations created by impact with a blade were within 10% of those with machined notches of the same size (as the blade) in most cases as shown in Figure 5-4 [14]. One exception in which the residual strength of the lone toughened-matrix laminate with a through-penetration was significantly (~20%) lower than with a machined notch was likely a result of fiber failure beyond the width of the blade during the impact event. This impact damage state was identified via destructive evaluation (thermal deply). Significantly higher through-penetration residual strengths were observed in two of the thickest laminates with untoughened matrices. A large amount of matrix damage sustained during the impact event may have acted to blunt the stress concentration in these coupons.

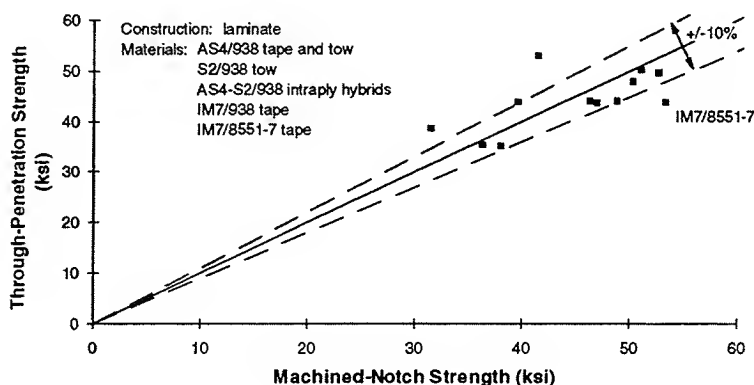


Figure 5-4. Comparison of the Residual Tensile Strength of Laminates with Through-Penetrations and Machined Notches.

Non-classical material responses were observed in tension test coupons with machined notches. Notch tip strain distributions were less severe than predicted by classical methods, even before damage initiation as shown in Figure 5-5 [15, 17]. Reduced notch sensitivity was noted in coupons with greater deviation from a classical square-root singularity. A strain softening effect which results in further deviation from a classical linear-elastic response has been shown to accompany the accumulation of notch tip damage [5].

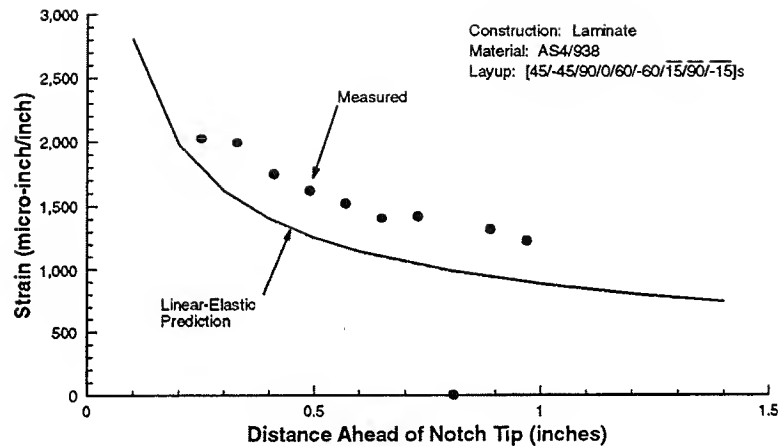


Figure 5-5. Non-Classical Material Response in a Fiber Placed AS4/938 Laminate Prior to Notch Tip Damage Formation.

Strong coupon finite width effects were also observed, particularly in those materials which demonstrated reduced notch sensitivity. Isotropic finite width correction factors, which have been found to differ only slightly from similar orthotropic factors [25], did not adequately account for finite width effects as shown in Figure 5-6 [14, 15]. Failure of the correction factors to account for finite width effects is another indication of the non-classical material response.

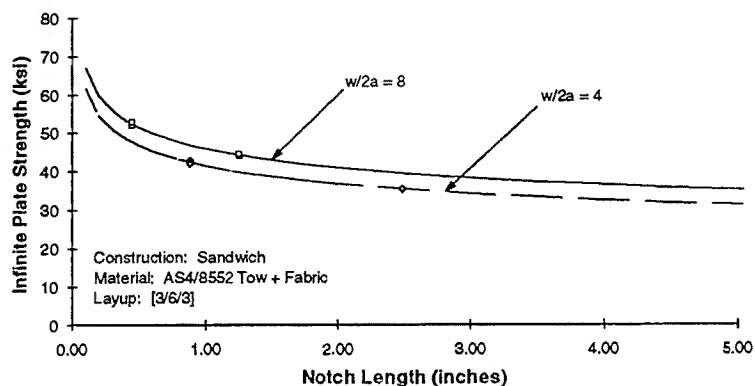


Figure 5-6. Failure of Linear-Elastic Correction Factor to Account for Finite Width Effects in Tension ([X/Y/Z] indicates the number of plies in the [0/± 45/90] orientations).

The non-classical elastic material response and strain softening which accompany notch tip damage accumulation result in flatter residual strength curves than are predicted by classical methods. The functional form of the Mar-Lin fracture model allows reduced

notch sensitivity to be addressed through the use of non square-root singularities [26]. This functional form has been used to predict large-notch strength from small-notch data with moderate success as shown in Figure 5-7 [14, 15, 17]. Residual strength vs. notch length curves were constructed from test data with this method to aid in the following discussions.

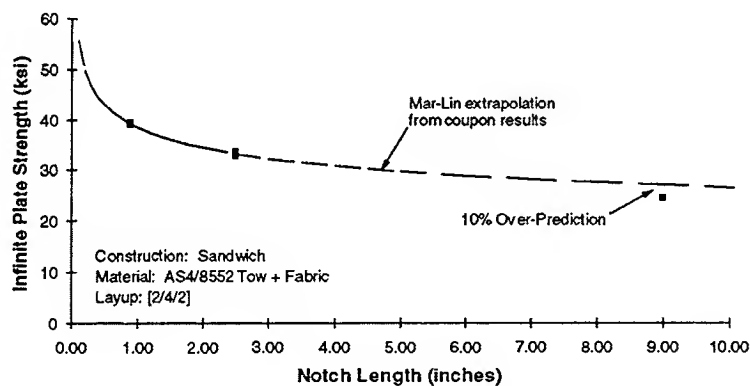


Figure 5-7. *Prediction of Large Notch Strength from Small Notch Data with the Functional Form of the Mar-Lin Fracture Model ([X/Y/Z] indicates the number of plies in the [0/ \pm 45/90] orientations).*

Influence of Material Type and Construction on Tension Fracture Performance

A wide range of material variables affected the tensile strength of coupons with machined notches. Laminates constructed with intermediate modulus fiber in an untoughened matrix (e.g., IM6/937A) exhibited residual strengths which were superior to similar laminates made with standard modulus fiber as shown in Figure 5-8 [14].

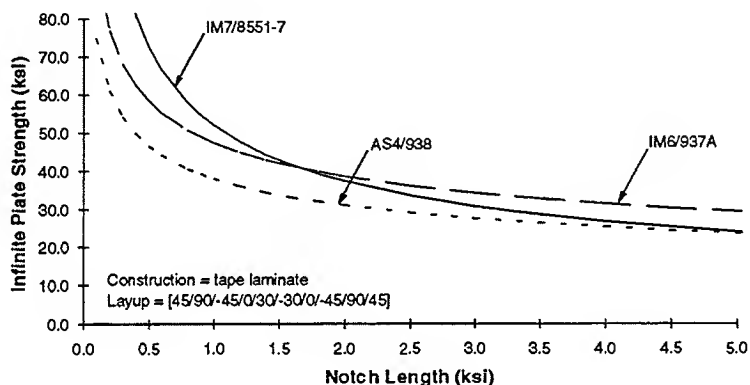


Figure 5-8. *Tensile Notch Sensitivity of Several Candidate Fuselage Skin Materials.*

Laminates with toughened matrices (e.g., IM7/8551-7), which inhibited the creation of notch tip damage, demonstrated higher small-notch strengths [14, 15, 17]. However, laminates with untoughened matrices, which exhibited a large amount of notch tip damage at low stress levels, exhibited higher large-notch strengths. A trade-off between small-notch performance (i.e., strength) and large-notch performance (i.e., toughness) is the result, as shown in the figure. This trade-off was most pronounced in hard layups (with a high percentage of plies oriented in the loading direction). The superior large-notch performance of the untoughened matrix composite is due to a reduction of the notch tip stress concentration with the accumulation of damage. The inferiority of the untoughened matrix composite in the small notch regime may have been exaggerated by the use of small coupons, in which little edge margin was available for damage growth. A significant implication of these behaviors is that small notch tests (e.g., 1/4" open- or filled-hole tension) should not be used to screen materials for applications in which large-notch behavior is critical.

A similar strength-toughness trade-off was observed between laminates of the same material with differing layups [14, 15, 17]. Hard layups demonstrated high strength but low toughness when compared to soft layups, as shown in Figure 5-9. This behavior was most pronounced in toughened matrix composites.

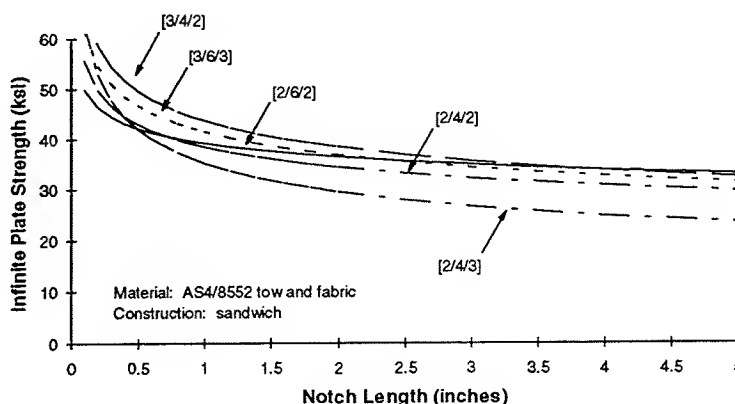


Figure 5-9. *Influence of Layup on Tensile Notch Sensitivity of AS4/8552 Sandwich Structure ([X/Y/Z] indicates the number of plies in the $[0/\pm 45/90]$ orientations).*

Intraply hybrids of AS4 carbon and S-2 glass fiber in a 938 matrix (described in Section 4.1.2) demonstrated superior large-notch tension fracture performance as shown in Figure 5-10 [14, 15, 17].

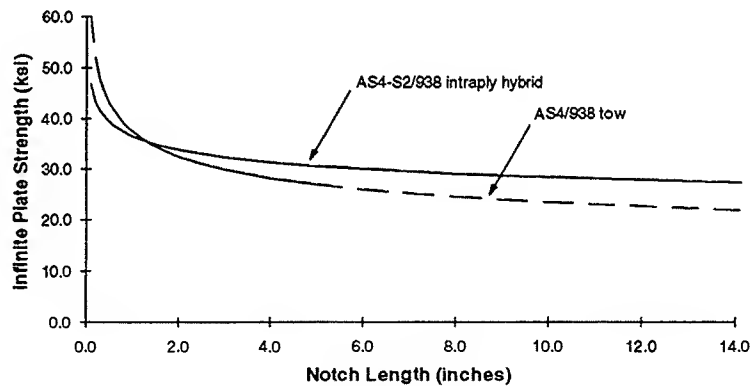


Figure 5-10. Superior In-Plane Fracture Toughness of AS4-S2/938 Intraply Hybrids

The use of fabric plies on the surfaces of the facesheets in AS4/8552 sandwich structures resulted in comparable strength and improved toughness relative to panels constructed of AS4/8552 tow only, as shown in Figure 5-11 [15]. This implies that the impact damage resistance advantages of toughened-matrix materials may be exploited while retaining tension fracture performance comparable to untoughened-matrix materials.

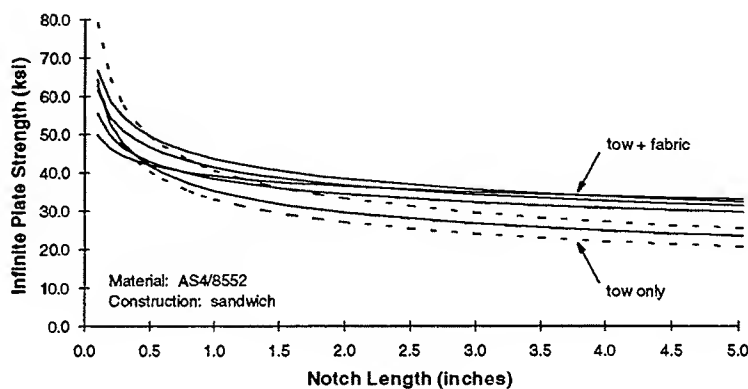


Figure 5-11. Improved Toughness Provided by Fabric Surface Plies in AS4/8552 Sandwich Panels.

Little difference was observed between the performance of laminates and sandwich structures constructed of similar materials, as shown in Figure 5-12 [15].

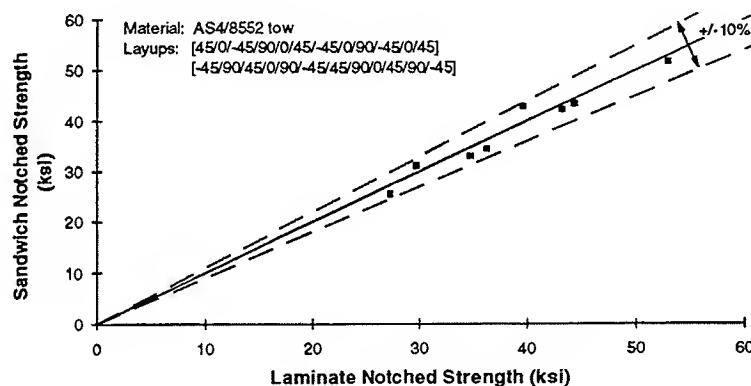


Figure 5-12. Comparable Tensile Notch Sensitivity of Laminate and Sandwich Structures.

Influence of Manufacturing Process and Process Variations on Tension Fracture Performance

The manufacturing process and process variations were also found to have a significant influence on tension fracture performance [14, 15]. AS4/938 laminates which were fiber placed with the BCA head exhibited reduced notch sensitivity relative to laminates made of prepreg tape as shown in Figure 5-13. It is hypothesized that the improved fracture toughness is a result of the inhomogeneous nature of the fiber placed laminates (described in Section 4.1). The improved performance, however, does not appear to be robust with respect to process variations. Inferior performance observed in subsequent fiber placed test panels may have been a result of: (1) the use of a different fiber placement head and the associated difference in microstructure, (2) lower fiber areal weight and resin content, and/or (3) lower tensile strength of the prepreg tow material. A significant developmental effort would be needed to achieve the level of process control required to exploit the improved performance of the fiber placed material in structural design.

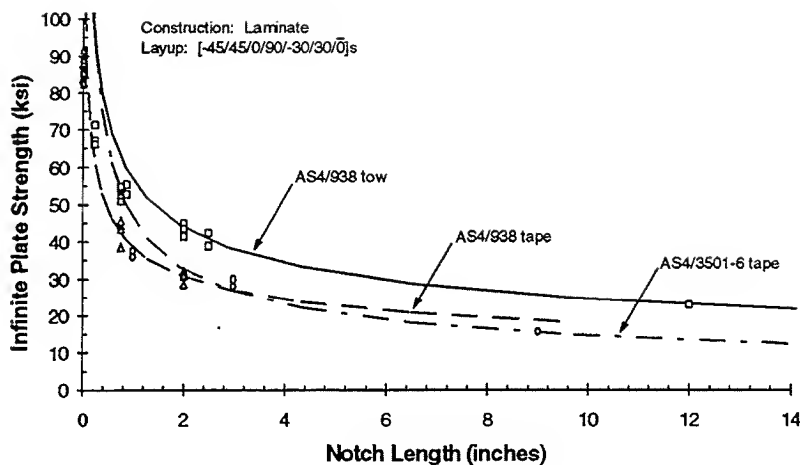


Figure 5-13. Improved In-Plane Fracture Toughness of Fiber Placed AS4/938 Laminates. (Note: 3501-6 and 938 are theoretically identical resin systems produced by two different material suppliers).

Strain Rate Effects on Tension Fracture

The notched tensile strength of AS4/938 laminates manufactured with the tape lamination process was observed to be strongly dependent on strain rate with reduced strengths at higher strain rates [27]. Fiber placed AS4/938 laminates, however, exhibited little strain rate sensitivity. The notched strength of IM7/977-2 tape laminates was also found to be strain rate independent.

Analytical Representation of Tension Fracture

The effects of an inhomogeneous (e.g., fiber-placed) microstructure on the fracture properties of composite laminates were modeled by Cairnes, et. al. [28]. A hierarchical finite element modeling scheme employing a global model for the center-notched test panel and a local model for the inhomogeneous material at the notch tip was developed. A stacked membrane model was also developed to study ply splitting and delaminations at the lamina level. Results indicate the greatest improvements in tension fracture performance in the fiber-placed laminates may be a result of increased ply splitting and delamination relative to tape laminates. This is consistent with experimental results.

The use of couple stress (Cosserat Theory) finite elements for modeling the influence of material inhomogeneities on fracture performance was also investigated by Cairnes [29]. Results indicate that the stress singularities at the notch tip are relieved by couple stresses. Good correlation with experimental strength results were achieved with strain energy release rate based failure criteria.

A promising analytical method of accounting for the non-classical material response (especially in analysis of configured structure) is the strain softening law [15]. Such an approach has several attractive features. It is a generalized continuum approach, and is therefore compatible with the complex finite element models required to properly approximate structural configurations. The approach also captures the load redistribution caused by local damage formation and growth, which is essential to predicting structural damage tolerance.

In practice, a strain softening law is incorporated into the finite element analysis as a nonlinear material response, as illustrated in Figure 5-14. The analysis becomes a structural collapse problem, as the damage grows and the load redistributes toward the edge of the coupon (or structure) until insufficient material exists to sustain the applied load, as illustrated in Figure 5-15.

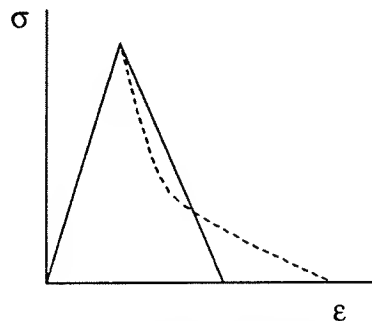


Figure 5-14. Material Strain Softening Laws.

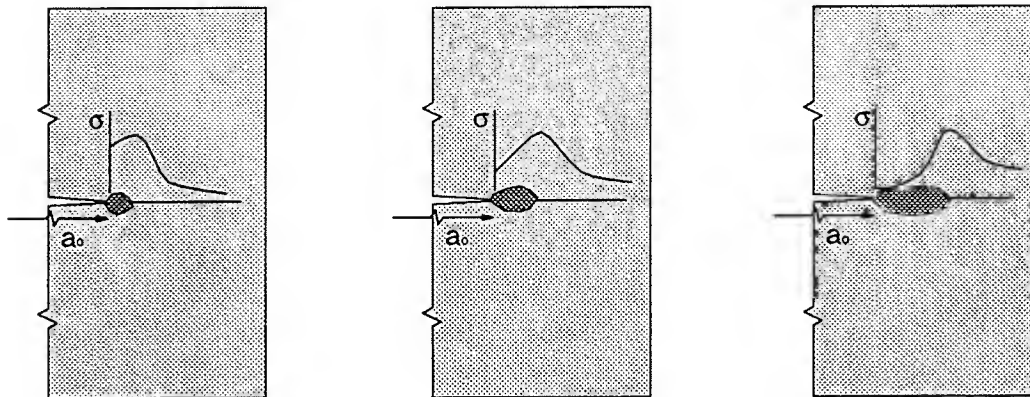


Figure 5-15. Modeling of Structural Collapse Due to Damage Growth.

Strain softening laws are currently determined through a process of trial and error until predictions match coupon test results for a range of notch lengths. The laws have been found to be unique to each material and layup. Material laws with relatively high maximum stresses but low total fracture energy were required to predict high strength, low toughness response as illustrated in Figure 5-16. These laws also captured the relatively small notch-tip damage zones and small specimen size effects. Conversely,

laws with low maximum stresses but high total fracture energies were necessary to capture low strength, high toughness behavior. They also predicted the large notch-tip damage zones and the significant specimen size effects observed in the tests.

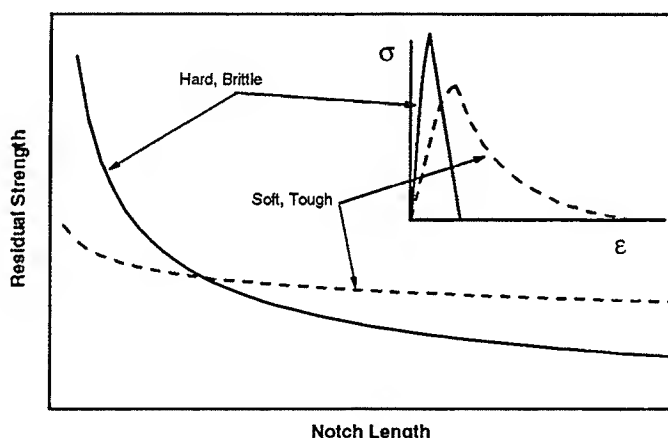


Figure 5-16. *Effect of Strain Softening Material Law on Notch Sensitivity.*

Determination of material strain softening laws through trial and error requires a relatively large number of tests, and is computationally intensive. An approach for determining strain softening laws directly from test results via energy methods has been proposed by Basham [30]. The method requires measurement of crack opening displacements (COD) for two specimens of identical geometry and differing notch lengths. Attempts to accomplish this with center-notch specimen configurations were unsuccessful. Two specimens each of two notch lengths were tested. The resulting strain softening laws for the four specimen combinations are shown in Figure 5-17 along with an average response. The scatter is unacceptably large, and is likely a result of the small differences in compliance of coupons with differing notch lengths relative to experimental error.

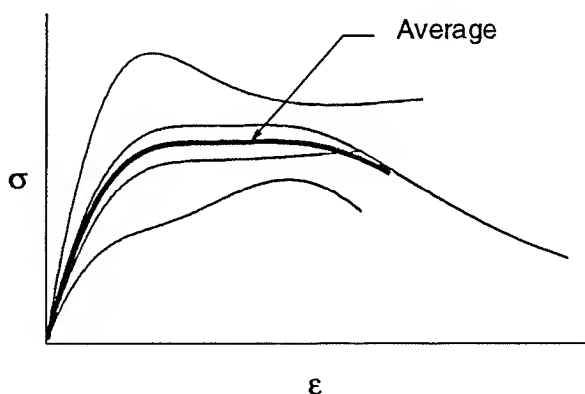


Figure 5-17. *Strain Softening Laws Determined from Center-Notch Specimens Using the Energy Method of Basham.*

Development of improved specimen geometries is being pursued outside the ACT program (e.g., University of British Columbia). In particular the over-height compact tension specimen, shown in Figure 5-18, is being evaluated. The greater dependence of coupon compliance on notch length should resolve the problems associated with the center-notch specimens. Test measurements and destructive evaluations are being conducted to provide further insights into the damage growth mechanisms. One unresolved issue with this specimen configuration is the effect of the bending stress distribution on the strain-softening law.

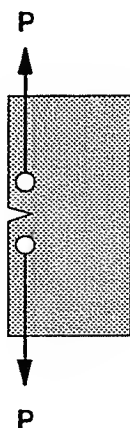


Figure 5-18. Over-Height Compact Tension Specimen for Strain Softening Law Determination.

Compression Strength and Notch Sensitivity

Notched compression tests were performed only on materials of interest for the keel and side panels. Notched compression strengths of T300/F584 sandwich panels with through-penetrations were measured to be only 75 to 80% of those with machined notches of the same size (as the impact blade). A significant amount of delamination which accompanied the blade impact may have contributed to the reduced strengths by promoting a local instability driven failure. No compression tests were performed on AS4/8552 sandwich panels with through-penetrations.

Notched compression strengths were significantly lower than tension strengths as shown in Figure 5-19 [15]. The influence of layup was similar to that for tension, although less pronounced.

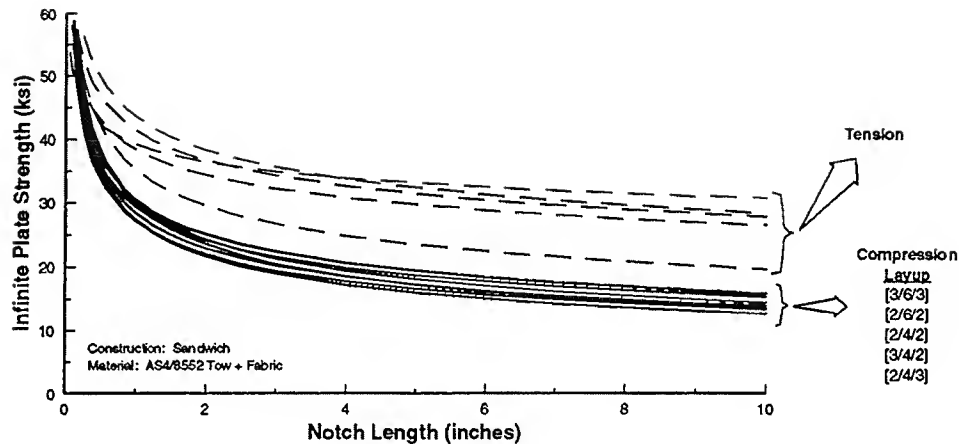


Figure 5-19. Comparison of Notched Tension and Compression Strengths (*[X/Y/Z]* indicates the number of plies in the $[0/\pm 45/90]$ orientations).

The strongest effect on notched compression strength was that of thickness as shown in Figure 5-20 [15]. The notched strengths of a wide range of materials, layups, core materials, and construction with total laminate/facesheet thicknesses between 0.11" and 0.20" are within approximately $\pm 10\%$ of an average curve. The strengths of sandwich panels with total facesheet thicknesses of 0.44" were approximately 25% higher than those of the thinner laminates. This insensitivity to material and layup variables and the strong sensitivity to thickness suggest that local instability may induce failure.

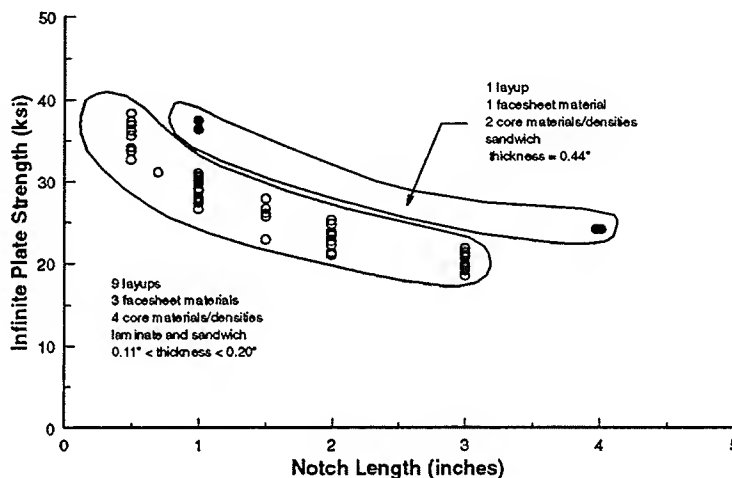


Figure 5-20. Thickness Effects on Notched Compression Strength.

Finite width effects did not differ significantly from those predicted by isotropic correction factors as shown in Figure 5-21 [15]. This suggests that large damage zones and the accompanying strain softening material response are not present prior to coupon failure, which is consistent with experimental observations.

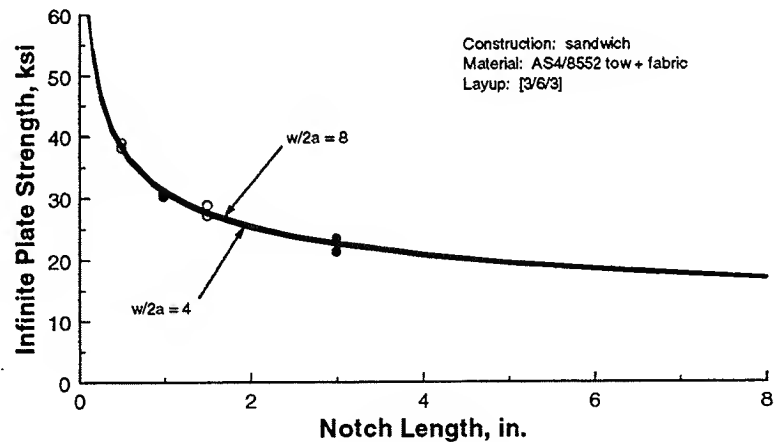


Figure 5-21. Successful Correction for Finite Width Effects in Compression with Linear-Elastic Correction Factor.

The use of strain softening laws for modeling notched compression response was also investigated [15]. In compression, it was found that lower maximum stresses (relative to tension), steep unloading curves, and relatively large element sizes were necessary to predict the reduced notch-length sensitivities while avoiding large finite width effects, as shown in Figure 5-22. The less-severe and broader notch-tip stress concentrations associated with these larger element sizes are consistent with the stress distributions predicted by non-local material theories [31].

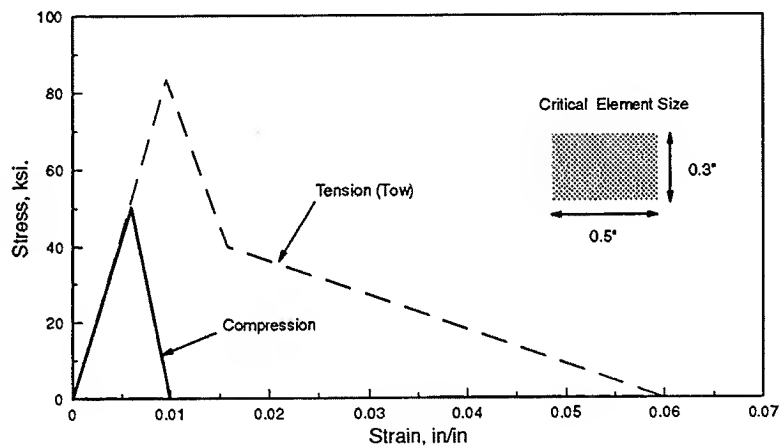


Figure 5-22. Strain Softening Law and Critical Element Size Required for Predicting Notched Compression Response.

5.1.3 Bearing/Bypass

Bearing/bypass properties of candidate fuselage skin materials were investigated in support of panel splice joint design and analysis.

AS4/938 and Intraply Hybrids

The bearing/bypass properties of fiber placed AS4/938 and of several fiber placed intraply hybrids of AS4/938 and S-2/938 were characterized. Filled hole tension, bearing, and tension bearing/bypass interaction tests were performed. The effects of specimen geometry and countersink were considered. Bearing tests were performed with reduced clamp-up equivalent to 40% of normal installation torque to simulate stress relaxation which typically occurs in service. Tension bearing/bypass interaction tests were performed to verify the ability of Boeing's BEARBY analysis code to predict the strength of the material under combined bearing and bypass loads. BEARBY predicts bearing/bypass failure via application of a point stress criterion at a characteristic dimension away from the hole. Characteristic dimensions are determined semi-empirically from unnotched and open- or filled-hole data. The Bolted Joint Stress Field Model developed by McDonnell Douglas [32] is used to determine the stress field around the hole. Detailed test methods and results are described in Appendix C. A summary of the results follows.

A strong correlation between filled-hole tension strain at failure and linear-elastic stress concentration factor was observed for the fiber placed AS4/938 material (Figure 5-23). Bearing strength was found to be independent of layup. The influence of reduced edge margin on filled hole tension strength and reduced end margin on bearing strength were consistent with existing correction factors for tape laminates. Countersinking resulted in small filled hole tension strength reductions ($\leq 3\%$) and significant reductions in bearing strength (up to 13%). These results are also consistent with the behavior of tape laminates. Results of tension bearing/bypass interaction tests were consistent with predictions of the BEARBY code as shown in Figure 5-24.

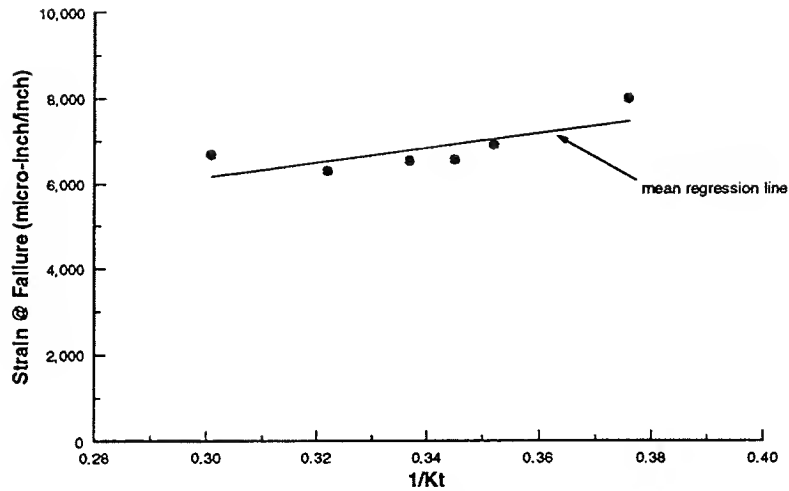


Figure 5-23. Filled-Hole Tension Strain at Failure of Fiber Placed AS4/938.

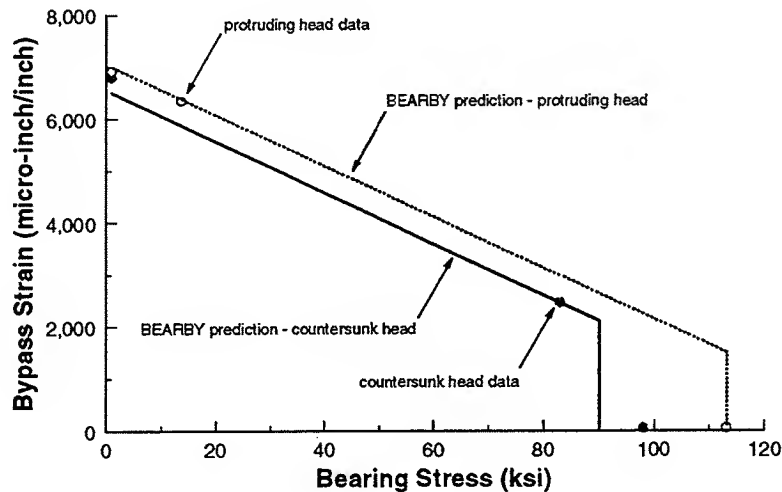


Figure 5-24. Prediction of Bearing/Bypass Interaction with the BEARBY Analysis Code.

The filled-hole tension strength of intraply hybrid laminates was found to be dependent on the location of the hole with respect to the hybridizing glass tows. Laminates in which a high percentage of glass tows were employed in the loading direction only were strongly affected by hole location. Intraply hybrids with a smaller percentage of glass tows distributed through all plies were less sensitive to hole location. The filled-hole tension strengths of laminates with glass tows distributed through all plies were comparable to those of AS4/938 laminates. The bearing strengths of intraply hybrid laminates were less dependent on fastener hole location. The bearing strengths of

laminates with glass tows in all plies were comparable to those for AS4/938 laminates and were distinctly higher than those of laminates with glass only in the axial plies.

AS4/8552

The bearing/bypass properties of fiber placed AS4/8552 laminates with and without fabric surface plies were also characterized. Open- and filled-hole tension and open-hole compression tests were performed on a variety of laminates. Bearing and transverse-bearing/compression-bypass interaction tests were performed with reduced clamp-up equivalent to 40% of the normal installation torque. Tension bearing/bypass interaction tests were performed with full clamp-up. The performance of a single-lap bolted joint with a thick spacer was investigated. The influence of absorbed moisture and extreme temperatures were evaluated. A detailed description of test methods and results is presented in Appendix D. A summary of the results follows.

Good correlation was observed between bypass strain-at-failure and orthotropic stress concentration factor for open- and filled-hole tension and open-hole compression as shown in Figures 5-25 and 5-26. Tension bypass strengths were slightly superior to those obtained with the AS4/938 material. Little difference was observed between results of open- and filled-hole tension tests. Comparable open-hole tension and compression strengths were observed in laminates with and without fabric surface plies. Hot/wet conditions resulted in a 5% reduction in open-hole tension strength and a 20% reduction in open-hole compression strength.

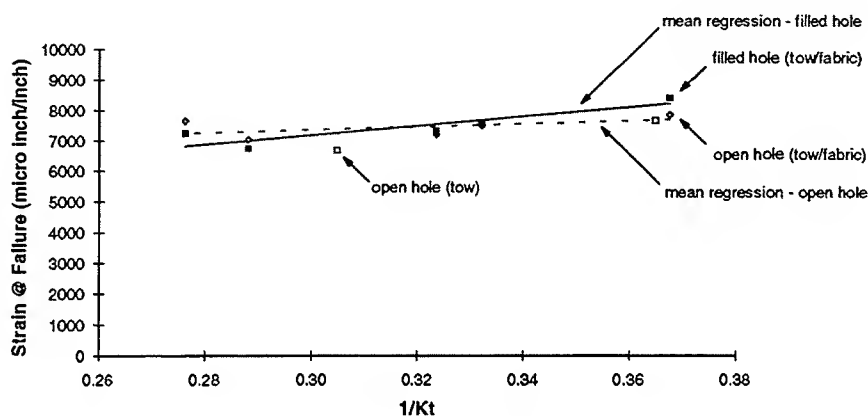


Figure 5-25. Open- and Filled-Hole Tension Strain at Failure of AS4/8552.

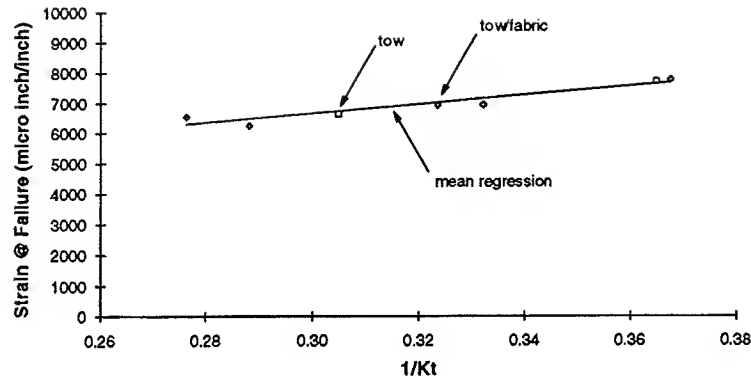


Figure 5-26. Open-Hole Compression Strain at Failure of AS4/8552.

Bearing strengths were insensitive to layup and were comparable to those obtained with the AS4/938 material. A 10% reduction in ultimate bearing strength and a 16% reduction in the proportional limit load (2% offset) were observed for hot/wet conditions.

Predictions of tension bearing/bypass strength using the BEARBY analysis code were slightly conservative. Significantly conservative predictions of transverse-bearing/compression-bypass strength (Figure 5-27) were likely a result of the use of open-hole (instead of filled-hole) compression strength values for generation of bypass failure criteria.

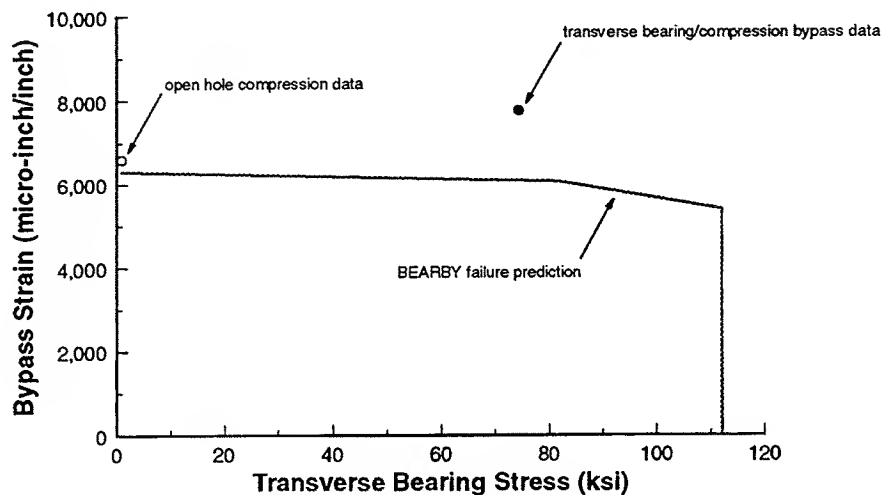


Figure 5-27. Prediction of Transverse-Bearing/Compression-Bypass Interaction with the BEARBY Analysis Code.

The use of thick spacers between fastened laminates caused reduced joint stiffness, a reduction in the proportional limit load, and an increased ultimate strength as a result of

increased fastener bending and additional bearing load carrying capability provided by the spacer.

Thick Laminates

The bearing/bypass properties of thick (52 ply) AS4/8553-40 laminates were characterized in support of design and analysis of the forward keel circumferential panel splice joint [33]. Open-hole compression, bearing, and fastener shear-out tests were performed. The effects of fastener diameter, coupon geometry and fastener clamp-up were considered. A small diameter bolt and aluminum splice plates were used to provide clamp-up without impeding hole deformation in bypass tests.

Hole diameter, edge margin and clamp-up were all found to influence bypass strength. The influence of fastener clamp-up was greater for coupons with small edge margins. Fastener clamp-up was observed to promote net-section compression failures as opposed to the shear failures observed in some coupons without clamp-up.

The bearing response in clamped conditions was similar to that for unclamped conditions except that a higher proportional limit load was achieved. Net-section tension failures preempted large hole deformations in bearing coupons with clamp-up. Results of fastener shear-out tests were similar to those for bearing with shear failures occurring prior to large hole deformations because of the reduced end margin.

5.2 Sandwich Core Materials

Sandwich core materials of interest for use in fuselage applications include Hexcel's HRP and Du Pont's Korex honeycombs. Other types of honeycomb, foam-filled honeycombs and foams were also considered as discussed in Sections 3.0 and 4.0. Little effort was expended in characterizing the mechanical properties of candidate core materials. The property of greatest interest is the through-thickness shear stiffness which is generally available from the supplier. The influence of temperature and absorbed moisture on the performance of the core materials is also of interest but was determined to be beyond the scope of the current program.

5.3 Sandwich Core Close-Outs

The primary design requirements of sandwich core close-outs are to react fastener clamp-up loads and to protect the core from fluid ingress. Ramped core close-outs may influence the load carrying capability of the skin by imposing an eccentric load path. The bearing capability of the skin may be degraded by increased fastener bending in full-depth close-outs. Additional bearing/bypass capability may be provided by the close-out itself.

5.3.1 Longitudinal Panel Splices

The static and fatigue bearing performance of AS4/8552 sandwich panels with braided/resin transfer molded core close-outs illustrated in Figure 4-16 were characterized [see Appendix E]. Fasteners were installed with 40% of normal installation torque to simulate stress relaxation in service. Static and fatigue bearing strengths were on the order of 60 to 75% of comparable AS4/8552 laminates. Reduced bearing strengths were likely a result of fastener bending and brooming of the unsupported interior surfaces of the close-out. Bearing failure modes included significant hole elongation and brooming of the unsupported side of the close-out for both static and fatigue loading. Hole elongation progressed rapidly under fatigue loading after 2-3% elongation was achieved.

5.3.2 Circumferential Panel Splices

The primary concern with the circumferential panel splice core close-out design concepts is the strength of the facesheet and bondline in the region of chamfered core. Tension and compression tests were performed on representative test coupons illustrated in Figure 4-23. Coupons with solid laminate extending through the chamfered region were also tested. It should be noted that the coupons with solid laminate in the chamfered region exhibited significant out-of-plane facesheet distortion which was caused by mismatch of the core and close-out thickness. Greater variation observed in mechanical test results may have been a result of these anomalies. Detailed test methods and results are described in Appendix E. A summary of results follows.

Initial failures under tensile loading were non-catastrophic disbonds between the facesheet and close-out which resulted in greater joint compliance. Ultimate failure of the facesheets occurred in the radii at the ends of the chamfered region. Interlaminar shear failures between continuous and discontinuous ply packs in the solid laminate plug which extended into the chamfered region in some coupons may have precipitated facesheet failure by causing unequal loading and increased local bending strains. The initial failure stress and ultimate failure strength of the coupons with solid laminate in the chamfered region were 69% and 32% higher than the coupons with honeycomb in the chamfered region. The higher strengths are attributed to lower facesheet stresses in the chamfered area which are a result of load sharing with the solid laminate plug.

Disbond of the facesheet and core resulted in catastrophic failure under compression loading. The compression strength of coupons with solid laminate in the chamfered region were 27% greater than those with honeycomb.

5.3.3 Window Cutouts

Fastener clamp-up tests were performed on representative window belt panels with braided/RTM'd window cutout core close-outs (illustrated in Figure 4-25) under Task 20 of the task order contract NAS1-18954 [20]. An instrumented torque wrench, LVDT displacement indicator, and strain gaged washers were used to monitor the response of the panel and fastener during the tests. Initial clamp-up tests with reduced-head 1/4"

HiLock fasteners resulted in failure at normal torque levels when the tapered fastener head was pulled through the countersunk facesheet. Improved pull-through strengths were observed for fasteners with larger heads. The window panel exhibited adequate resistance to fastener pull-through for 1/4" and 3/16" HiLock fasteners with full size heads and for 1/4" Eddie bolts. Additional testing indicated that the pull-through strength could be improved by increasing facesheet thickness and by using a heavier core material if necessary.

5.4 Braided Textile Elements

The performance of braided textile composites were investigated analytically and experimentally. Efforts were focused on the baseline material selected for fuselage circumferential frames (2-D triaxial AS4/RSL 1895). A variety of other 2-D and 3-D fiber architectures and matrix resins were included. Resin transfer molding of dry preforms and consolidation of commingled carbon/thermoplastic preforms were employed for test panel fabrication. It should be noted that many of the test panels manufactured early in the program were of poor quality with respect to braid angle and porosity. Additional characterization of braided/RTM'd composite materials including the AS4/PR-500 of interest for fuselage circumferential frames were performed by Lockheed under their ACT contract [NAS1-18888].

5.4.1 Textile Composites Analysis Model (TECA)

The textile composites analysis (TECA) model was developed to predict the stiffness and strength of 2-D and 3-D braided composites [21]. TECA is based on the concept of representing internal fiber architecture with a series of repeating unit cells (Figure 5-28) which are defined by the model from the braiding parameters. The stiffness matrix of the unit cell is determined by volumetric averaging of the geometrically transformed stiffness matrices of elemental tows. An elastic strain energy approach employing beam elements to represent the bending behavior of an elemental tow is used to account for stiffness reductions which are a result of the fiber distortion typical of braided composites. Extensional and bending stiffness matrices of the braided structure are then determined for use in shear-deformable plate analyses or shell analyses. Mechanical and hygrothermal loads may be applied. Maximum stress or maximum strain failure criteria are then applied such that progressive failure is predicted. Matrix cracking is accounted for by adjustments to the elemental stiffnesses and local stress field.

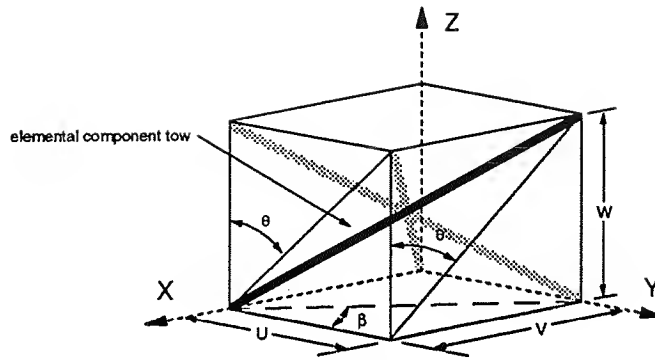


Figure 5-28. Braided Fiber Architecture Unit Cell.

Values of tensile and compression moduli predicted by TECA were within 5% of measured values for 2-D and 3-D AS4/PEEK. The model was also used by Masters, et. al., to accurately predict the tensile strength and modulus of three 2-D triaxial AS4/RSL 1895 composites [34].

5.4.2 Stiffness and Strength

Tension, compression, and Iosipescu shear tests were performed to characterize the in-plane stiffness and strength of braided textile composites [21]. Out-of-plane tension and shear strengths were characterized with flange bending and Iosipescu tests, respectively. The dependence of strain measurements on strain gage size relative to material unit cell size was investigated. The influence of hot/wet conditions on compression performance were determined.

The in-plane strength and moduli of 3-D braid architectures were significantly lower than comparable 2-D architectures in most cases. A notable exception was the higher moduli of the 3-D architecture in fully braided composites (i.e. no axial tows). The compression moduli of AS4/PEEK were measured to be higher than the tension moduli. A 27% reduction in compression strength was observed for a 2-D triaxial AS4/RSL 1895 composite in hot/wet conditions (30 day soak at 180°F/100% R.H).

Very high values of Poisson's ratio (up to unity) were observed in coupons with small braid angles ($\leq 35^\circ$ with respect to loading direction). Coupons with braid angles $\geq 63^\circ$ exhibited typical values for Poisson's ratio.

Strain measurements with gages of the same size as the braid architecture unit cells were found to be sensitive to local effects. A preliminary recommendation for strain gage length is a minimum of 1.5 times the unit cell length.

Results of in-plane and out-of-plane Iosipescu shear tests were deemed unreliable because of the small size of the coupon used and the size of the strain gages relative to the material unit cell.

Out-of-plane tension strengths of the braided composites were significantly higher than those of comparable laminated tape materials. Only a small difference was observed between out-of-plane tension strengths of 2-D and 3-D braided/RTM'd materials.

5.4.3 Bearing/Bypass

Open- and filled-hole tension, open-hole compression, and bearing/bypass tests were performed on braided textile composites of interest [21, Appendix C]. The filled-hole tension strength of the triaxial AS4/RSL 1895 braided composite selected for use in circumferential frames was comparable to that of AS4/938 tow laminates. Results of open-hole tension tests suggest that 2-D braid architectures are more notch sensitive than 3-D architectures. Greater notch sensitivity was also observed in triaxial braids relative to braids with no axial tows as a result of a greater stress concentration factor.

Bearing strengths of the braided composites were generally low relative to conventional laminates. The bearing strength of the triaxial AS4/RSL 1895 was also found to be very dependent on end margin, suggesting a propensity for shear-out. The bearing strengths of fully braided composites were lower than those of triaxial braids due to the lack of axial tows.

The effects of bearing stress on the tension bypass strength of the triaxial AS4/RSL 1895 were similar to those observed in conventional laminates. Tension bearing/bypass strengths were accurately predicted with the BEARBY analysis code.

5.5 Bonded Joints

The fracture attributes of adhesively bonded joints representative of the crown skin-to-stringer and skin-to-frame interface were investigated by Drexel University [35]. Double-cantilever-beam (DCB) and end-notch-flexure (ENF) tests were performed on coupons constructed of precured AS4/938 and braided AS4/RSL 1895 adherends bonded with Metalbond 1515 epoxy film adhesive. Tests were performed on coupons with similar (e.g. AS4/938 to AS4/938) and dissimilar (e.g. AS4/938 to AS4/RSL 1895) adherends. The fracture propagated from the adhesive bondline into one of the composite plates in all cases. The fracture propagated into the AS4/938 plate in coupons with dissimilar adherends in every case except for mode II (ENF) testing of coupons where the adhesive layer was not at the mid plane of the coupon. A significant effect of layup on fracture toughness was observed for both adherend materials. The highest values of fracture toughness for the braided composite were observed in the axial direction for mode I and in the transverse direction for mode II loading. The mode I fracture toughnesses of the braided composite was significantly higher than those of the tape laminate. The mode II fracture toughnesses of the two materials were comparable.

The fracture toughness of other materials (IM7/8552, IM7/8551-7, and T800H/3900-2) which were of interest for fuselage skins were also characterized [35].

The viscoelastic properties of the Metalbond 1515 film adhesive were investigated by the University of Washington [36]. Creep and stress relaxation were characterized as a

function of temperature and absorbed moisture content. The principals of time-temperature superposition were applied to estimate the long term viscoelastic behaviour of the adhesive.

6.0 DURABILITY

The durability of the structure under service conditions may have a significant influence on operating costs through maintenance requirements. Although composite structures exhibit excellent fatigue and corrosion resistance, they have historically been susceptible to foreign object impact damage. Absorption of water and other fluids typically degrade the performance of polymer matrix composites, particularly at elevated temperatures. Some composite sandwich structures have also been susceptible to bulk fluid ingress, resulting in weight gain and damage to the structure by the expansion of freezing water.

The impact damage resistance and post-impact load carrying capability of stiffened skin and sandwich structures were investigated. The effects of absorbed fluids on structural performance and the resistance of sandwich structures to fluid ingress were also studied.

6.1 Impact Damage Resistance and Tolerance

Traditional design objectives regarding impact damage resistance of composite structure are related to the ability of exposed structure to withstand a reasonable foreign object (e.g. tool) impact without visible damage. An additional objective is the ability to endure a severe hail storm without sustaining damage which would require immediate repair. These objectives are closely tied to the requirement for the structure to carry ultimate loads with non-visible impact damage.

Specific criteria which have been established to meet these objectives include the following: The structure must be capable of withstanding a 48 inch-pound impact with a one inch diameter hemispherical impactor without sustaining visible damage. Visible damage is defined as a 0.05 inch dent depth or a one inch surface crack. Fixed primary structure exposed to ground hail must be capable of enduring a 300 inch-pound impact with a 2.5 inch diameter hail stone on vertical surfaces or a 500 inch-pound impact on horizontal surfaces without sustaining damage which would require immediate structural repair. The structure must be capable of carrying ultimate load with non-visible damage created by either type of impact event. Compression-after-impact (CAI) tests are generally performed on coupons and panels with "barely visible impact damage" (i.e. dent depth just over 0.05") to satisfy this requirement. Tension tests are rarely performed because the effects of impact damage on tension strength have been found to be small relative to other criteria.

A significant effort has been expended to understand the impact damage resistance and post-impact load carrying capability of composite laminate and sandwich structures. The following discussion is focused on the impact damage resistance and tolerance of composite laminates and sandwich structures in general. The performance of specific ATCAS design configurations are discussed in [4].

6.1.1 Laminate Structure

Impact Damage Resistance

The impact damage resistance of stiffened skin structure was studied experimentally using a statistically based designed experiment [16]. Material, laminate, structural, environmental, and impactor variables were considered. The study utilized 32 three-stiffener panels representative of potential fuselage crown, keel, and lower side-panel designs, each with a unique combination of material type, material form, and structural configuration. Two manufacturing techniques, fiber placement and tape lamination, were used to build the panels. Various combinations of impact variables representing a range of foreign object impact threats to the aircraft were examined. Parallel experiments examined impacts performed at the skin mid-bay, at the edge of the stiffener attaching flange, and over the stiffener vertical web. The relative importance and a quantitative measure of the effect of each variable and variable interactions on selected damage state metrics were determined. These damage state metrics included indentation depth, local matrix damage area, stiffener flange separation area, fiber failure, and damage region flexural stiffness. Major conclusions which have been drawn from this effort are summarized below. A thorough discussion of test methods and results are provided in [16].

An important observation in this experiment was that the severity of the damage was a strong function of impact variables and variable interactions. Certain impact variable levels which increased the amount of internal damage (such as larger impactor diameters) decreased the external visibility. The inverse relationship between damage severity and visibility for variables relating to the impactor geometry suggests the barely visible impact damage criteria and related requirements may be flawed. Strong couplings between extrinsic impact variables and damage characteristics suggest the need for a more comprehensive material and design screening approach for composite structures. The use of a single, arbitrary value of an extrinsic variable (e.g., impactor diameter) in a test program may lead to conclusions which do not apply over the full range of potential impact conditions.

Matrix toughness had little effect on the damage area in minimum gage structure (i.e., 0.09 inch thick), which is characteristic of 70% of a fuselage shell, but did reduce the damage area in thicker skins. This observation is based on an interaction between matrix type and laminate thickness identified for the local matrix damage response. Fiber type, by itself, was found to have little effect on impact damage, but may interact with fiber volume to affect permanent indentation (visibility).

The manufacturing processes and material forms used to fabricate the panels affected the mechanisms of fiber failure during an impact event. Analysis of deplied coupons showed that tape laminates exhibited fiber breakage that occurred in a self-similar manner as illustrated in Figure 6-1. Fiber-placed laminates, however, exhibited fiber breakage which occurred incrementally on a tow-by-tow basis. Additionally, plies in fiber-placed stiffeners tended to have more fiber breakage than their tape counterparts. The relationships between manufacturing processes and structural performance must be better

understood so that composite structure which is both safe and cost effective can be developed.

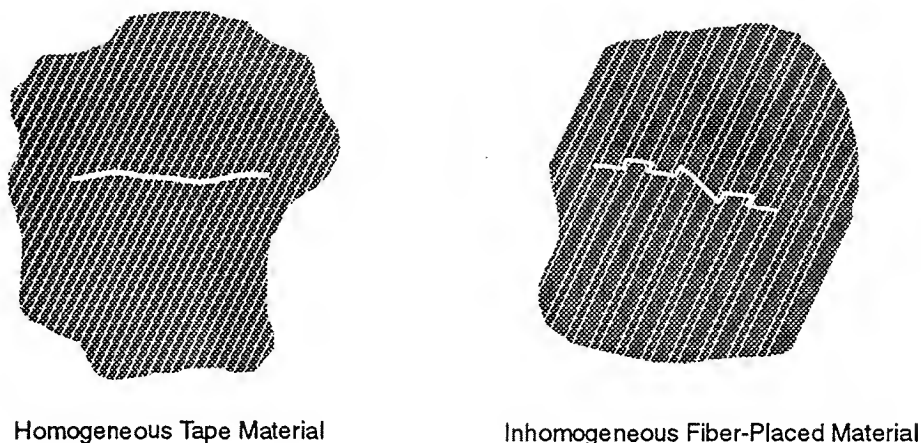


Figure 6-1. Fiber Failure Mechanisms During Impact in Fiber-Placed and Laminated Tape Composites .

The addition of an adhesive layer between the stiffener attaching flange and skin for cocured stiffeners to minimize flange separation created during an impact event is most beneficial for thin blade-stiffened structure. Hat-stiffened structure received little benefit from the adhesive. Skin layup also had an influence on the importance of the adhesive layer, possibly because layers just outside of the flange/skin interface became critical locations for separation.

A non-destructive inspection technique using flexural wave propagation was found to accurately characterize the flexural stiffness of impact damaged laminates. Experimental results were within 5% of theory for undamaged laminate measurements and correlated well with mechanical measurements for the damage region. This technique, also termed "automated coin tap," has the potential to not only detect damage, but also to quantify its effect on the load carrying capability of the structure.

Compression Strength After Impact

An approach for analytically predicting the CAI strength of composite laminates has been developed and verified through comparison with results from standard coupons [37, 38]. The analysis method involves impact damage state characterization, sublaminates stability analysis, analysis of load redistribution around the damaged material, and application of failure criteria. Damage state characterization is accomplished through a combination of non-destructive (e.g. pulse-echo ultrasonic inspection) and destructive (e.g. cross-sectioning) methods. An analytic series solution for predicting sublaminates stability [39] was modified to account for the reduced bending stiffness in unsymmetric laminates due to coupling of bending and extensional deformations. A reduced stiffness

approach was used to determine in-plane load redistribution as a function of sublaminate stability. The load carried by sublaminates after buckling was assumed to be constant, as in Euler buckling. A maximum strain failure criteria was applied for prediction of CAI strength.

Good correlation with experimental results was observed for coupons with large (≥ 1.0 inch) damage area (Figure 6-2). Poor correlation for small damage areas is believed to be a result of failure to account for fiber damage in the sublaminate stability based model.

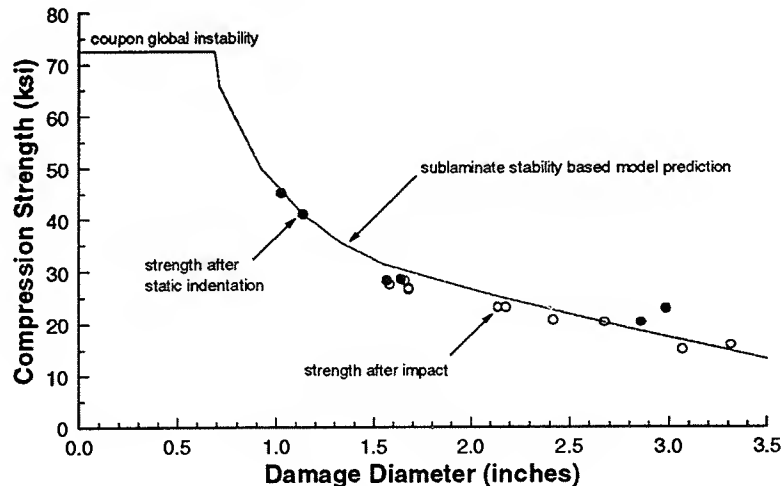


Figure 6-2. Correlation of Sublaminates Stability Based CAI Strength Prediction with Experimental Data for Damage Induced by Impact and by Static Indentation.

CAI specimen geometry, matrix toughness, and ply group thickness were considered in a parametric study performed with the model. The maximum load for global instability of various standard test coupons was estimated. This provided an upper bound for CAI strength which was not necessarily equal to the compression strength of the material. The ratio of coupon width to damage area for which finite width effects became significant was found to be dependent on factors affecting sublaminate stability (e.g. ply thickness). Finite width effects can mask true material performance and must be accounted for in interpretation of test results. Matrix toughness has been observed to influence CAI strength through the extent of delamination type damage created during an impact event. However, matrix toughness does not significantly influence compression strength after impact for a given damage state so long as delamination growth is not a predominant failure mode. This hypothesis is supported by test results for untoughened and toughened matrix composites which exhibit similar CAI strengths for similar damage states. Ply thickness also affects CAI strength through competing mechanisms. Thin plies tend to sustain damage over smaller areas for a given impact event because of the increased amount of energy absorbed by the greater number of delaminations created.

However, thicker plies are more stable and therefore provide greater CAI strength for a given damage area.

A strong influence of stacking sequence on impact damage resistance and CAI strength in IM7/8551-7 laminates was observed [40]. Quasi-isotropic laminates with $\pi/6$ type layups (i.e. 0° , $\pm 30^\circ$, $\pm 60^\circ$, and 90° plies) were compared with traditional $\pi/4$ layups. Variations in m and n for $[45_m/0_m/-45_m/90_m]_{ns}$ laminates provided insight into the effect of ply group thickness. Heterogeneous stacking sequences expected to result in strong shear/extension and bending/twisting couplings in post-impact sublaminates were also considered. Characteristic damage states (CDS) were determined with the aid of pulse-echo ultrasonic inspection prior to CAI testing. Laminates with homogeneous stacking sequence and ply orientation which change from ply to ply in an incremental manner were found to yield a sublaminate size distribution that was nearly symmetric through the laminate thickness. The damage size distribution for heterogeneous stacking sequences were found to be unsymmetric through the thickness.

Predictions of undamaged specimen stability were shown to provide an upper bound for CAI strength. Results from tests of coupons with varying ply thickness combined with analysis showed that failure initiated by local fiber failures may preempt sublaminate instability induced failure in laminates with thick plies and small damage states. The CAI strength analysis method described above was found to be accurate for some laminates but not others. A geometrically nonlinear finite element analysis that discretely modeled impact damage indicated that the large unsymmetric damage distribution typical of some layups alters coupon stability. Out-of-plane displacement measurements confirmed this prediction.

The post-impact response of composite laminates to compression loads was also investigated experimentally by the University of Washington [41]. CAI tests were performed for comparison with the results of the sublaminate stability based model. The Moiré interferometry and shadow Moiré techniques were used to measure in-plane and out-of-plane deformations. Predictions of CAI strength proved to be reasonably accurate for coupons with damage diameter of 0.8 to 2.0 inches (as determined by ultrasonic inspection). The model was found to be unconservative for coupons with small damage whose failure is probably not initiated by sublaminate instability as discussed above. The model proved to be conservative for coupons with greater damage states. This may be a result of non-classical material response or of failure to account for (stabilizing) edge effects in coupons with large damage areas.

Strain contours generated from Moiré fringe images indicate the predictive model is roughly accurate, although several discrepancies were noted. The model predicts a symmetric strain distribution around a circular soft inclusion. Experimental results exhibit a less symmetric strain distribution around an elongated damage region oriented at an angle to the applied load. The elongated damage state is a result of the differing extent of delamination in plies of differing orientation. The experimental results also indicate a more localized stress concentration than that predicted by the model.

6.1.2 Sandwich Structure

The impact damage resistance of composite sandwich structure has also been investigated in support of the design and analysis of ATCAS keel and side panels. Impact surveys were performed to screen candidate sandwich core materials, to gain insight into structural and impact variables which influence damage resistance and to characterize the damage resistance of ATCAS design concepts. Following impact, the depth of the indentation was measured and the planar extent of damage was determined with through-transmission ultrasonic inspection (TTU). Coupons not intended for CAI tests were then sectioned to characterize the internal damage state and verify the results of TTU. Thermal deply was used to determine the extent of fiber damage in selected coupons. In general, the planar extent of core and facesheet damage were found to be roughly equal (Figure 6-3). Results of TTU correlated well with the extent of damage observed in cross-sections (Figure 6-4). CAI tests were performed on selected coupons to characterize impact damage tolerance.

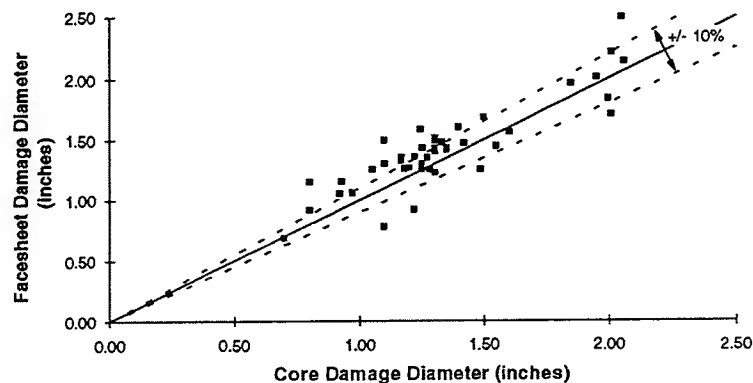


Figure 6-3. *Comparison of Planar Extent of Impact Damage in Sandwich Facesheet and Core Materials. The Line Represents Equal Damage in Facesheet and Core.*

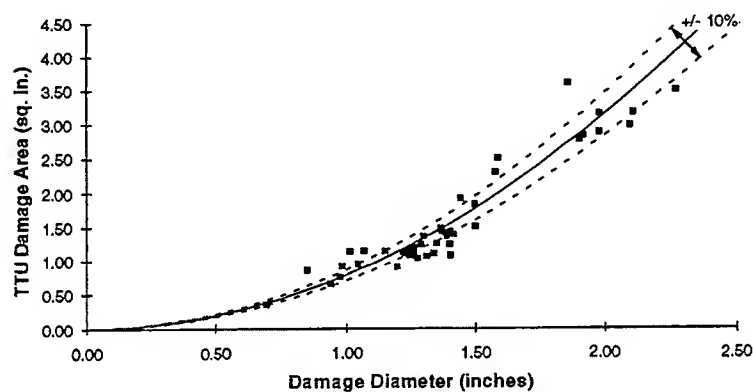


Figure 6-4. *Correlation of TTU Inspection Results with Extent of Impact Damage Determined by Destructive Evaluation. The Arc Represents the Area of a Circle for a Given Diameter.*

Core Material Screening

Initial impact damage resistance tests were used to screen candidate sandwich core materials [9]. The test matrix was based on core material availability but offered comparisons of fiber type, fiber architecture and resin type (Table 6-1). Test panels were representative of minimum gage fuselage skin panels. Detailed test methods and results are presented in Appendix F. A discussion of the test results follows.

Table 6-1. Candidate Sandwich Core Materials for Impact Damage Resistance Testing.

Manufacturers Designation	Description
HRP-3/16-5.5	0/90 glass/phenolic honeycomb
HFT-1/8-5.5	+/-45 glass/phenolic honeycomb
TPC-3/16-5.5	+/-45 glass/thermoplastic honeycomb
HFT-G-3/16-6.0	+/-45 carbon/polyimide honeycomb
HRH-10-1/8-5.0	aramid paper/phenolic honeycomb
HRP-3/16-5.5 K foam	0/90 glass/phenolic honeycomb cyanate-ester foam
HRH-10-1/8-5.0 K foam	aramid paper/phenolic cyanate-ester foam

Impact dent depth was found to be essentially unaffected by core material type except in cases where the facesheet was perforated. None of the panels sustained visible damage from impacts of 100 inch-pounds or less with a one inch diameter tup. Impacts of 200 inch-pounds resulted in visible damage, and 500 inch-pound impacts resulted in perforation of the first facesheet in all cases and subsequent impact of the far-side facesheet in most cases.

The planar extent of damage was generally observed to approach an asymptote for increasing impact energy as the impacted facesheet was perforated at high energy levels as shown in Figure 6-5. The greatest effect of any core material variable was that of resin matrix type, with greater impact damage resistance provided by the thermoplastic matrix. Carbon and aramid fiber also provided significantly improved impact damage resistance relative to glass. Core materials with 0/90 fiber orientation performed better than those with a bias weave.

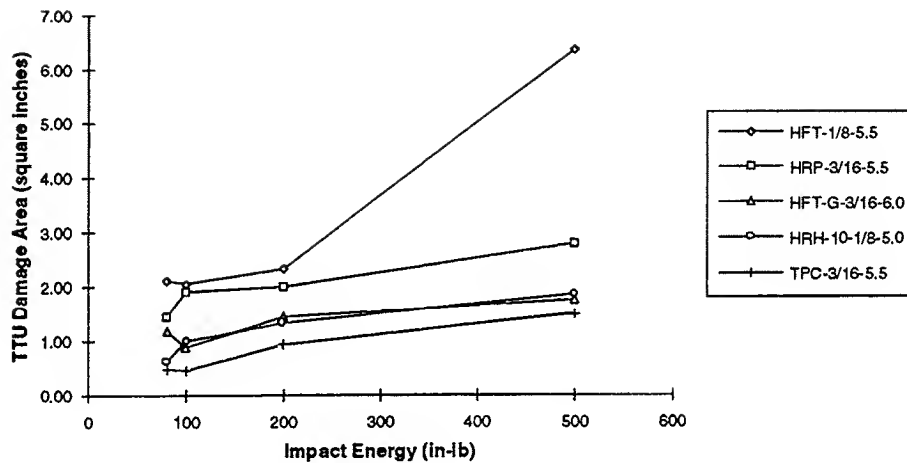


Figure 6-5. Impact Damage Resistance of Representative Minimum Gage Sandwich Structure with Candidate Honeycomb Core Materials.

In most cases the damage area of foam-filled honeycomb was slightly greater than that of unfilled as shown in Figure 6-6. High energy impact (500 in-lbs) of the panel with foam-filled HRP resulted in disbond of the far-side facesheet from the core. The disbond was likely a consequence of low flatwise tensile strength which accompanied a lack of adhesive fillets to the honeycomb cell walls in the foam-filled materials.

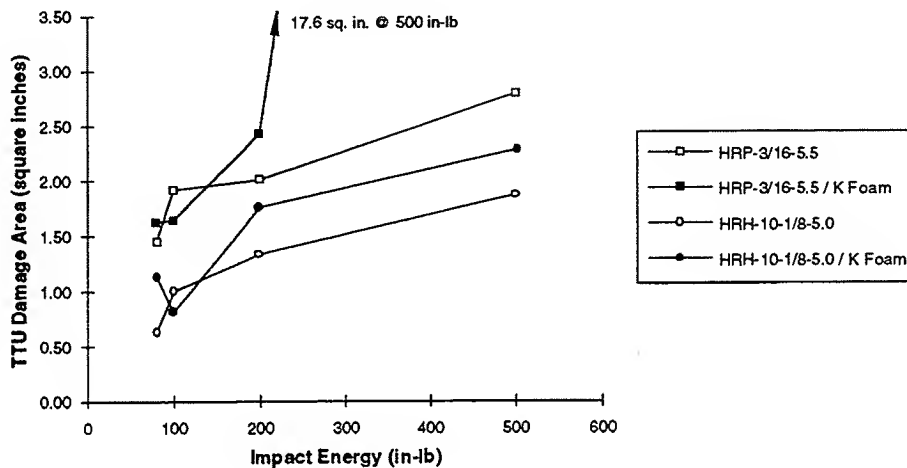


Figure 6-6. Impact Damage Resistance of Representative Minimum Gage Sandwich Structure with Foam-Filled Honeycomb Core Materials.

The strong correlation between impact damage area and residual strength typical of laminate CAI coupons was not observed in the sandwich coupons (Figure 6-7). This may be a result of competing failure modes driven by the stress concentrations resulting from fiber damage and from local buckling of the delaminated facesheet around the impact.

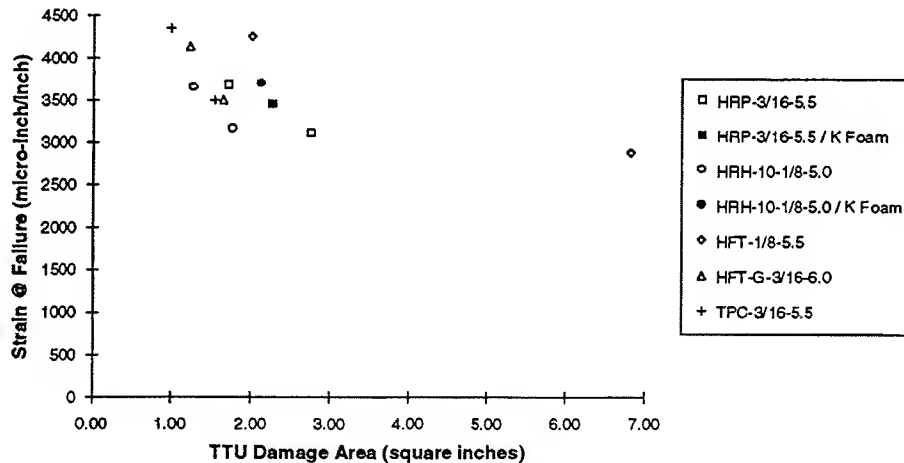


Figure 6-7. CAI Strength of Representative Minimum Gage Sandwich Panels with Candidate Honeycomb Core Materials.

Influence of Intrinsic and Extrinsic Variables on Impact Damage Resistance and Tolerance

The influence of several material, structural and extrinsic variables on the impact damage resistance and tolerance of composite sandwich structures was investigated. Test panels were representative of aft- and mid-keel sandwich structure. Core material type and density, facesheet thickness, impact event support type, impactor size, and impact energy were considered. Detailed test methods and results are presented in Appendix G. A summary of conclusions which have been drawn from the effort follows.

Impact event support type had only a minor influence on damage resistance. Rigid and simple supports were intended to simulate impact over and between panel stiffeners (circumferential frames). Impact over a rigid support resulted in greater dent depth than impact over simple supports. A potential interaction between impact support type and impact energy was identified. Rigid support generally resulted in greater damage at low impact energy, but less damage at high energy. Greater damage at low energy may be a result of the inability of the panel to absorb energy through flexure. The same inability to bend may have resulted in earlier perforation of the impacted facesheet and therefore less planar damage propagation at high energy. The magnitude of the effects of support type may have been suppressed because of the small span length (8 inches) used for impact over simple support.

Impact with a large impactor resulted in a smaller indentation and greater damage area than with a small impactor in nearly every case. This behavior is consistent with that observed in stiffened skin structure [16].

Core type and density also proved to have a significant influence on impact damage resistance. A panel with 12.0 pcf HRP core sustained less indentation in most cases and less damage area in all cases than a similar panel with 5.5 pcf HRP core. The panel with dense core sustained damage over a smaller area even when impacted at levels high enough to cause comparable indentation depths. A panel with 5.5 pcf TPC core exhibited superior performance relative to the panel with HRP core of comparable density.

Panels with thicker facesheets sustained smaller indentations and damage over a smaller area than those with thin facesheets for a given energy level, as expected. However, damage area appeared to approach a higher asymptote with increasing impact energy for panels with thicker facesheets as shown in Figure 6-8.

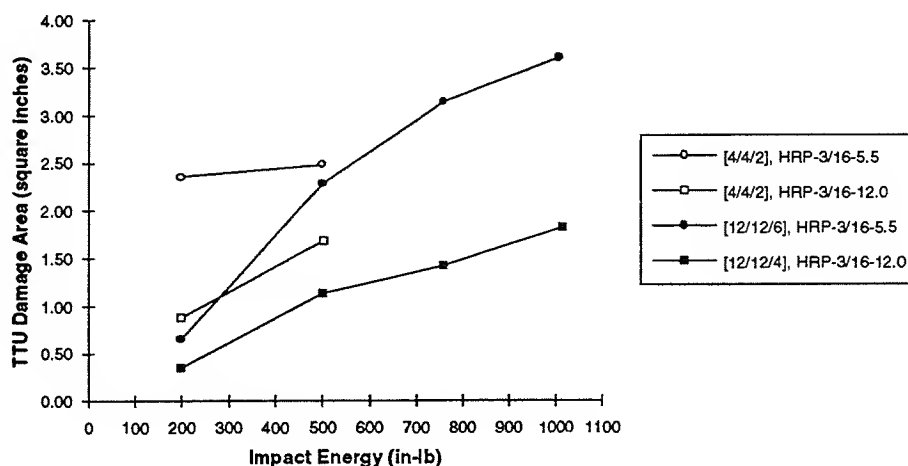


Figure 6-8. Influence of Facesheet Thickness on Impact Damage Resistance of Sandwich Structures.

A variety of failure modes and associated residual strengths were observed in CAI coupons. Local buckling of the facesheet around the impact indentation was observed in two panels impacted at high energy with a large impactor. These panels exhibited the highest strain at failure. A low energy impact with a small impactor resulted in lower residual compression strength in a panel of identical construction even though the apparent damage (dent depth and damage area) was less severe. Local buckling was not observed in this panel. Facesheet wrinkling combined with extension of an existing crack from the impact dent was observed in a fourth panel. This failure mode also resulted in comparatively low residual strength.

Representative Minimum Gage Keel Structure

The impact damage resistance and tolerance of aft keel sandwich structural concepts were investigated [8]. The baseline configuration (12 ply AS4/8552 facesheets and HRP-3/16-8.0 core) and variations in facesheet material (T300/F584), facesheet ply orientation, and core material (TPC-3/16-5.5) were considered. The influence of the manufacturing process (AFP vs. hand layup) was evaluated. Impact event variables including impactor size and impact energy were also considered.

Indentation depth was again found to be independent of variations in materials. Visible damage was created by impact with a one inch diameter tup at 200 in-lbs for all configurations. Impact damage area approached an asymptote of approximately 1.3 square inches in the baseline configuration for impact with a one inch tup. Impact with a two inch tup resulted in lesser indentation depth and damage over a larger area (Figure 6-9) as noted for other sandwich constructions. Panels constructed of AS4/8552 facesheet material were found to be more resistant to impact damage than those made of T300/F584. This may be due to the higher fracture toughness of the 8552 matrix resin. The baseline facesheet ply orientation [45/0/-45/90/0/-45/45]s sustained damage over a smaller area than two highly orthotropic layups. Panels with 8.0 pcf HRP core were more resistant to impact damage than panels with 5.5 pcf TPC core. The two manufacturing processes (fiber placement and tape lamination) produced panels with comparable impact damage resistance.

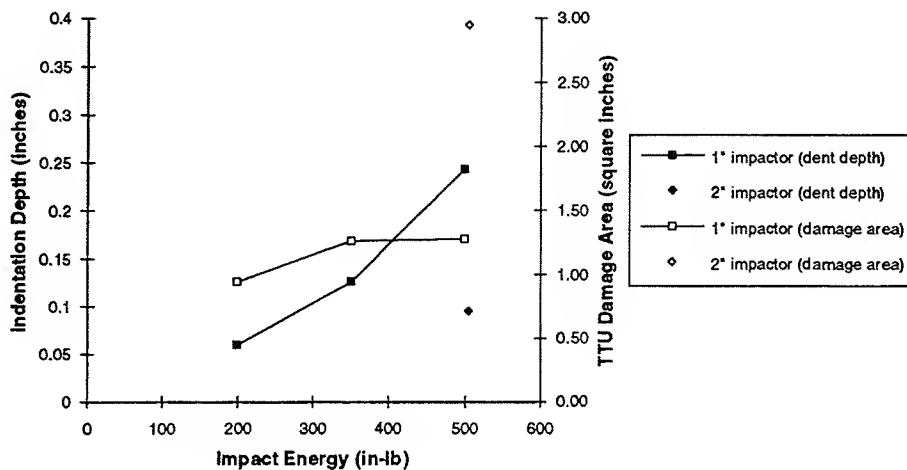


Figure 6-9. Impact Damage Resistance of Baseline Aft Keel Sandwich Structure.

Comparable CAI strengths were also observed in panels made with the two manufacturing processes. The AS4/8552 material provided higher CAI strength than T300/F584 for similar impact conditions. Sandwich panels with 8.0 pcf HRP core exhibited higher CAI strengths than those with 5.5 pcf TPC. These results are consistent with differences in impact damage resistance.

6.2 Environmental Durability

Fuselage structure is exposed to a variety of environments in service. A composite fuselage structure is expected to absorb water and other fluids by diffusion. Absorbed fluids may result in degradation of material properties and structural performance, especially at elevated temperatures. The effects of absorbed fluids on material performance must therefore be considered in design and analysis of the structure.

Bulk liquids may be transported to the interior of a sandwich structure through cracks in the finish and facesheets caused by thermal and mechanical loads. Damage at design details (e.g. core close-outs) from stress concentrations may provide a path for fluid ingress on a local scale. Foreign object impact damage may also provide a path for localized fluid ingress. Significant weight gain may accompany accumulation of liquids in a sandwich structure. Trapped liquids also complicate attempts to repair damaged structure and may result in poor quality repairs. Internal pressure generated by volatilization of trapped liquids during cure of a repair patch may result in additional damage to sandwich structure. Fluid ingress on a global scale through facesheet matrix cracks is therefore unacceptable. Although fluid ingress on a local scale may be avoided under expected service conditions by robust design practices, it must be expected to occur on occasion. Therefore, internal migration of liquids from local points of ingress must be inhibited such that damage may be repaired before significant weight gain or structural degradation occur.

6.2.1 Moisture Sorption by Diffusion

The diffusion characteristics of AS4/8552 tape and fabric materials were characterized to aid prediction of moisture sorption by the structure in service. Laminate coupons were dried in an oven prior to exposure to constant temperature and humidity environments. A single phase Fickian diffusion model exhibited poor correlation with test results as shown in Figure 6-10. The deviation from single phase Fickian behavior may be a result of differing diffusivities of the resin matrix components, a phenomenon which has been observed in some multi-phase systems. A two phase Fickian model [42] has been found to provide a reasonable representation of the data as shown in the figure. Values for equilibrium moisture content (M_{eq}), matrix resin phase volume fraction (V), and diffusion coefficients (D) determined by a least squares fit of test data are listed in Tables 6-2 and 6-3. Also listed are the absorptivity (α), diffusion constants (D_0), and activation energies (E_a).

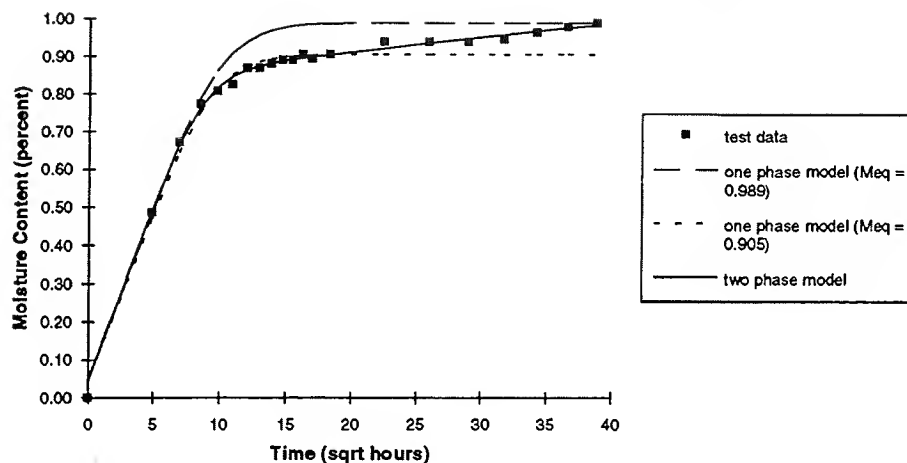


Figure 6-10. *Application of One and Two Phase Fickian Models to Diffusion of Water in AS4/8552 Tape (160F, 70% R.H.).*

Table 6-2. *Two Phase Fickian Moisture Sorption Constants for AS4/8552 Tape.*

	Temperature (F):	160			120	80
	Relative Humidity (%):	70	85	100		
	M_{eq} (%):	1.04	1.26	1.61	1.50	1.59
	α (%/% RH):	0.0155				
Phase 1	V (%):	79.8	81.0	75.2	74.7	76.7
	D (in ² /hr):	2.35E-06	2.86E-06	3.38E-06	1.69E-06	2.90E-07
	D ₀ (in ² /hr):	63.9				
	E _a (in-lbf/lbm):	1.92E08				
Phase 2	V (%):	20.2	19.0	24.8	25.3	23.3
	D (in ² /hr):	7.05E-08	1.81E-07	1.02E-07	2.38E-07	2.73E-08
	D ₀ (in ² /hr):	0.00134				
	E _a (in-lbf/lbm):	1.06E08				

Table 6-3. Two Phase Fickian Moisture Sorption Constants for AS4/8552 Fabric.

	Temperature (F):	160		120	80
	Relative Humidity (%):	70	85	100	
	M_{eq} (%):	1.12	1.376	1.826	1.916
	α (%/% RH):	0.0173			
	V (%):	80.5	77.6	73.9	69.2
Phase 1	D (in ² /hr):	2.15E-06	2.38E-06	2.61E-06	2.53E-07
	D ₀ (in ² /hr):	20.2			
	E _a (in-lbf/lbm):	1.82E08			
	V (%):	19.5	22.4	26.1	30.8
Phase 2	D (in ² /hr):	7.99E-08	2.11E-07	1.01E-07	1.66E-08
	D ₀ (in ² /hr):	0.149			
	E _a (in-lbf/lbm):	1.60E08			
	V (%):	19.5	22.4	26.1	30.8

Although the two phase model can be used to adequately represent the test data, the validity of this modeling approach is questionable. The 8552 resin system is actually a blend of two epoxies and a thermoplastic toughener. The epoxies may have sorption characteristics which are similar enough to be represented as a single phase leaving the thermoplastic as the second phase with distinctly different characteristics. However, Hercules reports that the morphology of the 8552 system does not exhibit two distinct phases, and that they believe the thermoplastic is dissolved into the epoxy during mixing and incorporated into the epoxy polymer during cure. They have no prior experience with the material behaving as a two phase system.

The deviation from single phase Fickian behavior may be a result of a dependence of diffusivity on moisture content. Absorbed moisture tends to cause swelling in polymers, altering the residual internal stress state in the laminate. Moisture sorption models which account for changes in diffusivity with moisture content may be more appropriate for modeling the behavior of the material.

The moisture sorption attributes of Metalbond 1515-3 and two 250°F curing film adhesives were also determined by weight gain measurements [36]. The use of dielectric sensors for monitoring moisture sorption in film adhesives was also investigated. The dielectric sensors were found to be useful in determining diffusion coefficients, but could not be used to measure equilibrium moisture content due to sensor failure at higher moisture concentrations.

6.2.2 Sandwich Structure Fluid Ingress

The matrix crack resistance of composite laminates with resin-rich interlaminar layers (RIL) of interest for the keel panel was investigated [43]. Finite element analyses

incorporating a crack closure technique were used in a parametric study of factors affecting strain energy release rates for matrix cracking. Ply group thickness, neighboring ply orientation, environment dependent material properties, and RIL stiffness were considered. The stiffness of the RIL was found to have the most significant effect, with reduced stiffness resulting in higher strain energy release rates due to an effective decoupling from the constraining effects of adjacent plies.

Intralaminar fracture toughness and matrix crack resistance tests performed on Hercules' IM7/8551-7 material yielded unexpected results [43]. Ply group thickness was found to have little effect on the onset of matrix cracking. This behavior is attributed to the reduction in effective constraint by adjacent plies discussed above. Matrix cracking was observed at lower strain levels in many wet laminates than in their dry counterparts. This is unusual because absorbed moisture tends to relieve transverse tensile stresses caused by differences in thermal expansion. The reduced matrix crack resistance in moisture saturated conditions may be a result of changes in material properties, such as intralaminar fracture toughness and modulus of the RIL. Moderate resistance to matrix cracking was observed in the IM7/8551-7 material, even without the in-situ strengthening effect of neighboring plies.

Experimental results confirmed the need for discrete modeling of the RIL. Predictions may be improved with more accurate modeling schemes and measured material properties for the RIL.

The thermo-mechanical strain required to initiate matrix cracking in AS4/8552 facesheet materials was investigated by the University of Wyoming [44]. The influence of temperature and absorbed moisture was examined. Matrix cracking occurred at lower strain levels for lower temperatures because of the higher thermal stresses. Absorbed moisture inhibited matrix cracking by relieving those same thermal stresses. Microstructural effects related to manufacturing process variations were also explored. The effects of ply group thickness, fabrication with the automated fiber placement process (instead of prepreg tape), and of the fiber distortion typical of processing over honeycomb core materials were considered. The influence of porosity was also studied. Matrix cracking was observed at reduced strain levels in tape laminates with greater ply group thickness. Porosity was found to significantly reduce the matrix crack resistance of both tape and fabric laminates.

Classical lamination theory was used to estimate the laminate strain at onset of matrix cracking for three layups typical of the side panel (Figure 6-11). A variety of conditions which may be expected in service were considered. The "nominal" case represents a laminate without porosity but with the ply distortion typical of sandwich facesheets. The strain at onset of matrix cracking was estimated for the -65F/dry condition. The "compression set" case represents a similar laminate in the -65F/dry condition which has previously been exposed to environmental conditions which would allow compression stress relaxation in the matrix as described in [45]. The "porous" case represents a porous laminate under the same conditions. Based on the results of this evaluation, matrix cracking is not expected to occur in a good quality laminate below design limit

strain levels, even under extreme environmental conditions. However, the presence of porosity could result in matrix cracking under normal service conditions. The estimates are close enough to expected strain levels to warrant a more rigorous analysis. The potential for matrix cracking under cyclic loading conditions should also be investigated.

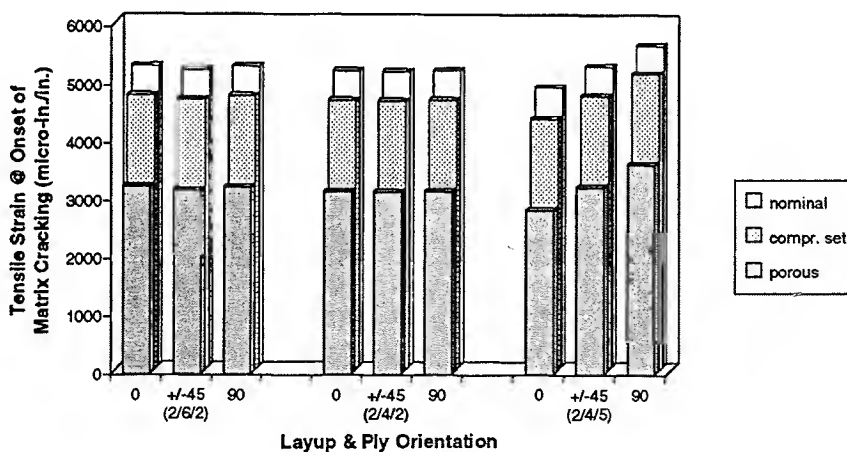


Figure 6-11 *Estimated Tensile Strain at Onset of Matrix Cracking in AS4/8552 Facesheet Materials. (X/Y/Z) Indicates the Number of (0/ \pm 45/90) Plies.*

6.2.3 Sandwich Structure Internal Fluid Migration

Two theoretical mechanisms for internal migration of water from a local point of ingress were investigated. First, it has been hypothesized that a core material which is permeable to air (and water vapor) will allow water to be transported in the vapor phase into the sandwich core from a local penetration. The water vapor is carried into the sandwich core as the airplane descends from flight altitude and the ambient pressure rises above the core internal pressure. The vapor condenses inside the core because the part temperature is below the rising dew point. Dry air is then expelled from the core as the airplane ascends again to flight altitude and the ambient pressure drops. Repetition of this phenomena would result in accumulation of water in the sandwich core. A second hypothesis states that the core which is exposed to the ambient environment in a local area becomes damaged from the expansion of water as it freezes. A larger area of core is then exposed to the environment. Cyclic freezing and thawing results in damage to a progressively larger area of core and an associated accumulation of water. Damage from thermal and mechanical loads would accelerate migration by either mechanism.

Flight Cycle Simulation

A series of sandwich panels with exposed core material were subjected to a cyclic environment representative of an extreme service environment. The sandwich panels

were constructed with a variety of core materials as illustrated in Figure 6-12. The core materials include low and high density Korex and HRP honeycombs. A particular block of Korex-1/8-3.0 has been selected for study because it was determined to be permeable to air. A similar block of Korex-1/8-3.0 found to be impermeable was included as a control panel. The low density HRP material was included in an attempt to duplicate results of Beech Starship certification efforts [46] which indicated the HRP material was not resistant to fluid migration. The panels were instrumented with pressure and temperature sensors as indicated in the Figure 6-12.

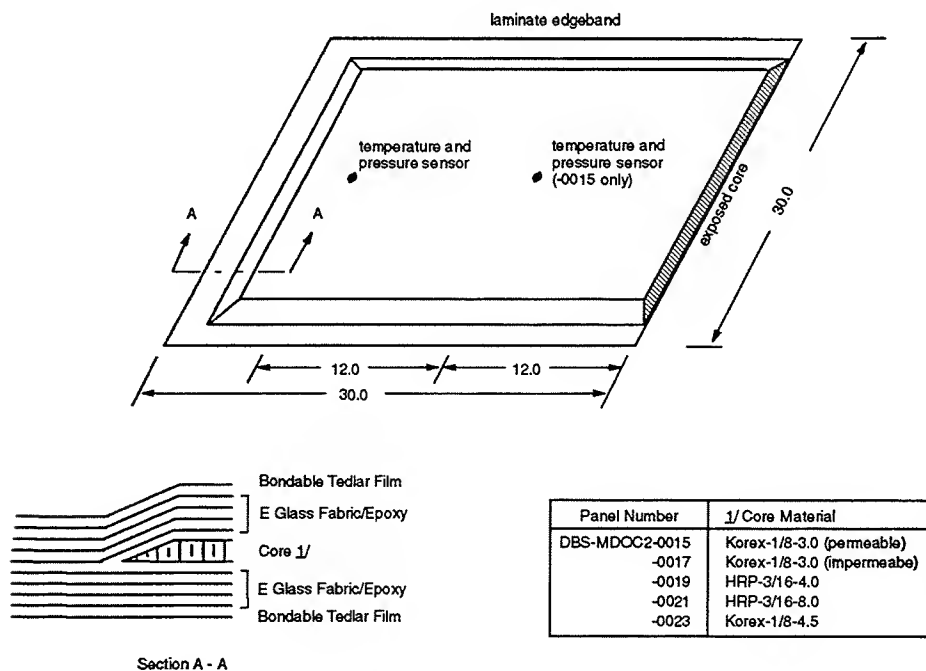


Figure 6-12. Sandwich Flight Cycle Test Panels.

The panels were first exposed to a constant environment of 2.15 psia (representing an altitude of 45,000 feet), ambient temperature, and no humidity for 18 hours. The purpose of this test was to measure the initial permeability of the core materials. The only significant response was observed in the panel with permeable Korex-1/8-3.0 core as shown in Figure 6-13.

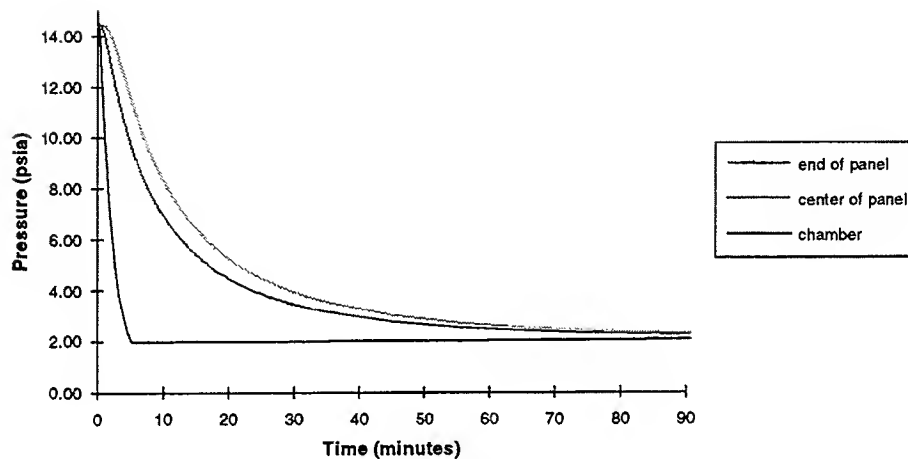


Figure 6-13. Internal Pressure Response of Flight Cycle Test Panel with Permeable Korex-1/8-3.0 Core to Reduced Pressure at Constant Temperature.

The chamber temperature was then cycled between -65°F and 140°F while holding pressure constant with no humidity. The panels were exposed to a total of 50 thermal cycles. This test was performed to determine whether the cyclic thermal stresses would result in damage (and permeability) in the core. Following thermal cycling, the initial permeability test was repeated to identify any change in panel response. No significant changes were observed.

The panels were subsequently exposed to simulated flight cycle environments. The chamber environment was cycled between -65F, 2.15 psia, and no humidity; and 140F, 14.7 psia and 95% relative humidity. The panels were inspected periodically for weight gain and with film radiography to monitor water ingress. A total of 485 simulated flight cycles were completed. Weight gain by the panels is presented in Figure 6-14. Initial weight gain appears to be consistent with moisture sorption by diffusion. Note that the panel with permeable Korex core initially gained the least. The acceleration in weight gain after 234 cycles indicates a potential change in sorption mechanisms. This is supported by results of film radiography which did not exhibit liquid water ingress after 234 cycles, but did show water ingress along the edges of all panels after 485 cycles. The greatest extent of water ingress was noted in the panel with permeable Korex core (this is consistent with weight gain data). Destructive evaluation of the panels to identify paths of water ingress were not completed at the time of this report but will be performed under the follow-on contract (NAS1-20553).

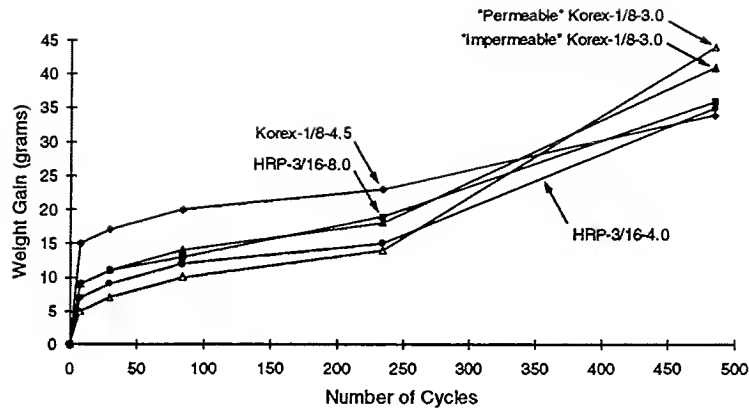


Figure 6-14. Weight Gain by Sandwich Panels with Core Materials Exposed to Simulated Flight Cycle Environments.

Sandwich Core Material Permeability

The permeability of sandwich core materials after static mechanical loading has been measured. The intent of this effort was to determine the maximum shear stress which could be applied to the core materials without causing damage which would result in a path for internal fluid migration. Sandwich coupons constructed of AS4/8552 facesheets and HRP-3/16-8.0 or Korex-1/8-4.5 honeycomb core were loaded in three point flexure to apply transverse shear stress to the core. Shear stresses were applied parallel and perpendicular to the core ribbon direction. A six inch square permeability test coupon was then cut from each flexure coupon as shown in Figure 6-15. Permeability tests were performed in a test fixture developed by Du Pont which measures air flow through the core from a central point where air pressure is applied (Figure 6-16). A liquid leak detector was used to identify the path of air flow, where possible.

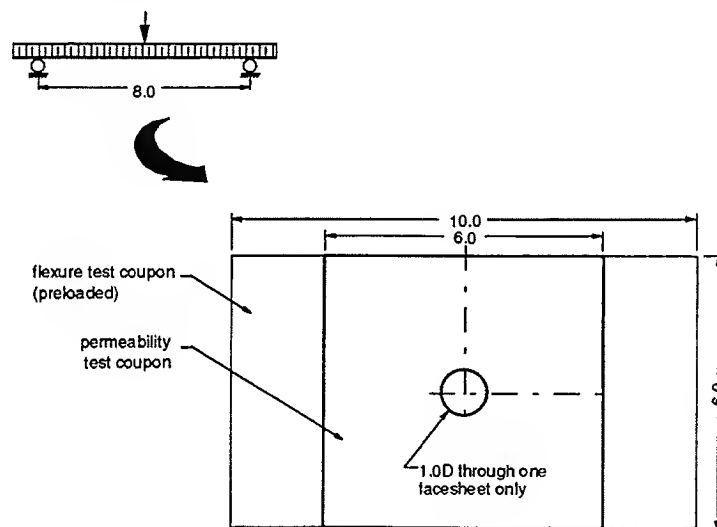


Figure 6-15. Sandwich Core Permeability Test Coupon from Flexure Coupon.

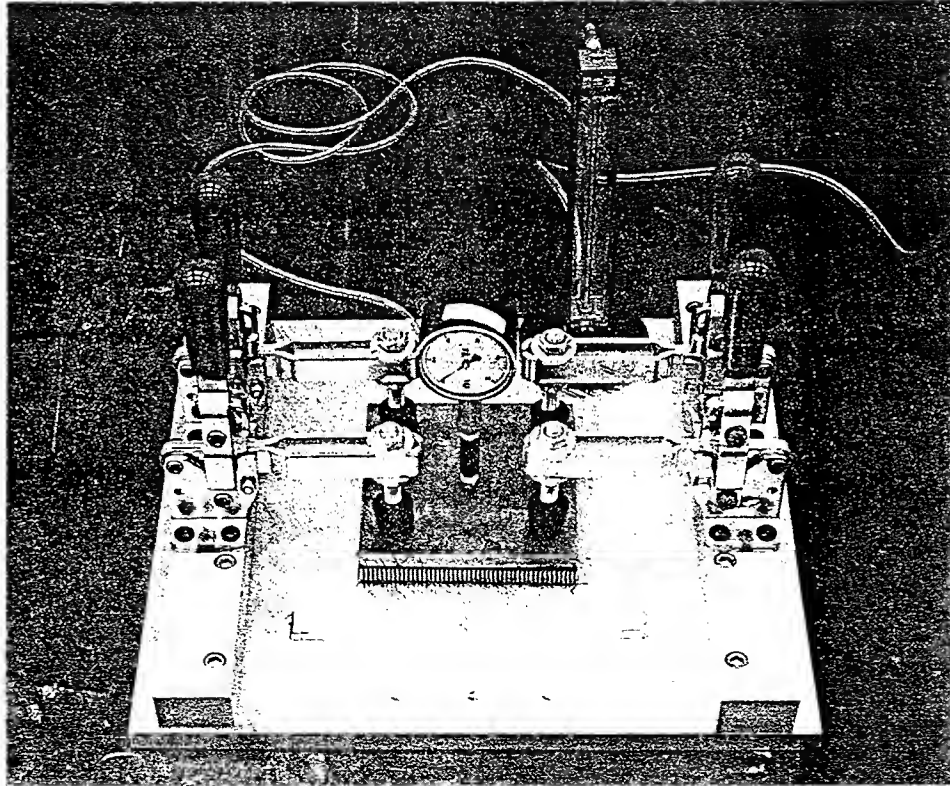


Figure 6-16. Sandwich Core Permeability Test Fixture Developed by Du Pont.

Results of the permeability tests for HRP-3/16-8.0 core material are presented in Figure 6-17, where "permeability" is defined as the measured flow rate divided by the applied pressure. The HRP material exhibited resistance to air flow at shear stress levels up to sixty percent of the material strength in the ribbon direction and up to seventy percent of the strength perpendicular to the ribbon direction. The node bonds provided the first path for air flow in coupons loaded in the ribbon direction. Loading perpendicular to the ribbon direction resulted in air flow through shear failures in the honeycomb cell walls. No significant air flow could be measured through Korex coupons which had been loaded up to seventy-five percent of the reported shear strength in the ribbon direction and up to ninety percent of the strength perpendicular to the ribbon direction.

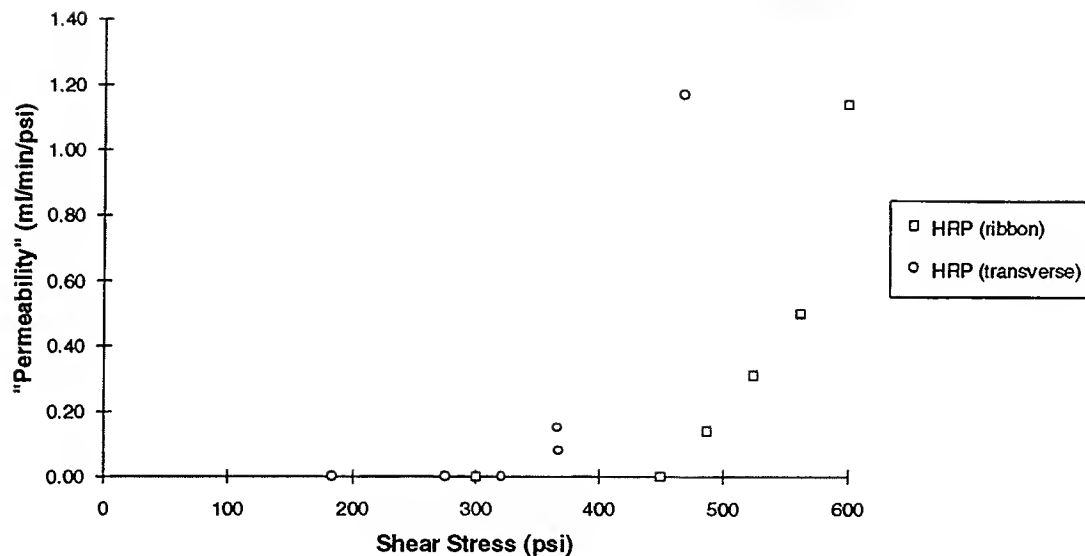


Figure 6-17 *Air Permeability of HRP-3/16-8.0 Honeycomb Core Material Following Application of Static Shear Stress.*

The influence of static and cyclic shear loads on the air permeability of honeycomb core materials was studied further by Analytical Services and Materials under subcontract to Boeing [47]. A test apparatus (illustrated in Figure 6-18) which is capable of concurrently applying shear loads and measuring air permeability of the core was constructed. A six inch square sandwich coupon representative of minimum gage fuselage structure (i.e. same materials and manufacturing process) was used for characterization of HRP-3/16-8.0 and Korex-1/8-4.5 core materials.

Results of static tests indicate permeability in the HRP material prior to core failure, and at lower shear stress levels than those determined from the flexure tests described above. Air flow was first measured at shear stress levels of approximately 375 and 200 psi, for loading parallel and perpendicular to the core ribbon direction, respectively. The permeability of the core increased under greater loads until failure occurred at the core to facesheet bondline. The bondline failures may have been a result of poor adhesive filleting to the honeycomb cell walls, which is typical for the cure cycle described in Section 4.6.2. Air permeability was not detected in the Korex material prior to core failure at approximately 350 and 225 psi for static shear loading parallel and perpendicular to the core ribbon, respectively.

Non-reversed cyclic shear loading of the HRP core material again resulted in permeability prior to failure of the core to facesheet bond. The permeability was aggravated with additional load cycles until failure as shown in Figure 6-19. The Korex material again exhibited resistance to air flow prior to core failure under cyclic loads. Korex also exhibited greater resistance to the effects of cyclic loading, resulting in flatter s-n curves than for HRP. Reversed cyclic loading resulted in earlier failures in both materials.

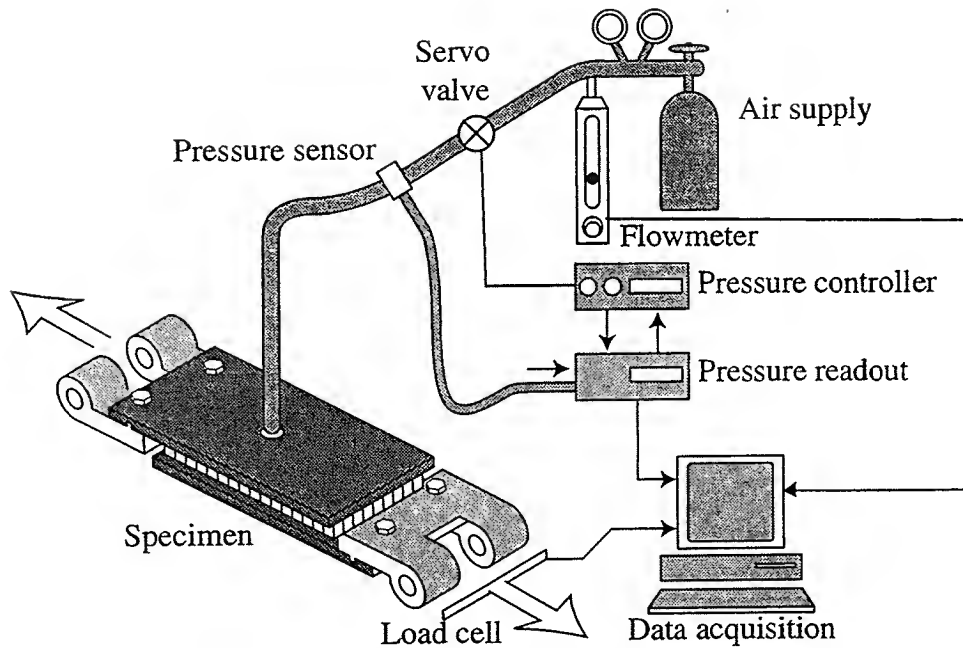


Figure 6-18. *Schematic of Test Apparatus for Measuring Sandwich Core Air Permeability While Applying Static or Cyclic Shear Loads.*

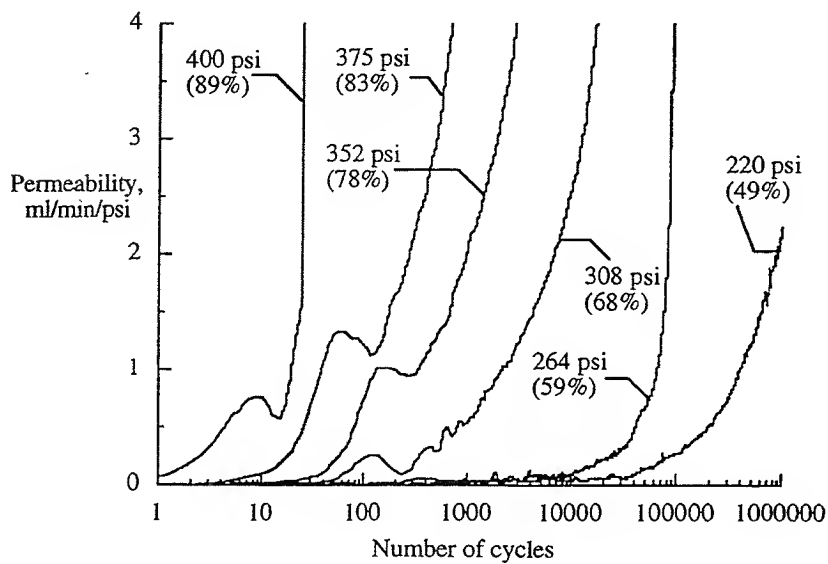


Figure 6-19. *"Permeability" of HRP-3/16-8.0 Honeycomb Sandwich Core as a Function of Non-Reversed Cyclic Shear Stress..*

6.2.4 Material Degradation by Absorbed Fluids

The lamina shear modulus (G_{12}) of AS4/8552 was measured via $\pm 45^\circ$ tension tests following exposure to a variety of fluids commonly encountered in the aviation industry as a preliminary indicator of solvent resistance. No significant degradation of the material was observed (Figure 6-20).

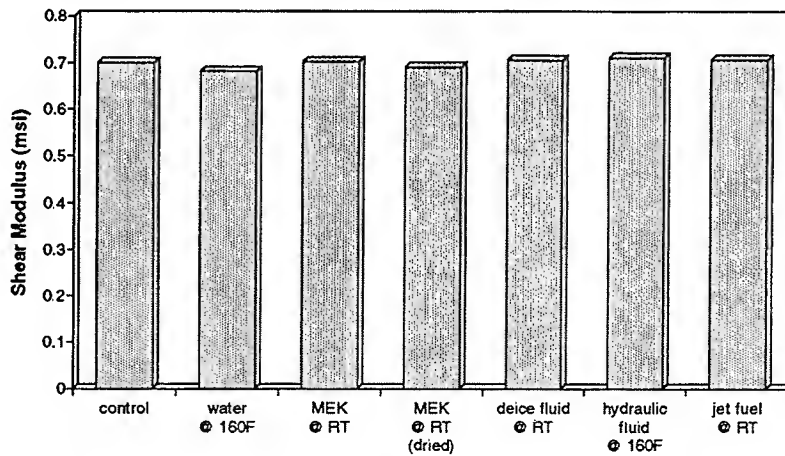


Figure 6-20. In-Plane Lamina Shear Modulus (G_{12}) of Hercules' AS4/8552 Following Exposure to Fluids Typical of the Aviation Industry. The Tests were Performed at Room Temperature Following a Six Day Exposure to the Fluids Indicated.

The mechanical properties of AS4/8552 were characterized as a function of absorbed moisture content and temperature. Unnotched and open-hole tension and compression, and bearing coupons were conditioned to near saturation (approximately 250 days) in 70% and 85% relative humidity environments and then tested at a temperature of 180°F. Hot/wet conditions had no significant effect on tensile modulus, but compression modulus was degraded by 4%. Tensile strengths were relatively unaffected by hot/wet environments while compression and bearing strengths were significantly degraded as shown in Figure 6-21.

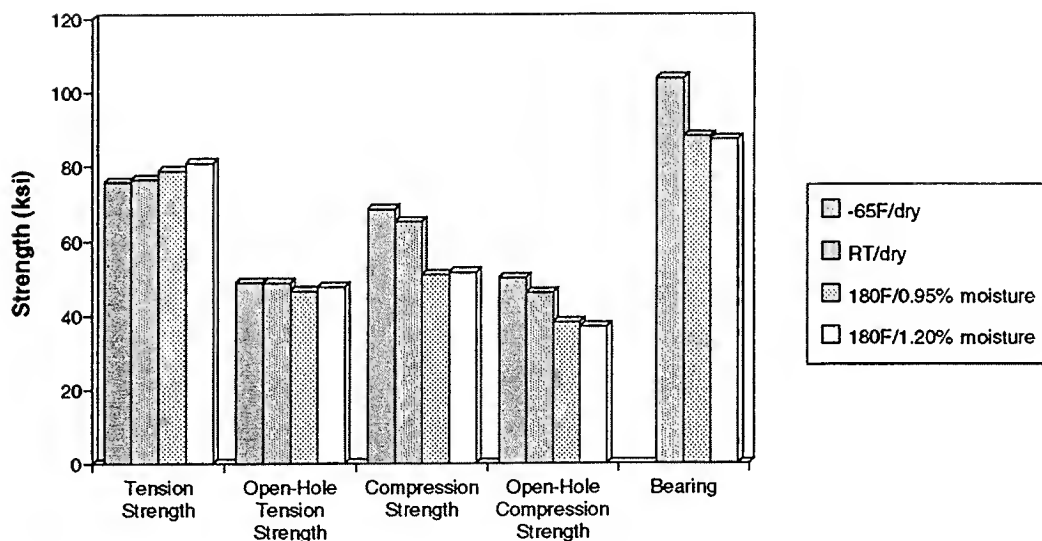


Figure 6-21. Influence of Absorbed Moisture and Elevated Temperature on the Mechanical Performance of AS4/8552.

The viscoelastic properties of Narmco's Metalbond 1515-3 epoxy film adhesive were characterized by the University of Washington to support analysis of bonded joints [36]. The use of DMA to measure changes in viscoelastic properties during moisture sorption was investigated. The technique provided promising results although control of water bath temperature was inadequate with available equipment. The glass transition temperature of the material was measured with DMA as a function of absorbed moisture content. The influence of temperature, absorbed moisture, and strain rate on storage (elastic) modulus were determined by DMA. Creep and stress relaxation were characterized as a function of temperature and absorbed moisture content.

7.0 FIRE WORTHINESS

A cursory investigation of the fire worthiness of a composite fuselage was performed. The primary concern is whether the use of composite materials would result in greater hazard to passengers and crew during aircraft evacuation in the event of a post-crash fuel-fed external fire. An evaluation of the fire worthiness of a composite fuselage should be based on the habitability of the passenger compartment during such an event. Criteria for an evaluation should be based on comparison with the response of comparable aluminum structure.

Composite materials are expected to exhibit better retention of stiffness and strength in a fire than aluminum. This would delay loss of structural integrity which would impede evacuation. Composites have been shown to be more resistant to burn-through than aluminum and are expected to provide a more effective barrier between an external fire and the passenger compartment. Composite materials are also expected to act as an insulator, reducing the risk of auto-ignition and smoke emission from interior materials. However, the composite itself may ignite, introducing fire into the interior of the fuselage. Smoke produced by the composite could enter the passenger cabin and inhibit passenger egress. Generation of combustible smoke could result in a flash fire within the fuselage.

A secondary concern is related to the integrity of structure which has been exposed to a fire. A hardness test is typically used to evaluate metal structure which has endured a fire. A non-destructive method of evaluating a composite airframe following a fire is needed.

Verification of the fire worthiness of the configured structure was determined to be beyond the scope of the current contract. However, standard flammability and smoke release tests were performed on materials selected for use in the ATCAS program as listed in Table 7-1. There are currently no flammability or smoke release requirements in FAR Part 25 for fuselage skin or stiffening elements. However, the results may be compared with FAA requirements for interior panels as a reference. All of the materials met the sixty-second vertical flammability test requirements for burn length (≤ 6 inches) as shown in Figure 7-1 and for drip extinguishing time (≤ 3 seconds), as no drips were observed. However, only the braided AS4/PR-500 met the requirement for self extinguishing time (≤ 15 seconds) as shown in Figure 7-2. The braided AS4/PR-500 material exceeded the FAA limit for smoke emission ($D_s \leq 200$ @ 4 minutes) as shown in Figure 7-3. A comparison of toxic gas emission test results with Boeing design requirements for interior panels is presented in Figure 7-4. The AS4/938 tow and AS4/8552 fabric/tow laminates failed to meet limits for emission of sulfur dioxide.

Performance of the flammability and smoke release tests has served as a bench marking exercise. The acceptability of the materials for use in fuselage applications, however, can not be determined solely by this type of test. The behavior of the configured structure in conditions representative of a post-crash fuel-fed external fire must be studied so that appropriate criteria may be established.

Table 7-1. Flammability and Smoke Release Test Matrix. Three Tests Each were Performed in Accordance with Standard Methods.

Material System	Structure Represented	Test Specimen Form
AS4/938 tow	crown skins and stringers	laminate coupons
AS4/8552 tow and fabric Korex honeycomb	side and keel skins	laminate and sandwich coupons
AS4/RSL 1895 braided and resin transfer molded	circumferential frames and other curved stiffening elements	elements
AS4/PR500 braided and resin transfer molded	circumferential frames and other curved stiffening elements	elements

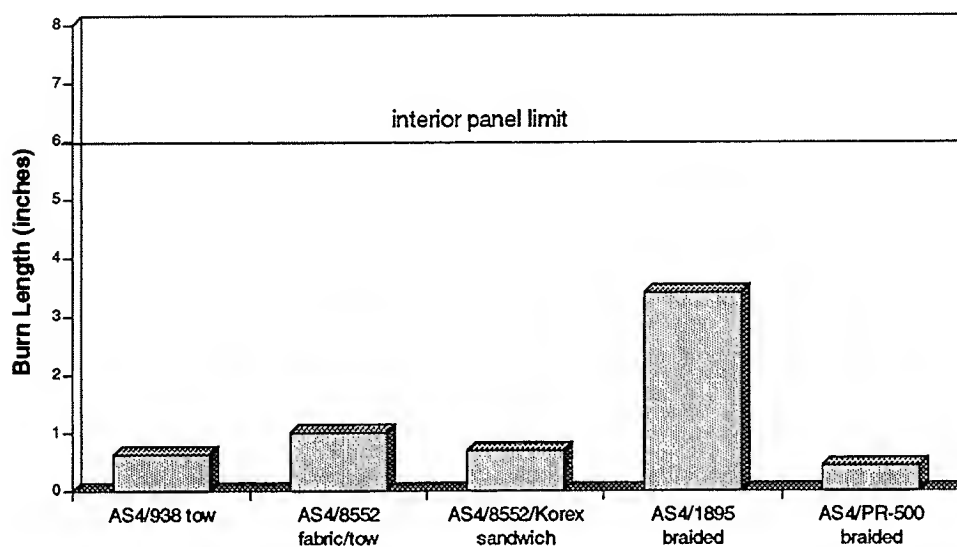


Figure 7-1. Results of Sixty Second Vertical Flammability Tests (Burn Length).

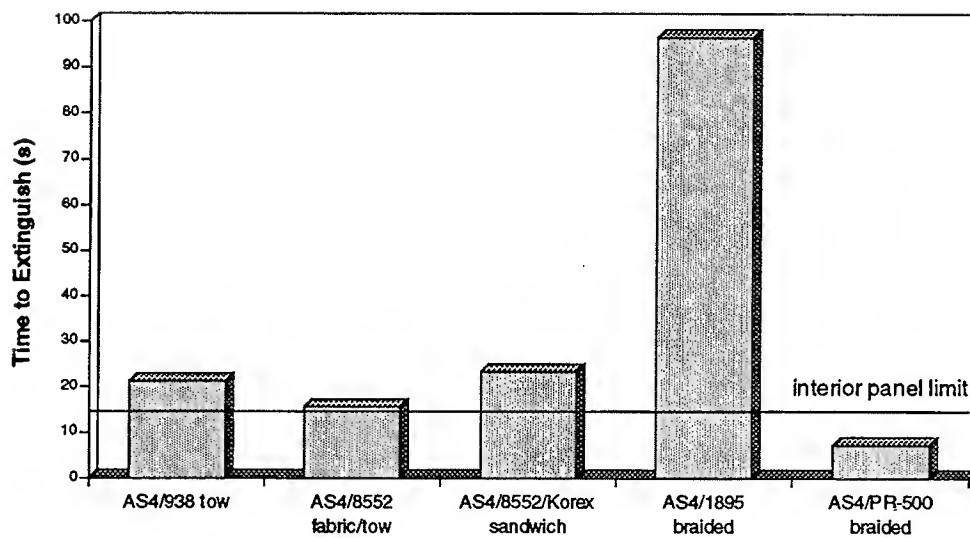


Figure 7-2. Results of Sixty Second Vertical Flammability Tests (Time to Extinguish).

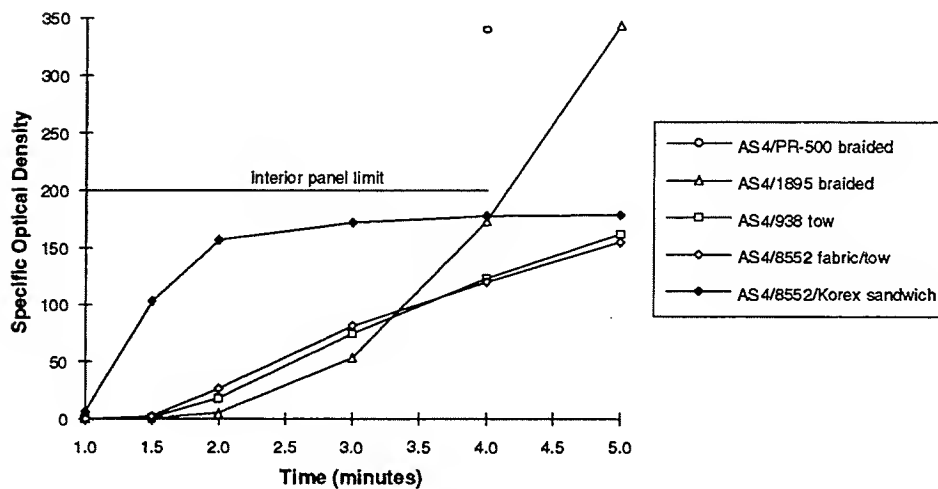


Figure 7-3. Results of NBS Smoke Release Tests (Optical Density).

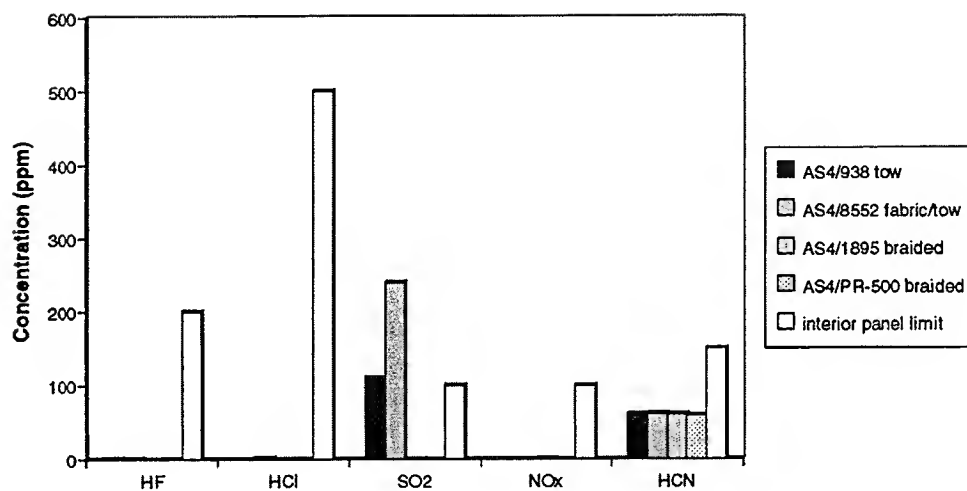


Figure 7-4. Results of NBS Smoke Release Tests (Toxic Gas Generation).

8.0 CONCLUDING REMARKS

Material and Process Selection

Candidate fibrous composite materials and associated manufacturing processes were identified for use in commercial transport fuselage applications. Cost/weight trade studies based on detailed designs and manufacturing plans were performed to aid selection of optimal materials and processes. The automated fiber placement process was selected for fabrication of fuselage skin panels based on projected raw material cost reductions, improved ply drop/add efficiency relative to tape lamination, and the ability to lay-up on compound contours typical of nose and tail sections. Two types of automated fiber placement were employed in fabrication of test panels and manufacturing demonstration articles with a variety of prepreg tow materials. The feasibility, although not the reliability, of the process has been established. Prepreg tow material characteristics critical for use in the fiber placement process were identified. Significant differences in the performance of fiber-placed and laminated tape materials, and a strong influence of manufacturing process variations on performance indicate a need for a better understanding of the fiber placement process and improved process control methods.

Fiberite's AS4/938 was selected for fabrication of fuselage crown panel skins, primarily because of its low cost and superior tension fracture properties. However, significant variations in tow width and resin content were observed in AS4/938 prepreg tow materials. These variations may have been a result of the solution coating process employed by Fiberite in manufacture of the prepreg tow. Tow width variations may result in reduced fiber placement rates and inconsistent mechanical performance. Prepreg tow resin content variations and resin flow during cure resulted in significant variations in resin content and thickness of finished parts which would contribute to inconsistent performance and would aggravate the need for shimming during assembly operations. More robust prepregging and autoclave cure processes are needed for the AS4/938 material system.

An intraply hybrid of carbon and glass fiber reinforced epoxy is a promising candidate for fuselage skins where tension damage tolerance is a design constraining requirement. However, variations in ultrasonic attenuation for the differing fiber types would complicate ultrasonic inspection of this material system.

Hercules' AS4/8552 was chosen for keel and side panel sandwich skins based on cost, compatibility with the automated fiber placement and sandwich cocure processes, and balanced mechanical properties. The use of plain weave carbon fabric on the surfaces of the facesheets resulted in improved tension fracture properties, making this material attractive for crown applications as well. Glass fabric surface plies would provide inherent isolation from aluminum components for protection from galvanic corrosion and may also improve the fire resistance properties of the material. An autoclave cure process was developed for fabrication of thick laminate/sandwich structure with the

AS4/8552 material. However, the cure cycle should be modified to provide better adhesive fillets between the facesheets and core. Alteration of the prepreg resin curative to provide a material which is more stable in the manufacturing environment may require further adjustment of the cure cycle.

Du Pont's Korex honeycomb was identified as a cost- and weight-efficient sandwich core material with the potential for excellent resistance to impact damage and fluid ingress. The durability of the material has not been verified. Hexcel's HRP honeycomb is a solid alternative core material with a good balance of cost, mechanical properties and durability. A process envelope for heat forming HRP core without degrading the material was developed. A similar effort will likely be required for the Korex material.

A variety of sandwich core close-out design concepts were investigated for use in fuselage skin panels. The desire for non-eccentric load paths through panel splice joints make full-depth core close-outs attractive. However, the fastener clamp-up and bearing/bypass capability of these concepts must be demonstrated, as well as their resistance to fluid ingress. Although a rigorous close-out development effort was not expended, progress was made through manufacture and test of a number of demonstration articles.

The braiding and resin transfer molding processes were selected for fabrication of circumferential frames, window frames, and other curved stiffening elements. An innovative and efficient process for manufacturing circumferential frames was demonstrated by Fiber Innovations. However, process development and characterization efforts were performed with Shell's RSL 1895 resin which is no longer produced. Additional development with a likely alternative matrix resin (3M's PR-500) was performed by Lockheed under their ACT contract.

The pultrusion process was identified for fabrication of linear stiffening elements with constant cross-section. However, no effort was expended on development of the pultrusion process.

Mechanical Performance of Candidate Materials

The stiffness, strength, notch sensitivity and bearing/bypass properties of selected skin materials were characterized. The use of lamina moduli obtained from unidirectional test coupons for predicting laminate modulus with classical lamination theory was found to be inaccurate. Axial lamina moduli were more accurately derived from multidirectional laminate test data.

A significant effort was expended in the study of notch sensitivity in composite materials because damage tolerance was found to be the design constraining material property for a majority of the fuselage structure. The use of machined notches to represent through-penetrations was found to be reasonably accurate for tensile loading in most cases. However, the compression strength of sandwich panels with through-penetrations were only 75 to 80% of those with machined notches of the same size. These observations are based on a limited number of tests. A wide range of material variables including fiber

type, matrix type, layup, intraply hybridization, and the use of fabric surface plies affected tensile notch sensitivity. A trade-off between small-notch and large-notch tensile strength was observed for many of the variables. A significant implication of this behavior is that small-notch test data should not be used to screen materials for applications in which large-notch behavior is critical. The manufacturing process and process variations were also observed to have a significant influence on tensile notch sensitivity. Notched compression strength was observed to be relatively insensitive to material and manufacturing process variables, with the exception of thickness.

Non-classical material responses to tensile loading were observed in the form of notch-tip strain distributions which were less severe than predicted by linear-elastic fracture mechanics even prior to creation of notch-tip damage. Further deviation from classical material response accompanied an accumulation of notch-tip damage prior to failure of tensile coupons. The strong dependence of notched compression strength on thickness and near linear-elastic material behavior suggest a local instability driven failure mode which preempts accumulation of a significant amount of notch tip damage. Finite element analyses incorporating strain-softening material laws were identified as the analytical approach with the greatest potential for modeling the observed non-classical material responses. However, an efficient method for determining the strain-softening law directly from test results is needed. Energy methods appear promising, although an appropriate test coupon configuration must be developed for composite materials.

The bearing/bypass properties of candidate fuselage skin materials were also characterized. Results for fiber-placed laminates were comparable to those previously observed for tape laminates. A strong correlation between bypass strain-at-failure and linear-elastic stress concentration factor was observed. Bearing strength was found to be independent of layup. The influence of end/edge margin and countersink on bearing/bypass properties were also consistent with those previously observed for tape laminates. The bearing/bypass properties of an AS4-S2/938 intraply hybrid material were found to be moderately dependent on hole location and were comparable to those of AS4/938.

Predictions of uniaxial bearing/tension bypass strength with Boeing's BEARBY analysis code were consistent with results of tension bearing/bypass interaction tests. Significantly conservative predictions of transverse-bearing/compression-bypass strength relative to test results were likely a result of the use of open-hole (instead of filled-hole) compression strength values for generation of bypass failure criteria.

The bolted joint performance of candidate sandwich core close-outs were also investigated. Design concepts with adequate load carrying capability were identified. Optimization of the design including incorporation of innovative concepts will require additional work.

The performance of braided textile composite materials of interest for use in circumferential frames and other curved stiffening elements were investigated. A textile composites analysis model (TECA) was developed to predict the stiffness and strength of 2-D and 3-D braided composites. The properties of several 2-D and 3-D braided

composites were characterized. Good correlation was observed between analytical and experimental results. However, the matrix resin used for fabrication of test panels (Shell's RSL 1895) is no longer produced. The properties of braided composites with a likely alternative resin (3M's PR-500) were characterized by Lockheed under their ACT contract.

Impact Damage Resistance

The impact damage resistance of stiffened skin and sandwich structures were studied. A significant database was generated for baseline and alternative materials and structural configurations. The severity of the sustained impact damage was observed to be a strong function of impact variables and variable interactions. An inverse relationship between the extent and visibility of impact damage for some variables (e.g. impactor diameter) suggests the traditional "barely visible impact damage" criteria and related requirements may be flawed. Furthermore, the use of a single value for an extrinsic variable in a test program may produce misleading results. Material and structural variable interactions were also observed. For example, matrix toughness, which has been shown to have a strong influence on the impact damage resistance of relatively thick laminate coupons, had little effect on damage area in configured minimum gage stiffened skin structure. Material screening and structural impact damage resistance tests should therefore be performed in conditions representative of those expected in service.

A sublaminar stability based approach for predicting the compression-after-impact strength of composite laminates was developed. The method has been verified for laminates with large, symmetric impact damage states. Failure to account for the effects of fiber damage resulted in poor correlation with results for laminates with small damage areas where sublaminar instability did not initiate failure. Poor correlation with results for coupons with large, unsymmetric damage states were shown to be a result of coupon general instability.

Environmental Durability

The environmental durability of AS4/8552 sandwich structures was also investigated. The moisture diffusion attributes of the material were characterized to aid in prediction of moisture sorption of the structure in service.

The potential for fluid ingress through matrix cracks in the AS4/8552 sandwich facesheets was investigated. Matrix cracking is not expected to occur under static loads below design limit strain levels, even in extreme environmental conditions. However, the matrix crack resistance of the material was shown to be significantly degraded by microstructural features such as porosity. The resistance of the material to matrix cracking under cyclic loading conditions should be verified.

The mechanisms of internal fluid migration in sandwich structures were also studied. Sandwich panels with exposed HRP and Korex core materials were subjected to cyclic environments representative of extreme service conditions. Liquid water migration

through the core was observed by film radiography in each of the panels tested. Although the paths of water ingress could not be identified under the current contract due to schedule constraints, this task will be performed during the follow-on contract (NAS1-20553).

The influence of static and cyclic shear stresses on sandwich core air permeability were characterized. Permeability was observed in HRP core materials at static shear stress levels significantly lower than the strength of the material. Cyclic shear loading of the HRP core material also resulted in permeability prior to failure. The Korex core material was found to be impermeable prior to mechanical failure under both static and cyclic shear loads.

Finally, the influence of absorbed water and other fluids typical of the aviation industry on the performance of AS4/8552 and Metlbond 1515-3M film adhesive were characterized.

Fire Worthiness

A cursory investigation of the fire worthiness of a composite fuselage was performed. The primary concern is whether the use of composite materials would result in greater hazard to passengers and crew during aircraft evacuation in the event of a post-crash fuel-fed external fire. Verification of the fire worthiness of the configured structure was determined to be beyond the scope of the current contract. However, standard flammability and smoke release tests were performed on materials selected for use in the ATCAS program. None of the materials met all Boeing and FAA requirements for interior panels. However, the acceptability of the materials for use in fuselage applications can not be determined solely by these tests. The behavior of the configured structure in conditions representative of a post-crash fuel-fed external fire should be studied so that appropriate criteria may be established.

9.0 REFERENCES

1. Flynn, B. W.; et. al.: "Advanced Technology Composite Fuselage - Maintenance," NASA CR-4733, 1997.
2. Ilcewicz, L. B.; et. al.: "Advanced Technology Composite Fuselage - Program Overview," NASA CR-4734, 1997.
3. Ilcewicz, L. B.; et. al.: "Application of a Design-Build Team Approach to Low Cost and Weight Composite Fuselage Structure," NASA CR-4418, December 1991.
4. Walker, T. H.; et. al.: "Advanced Technology Composite Fuselage - Structural Performance," NASA CR-4732, 1997.
5. Ilcewicz, L. B.; et. al.: "Tension Fracture of Laminates for Transport Fuselage Part 4: Damage Tolerance Analysis," Fourth NASA/DoD Advanced Composites Technology Conference, NASA CP-3229, December 1993.
6. Willden, K. S.; et. al.: "Advanced Technology Composite Fuselage - Manufacturing," NASA CR-4735, 1997.
7. Flynn, B. W.; et. al.: "Global Cost and Weight Evaluation of Fuselage Keel Design Concepts," NASA CR-4541, December 1993.
8. Avery, W. B.; et. al.: "Design and Structural Development of a Composite Fuselage Keel Panel," Fifth NASA/DoD Advanced Composites Technology Conference, NASA CP-3294, May 1995.
9. Scholz, D. B.; et. al.: "Material and Processing Developments for Composite Fuselage Sandwich Structure," Fifth NASA/DoD Advanced Composites Technology Conference, NASA CP-3294, May 1995.
10. Polland, D. R.; et. al.: "Global Cost and Weight Evaluation of Fuselage Side Panel Design Concepts," NASA CR-4730, 1997.
11. Hanson, C. T.; et. al.: "Design Integration of a Composite Aft Fuselage Barrel Section," Sixth NASA/DoD Advanced Composites Technology Conference, NASA CP-3326, 1996.
12. Ilcewicz, L. B., et. al.: "Advanced Technology Composite Fuselage - Design Cost Methods," NASA CR-4737, 1996.
13. Swanson, G. D.; et. al.: "Compression Test Results for Stiffened Composite Fuselage Structure," Fourth NASA/DoD Advanced Composites Technology Conference, NASA CP-3229, December 1993.

14. Walker, T. H.; et. al.: "Tension Fracture of Laminates for Transport Fuselage, Part 1: Material Screening," Second NASA Advanced Composites Technology Conference, NASA CP-3154, June 1992.
15. Walker, T. H.; et. al.: "Damage Tolerance of Composite Fuselage Structure," Sixth NASA/DoD Advanced Composites Technology Conference, NASA CP-3326, 1996.
16. Dost, E. F.; et. al.: "Impact Damage Resistance of Composite Fuselage Structure," NASA CR-4658, 1997.
17. Walker, T. H.; et. al.: "Tension Fracture of Laminates for Transport Fuselage, Part 2: Large Notches," Third NASA Advanced Composites Technology Conference, NASA CP-3178, January 1993.
18. Saatchi, H.; et.al.: "In-situ Processing Methods for Composite Fuselage Sandwich Structures," Third NASA Advanced Composites Technology Conference, NASA CP-3178, January 1993.
19. Wang, Y. S.; et. al.: "Development of High Performance Cyanate Esters Foam," Proceedings of the 36th International SAMPE Symposium, April 1991.
20. Nelson, K. M.: "All Composite Fuselage Window Close-Out Resin Transfer Molding," NAS1-18954, Task 20 Final Report August 31, 1995.
21. Fedro, M. J. and K. S. Willden: "Characterization and Manufacture of Braided Composites for Large Commercial Aircraft Structures," Second NASA Advanced Composites Technology Conference, NASA CP-3154, June 1992.
22. Willden, K. S.; et. al.: "Manufacturing Scale-Up of Composite Fuselage Crown Panels," Third NASA Advanced Composites Technology Conference, NASA CP-3178, January 1993.
23. Chamis, C. C.: "Simplified Composite Micromechanics Equations for Hygral, Thermal and Mechanical Properties," NASA TM-83320, February 1983.
24. McGowan, D.; et. al.: "Compression Tests and Nonlinear Analyses of a Stringer- and Frame-Stiffened Graphite-Epoxy Fuselage Crown Panel," Fifth NASA/DoD Advanced Composites Technology Conference, NASA CP-3294, May 1995.
25. Awerbuch, J. and M. S. Madhukar: "Notched Strength of Composite Laminates: Predictions and Experiments - A Review," Journal of Reinforced Plastics and Composites, vol. 4, number 1, January 1985.
26. Mar, J. W. and K. Y. Lin: "Fracture Mechanics Correlation for Tensile Failure of Filamentary Composites with Holes," Journal of Aircraft, vol. 14, no. 7, July 1977.
27. Mak, Y.: "Strain Rate Effects on Tensile Fracture and Damage Tolerance of Composite Laminates," TELAC Report 92-5, Massachusetts Institute of Technology Department of Aeronautics and Astronautics, May 1992.

28. Cairns, D. S.; et. al.: "Far-Field and Near-Field Strain Response of Automated Tow Placed Laminates to Stress Concentrations," Third NASA Advanced Composites Technology Conference, NASA CP-3178, January 1993.
29. Cairns, D. S.; et. al.: "The Consequence of Material Inhomogeneity on the Strain Response of Automated Tow Placed Structures with Stress Concentrations," Fourth NASA/DoD Advanced Composites Technology Conference, NASA CP-3229, December 1993.
30. Basham, K. D.; et. al.: "A New Method to Compute Size Independent Fracture Toughness Values for Brittle Materials," Engineering Fracture Mechanics, Vol. 46, 1993.
31. Bazant, Z. P.; and L. Cedolin: "Stability of Structures," Oxford University Press, 1991.
32. Garbo, S.; and J. Ogonowski: "Effect of Variances and Manufacturing Tolerances on the Design Strength and Life of Mechanically Fastened Composite Joints. Volume I: Methodology Development and Data Evaluation," AFWAL TR-81-3041, April 1981.
33. Cohen, D.; et. al.: "Analysis and Testing of Thick Automated Tow Placed (ATP) Joint Structures," Fourth NASA/DoD Advanced Composites Technology Conference, NASA CP-3229, December 1993.
34. Masters, J. E.; et. al.: "Experimental and Analytical Characterization of Triaxially Braided Textile Composites," Third NASA Advanced Composites Technology Conference, NASA CP-3178, January 1993.
35. Miller, A. W.: "An Investigation of the Mode I and Mode II Fracture Toughness of Graphite/Epoxy Composites," Masters Thesis, Drexel University, December 1994.
36. Seferis, J. C.: "Durability of Epoxy Matrices in Advanced Technology Aircraft Structures," University of Washington Polymeric Composites Laboratory Report 92:174, May 1992.
37. Dost, E. F.; et. al.: "Sublamine Stability Based Modeling of Impact Damaged Composite Laminates," Proceedings of the 3rd Technical Conference of the American Society for Composites, 1988.
38. Ilcewicz, L.B.; et. al.: "A Model for Compression After Impact Strength Evaluation," Proceedings of the 21st International SAMPE Technical Conference, 1989.
39. Shivakumar, K.N.; and J.D. Whitcomb: "Buckling of a Sublamine in a Quasi-Isotropic Composite Laminate," Journal of Composite Materials, Vol. 19, January 1985.
40. Dost, E.F.; et. al.: "The Effects of Stacking Sequence on Impact Damage Resistance and Residual Strength for Quasi-Isotropic Laminates," Proceedings of the Third Symposium for Composite Materials: Fatigue and Fracture, ASTM STP 1110, 1991.

41. Lin, K.Y.; et. al.: "Characterization of Post-Impact Compressive Behavior of Composite Laminates; Interim Report for Period: January 1990 - December 1991, subcontractor report, University of Washington Department of Aeronautics and Astronautics, May 1992
42. Jacobs, P. and F. Jones: "Diffusion of Moisture into Two Phase Polymers, Part 1 The Development of an Analytical Model and its Application to Styrene-Ethylene/Butylene-Styrene Block Copolymer," Journal of Materials Science, 1989.
43. Ilcewicz, L. B.; et. al.: "Matrix Cracking in Composite Laminates with Resin-Rich Interlaminar Layers," Proceedings of the Third Symposium for Composite Materials: Fatigue and Fracture, ASTM STP 1110, 1991.
44. Coguill, R.J.; et. al.: "Matrix Cracking in Composite Sandwich Facesheets," University of Wyoming Composite Materials Research Group Report UW-CMRG-R-95-104, March 1995.
45. Rothschilds, R.J.; et. al.: "The Effect of Hygrothermal Histories on Matrix Cracking in Fiber Reinforced Laminates," Journal of Engineering Materials and Technology, Vol. 110, April 1988.
46. Wong, R.B.; et. al.: "Durability and Damage Tolerance of Graphite/Epoxy Honeycomb Structures," Proceedings of the 35th International SAMPE Symposium, April 1990.
47. Glass, D.E; et. al.: "Honeycomb Core Permeability Under Mechanical Loads," AS&M-R53-96-01, Analytical Services & Materials, Hampton, VA, February 1996.

APPENDIX A

Quality Assurance Test Results for Prepreg Tow Materials

Physical Properties

Results of physical property tests performed on prepreg tow materials are presented in Table A-1. Fiber lineal weight and resin content were determined by solvent wash. Three samples were tested from each spool of material provided by Fiberite and Hexcel. A sampling plan was adopted by Hercules. The samples were taken from near the end of the spool in all cases. Fiber lineal weight and resin content test results are presented graphically in Figures A-1 and A-2. The nominal (target) and mean values are indicated by the open and closed points, respectively. Variation (three standard deviations) is indicated by the upper and lower cross-marks.

The width of the prepreg tow was measured manually with an optical microscope or comparator for each spool of material provided by Fiberite and Hexcel. A sampling plan was again employed by Hercules for tow width measurement with an automated photo-electric system. Samples were taken from near the ends of the spools. Representation of the length of the prepreg tow with samples from the ends of the spools has been verified by Hercules. Results of tow width measurements are presented graphically in Figure A-3.

Mechanical Properties

Mechanical property test results are presented in Table A-2. Laminates for mechanical property testing were filament wound by Fiberite and Hexcel. Hercules fabricated test laminates from the "parent tape" employed in fabrication of prepreg tow with the hot melt film process. All of the results presented are for unidirectional layups with the exception of the final three lots of AS4/8552 which were quasi-isotropic laminates.

Table A-1: Physical Properties of Prepreg Tow Materials

SUPPLIER	FIBER TYPE	BUNDLE SIZE	SIZING	RESIN TYPE	PREPREG METHOD	LOT NUMBER	DATE OF MFG	LINEAL WEIGHT (g/m)			RESIN CONTENT (percent)			Volatiles (percent)	Moisture (percent)	TOW WIDTH (Inches)			
								nom.	X	s	nom.	X	s	X	X	nom.	X	s (spool)	s (lot)
Fiberite	AS4	6K	solvated epoxy	938	solution	M90-0031	4/26/90	0.428	0.423	0.006	35.0	34.8	1.1	0.7	n/a	0.070	0.068	n/a	0.005
						M90-0098	7/12/90	0.428	n/a	n/a	35.0	34.7	0.9	0.5	n/a	0.080	0.084	n/a	0.005
						00125M	10/30/90	0.428	0.423	0.005	35.0	35.4	0.8	0.7	0.07	0.080	0.076	n/a	0.008
						10600M	4/19/91	0.428	0.435	0.006	35.0	35.1	1.0	0.7	0.10	0.080	0.083	n/a	0.006
						11093M	7/21/91	0.428	0.427	0.007	35.0	35.3	1.2	0.6	0.06	0.080	0.080	n/a	0.012
						11627M	10/21/91	0.428	0.422	0.009	35.0	35.2	1.2	0.3	n/a	0.080	0.077	n/a	0.009
						20643M	5/22/92	0.428	0.421	0.006	35.0	35.5	1.0	0.7	n/a	0.080	0.074	n/a	0.006
						M90-0030	2/28/90	0.428	0.420	0.007	44.8	44.4	0.8	0.6	0.17	0.070	0.070	n/a	0.012
						M90-0112	9/6/90	0.428	0.425	0.004	44.8	45.6	0.6	0.5	0.11	0.070	0.066	n/a	0.006
				977-2	solution	M90-0007	2/5/90	0.428	0.417	0.006	35.0	35.8	1.5	0.7	0.10	0.070	0.075	n/a	0.004
						M90-0033	2/22/90	0.428	0.421	0.006	36.7	37.2	0.9	0.6	0.17	0.070	0.061	n/a	0.004
								0.428			36.7					0.070			
		12K	solvated epoxy	977-2	solution	M90-0001	2/7/90	0.857	n/a	n/a	35.0	n/a	n/a	n/a	0.19	0.070	n/a	n/a	n/a
	IM7	12K	emulsified epoxy	938	solution	M90-0029	2/22/90	0.450	0.445	0.006	35.7	34.6	0.7	0.6	0.04	0.070	0.072	n/a	0.004
								0.450			35.7					0.070			
				977-2	solution	M90-0058	4/24/90	0.450	0.445	0.008	43.9	44.0	1.7	0.7	0.08	0.070	0.070	n/a	0.006
M90-0059						4/26/90	0.450	0.446	0.016	43.9	44.0	0.9	0.6	0.06	0.070	0.067	n/a	0.005	
T1000G		12K	solvated epoxy	938	solution	M90-0100	7/11/90	0.485	n/a	n/a	34.7	34.4	0.6	0.6	n/a	0.080	0.073	n/a	0.007
S-2		20 end	n/a	938	solution	M90-0099	7/11/90	0.663	0.672	0.008	27.8	28.6	0.8	0.5	n/a	0.080	0.090	n/a	0.005
Hercules	AS4	12K	emulsified epoxy	8553-40	hot melt	TPH0366	10/5/92	0.857	0.852	0.008	40.0	40.5	1.5	n/a	n/a	0.150	0.162	0.004	0.015
			none	8552	hot melt	TPH0413	7/28/93	0.856	0.868	0.013	35.0	35.0	0.6	n/a	n/a	0.150	0.156	0.004	0.006
						TPH0455	1/24/94	0.856	0.855	0.013	35.0	35.0	0.6	n/a	n/a	0.182	0.187	0.004	0.007
						TPH1033	5/15/95	0.856	0.864	0.007	35.0	35.0	0.7	n/a	n/a	0.182	0.179	0.004	n/a
						TPH1012	1/20/95	0.856	0.864	0.012	35.0	35.2	0.7	n/a	n/a	0.182	0.180	0.003	0.005
Hexcel	T300	12K	solvated epoxy	F584	solution	50339	1/27/93	0.792	n/a	n/a	38.0	37.9	1.0	1.7	n/a	0.150	n/a	n/a	n/a
						51114	3/24/93	0.792	n/a	n/a	38.0	37.6	0.9	1.6	n/a	0.150	0.133	n/a	0.012
						50743	4/9/93	0.792	n/a	n/a	38.0	38.2	1.0	1.6	n/a	0.150	0.141	n/a	0.019

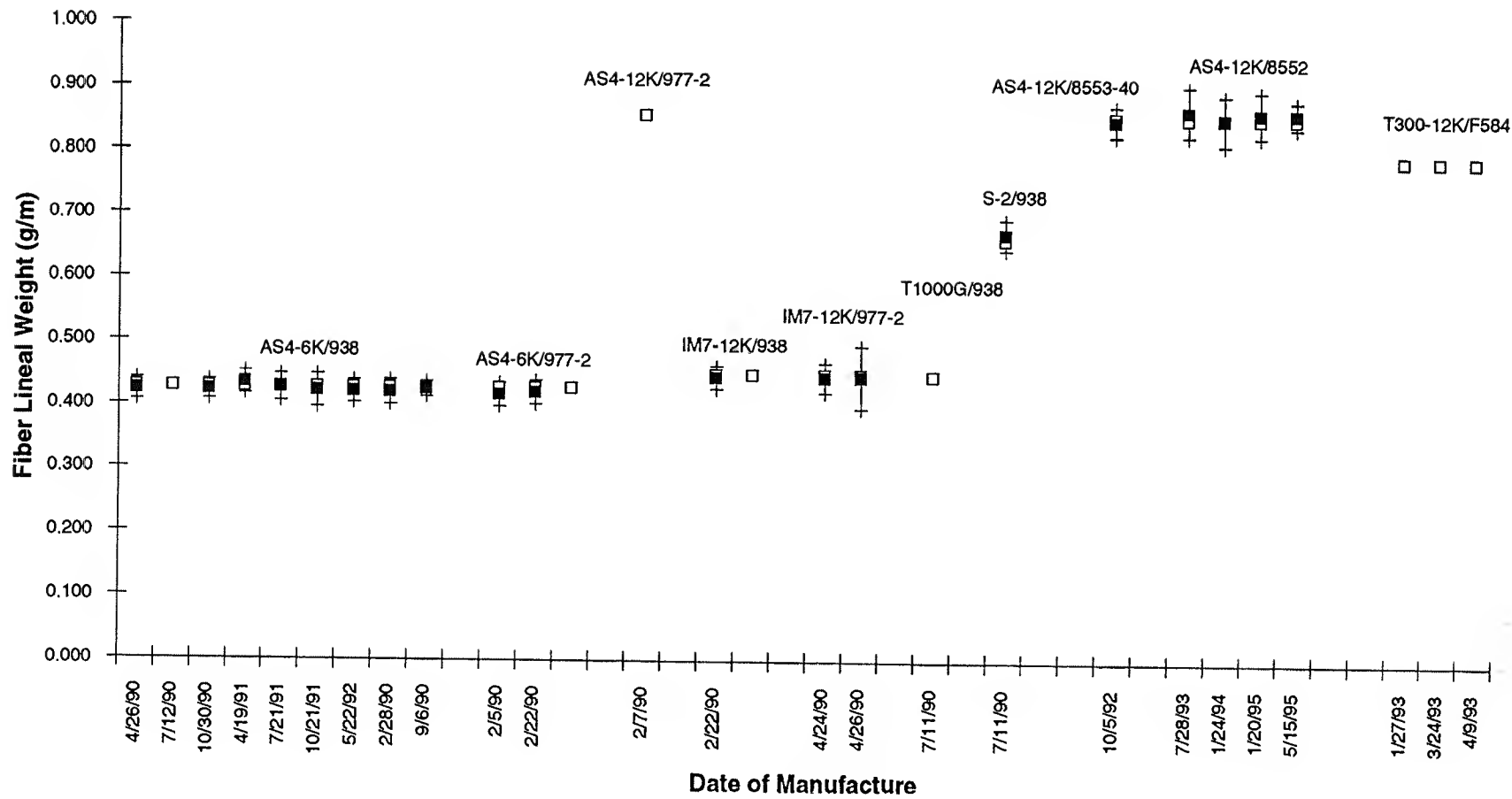


Figure A-1: Fiber Lineal Weight of Prepreg Tow Materials

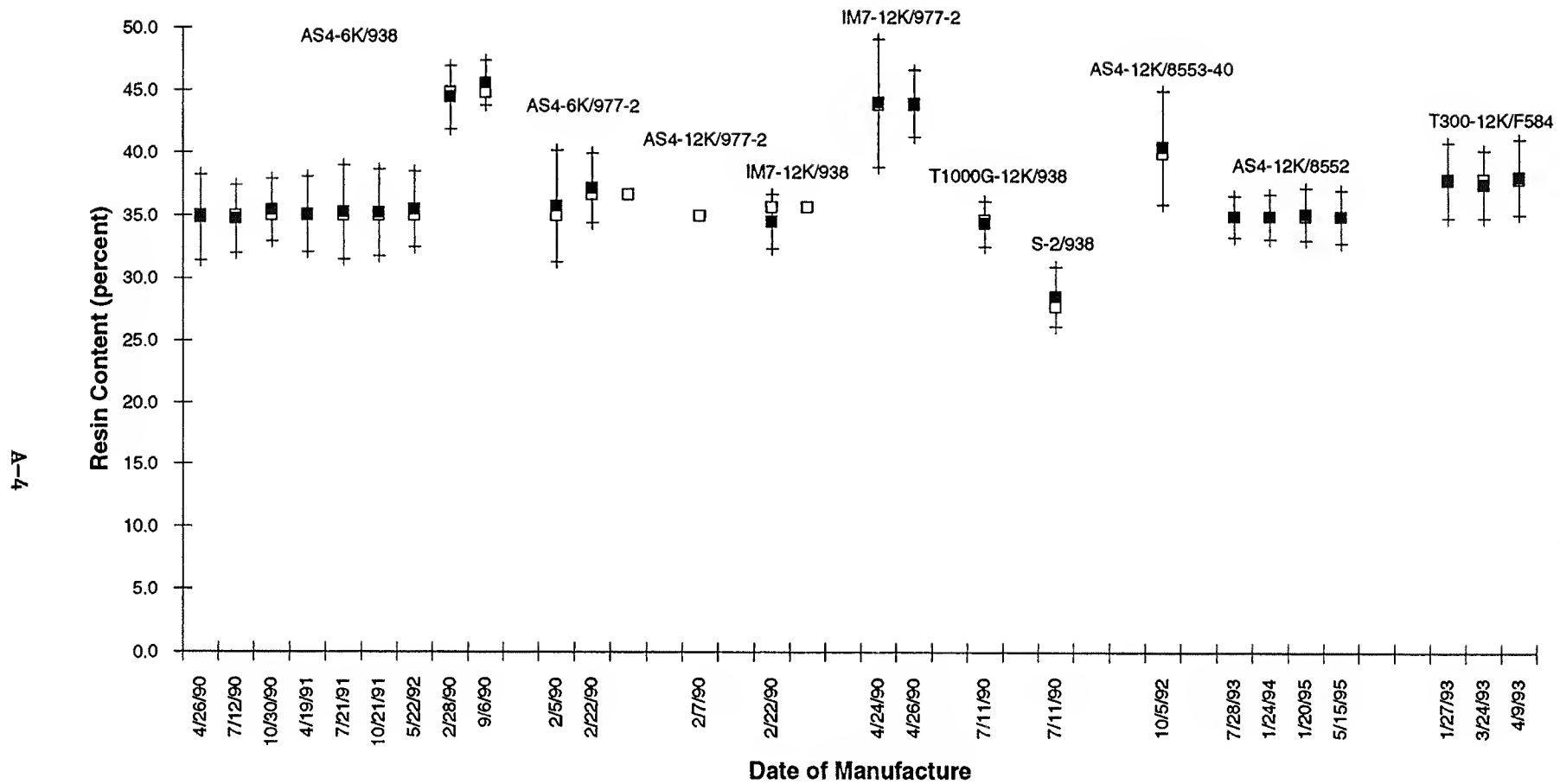


Figure A-2: Resin Content of Prepreg Tow Materials

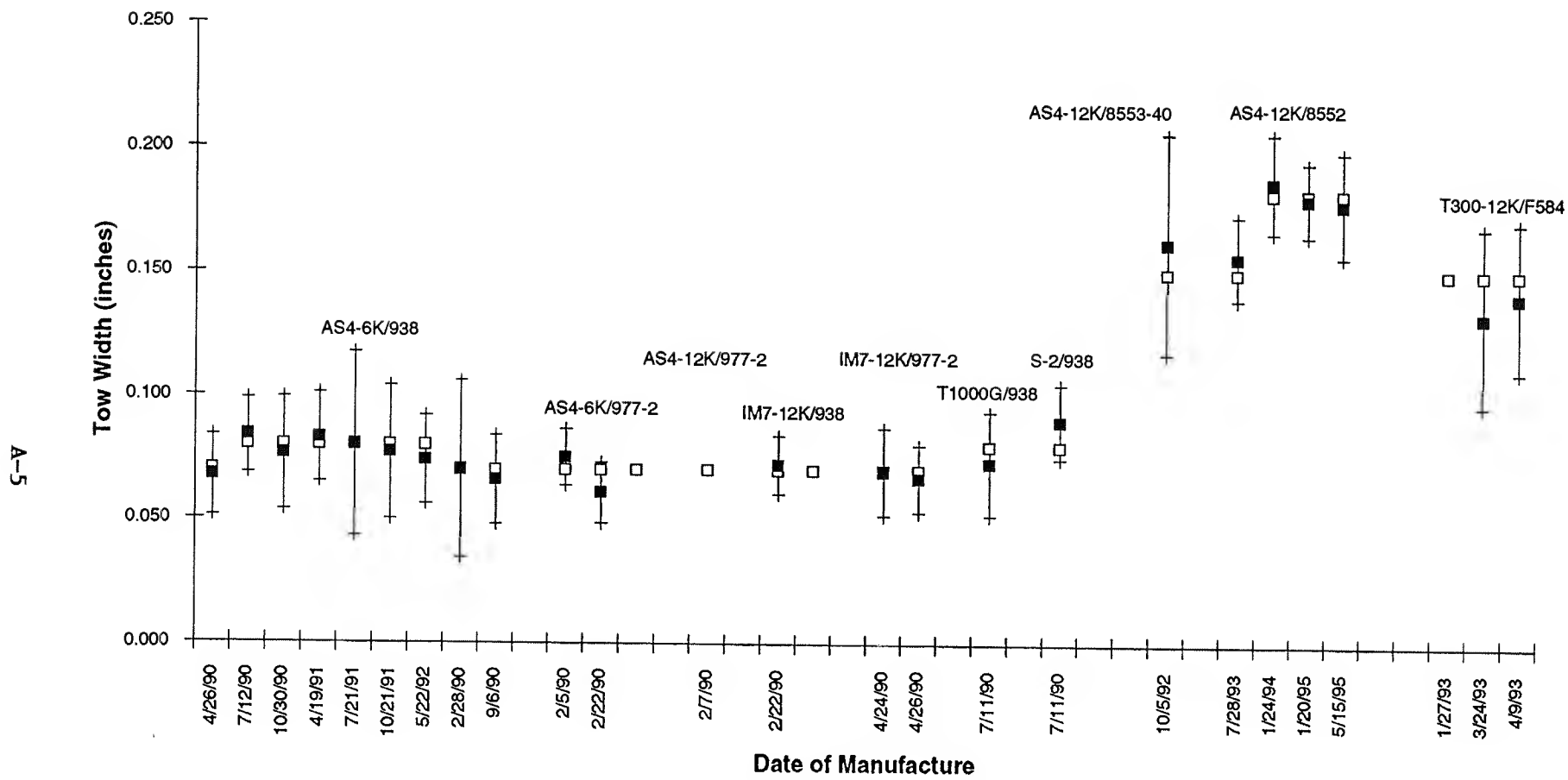


Figure A-3: Width of Prepreg Tow Materials

Table A-2: Mechanical Properties of Laminates Fabricated with Prepreg Tow Materials

SUPPLIER	FIBER TYPE	BUNDLE SIZE	SIZING	RESIN TYPE	PREPREG METHOD	LOT NUMBER	DATE OF MFG	CURED Tg (C)	CURED DENSITY (g/cm³)	CURED VI (percent)	PLY THICKNESS (inches)	TENSILE STRENGTH (ksi)	TENSILE MODULUS (msi)	COMPRESSION STRENGTH (ksi)	COMPRESSION MODULUS (msi)	COMPRESSION STRENGTH (180F) (ksi)	
Fiberite	AS4	6K	solvated epoxy	836	solution	M90-0031	4/28/90	187	1.52	46.6	0.0071	220	17.4	199	18.2	177	
						M90-0098	7/12/90	209	n/a	n/a	0.0078	296	20.0	266	16.8	209	
						00125M	10/30/90	193	n/a	n/a	0.0075	291	18.8	244	17.0	203	
											0.0073	305	18.8	251	13.4	209	
											0.0075	308	19.3	263	18.2	184	
											0.0072	291	18.8	243	13.2	222	
											0.0083	277	19.1	230	13.3	213	
						10600M	4/19/91	192	n/a	n/a	0.0071	283	19.0	242	17.3	214	
											0.0067	282	18.9	260	17.8	248	
											0.0089	295	19.2	244	17.7	189	
						11093M	7/21/91	189	n/a	n/a	0.0068	271	18.7	271	18.9	231	
											0.0067	233	18.4	270	16.2	228	
											0.0073	244	17.8	230	15.9	193	
						11827M	10/21/91										
						20643M	5/22/92	188	n/a	n/a	n/a	238	19.0	235	17.0	272	
											n/a	221	19.0	254	18.0	281	
											n/a	239	19.0	224	18.0	265	
											n/a	218	19.0	220	17.0	251	
											n/a	204	19.0	233	18.0	254	
						M90-0030	2/28/90	192	1.58	58.0	0.0079	213	18.2	228	14.7	155	
						M90-0112	9/6/90	n/a	n/a	n/a	n/a	268	19.4	n/a	n/a	n/a	
					977-2	solution	M90-0007	2/5/90	159	1.59	59.0	0.0071	326	21.2	262	21.8	235
							M90-0033	2/22/90	158	1.58	55.6	0.0070	265	17.7	206	14.6	158
										1.57	54.2	0.0078	303	19.5	258	20.5	230
										1.57	55.0	0.0075	268	17.7	203	15.5	158
								1.58	52.7	0.0079	300	19.4	250	20.7	220		
	12K	solvated epoxy	977-2	solution	M90-0001	2/7/90	154	1.58	55.2	0.0078	278	18.2	243	16.3	178		
IM7	12K	emulsified epoxy	938	solution	M90-0029	2/22/90	193	1.58	58.6	0.0074	320	22.8	248	19.0	209		
								1.58	62.4	0.0075	341	24.7	n/a	21.7	n/a		
								1.58	58.4	0.0073	278	22.3	287	19.9	196		
								1.58	62.8	0.0076	303	24.8	n/a	27.7	n/a		
				977-2	solution	M90-0058	4/24/90	156	1.54	50.0	0.0074	332	20.0	211	18.2	175	
								1.55	52.2	0.0077	302	18.3	197	17.7	173		
							M90-0059	4/26/90	162	1.54	50.0	0.0080	314	20.3	217	19.8	204
T1000G	12K	solvated epoxy	938	solution	M90-0100	7/11/90	214	n/a	n/a	0.0084	452	25.8	281	23.3	236		
S-2	20 end	n/e	938	solution	M90-0099	7/11/90	207	n/a	n/a	0.0084	297	8.4	257	9.0	188		
Hercules	AS4	12K	emulsified epoxy	8553-40	hot melt	TPH0388	10/5/82	178	1.59	53.5	0.0092	282	17.8	222	15.5	200	
			none	8552	hot melt	TPH0413	7/28/93	220	1.59	59.2	0.0083	285	19.8	225	17.3	235	
						TPH0455	1/24/94	216	1.58	57.1	0.0065	79	8.8	69	6.2	55	
						TPH1033	5/15/95	213	1.59	59.2	n/a	78	7.2	113	6.7	96	
						TPH1012	1/20/95	212	1.59	59.2	n/a	80	7.6	74	8.8	82	
Hexcel	T300	12K	solvated epoxy	F584	solution	50339	1/27/93	n/a	n/a	n/a	n/a	207	17.0	n/e	n/a	160	
											n/a	193	18.7	n/a	n/a	158	
						51114	3/24/93	n/a	n/a	n/a	n/a	218	17.8	n/e	n/a	178	
											n/a	220	18.1	n/a	n/a	183	
						50743	4/9/93	n/a	n/a	n/a	n/a	233	18.9	n/a	n/a	163	
											n/a	198	17.6	n/a	n/a	154	

APPENDIX B

Summary of Work Performed with Cellular Solids at the University of Iowa

Experimental micro mechanics methods for conventional and negative Poisson's ratio cellular solids as Cosserat continua [B-1]

Continuum representations of micromechanical phenomena in structured materials are described, with emphasis on cellular solids. These phenomena are interpreted in light of Cosserat elasticity, a generalized continuum theory which admits degrees of freedom not present in classical elasticity. These are the rotation of points in the material, and a couple per unit area or couple stress. Experimental work in this area is reviewed, and other interpretation schemes are discussed. The applicability of Cosserat elasticity to cellular solids and fibrous composite materials is considered as is the application of related generalized continuum theories. New experimental results are presented for foam materials with negative Poisson's ratios.

Deformation mechanisms of negative Poisson's ratio materials: structural aspects [B-2]

Poisson's ratio in materials is governed by the following aspects of the microstructure: the presence of rotational degrees of freedom, non-affine deformation kinematics, or anisotropic structure. Several structural models are examined. The non-affine kinematics are seen to be essential for the production of negative Poisson's ratios for isotropic materials containing central force linkages of positive stiffness. Non-central forces combined with pre-load can also give rise to a negative Poisson's ratio in isotropic materials. A chiral microstructure with non-central force interaction or non-affine deformation can also exhibit a negative Poisson's ratio. Toughness and damage resistance in these materials may be affected by the Poisson's ratio itself, as well as by generalized continuum aspects associated with the microstructure.

Holographic study of conventional and negative Poisson's ratio metallic foams: elasticity, yield, and micro-deformation [B-3]

This article presents an experimental study by holographic interferometry of the following material properties of conventional and negative Poisson's ratio copper foams: Young's moduli, Poisson's ratios, yield strengths, and characteristic lengths associated with inhomogeneous deformation. The Young's modulus and yield strength of the conventional copper foam were comparable to those predicted by microstructural modelling on the basis of cellular rib bending. The re-entrant copper foam exhibited a negative Poisson's ratio as indicated by the elliptic contour fringes on the specimen surface in the bending tests. Inhomogeneous, non-affine deformation was observed holographically in both foam materials.

The time-dependent Poisson's ratio of viscoelastic materials can increase or decrease [B-4]

In viscoelastic materials, the Poisson's ratio is not a material constant but can depend upon time. For polymeric solids, the shear modulus relaxes much more than the bulk modulus, therefore, the Poisson's ratio $\nu(t)$ is an increasing function of time. In this article we demonstrate that such time dependence is not a necessary consequence of the theory of viscoelasticity. Composite microstructures are presented which result in $\nu(t)$ which decreases with time.

Nonlinear properties of polymer cellular materials with a negative Poisson's ratio [B-5]

Negative Poisson's ratio polymeric cellular solids (re-entrant foams) were studied to ascertain the optimal processing procedures which give rise to the smallest value of Poisson's ratio. The nonlinear stress-strain relationship was determined for both conventional and re-entrant foams; it depended upon the permanent volumetric compression achieved during the processing procedure. Poisson's ratio measured as a function of strain was found to have a relative minimum at small strains. The toughness of re-entrant foam increased with permanent volumetric compression, hence density.

Saint-Venant end effects for materials with negative Poisson's ratios [B-6]

In this article we analyze end effects for materials with negative Poisson's ratios. We present an example of slow decay of stress arising from self equilibrated stress at the end of a circular cylinder of elastic negative Poisson's ratio material. By contrast a sandwich panel containing rigid face sheets and a compliant core exhibits no anomalous effects for negative Poisson's ratio, but exhibits slow stress decay for core Poisson's ratio approaching 0.5. In sandwich panels with stiff but not perfectly rigid face sheets, slow decay of stress is known to occur; a negative Poisson's ratio results in end stress decay which is faster than it would be otherwise.

Nonlinear properties of metallic cellular materials with a negative Poisson's ratio [B-7]

Negative Poisson's ratio copper foam was prepared and characterized experimentally. The transformation into re-entrant foam was accomplished by applying sequential permanent compressions above the yield point to achieve a triaxial compression. The Poisson's ratio of the re-entrant foam depended on strain and attained a relative minimum at strains near zero. Poisson's ratio as small as -0.8 was achieved. The strain dependence of properties occurred over a narrower range of strain than in the polymer foams studied earlier. Annealing of the foam resulted in a slightly greater magnitude of negative Poisson's ratio and greater toughness at the expense of a decrease in the Young's modulus.

No contractile obligations [B-8]

Recent advances in negative Poisson's ratio materials have provided scope for creativity in the design of new material microstructures with unusual material properties. Since negative Poisson's ratio materials are now available in the form of polymers and laminates as well as foams, there is a possibility that such solids will find use in structural applications.

Design considerations for materials with negative Poisson's ratios [B-9]

This article presents a study of the implications of negative Poisson's ratios in the design of load bearing structural elements. Stress concentration factors are reduced in some situations, and unchanged or increased in others, when the Poisson's ratio becomes negative. Stress decay according to Saint Venant's principle can occur more or less rapidly as the Poisson's ratio decreases. Several design examples are presented, including a core for a curved sandwich panel and a flexible impact buffer.

Advances in negative Poisson's ratio materials [B-10]

This article deals with materials with negative Poisson's ratios, how they can be created with specified properties, implications of these unusual physical properties, and recent advances. Applications of negative Poisson's ratio materials may be envisaged based on the Poisson's ratio itself, or based upon another unusual physical property which results from the underlying structural casual mechanism. The Poisson's ratio of a material influences the transmission and reflection of stress waves, the decay of stress with distance according to Saint Venant's principle, and the distribution of stress around holes and cracks. The lateral deformation of negative Poisson's ratio materials may be of use in new kinds of fasteners. Such materials may also find use in sandwich panels; when a plate or bar is bent, it assumes a saddle shape if Poisson's ratio is positive, and a convex shape if Poisson's ratio is negative.

Strongly Cosserat elastic lattice and foam materials for enhanced toughness [B-11]

Some foams exhibit size effects and other phenomena not describable by classical elasticity. These foams are describable by Cosserat elasticity, which is a continuum theory with more freedom than classical elasticity. Cosserat solids have a characteristic length which is greater than zero. Strongly Cosserat elastic materials are considered to be those materials for which the Cosserat characteristic length is substantially greater than the structure size and for which the coupling number is large. Such materials are predicted to exhibit superior toughness. A mechanically isotropic lattice model is presented for the study of foams. Ordinary open cell foams are shown to be weakly Cosserat elastic. If cell rib properties are modified, strongly Cosserat elastic effects can occur in the foam. Anisotropic laminate and fibrous materials can also be made to exhibit strongly Cosserat elastic effects.

Microbuckling instability in elastomeric cellular solids [B-12]

Compressive properties of elastic cellular solids are studied via experiments upon foam and upon single cell models. Open cell foam exhibits a monotonic stress-strain relation with a plateau region; deformation is localized in transverse bands. Single cell models exhibit a force-deformation relation which is not monotonic. In view of recent concepts of the continuum theory of elasticity, the banding instability of the foam in compression is considered to be a consequence of the non-monotonic relation between force and deformation of the single cell.

Materials with structural hierarchy [B-13]

Many natural and man-made materials exhibit structure on more than one length scale; in some materials, the structural elements themselves have structure. This structural hierarchy can play a major part in determining the bulk material properties. Understanding the effects of hierarchical structure can guide the synthesis of new materials with physical properties which are tailored for specific applications.

Identability of conventional and negative Poisson's ratio foams [B-14]

The indentation resistance of foams, both of conventional structure and of a novel re-entrant structure giving rise to negative Poisson's ratio, was studied using holographic interferometry. In holographic indentation tests, re-entrant foams had higher yield strengths σ_y and lower stiffness E than conventional foams of the same original relative density. Damage in both kinds of foam occurred primarily directly under the indenter. Calculated energy absorption for dynamic impact is considerably higher for re-entrant foam than conventional foam.

Holographic study of non-affine deformation in copper foam with a negative Poisson's ratio -0.8 [B-15]

The present study applies double-exposure holographic interferometry to examine micro-deformation of re-entrant copper foam with a negative Poisson's ratio of -0.8. The principal purpose of this study is to examine the non-affine (inhomogeneous) deformation of re-entrant foam. Negative Poisson's ratio copper foam ($\nu = -0.8$) with a permanent volumetric compression ratio of 2.2 exhibits a greater non-affine (inhomogeneous) deformation than either conventional foam or negative Poisson's ratio foam ($\nu = -0.1$) with a volumetric compression ratio of 3.

Experimental study of size effects and surface damage of polymethacrylimide closed-cell foam [B-16]

This article describes experimental investigations of size effects in torsion and bending of lathe cut closed-cell polymethacrylimide and open cell copper foams. Slender specimens were found to have a slightly smaller effective stiffness than thick ones. This behavior is

consistent with a model of surface damage to the outermost cells of the foam. The surface damage layer was inferred to be from 0.13 to 0.37 cell diameters for polymethacrylimide, depending on the grade of foam, and from 0.3 to 0.4 cells in the copper foam. Effects of Cosserat (micropolar) elasticity, which would give rise to an effective stiffening of slender specimens, were not observed.

Relating the properties of foam to the properties of the solid from which it is made [B-17]

Properties of foam and the solid (neat resin) from which it was derived were compared experimentally for polymethacrylimide (PMI). Viscoelastic properties of the foam and neat resin differed significantly in the range 50 Hz to 5 kHz. No significant difference in thermal properties was observed in differential scanning calorimetry. However, it was observed that the stiffness of the solid material from which the foam was made was increased after heat treatments. It is therefore likely that the properties of the solid material in the foam are changed by the foaming process, which involves elevated temperature. The properties of the solid material in the foam were also inferred from the measured foam properties substituted into the given foam structure-property relations.

Size effects due to Cosserat elasticity and surface damage in closed-cell polymethacrylimide foam [B-18]

This article describes the experimental investigation of Cosserat (or micropolar) elasticity and surface damage effects in closed cell polymethacrylimide foams of different densities. The method of size effects was used to find the degree of Cosserat behavior for both cylindrical and square cross section specimens in bending and torsion. The foams were found to behave as Cosserat materials (slender specimens appear less stiff than thick ones), provided sufficient care is taken when machining the specimens. Surface damage caused by the machining process may cause the apparent stiffness to decrease with decreasing specimen size, giving an opposite softening size effect.

Nonlinear analysis of the Poisson's ratio of negative Poisson's ratio foams [B-19]

This article contains analytical study of Poisson's ratio of re-entrant foam materials with negative Poisson's ratio. These materials get fatter when stretched and thinner when compressed. The Poisson effect is so fundamentally important to the properties of a material that a large change in the value of the ratio will have significant effects on the material's mechanical performance. Isotropic foam structures with negative Poisson's ratio have been fabricated through a permanent volumetric transformation. The cells were converted from the convex polyhedral shape of conventional foam cells to a concave or "re-entrant" shape. Mechanical behavior of a re-entrant open cell foam material will differ from that of a conventional foam in ways not addressed by existing theoretical treatment. Poisson's ratio as a function of strain is obtained by modeling the three dimensional unit

cell as an idealized polyhedron unit cell. Poisson's ratio is predicted to approach the isotropic limit of -1 with increasing permanent volumetric compression ratio of idealized cells, in comparison with experimental values as small as -0.8.

Analysis of elastic modulus of conventional foams and of re-entrant foams with a negative Poisson's ratio [B-20]

Foam materials with negative Poisson's ratio can be made by transforming the cell structure from the convex polyhedral shape of conventional foam cells to a concave or "re-entrant" shape. Mechanical behavior of re-entrant foams differs from that of conventional foams. Most of the difference is attributed to the change in cell shape. In this study, Young's moduli of conventional and re-entrant open cell foams are obtained by modeling the three-dimensional unit cell as an idealized 14-sided unit cell. Young's modulus of re-entrant foams decreases with permanent volumetric compression ratio in both modeling and experiments.

Holographic evaluation of warp in the torsion of a bar of cellular solid [B-21]

Holographic methods are utilized to examine deformations in a cellular solid, polymethacrylimide closed cell foam. A square cross section bar is subjected to static torsional deformation. The warp deformation is observed to be less in a foam bar than in a homogeneous polymeric bar used as a control. The homogeneous bar obeys the predictions of classical elasticity. Behavior of the foam bar is consistent with Cosserat elasticity. In a Cosserat solid, points in the continuum rotate as well as translate, and the material supports couple per unit area as well as force per unit area. Cosserat effects are important since they can lead to enhanced toughness.

Finite element analysis of Saint Venant end effects in micropolar elastic solids [B-22]

Distributions of stress and strain in composite and cellular materials can differ significantly from the predictions of classical elasticity. For example, concentration of stress and strain around holes and cracks is consistently less than classical predictions. Generalized continuum theories such as micropolar (Cosserat) elasticity offer improved predictive power. In this article Saint Venant end effects for self equilibrated external forces in micropolar solids are investigated in two dimensions. A two dimensional finite element analysis is used which takes into account the extra degrees of freedom, to treat the problem of localized end loads acting upon a strip. The rate of decay of strain energy becomes slower in a two dimensional strip as the micropolar characteristic length l is increased (for l sufficiently less than the strip width). For the strip geometry a Cosserat solid exhibits slower stress decay than a classical solid.

References

- B-1. Lakes, R.S., "Experimental micro mechanics methods for conventional and negative Poisson's ratio cellular solids as Cosserat continua", *J. Engineering Materials and Technology*, 113, 148-155, (1991).
- B-2. Lakes, R.S., "Deformation mechanisms of negative Poisson's ratio materials: structural aspects", *J. Materials Science*, 26, 2287-2292, (1991).
- B-3. Chen, C.P. and Lakes, R.S., "Holographic study of conventional and negative Poisson's ratio metallic foams: Elasticity, yield, and micro-deformation", *J. Materials Science*, 26, 5397-5402, (1991).
- B-4. Lakes, R.S., "The time dependent Poisson's ratio of viscoelastic cellular materials can increase or decrease", *Cellular Polymers*, 11, 466-469, (1992).
- B-5. Choi, J.B. and Lakes, R.S., "Nonlinear properties of polymer cellular materials with a negative Poisson's ratio", *J. Materials Science*, 27, 4678-4684, (1992). Cover issue.
- B-6. Lakes, R.S., "Saint Venant end effects for materials with negative Poisson's ratios", *J. Applied Mechanics*, 59, 744-746, (1992).
- B-7. Choi, J.B. and Lakes, R.S., "Nonlinear properties of metallic cellular materials with a negative Poisson's ratio", *J. Materials Science*, 27, 5373-5381, (1992).
- B-8. Lakes, R.S., "No contractile obligations", *Nature*, 358, 713-714, (1992).
- B-9. Lakes, R.S., "Design considerations for negative Poisson's ratio materials", *ASME Journal of Mechanical Design*, 115, 696-700, (1993).
- B-10. Lakes, R.S., "Advances in negative Poisson's ratio materials", *Advanced Materials*, (Weinheim, Germany), 5, 293-296, (1993).
- B-11. Lakes, R.S., "Strongly Cosserat elastic lattice and foam materials for enhanced toughness", *Cellular Polymers*, 12, 17-30, (1993).
- B-12. Rosakis, P., Ruina, A., and Lakes, R.S., "Microbuckling instability in elastomeric cellular solids", *J. Materials Science*, 28, 4667-4672, (1993).
- B-13. Lakes, R.S., "Materials with structural hierarchy", *Nature*, 361, 511-515, (1993).
- B-14. Lakes, R.S. and Elms, K., "Indentability of conventional and negative Poisson's ratio foams", *J. Composite Materials*, 27, 1193-1202, (1993).
- B-15. Chen, C.P. and Lakes, R.S., "Holographic study of non-affine deformation in copper foam with a negative Poisson's ratio -0.8", *Scripta Metall et Mater*, 29, 395-399, (1993).
- B-16. Anderson, W.B., Chen, C.P., and Lakes, R.S., "Experimental study of size effects and surface damage of polymethacrylimide closed-cell foam", *Cellular Polymers*, 13, 1-15, (1994).

- B-17. Chen, C.P., Anderson, W.B., and Lakes, R.S., "Relating the properties of foam to the properties of the solid from which it is made", *Cellular Polymers*, 13, 16-32, (1994).
- B-18. Anderson, W.B. and Lakes, R.S., "Size effects due to Cosserat elasticity and surface damage in closed-cell polymethacrylimide foam", *Journal of Materials Science*, 29, 6413-6419, (1994).
- B-19. Choi, J.B. and Lakes, R.S., "Nonlinear analysis of the Poisson's ratio of negative Poisson's ratio foams", *J. Composite Materials*, 29, (1), 113-128, (1995).
- B-20. Choi, J.B. and Lakes, R.S., "Analysis of elastic modulus of conventional foams and of re-entrant foams with a negative Poisson's ratio", *Int. J. of Mechanical Sciences*, 37, 51-59, (1995).
- B-21. Anderson, W.B., Lakes, R.S., and Smith, M.C., "Holographic evaluation of warp in the torsion of a bar of cellular solid", *Cellular Polymers*, 14, 1-13, (1995).
- B-22. Nakamura, S. and Lakes, R.S., "Finite element analysis of Saint Venant end effects in micropolar elastic solids", *Engineering Computations*, 12, 571-587, (1995).

APPENDIX C

Mechanical Splices for Commercial Transport Fuselage Utilizing Tow-Placed and Textile Composites - Revision A (November 1995)

Introduction

Tow-placed and textile composite materials are material forms which have significant cost savings capability due to their ability to form complex shapes and their high rate capability through automation. As composite materials gain acceptance in the production of commercial aircraft primary structure, it will be necessary to provide manufacturing flexibility as well as the required stiffness and strength.

Boeing has examined the manufacturing and performance issues associated with composite primary structure in the Advanced Technology Aircraft Structures (ATCAS) program. The goal of this program is to demonstrate a confidence level that permits cost and weight-effective use of advanced composites in primary structures, with an emphasis on pressurized wide body commercial transport fuselages. An aft section directly behind the wing-to-body intersection was selected for technology development and verification purposes. The crown quadrant of this section was chosen as the first quadrant of focus.

The ATCAS program utilizes a 3 step design process, which incorporates the selection of baseline concepts, global evaluation of selected concepts, and local cost and weight optimization of concepts. As shown in Figure C-1, the optimized panel developed for the aft fuselage section is a skin-stiffener concept, which utilizes tow-placed skins, drape-formed tow-placed hat section stringers, and textile frames. The stringers are cocured with the skin, while the frames are cobonded to the skin; these processes eliminate the need for extensive mechanical fastening. However, mechanical fastening of these materials is required for integration of the crown panel with the rest of the fuselage; consequently, the performance of tow-placed and textile materials in mechanically fastened joints must be assessed.

Three critical crown panel splices, shown in Figure C-2, were selected for study. The circumferential skin splice consists of tow-placed skins (locally reinforced for bearing capability) and a splice strap. The longitudinal splice consists of tow-placed crown and side-panel skins fastened to a stringer. The frame splice consists of textile web and inner frame cap splice straps.

In examining the capabilities of tow-placed and braided laminates in mechanical splices, it was necessary to perform tests of several joint configurations to understand material behavior under various load conditions. Previous work in mechanical splicing of composites [C-1, C-2] has shown that composites exhibit a greater degree of interaction between bearing and bypass stresses than do metals (see Figure C-3). The degree of interaction is dependent upon the laminate configuration, and, more specifically, the anisotropic stress concentration at the fastener hole. Therefore, it was necessary to evaluate the pure bearing, pure bypass, and bearing-bypass interaction behavior of tow-placed and textile composites for various laminate configurations. Additionally, as the assembly of large cobonded structure requires robust splicing techniques, it was necessary to account for the presence of shims, short end margin, side margin, and other geometric factors.

The data obtained during this investigation is presented in three sections. The first section discusses the results obtained for tow-placed graphite/epoxy laminates utilized in the circumferential and longitudinal splices. The second section compares bearing and filled hole tension test results of glass-graphite intraply hybrid laminates with those of tow-placed graphite/epoxy laminates. The third section discusses the results obtained in tests of braided/RTM laminates. Layups of the laminates examined and a matrix of tests performed are shown in Tables C-1 and C-2; laminates are designated by their number of plies and whether they are hybridized. Mechanical properties used in data analysis are shown in Table C-3; tow-placed material engineering constants were calculated using laminated plate theory, based upon unidirectional AS4/938 and S2/938 constants, while the 2-D braided constants were determined using an analytical method developed by Fedro [C-3].

Performance of Tow-placed Graphite/Epoxy Laminates

The ATCAS program has performed extensive research in the application of tow-placed materials to fuselage skins. The ability to place material in concave curvatures, steer fibers around curves, and add or drop tows at any point make tow placement a highly attractive manufacturing method for fuselage skins. In this investigation, the performance of tow-placed AS4/938 graphite/epoxy laminates was examined to assess their potential application in mechanically fastened crown panel joints.

The critical design load condition for the crown panel quadrant under consideration was determined to be tension (due to internal pressure loading) for both the circumferential and longitudinal splices. Consequently, experimental and analysis efforts concentrated on issues which strongly affect the performance of the splices under tensile loads, such as the tension bypass strength, the tension bearing strength, and bearing-bypass interaction for tension bypass loading.

Tension bearing and tension bypass tests were performed for four tow-placed crown panels in both the longitudinal and transverse directions. 5% load transfer tests (5% of the total load applied to the specimen is carried between adherends at each fastener) were performed using specimens from panels 15, 20, and 22 to examine bearing-bypass interaction in bypass dominated joints and to support the development of a predictive methodology for bypass failure. 33% and 50% load transfer tests, simulating the actual design configurations of the ATCAS crown panel circumferential and longitudinal joints, were performed using specimens from panels 22 and 20 to examine bearing-bypass interaction in bearing dominated joints (it should be noted that the $\pm 60^\circ$ and $\pm 15^\circ$ plies in the actual crown padups were manufactured 90° off axis in panels 20 and 22, and therefore are listed as $\pm 30^\circ$ and $\pm 75^\circ$ plies in Table C-1). All tests were performed at room temperature ambient conditions.

Test panels were fabricated on the Hercules 6-axis fiber placement machine using a 12-tow Band Cut and Add head and autoclave cured at 350°F . 6K AS4/938 tows were used; nominal tow width was 0.09 in. Nominal cured ply thickness was 0.0074 in. Coupons were cut to oversize dimensions using a band saw and then abraded to final dimensions.

Tension Bypass Tests

Data developed at Boeing have indicated that tension bypass strength varies significantly with laminate configuration [C-4]. Historically, geometric laminate configuration parameters, such as AML (Angle Minus Loaded, or % ± 45 plies - % 0° plies), have been used in the development of bypass design allowables. Such parameters were typically restricted to the (0/ ± 45 /90) laminate family. The orientation flexibility of the tow placement process, as demonstrated by the $\pm 15^\circ$ and $\pm 60^\circ$ angle plies used in the crown panel laminates, precluded the use of such a parameter. It was decided to use the anisotropic stress concentration factor K_t as a laminate configuration parameter, which for uniaxial loading along a reference axis, x, is related to laminate moduli E_x , E_y , G_{xy} and Poisson's ratio ν_{xy} for symmetric, balanced laminates as follows [C-5]:

$$K_T^\infty = 1 + \sqrt{2 \left(\sqrt{\frac{E_x}{E_y}} - \nu_{xy} \right) + \frac{E_x}{G_{xy}}}$$

For unbalanced laminates (laminates which have unequal percentages of $+\theta$ and $-\theta$ angle plies in regard to the reference axis), a similar calculation is performed using the laminate extensional stiffness matrix to account for extension-shear coupling effects. Research has shown that ultimate tension bypass strain is inversely proportional to K_t for both tape and fabric laminates.

Previous experience has shown that tension bypass strength is highly dependent upon clamp-up loads provided by a fastener. Typical laminates appear to have greater ability to redistribute loads and relieve stress concentrations through non-catastrophic failure modes such as delamination when clamp-up loads are low or nonexistent. For this reason, high clamp-up filled hole tension strengths tend to be lower than open hole or low clamp-up tension strengths for most laminates. Consequently, filled hole tension strength was determined to be the critical criterion in evaluating the bypass capability of the crown panel splice laminates.

The standard filled hole tension test specimen used in this investigation is shown in Figure C-4. The specimens had a width to diameter (w/d) ratio of 6 and a hole diameter of 0.25 inches. All specimens used titanium lockbolts, which have a clamp-up level equivalent to that of a threaded titanium fastener torqued to 85 in-lbs.

Failure stresses and strains for baseline filled hole tension tests are shown in Table C-4; strain levels are estimates based upon laminate moduli shown in Table C-3. The relationship between failure strain and stress concentration factor at the fastener hole is shown in Figure C-5. The data demonstrate that failure strain and stress concentration factor are inversely proportional for tow-placed laminates, as is the case with tape and fabric laminates. Ultimate filled hole tension strain levels for the tow placed laminates were found to be comparable to those exhibited by tape thermoset composites such as IM6/3501-6.

Additional tests using the 15 ply graphite/epoxy laminate were performed to examine the effect of coupon width to hole diameter ratio upon filled hole tension strength. The results shown in Table C-5 indicate that longitudinal and transverse specimens with a w/d ratio of 5 had no significant reduction in filled hole tension strength. Additional transverse tests of specimens with two parallel fasteners (see Figure C-4) and a w/d ratio of 5 exhibited similar behavior.

Tests of laminates 20 and 22 with 100° countersunk tension head fasteners, shown in Table C-6, demonstrated 2.0% and 2.8% reductions from protruding head strength.

Tension Bearing Tests

Previous experience with tape and fabric angle ply laminates has shown that tension bearing strength is primarily dependent upon fastener clamp-up and joint configuration, and is relatively insensitive to laminate configuration for laminates with more than 30% $\pm 45^\circ$ plies [C-1, -4, -6, -7]. High fastener clamp-up levels increase fastener-laminate friction and inhibit delamination, which increases bearing strength. A reduced fastener clamp-up level should be used in order to simulate the reduction in fastener clampup over a lifetime of service due to relaxation of laminate through-the-thickness stiffness. For this reason, a clamp-up torque level of 35 in-lbs, or 40% of installation torque (as estimated by Shivakumar [C-8] for long term clamp-up relaxation), was used in this investigation.

The standard bearing test specimen used in this investigation is shown in Figure C-6. The specimens had a width to diameter (w/d) ratio of 6, an edge distance to diameter (e/d) ratio of 3, and a hole diameter of 0.25 inches. The specimen was designed to include the effects of outer ply brooming, caused by friction between the outer ply and the fastener head. All pure bearing specimens used threaded titanium fasteners torqued to 35 in-lbs.

Two measures of the bearing performance of the laminates were recorded, namely the maximum load carried by the specimen and the linear limit load, which was defined as the load at which joint deflection was offset 2% of the hole diameter from the initial load/deflection slope (see Figure C-7). Bearing load-deflection plots for these test specimens exhibited bearing damage-induced nonlinearity in load/deflection response. Bearing strengths, shown in Table C-7, were similar to those exhibited by other tape thermosets and were relatively insensitive to laminate configuration, although the bearing strength for the 22 ply laminate was noticeably lower than that of the other laminates. Examination of the specimens indicated that a higher degree of fastener bending (compared with previous bearing tests) was responsible for the reduction in bearing strength, as fastener bending increases the concentration of bearing stresses.

Additional tests of 15 ply graphite/epoxy laminates were performed to assess the effect of e/d ratio and shim thickness upon bearing strength and joint stiffness, as shown in Tables 8 and 9. Specimens with a e/d ratio of 2 showed a 6% reduction in ultimate bearing stress, but little change in linear limit stress. Specimens with an e/d ratio of 4 showed no significant difference in bearing strength or joint stiffness compared to specimens with e/d = 3.

Little variation in ultimate bearing strength was noted for specimens with 0.030" and 0.050" peelable Kapton shims. However, the linear limit stress and overall joint stiffness of these specimens decreased due to load-deflection nonlinearity. Fasteners used in bearing tests with shims exhibited permanent deformation after testing, indicating that the joint nonlinearity was caused by increased fastener bending.

Tests of laminates 20 and 22 with 100° tension head countersunk fasteners, shown in Table C-9, demonstrated 21% and 30% reductions from protruding head linear limit stress and 13% and 10% reductions from ultimate strength, indicating that fastener head rotation affected the overall stiffness of the joint to a greater degree than it affected joint strength.

Bearing - Bypass Interaction Tests

Three specimen types were utilized in evaluating the influence of bearing stresses upon filled hole tension strength for tow-placed AS4/938 laminates.

5% Load Transfer

5% load transfer specimens (see Figure C-8) were used to evaluate the effect of small bearing loads upon bypass dominated joints. Strain gages were used to measure the elongation of aluminum side plates caused by introduction of loads from the composite specimen. Typical load-strain data for the side plates, shown in Figure C-9, indicates load transfer levels in the side plates of approximately 8% at failure. The strain gage data suggest that initially loads were transferred through friction until a side plate strain of approximately 400-600 microstrain was attained. Proper load transfer through fastener bearing occurred at strain levels above 600 microstrain, or 0.001" elongation between fastener holes. This indicates that strains within the specimen were insufficient to overcome tolerance gaps in the fastener holes, and therefore longer spacing between fastener holes is suggested for future testing of this type.

As some of the load transfer in the specimens was accomplished through friction, it was necessary to use a lower load transfer level in bearing-bypass interaction analysis; a level of 5% load transfer through bearing was assumed. This level of load transfer produced the reductions from pure bypass strength shown in Table C-11 for panels 15, 20, and 22. Panel 15 demonstrated an 8% decrease in bypass strain in the longitudinal direction and an 8.4% decrease in the transverse direction. Panel 20 exhibited an 8.6% decrease in the transverse direction, while panel 22 demonstrated a 10.5% decrease in the longitudinal direction.

Circumferential Skin Splice

Circumferential skin splice specimens were used to evaluate the interaction of large bearing and bypass loads within the forward circumferential splice of the ATCAS crown panel. As shown in Figure C-8, this splice consisted of two panel 22 laminates, oriented in the longitudinal direction, attached to a splice plate made from panel 20, also oriented

in the longitudinal direction. Strain gages were used to measure the degree of load transfer between fasteners.

A finite element model was used to correlate strains with introduced loads and suggested that initial load transfer was lower in the center fastener, but was uniformly 33% at each fastener at failure. This indicates that bearing damage may equilibrate fastener loads in composites as plastic deformation does in metal joints.

The circumferential skin splice specimens exhibited variability in the location of failure, as specimens failed in both the 22 ply skin padups and the 20 ply splice straps (see Table C-12). The presence of fastener countersink appeared to reduce the strength of the 22 ply padup such that the two components failed at similar load levels. This indicated that the circumferential joint design was efficient in that the padup and splice strap components had similar strengths.

Examination of failure data indicated that low fastener clamp-up did not significantly reduce joint strength, but the presence of 0.050" thick shims reduced strength by 10%.

Longitudinal Skin Splice

The third specimen type was the representation of the longitudinal fuselage skin splice. As shown in Figure C-8, this splice consisted of one panel 20 laminate, oriented in the transverse direction, attached to one panel 13 laminate, also oriented in the transverse direction. An additional panel 13 laminate, oriented in the transverse direction, was attached at the splice to simulate the presence of a stiffener. This specimen demonstrated 50% load transfer at each row of fasteners. As was the case with the circumferential splice, fastener clampup did not appear to significantly affect joint strength, but the use of 0.050" shim reduced strength by 9% (see Table C-13).

The longitudinal splice specimens experienced delamination prior to ultimate bearing-bypass interaction failure. It appears that during the tests, delaminations grew between 0° and 15° plies, resulting in fastener pull-through in the upper sublaminates and in-plane bearing-bypass failure in the lower sublaminates. The depth of the countersink suggested that the concentration of bearing loads near the bottom of the countersink may have contributed to the delamination.

Comparison of Interaction Results with Analytical Predictions

Bearing-bypass test results were used to verify interaction predictions for the various laminates. Predictions were made using the BEARBY analysis code [C-9], which consists of pre and post processors to the Bolted Joint Stress Field Model (BJSFM) developed by McDonnell Douglas [C-10].

BJSFM determines the stress field around a loaded hole in a homogeneous anisotropic infinite plate under plane stress conditions using a closed form analytic solution based upon the anisotropic theory of elasticity and laminated plate theory. It assumes a cosine radial stress distribution for bearing loads and uses the principle of superposition for combined bearing and bypass loads.

BEARBY predicts bearing-bypass failure loads by applying a point stress criterion at the lamina level, with characteristic dimension generated semi-empirically using unnotched uniaxial and filled hole strain-stress concentration data. The characteristic dimension is thus expressed as a function of laminate stress concentration factor. BJSFM stress field predictions are then used to perform failure analysis at multiple bearing-bypass ratios.

BEARBY bearing-bypass interaction predictions for the 20 and 22 ply crown panel padups are shown in comparison with test data in Figure C-10; predictions and data for panels 13 and 15 are shown in Figure C-11. Pure bearing is defined as tension bearing. The data demonstrate that bearing loads have a slightly larger influence upon tension bypass strength in the longitudinal skin splice than in the circumferential splice. The reduction in strength due to the use of countersunk head fasteners and the influence of laminate configuration upon bypass dominated strength are also in evidence.

Examination of Graphite/Glass Intraply Hybrids

In order to improve the performance of crown skin panels, the ATCAS program examined the tension damage tolerance of intraply hybrid laminates. Laminates composed of AS4/938 graphite/epoxy and S2/938 glass/epoxy were manufactured and tested to examine the effects of intraply hybridization upon notch sensitivity.

It was also decided to examine the performance of such laminates in mechanically fastened joints. In order to compare the performance of the hybrid laminates with the tow-placed graphite/epoxy laminates previously discussed, bearing and filled hole tension tests were performed for three tow-placed crown panels, whose layups are shown in Table C-1. Panels were manufactured using the previously described tow-placement process.

Panel 12H was hybrid in the 0° direction only. Non- 0° plies were composed of 6K AS4/938 towpreg; 0° plies were 50% 6K AS4/938 tows, 50% 20 end 750 yd/lb S2/938 tows. The nominal width of the 6 tow AS4/938 and 6 tow S2/938 repeat unit was 1.1 in.

Panels 13H and 15H were hybrid in all plies. The laminate was tow-placed with 75% 6K AS4/938 tows, 25% 2K S2/938 tows by volume. The nominal width of the 6 tow AS4/938 and 2 tow S2/938 repeat unit was 0.73 in.

Tension Bypass Tests

Filled hole tension tests were performed for laminates from panels 12H, 13H, and 15H in both the longitudinal and transverse directions. The moduli used for the hybrid laminates, shown in Table C-3, were based upon the volume fractions of graphite and glass. In longitudinal tests of panel 12H specimens, the volume fractions in the 0° plies were assumed to be equivalent to the fraction of the specimen width occupied by glass and graphite tows, which varied between specimens. Volume fractions were assumed to be 75% graphite for panels 13H and 15H and 50% graphite in the 0° plies for transverse tests of panel 12H.

As was the case with the graphite/epoxy tension bypass data, it was necessary to use the stress concentration factor at the hole in lieu of a geometric parameter. The anisotropic stress concentration factor discussed in the previous section was found to be useful in the analysis of specimens from panels 13H and 15H because of the uniform hybridization of each ply. Glass tows were not aligned between similar plies through the thickness in these laminates. This reduced the degree of stratification and assured that a combination of graphite and glass fibers were tangential to the fastener hole edge in all specimens.

Specimens from panel 12H, however, exhibited strict alignment of 0° graphite and glass tows through the thickness, making the laminate highly stratified. The implication of this stratification was that the stress concentration at the hole edge could vary depending upon the location of the fastener hole relative to the glass tows. In order to determine the possible range of values for the stress concentration factor in such a laminate, a 2-D finite element analysis using NASTRAN and the pre- and post- processing code PATRAN was performed. The analysis modeled stress distributions in longitudinal specimens with holes centered in graphite and glass tows, as well as holes near the edge of a graphite or glass tow (see Figure C-12). As shown in Table C-15, specimens from panel 12H with holes in graphite tows had higher stress concentration factors than specimens with holes primarily in glass tows due to the higher stiffness of the graphite tows (as shown for the two sets of material properties of panel 12H in Table C-3) .

Tension stress and ultimate strain results for the hybrid laminates are shown in Figure C-13, and are compared to the AS4/938 tow-placed data. The stress concentration factors used for the longitudinal specimens of panel 12H correspond to the location of the fastener hole relative to glass and graphite tow boundaries. Although the position of the hole relative to the tow boundaries was not controlled during specimen manufacture, it was possible to correlate the concentration factors developed using finite element analysis with hole position upon examination of the failed specimens. The figures indicate that the failure strain of the intraply hybrid laminates is inversely proportional to the stress concentration factor, as was the case with the AS4/938 tow-placed laminates. Although the failure stresses for graphite/epoxy and glass-graphite/epoxy laminates are similar, the failure strains of glass-graphite/epoxy hybrids are higher because of their comparatively lower elastic moduli.

Tension Bearing Tests

Bearing tests were performed using standard tension bearing specimens manufactured from panels 12H, 13H and 15H, in both the longitudinal and transverse directions. As shown in Table C-16, the bearing strength of the intraply hybrid laminates was relatively unaffected by laminate configuration and was similar to that of AS4/938. The linear limit stress of these laminates was also similar to that of AS4/938. The reduction in stiffness of the intraply hybrids did not significantly effect the overall joint stiffness, which is primarily a function of fastener bending and shear stiffness.

The 0° hybrid laminates from panel 12H exhibited a lower bearing strength than the AS4/938 and 25% glass hybrid laminates. This may be due to the addition of angle plies in the other laminates and the strict alignment of glass tows in the 0° hybrid laminates.

Performance of Braided/RTM Laminates

The ATCAS program has examined 2-D and 3-D braided/RTM materials for application to fuselage frames. The net shape capability and high interlaminar tension strength of braided materials make them attractive for such structures. In this investigation, a 2-D braided/RTM laminate was examined to assess its performance in mechanically fastened joints.

As was the case with the crown panel circumferential and longitudinal joints, the critical load case for the frame splice was determined to be tension due to internal pressure loading. For this reason, tension bearing, filled hole tension, 5% and 33% load transfer tests were performed to evaluate the performance of the laminate in a tension loaded joint.

Additional bearing and bypass tests were performed using a new mechanical fastening system in lieu of standard titanium fasteners. A composite rivet, manufactured from IM7/PEEK thermoplastic, has been developed by the Cherry Division of Textron. The rivets are compression molded prior to installation to form the head and shank; during installation, the rivet tail is reconsolidated into a sombrero shape using spin-forming. The rivets provide a clamp-up load equivalent to that provided by a fastener torqued to 25 in-lbs (for comparison, the installation torque of a standard titanium fastener is 85 in-lbs). It is believed that the rivet forming process can be automated, and for this reason the fasteners are candidates for use in the web portion of the ATCAS frame splice. Supplier-generated data indicated the rivets, which have graphite fibers aligned parallel to exterior surfaces, have a shear strength to weight ratio approximately 1.4 times that of titanium fasteners.

The fiber architecture used in this investigation consisted of 6K braided tows, with a braid angle of 66.5°, and contained 37.4% 18K longitudinal tows. This architecture was optimized for high longitudinal and transverse stiffness and to match longitudinal and transverse coefficients of thermal expansion. The fiber volume fraction for the specimens was measured to be 48%.

The braided laminates used in this investigation were manufactured at Fiber Innovations Inc. using a 144 carrier New England Butt triaxial braider incorporating 72 longitudinal yarns in a 2/2 regular braid pattern. Preforms were formed on cylindrical mandrels and the desired preform thickness was achieved by over-braiding layers. The preforms were then resin transfer molded using Shell's 1895 resin cured at 350°F; comprehensive details of Fiber Innovations' RTM process were previously reported by Fedro [C-3]. Nominal laminate thickness was 0.131 in. Coupons were cut to oversize dimensions using a band saw and sanded to final dimensions.

Tension Bypass Tests

Nine filled hole tension tests were performed in this investigation. Six tests were performed using titanium lockbolts, comparing filled hole tension strength for coupons with w/d ratios of 4 and 6. Three tests were performed using Cherry-Textron thermoplastic rivets to assess the effects of the lower rivet clamp-up load upon filled hole tension strength. All tests were performed with specimens aligned in the longitudinal direction.

Results are shown in Table C-17. The recorded strain levels are estimates based upon a longitudinal modulus of 7.33 msi calculated using the TECA analysis program developed by Fedro and validated through test [C-3]. Little reduction in filled hole tension strength was found for specimens of w/d = 4. The filled hole tension strength of the laminate was 18% higher with thermoplastic rivets installed, verifying that the lower clamp-up load of the thermoplastic rivets improves the filled hole tension strength of the joint.

The filled hole tension failure strain of the braided laminate (5008 $\mu\epsilon$ mean) appeared to be inferior to those observed for AS4/938. At an equivalent stress concentration ($1/K_t = 0.305$), the AS4/938 regression line shown in Figure C-5 predicts an ultimate strain of 5911 $\mu\epsilon$, or 118% of the mean failure strain for the braided laminate.

As shown in Table C-18, the filled hole tension strength of the braided laminate with titanium lockbolt fasteners was 46% of the unnotched axial tension strength reported by Fedro [C-3]. Filled hole strength with thermoplastic rivets was 54% of the unnotched strength. When compared with other graphite-thermoset filled hole tension data utilizing titanium lockbolts [C-4], the B1 braided laminate architecture apparently was more notch sensitive than tape and fabric laminates of similar stress concentration. Notch sensitivity using thermoplastic rivets was equivalent to that of other laminate forms using titanium fasteners.

Static Bearing Tests

Stabilized single shear tests, using the composite bearing specimen shown in Figure C-6, were performed using 18 braided specimens. Tests were performed using titanium hiloks torqued to 35 in-lbs, as well as Cherry-Textron thermoplastic rivets.

Titanium Fasteners: Bearing Failures

Results for tests using titanium fasteners, which were bearing critical, are shown in Table C-19. Linear limit stresses and ultimate bearing strengths of the braided laminates were significantly lower than that of AS4/938. Ultimate strength appeared to be dependent upon edge margin and shim thickness; linear limit stress appeared to be constant regardless of shim thickness but highly dependent upon edge margin. It is hypothesized that the low bearing strength of the braid is a function of the relatively low in-plane shear strength of the fiber architecture, which makes the laminate subject to shear-out failures. Also, the uninterrupted layer of matrix surrounding the longitudinal inlaid tows may be susceptible to shear failure, lowering the bearing stress at which permanent deformation initiates.

Thermoplastic Fasteners: Fastener Shear Failures

Results for tests using thermoplastic fasteners, which were critical in fastener shear, are shown in Table C-20. The fasteners were found to have a ultimate shear strength of 44.8 ksi, which was reduced by 2.2% for joints with 0.050" thick shims. More significantly, the reduction in linear limit shear stress was 28.7%. As shown in Figure C-14, this was caused by a high degree of joint load-deflection nonlinearity due to the presence of shims. As previously discussed, this effect is present in shimmed joints using titanium fasteners, but at a much lower degree.

Fatigue Tests

Stabilized single shear fatigue tests were performed using braided laminates and Cherry-Textron thermoplastic rivets. All tests were performed in tension-tension ($R = +0.1$) fatigue in room temperature/ambient conditions at a frequency of 5 Hz.

Fatigue life and residual strength results for are shown in Table C-21. In all but one test, fastener shear was the critical failure mode. As shown in Figure C-15, one million cycles were achieved for maximum shear stress levels of 29 ksi, or 60% of static ultimate, for specimens with and without 0.050" shims. The overall joint stiffness was reduced through fatigue cycling, with fatigue failure typically occurring after the stiffness was reduced by 40%. Residual strengths after one million cycles at 29 ksi were within 90% of static ultimate except for the shimmed specimen, which had a residual strength equal to 85% of the mean static shimmed strength.

Bearing - Bypass Interaction Tests

Two specimen types were utilized in evaluating the influence of bearing stresses upon filled hole tension strength for braided/RTM materials. The first specimen was a 5% load transfer joint. The mean failure condition for these specimens was 4566 microstrain bypass, 10.6 ksi bearing, indicating a 8.8% reduction in bypass strain due to bearing loads relative to the pure bypass case (see Table C-22).

The second specimen, shown in Figure C-8, was a representation of the frame inner cap splice design for the ATCAS crown panel frames. As with the circumferential skin splice specimens, initial load transfer was lower in the center fastener, but was uniformly 33% at each fastener at failure. The mean failure condition for these specimens was 3083 microstrain bypass, 56.5 ksi bearing.

The bearing-bypass interaction test results were then compared to the BEARBY prediction for the braided frame. The results, shown in Figure C-16, demonstrate that this braided architecture and material system had tension bearing and bypass strengths inferior to those of the AS4/938 tow-placed laminates evaluated for bearing-bypass behavior. It should be noted, however that the bypass strength of the braided laminate was affected by bearing stresses in much the same manner as the tow-placed laminates; percentage changes in bearing stress produced similar percentage changes in bypass strength between the two material systems.

Discussion

AS4/938 Results

Filled hole tension, pure bearing, and bearing-bypass interaction tests demonstrated that the behavior of tow-placed AS4/938 is quite similar to that of other graphite-reinforced brittle thermoset composites. The relationship between ultimate filled hole tension strain and stress concentration factor is consistent with that of tape laminates; the tow nature of the material did not appear to affect ultimate strain or the failure modes exhibited.

Bearing strengths were slightly lower than those exhibited by tape thermosets such as IM6/3501-6 [C-1]. As AS4/938 failure modes were similar to IM6/3501-6 laminates, it is concluded that the tow nature of the material did not affect the bearing strength, but rather the bearing strength of AS4/938 is lower than that of IM6/3501-6 (AS4 fiber itself is weaker than IM6 fiber).

Bearing-bypass interaction results were similar to those of tape thermosets. The use of $\pm 15^\circ$ angle plies, however, appears responsible for the delaminations exhibited in the longitudinal skin splice tests. As the interface between 0° and $\pm 15^\circ$ plies is known to be especially susceptible to delamination [C-11], it is recommended that the padup stacking sequence be reexamined to reduce susceptibility to delamination.

Examination of effects induced through specimen geometry and shimming demonstrated relatively small correction factors for ultimate strength; the greatest reduction in filled hole tension strength was 2.84% for fastener countersink, while the greatest reduction in bearing strength was 13% for fastener countersink. The results for fastener countersink show good agreement with correction factors developed for tape and fabric and implemented in the BEARBY predictive code. Correction factors for w/d, e/d, fastener countersink and shims which can be used in design are listed in Table C-23; it should be noted that these factors are applicable to double shear and stabilized single shear joints and should be reduced for unstabilized joints to account for increased fastener rotation.

AS4/938- S2/938 Results

Filled hole tension tests demonstrated that the behavior of notched hybrid tow-placed laminates is highly dependent upon the location of the notch relative to the tow spacing. A relationship between ultimate filled hole tension strain and stress concentration factor was obtained, demonstrating a similarity in behavior with the AS4/938 laminates. The level of tow stratification significantly influenced behavior; laminates with distributed S2/938 tows (13H and 15H) were not as severely affected by hole location as were the highly stratified 12-ply laminates. The strength of the distributed hybrid laminates was equivalent to that of the AS4/938 laminates, resulting in higher failure strains.

Bearing strengths were less dependent upon the location of the fastener hole relative to the glass tows. However, the bearing strength of the distributed laminates were distinctly higher than that exhibited by the highly stratified laminates. It is therefore recommended

that in regions containing significant stress concentrations, hybridization should be accomplished using random glass fiber distributions.

AS4/1895 Results

Filled hole tension, pure bearing, and bearing-bypass interaction tests demonstrated that the performance of the 2-D braided laminates was inferior to that of typical tape and fabric thermosets. The B1 braided architecture appeared to be more notch sensitive than typical laminates in filled hole tension testing, based on a comparison with tape and fabric laminates of similar stress concentration factor.

The longitudinal bearing strength of the AS4/1895 braided laminate was particularly low ($< 75\%$ of AS4/938). It is hypothesized that the low fiber volume fraction (48%) and the low in-plane shear strength of the architecture examined, as well as the large longitudinal tows and surrounding resin-rich areas, were responsible for this low strength, as the bearing strength of the laminate was highly dependent upon specimen end margin.

IM7/PEEK Rivet Shear Results

Fatigue results for IM7/PEEK rivets indicated that one million cycles could be achieved in RTD, $R = +0.1$ fatigue at maximum stress levels 60% of static ultimate. Residual strengths after such cycling were at least 85% of static ultimate even though joint stiffness was reduced approximately 40%. It therefore appears that fatigue cycling affects stiffness to a greater degree than residual strength.

The results were consistent with RTD, $R = +0.1$ fatigue data generated for hilok-style IM7/PEEK fasteners [C-12], which also found more significant reductions in stiffness than for strength. This was determined to be representative of matrix damage, rather than fiber damage, as static strength is governed by fiber strength. Therefore, the fatigue-induced stiffness reduction is an indicator of an important failure mode, and should be considered in the development of fastener shear allowables.

The previous work described above indicated that the fastener limit allowable shear stress should be approximately 20 ksi (within the 15 to 25 ksi range), producing an allowable ultimate shear strength of 30 ksi. When potential $R = -1.0$ load cycles and environmental effects are considered, the static and fatigue data generated for the rivets are consistent with such allowables.

Conclusions

The following conclusions were developed during this investigation:

- 1) Relationships between filled hole tension strength and the stress concentration factor at the hole were shown to exist for tow-placed materials. It was not possible to correlate a parameter based solely upon laminate configuration, such as AML, with filled hole tension strength because of the various angle plies used

and because the stress concentration factor of the 0° hybrids depended upon hole location.

- 2) The effect of hole location upon filled hole tension strength was highly pronounced in the unidirectional 0° intraply hybrids. It was not as pronounced in the other hybrids because of the less-stratified distribution of glass tows.
- 3) The 25% glass hybrids exhibited filled hole tension strengths similar to those of AS4/938 laminates. However, the failure strain of the hybrids was greater due to the lower modulus of the glass tows.
- 4) The AS4/938 and 25% glass hybrids exhibited similar bearing strengths. Bearing strength appeared to be independent of stress concentration factor. No major difference was noted in the pure bearing joint stiffness of AS4/938 and AS4-S2/938 hybrid laminates, demonstrating that joint stiffness is dominated by fastener bending and shear stiffness.
- 5) The filled hole tension strength of the AS4/1895 2-D braided laminate was lower than those exhibited by AS4/938 tow-placed laminates of similar stress concentration. The braided architecture appeared to be more notch sensitive than typical laminates in filled hole tension testing, based on a comparison with tape and fabric laminate data.
- 6) The braided architecture examined was particularly susceptible to shear-out failures due to low shear stiffness and strength in the regions between longitudinal tows. The bearing strength could be improved by decreasing the angle of the bias tows to increase shear strength. Joint strength could be improved by using large ($e/D \geq 3$) end margins.
- 7) Bearing-bypass interaction tests validated the modifications to the BEARBY program for tow placed and braided laminates. Stress-strain data indicated that bearing damage may equilibrate fastener loads in multifastener joints much as plastic deformation does in metallic joints.
- 8) 5% load transfer test load-strain data indicated that strains within the specimen were insufficient to overcome tolerance gaps in the fastener holes. Longer spacing between fastener holes is suggested for future testing of this type.
- 9) Thermoplastic rivets are similar in performance to thermoplastic Hiloks and offer potential weight advantages compared with titanium fasteners when used in thin gage ($<0.15''$) laminates.

References

- C-1. Grant, P. and Sawicki, A., "Development of Design and Analysis Methodology for Composite Bolted Joints," American Helicopter Society National Technical Specialists' Meeting on Rotorcraft Structures, Williamsburg, VA, October 1991.
- C-2. Naik, R. and Crews, J., "Ply Level Failure Analysis of a Graphite/Epoxy Laminates under Bearing-Bypass Loading," ASTM STP 1059, Philadelphia, PA, 1990, pp. 191-211.
- C-3. Fedro, M., "Characterization and Manufacture of Braided Composites for Large Commercial Aircraft Structures," Proceedings of the Ninth DOD/NASA/FAA Conference on Fibrous Composites in Structural Design, November 1991, pp. 935-978.
- C-4. Kesack, W., Stevenson, K., et al, "V-22 Material Substantiating Data and Analysis Report," Contract No. N00019-85-C-0145, Report No. 901-930-022, Revision A, November 1991.
- C-5. Lekhnitskii, S.G.: "Anisotropic Plates," translated from the second Russian edition by S. W. Tsai and T. Cheron, Gordon and Breach, New York, 1968.
- C-6. Collings, T., "On the Bearing Strengths of CFRP Laminates," Royal Aircraft Establishment Technical Report 82033, April 1982.
- C-7. Ramkumar, R. and Tossavainen, E., "Strength and Lifetime of Bolted Laminates," ASTM STP 927, Philadelphia, PA, 1986, pp. 251-273.
- C-8. Shivakumar, K. and Crews, J., "Bolt Clampup Relaxation in a Graphite/Epoxy Laminate," ASTM STP 813, Philadelphia, PA, 1983, pp. 5-22.
- C-9. Sawicki, A. and Mabson, G., "BEARBY Bolted Joints Analysis - Program Description and User's Guide," Boeing Defense & Space Group, Helicopters Division Document # D210-12933-1, April 1993.
- C-10. Garbo, S. and Ogonowski, J., "Effect of Variances and Manufacturing Tolerances on the Design Strength and Life of Mechanically Fastened Composite Joints. Volume 1: Methodology Development and Data Evaluation," Report AFWAL-TR-81-3041, April 1981
- C-11. Lagace, P., "Delamination Fracture under Tensile Loading," Proceedings of the Sixth Conference on Fibrous Composites, AMMRC MS 83-2, Army Materials and Mechanics Research Center, November 1983, pp. IX 53-70.
- C-12. Sawicki, A., "Performance of Composite Joints Utilizing Thermoplastic Fasteners," Proceedings of the 49th Annual Forum of the American Helicopter Society, St. Louis, MO, May 1993, pp. 124-135.

Table C-1. Layups of AS4/938 - S2/938 intraply hybrid tow-placed panels.

Panel	Hybridization	Layup
13	100% AS4/938	$[\pm 45/90/0/\pm 60/90]_s$
15	100% AS4/938	$[\pm 45/90/0/\pm 60/-15/90/+15]_s$
20	100% AS4/938	$[\pm 45/90/0/\pm 30/\pm 45/-75/0/90/+75]_s$
22	100% AS4/938	$[\pm 45/90/0/\pm 30/\pm 45/-75/0/90_2/0/+75]_s$
12H	50% AS4, 50% S2 in 0° plys	$[+45/0/-45/90_2/0]_s$
13H	75% AS4, 25% S2 in all plys	$[\pm 45/90/0/\pm 60/90]_s$
15H	75% AS4, 25% S2 in all plys	$[\pm 45/90/0/\pm 60/-15/90/+15]_s$
2-D Braid	100% AS4/1895	37.4% 18K longitudinal, 62.6% 66.5° 6K braid, 5 plys

Table C-2. Tests performed using tow-placed and braided laminates.

Panel	Static				Fatigue
	Pure Bypass	Pure Bearing/ Fastener Shear	5% Load Transfer	Crown Splice	Pure Bearing/ Fastener Shear
13	6	6			
15	19	23	10		
20	6	6	5	9	
22	6	6	5	10	
12H	12	17			
13H	13	12			
15H	15	12			
2D braid	9	18	9	3	12

Table C-3. In-plane properties used in this investigation.

Panel ID	Longitudinal Modulus (msi)	Transverse Modulus (msi)	Major Poisson's Ratio	Shear Modulus (msi)	Nominal Thickness (in)
unidirectional AS4/938	19.20	1.36	0.32	0.72	0.0074
unidirectional S2/938	6.30	1.70	0.25	0.52	0.0074
12-H (graphite 0° tows)	8.56	8.56	0.21	2.13	0.0888
12-H (glass 0° tows)	4.31	8.24	0.22	1.98	0.0888
13	5.27	8.91	0.27	3.00	0.0962
13-H	4.58	7.55	0.27	2.56	0.0962
15	6.75	8.12	0.29	2.84	0.111
15-H	5.79	6.91	0.29	2.42	0.111
20	6.98	6.76	0.37	3.16	0.148
22	7.36	7.16	0.33	2.93	0.1628
2-D Braid	7.33	8.01	0.18	2.01	0.131

Table C-4. Results from AS4/938 filled hole tension tests.

Specimen	Number of Tests	Mean ultimate tension stress (ksi)	Mean estimated failure strain (μ strain)	Coefficient of Variation (%)
Panel 13				
longitudinal	3	42.1	7980	3.90
transverse	3	59.5	6680	3.03
Panel 15				
longitudinal				
one hole	3	44.2	6550	2.80
two holes	3	43.5	6440	3.00
transverse	3	51.2	6300	1.49
Panel 20				
transverse	3	46.7	6900	2.17
Panel 22				
longitudinal	3	48.0	6520	0.49

Table C-5. Effect of width to diameter ratio upon filled hole tension strength of panel 15.

Specimen	Number of Tests	Mean ultimate tension stress (ksi)	Mean estimated failure strain (μ strain)	Coefficient of Variation (%)
Longitudinal				
w/d = 6	3	44.2	6550	2.80
w/d = 5	4	43.3	6410	1.50
Transverse				
w/d = 6	3	51.2	6300	1.49
w/d = 5	6	51.1	6290	1.86

Table C-6. Effect of fastener countersink upon filled hole tension strength of panels 20 and 22.

Specimen	Number of Tests	Mean ultimate tension stress (ksi)	Mean estimated failure strain (μ strain)	Coefficient of Variation (%)
Panel 20 (transverse)				
Protruding Head	3	46.7	6900	2.17
Countersunk	3	45.7	6770	5.40
Panel 22 (longitudinal)				
Protruding Head	3	48.0	6520	0.49
Countersunk	3	46.6	6340	5.73

Table C-7. Results from AS4/938 bearing tests.

Specimen	Number of Tests	Mean bearing stress at 2% hole diameter offset (ksi)	Mean ultimate bearing stress (ksi)	Ultimate Stress Coefficient of Variation (%)
Panel 13				
longitudinal	3	107.9	117.3	2.50
transverse	3	97.4	108.9	5.16
Panel 15				
longitudinal	3	101.7	108.9	2.44
transverse	3	97.9	113.9	3.52
Panel 20				
transverse	3	77.1	97.6	1.39
Panel 22				
longitudinal	3	80.9	113.2	1.49

Table C-8. Effect of edge distance to diameter ratio upon bearing strength of panel 15.

Specimen	Number of Tests	Mean bearing stress at 2% hole diameter offset (ksi)	Mean ultimate bearing stress (ksi)	Ultimate Stress Coefficient of Variation (%)
Transverse				
e/d = 2	3	100.2	106.8	0.39
e/d = 3	3	97.9	113.9	3.52
e/d = 4	3	104.3	113.8	1.80

Table C-9. Effect of shim thickness upon bearing strength of panel 15.

Specimen	Number of Tests	Mean bearing stress at 2% hole diameter offset (ksi)	Mean ultimate bearing stress (ksi)	Ultimate Stress Coefficient of Variation (%)
Longitudinal				
no shims	3	101.7	108.9	2.44
0.030" shims	2	102.0	111.5	0.23
0.050" shims	2	104.9	108.6	1.17
Transverse				
no shims	3	97.9	113.9	3.52
0.030" shims	3	101.1	112.8	2.84
0.050" shims	3	100.4	116.0	2.96

Table C-10. Effect of fastener countersink upon bearing strength of panels 20 and 22.

Specimen	Number of Tests	Mean bearing stress at 2% hole diameter offset (ksi)	Mean ultimate bearing stress (ksi)	Ultimate Stress Coefficient of Variation (%)
Panel 20 (transverse)				
Protruding Head	3	80.9	113.2	1.49
Countersunk	3	63.7	98.2	2.29
Panel 22 (longitudinal)				
Protruding Head	3	77.1	97.6	1.39
Countersunk	3	53.9	87.3	4.08

Table C-11. Results from AS4/938 5% load transfer tests.

Specimen	No. of Tests	Mean ultimate bypass stress (ksi)	Mean estimated bypass strain (μ strain)	Mean ultimate bearing stress (ksi)	Coefficient of Variation (%)
Panel 15					
Longitudinal	8	40.6	6010	12.8	1.25
Transverse	2	46.8	5770	14.8	0.26
Panel 20					
Transverse	5	42.8	6330	13.9	3.05
Panel 22					
Longitudinal	5	42.9	5830	13.7	1.83

Table C-12. Results from circumferential skin splice tests of panel 22.

Fastener clamp-up (in-lbs)	Shim thickness (in)	No. of Tests	Mean ultimate load (lbs)	Coefficient of Variation (%)	Failure Locations
85	0.000	3	7667	2.34	2 in 22 ply laminate, 1 in 20 ply laminate
	0.050	3	6780	3.48	1 in 22 ply laminate, 2 in 20 ply laminate
35	0.000	2	7510	1.88	20 ply laminate
	0.050	2	6900	2.87	1 in 22 ply laminate, 1 in 20 ply laminate

Table C-13. Results from longitudinal skin splice tests of panel 20.

Fastener clamp-up (in-lbs)	Shim thickness (in)	No. of Tests	Mean ultimate bypass stress (ksi)	Mean estimated bypass strain (μ strain)	Mean bearing stress (ksi)	Coefficient of Variation (%)
85	0.000	2	16.8	2490	84.8	6.20
	0.050	3	15.8	2340	80.2	1.29
35	0.000	2	16.7	2470	83.4	3.98
	0.050	2	14.7	2180	73.3	1.29

Table C-14. Results from intraply hybrid filled hole tension tests.

Specimen	Number of Tests	Mean ultimate tension stress (ksi)	Mean estimated failure strain (μ strain)	Coefficient of Variation (stress based) (%)
Panel 12H				
longitudinal		52.5	-	27.76
hole in glass tow	3	63.7	9320	19.50
hole in gr tow	3	41.3	6650	0.84
transverse	6	60.1	7150	4.69
Panel 13H				
longitudinal	6	38.9	8490	5.82
transverse	7	62.9	8330	3.44
Panel 15H				
longitudinal	6	44.3	7650	5.54
transverse	9	51.7	7490	5.83

Table C-15. Stress concentration factors for panel 12H longitudinal specimens (based upon finite element model results).

Hole Edge Location	Laminate Stress Concentration Factor
edge of graphite tow	3.87
center of graphite tow	3.43
center of glass tow	2.69
edge of glass tow	2.27

Table C-16. Results from intraply hybrid bearing tests.

Specimen	Number of Tests	Mean shear stress at 2% hole diameter offset (ksi)	Mean ultimate bearing stress (ksi)	Ultimate Stress Coefficient of Variation (%)
Panel 12H				
longitudinal	8	83.8	92.2	2.91
transverse	9	90.7	96.6	3.49
Panel 13H				
longitudinal	5	94.7	105.8	4.55
transverse	7	99.1	111.9	4.97
Panel 15H				
longitudinal	6	98.2	110.3	1.76
transverse	6	98.9	111.2	1.88

Table C-17. Results from braided/RTM filled hole tension tests.

Fastener Type	Width -to- diameter ratio	Number of Tests	Mean ultimate tension stress (ksi)	Mean estimated failure strain (μ strain)	Coefficient of Variation (%)
titanium lockbolt	6	3	36.7	5008	3.15
	4	3	37.0	5043	9.99
IM7/PEEK rivet	6	3	43.6	5948	10.48

Table C-18. Filled hole tension notch sensitivity of selected laminates.

Laminate Type	Fastener Type	Ratio of ultimate filled hole tension strain to ultimate unnotched tension strain (%)
IM6/3501-6 Grade 190 tape $K_t = 3.64$	titanium lockbolt	53
AS4/3501-6 plain weave fabric $K_t = 3.26$	titanium lockbolt	53
AS4/1895 2-D triaxial braid $K_t = 3.28$	titanium lockbolt	46
	IM7/PEEK rivet	54

Table C-19. Results from braided/RTM bearing tests with titanium fasteners.

Shim thickness (in)	Edge margin-diameter ratio	No. of Tests	Mean shear stress at 2% hole diameter offset (ksi)	Mean ultimate bearing stress (ksi)	Ultimate Stress Coefficient of Variation (%)
0.000	3	3	68.0	74.8	3.24
0.000	2	3	60.5	63.1	6.17
0.030	3	3	66.3	68.2	14.65
0.050	3	3	69.2	80.8	3.43

Table C-20. Results from thermoplastic fastener tests.

Shim thickness (in)	No. of Tests	Mean shear stress at 2% hole diameter offset (ksi)	Mean ultimate shear stress (ksi)	Ultimate Stress Coefficient of Variation (%)
0.000	3	26.8	44.8	9.02
0.050	3	19.1	43.8	6.31

Table C-21. Results from fatigue bearing tests.

Shim thickness (in)	Minimum Load (lbs)	Maximum Load (lbs)	Maximum Fastener Shear Stress (ksi)	Fatigue Life (cycles)	Residual Strength (ksi)
0.000	220	2200	22.41	>1000000	47.0
0.000	290	2900	29.54	>1000000	43.3
0.000	360	3600	36.67	46313	0
0.000	360	3600	36.67	7074	0
0.000	290	2900	29.54	>1000000	45.6
0.000	320	3200	32.59	17350	0
0.000	320	3200	32.59	240191	0
0.000	320	3200	32.59	81607	0
0.000	360	3600	36.67	9421	0
0.050	320	3200	32.59	39274	0
0.050	290	2900	29.54	>1000000	34.9
0.050	320	3200	32.59	86464	0

Table C-22. Results from braided/RTM bearing-bypass interaction tests.

Test Type	No. of Tests	Mean ultimate tension stress (ksi)	Mean estimated failure strain (μstrain)	Mean bearing stress (ksi)	Coefficient of Variation (%)
5% Load Transfer	9	33.5	4566	10.6	6.39
Frame Cap Splice (33% Load Transfer)	3	22.6	3083	56.5	5.72

Table C-23. Correction Factors for Joint Geometry for AS4/938 and AS4/1895 .

Load Condition	Correction Requirement	Correction Factor
Bypass	w/d = 5 (standard w/d = 6)	0.97
Bypass	100° countersunk fasteners	0.96
Bearing	e/d = 2 (standard e/d = 3)	0.93 for AS4/938 tow 0.80 for AS4/1895 braid
Bearing	0.050" thick shims	0.88
Bearing	100° countersunk fasteners	0.85

- Crown Quadrant: 99° Segment
- Cocured Hat-Stiffeners and Cobonded J-Frames
 - Tow Placed Skin (AS4/938, 35% RC)
 - Tow Placed, Drape-Formed Stiffener (AS4/938, 35% RC)
 - 2-D Braided/RTM Frame (AS4/RSL 1895, 37% RC)

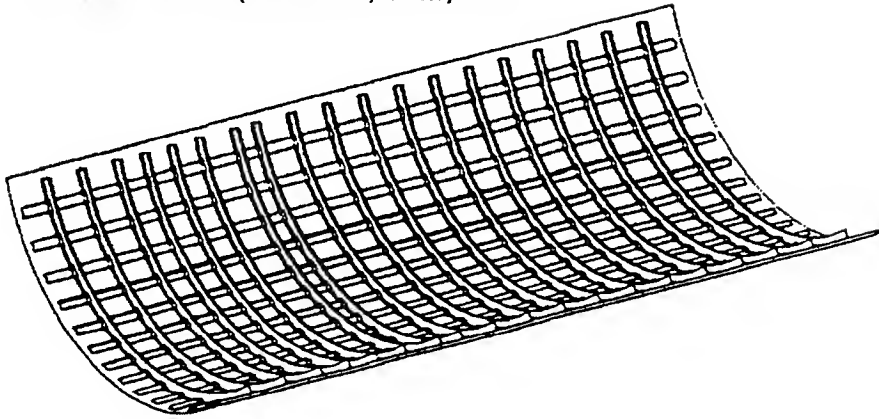


Figure C-1: ATCAS Fuselage Optimized Crown Panel

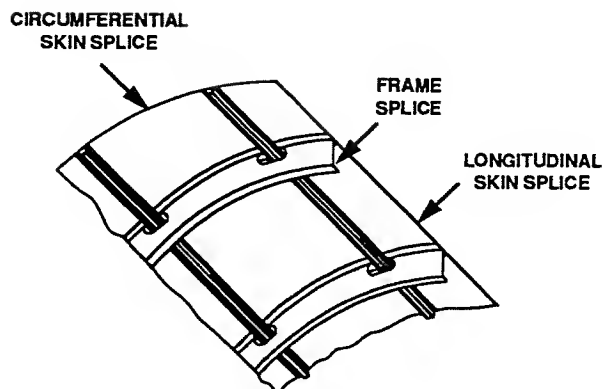


Figure C-2: Crown Panel Splices Examined In This Investigation

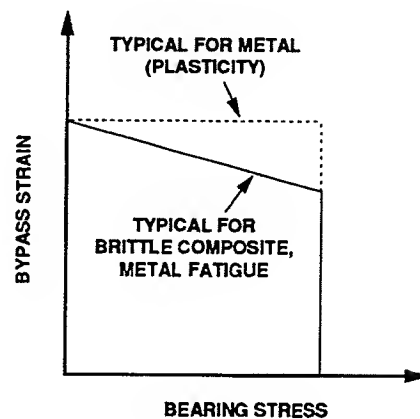


Figure C-3: Comparison of Typical Bearing-Bypass Allowables Envelopes for Metals and Composites, at Ultimate Loading

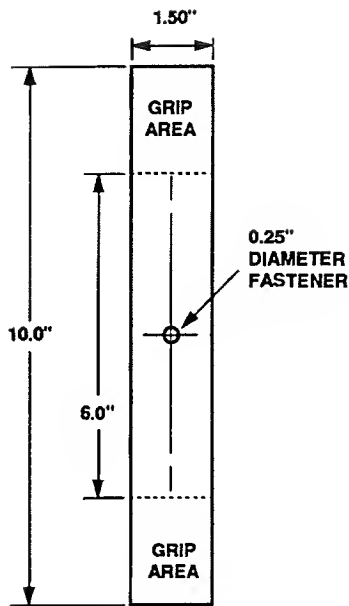


Figure C-4: Pure Bypass Test Specimen

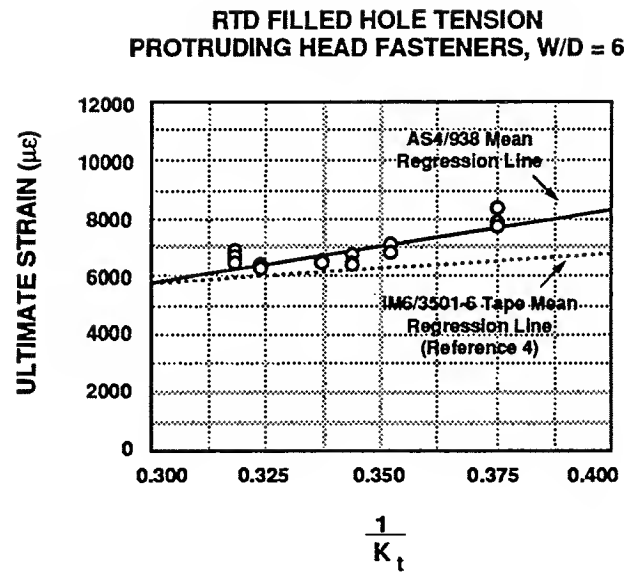


Figure C-5: Relationship Between Failure Strain and Stress Concentration Factor for AS4/938

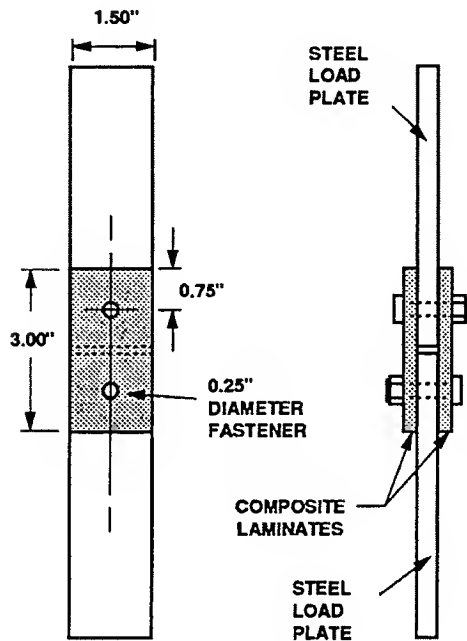


Figure C-6: Pure Bearing Test Specimen

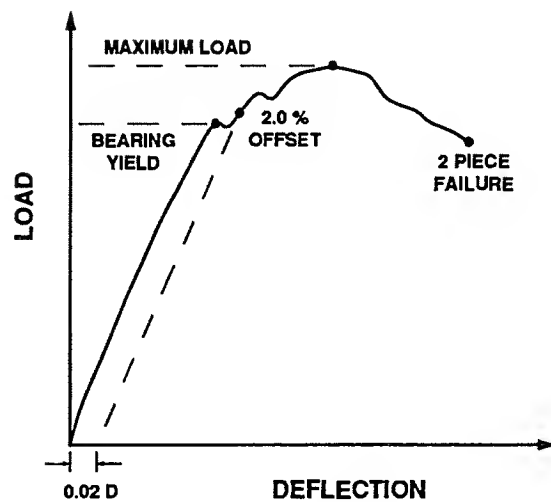
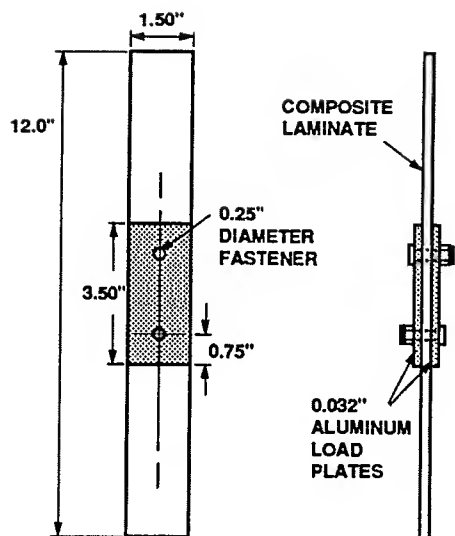
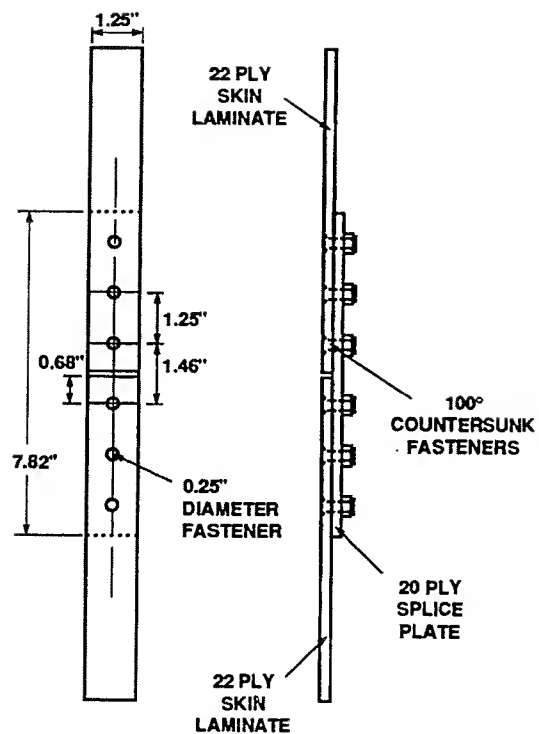


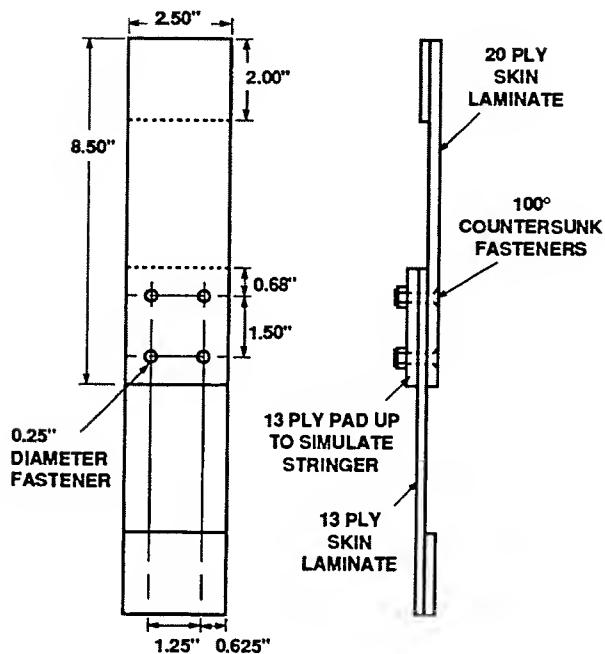
Figure C-7: Typical Bearing Specimen Load-Deflection: Definitions



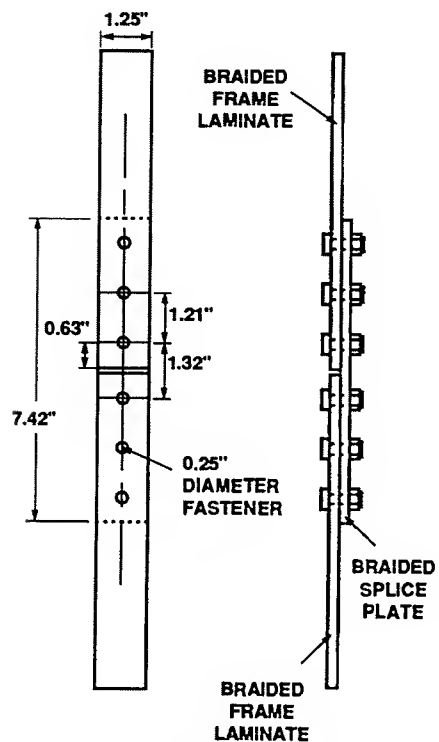
5% LOAD TRANSFER SPECIMEN



CIRCUMFERENTIAL SKIN SPLICE SPECIMEN



LONGITUDINAL SKIN SPLICE SPECIMEN



FRAME SPLICE SPECIMEN

Figure C-8: Bearing-Bypass Interaction Test Specimens

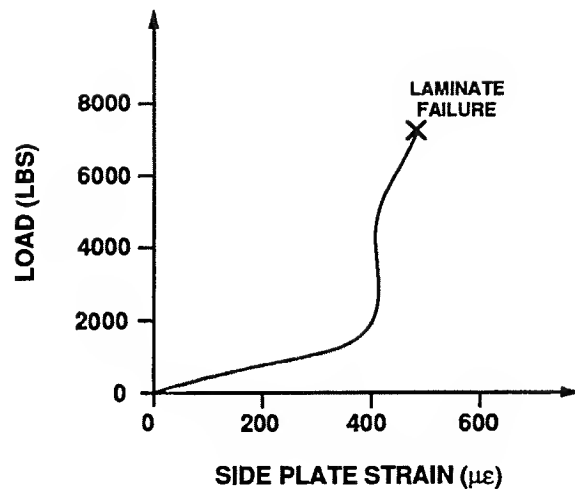


Figure C-9: Typical Side Plate Strains for 5% Load Transfer Tests

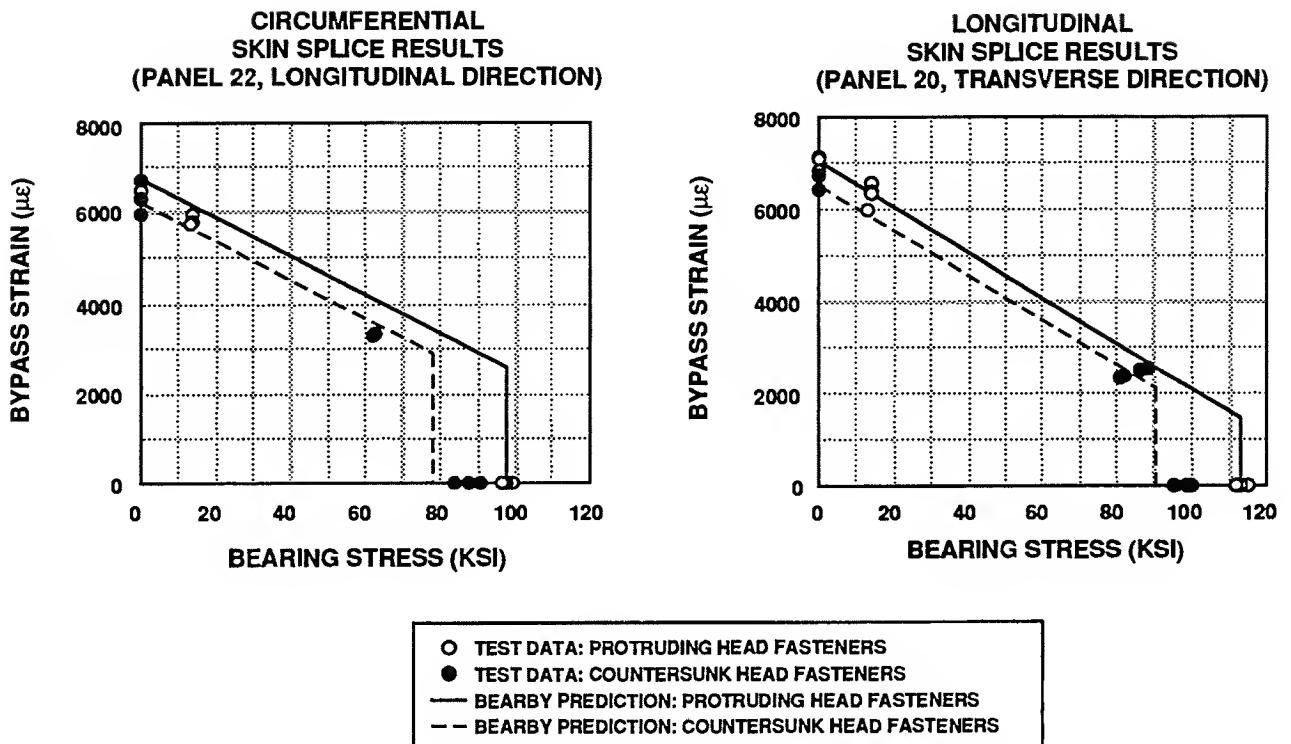


Figure C-10: Bearing-Bypass Interaction in Circumferential and Longitudinal Crown Splice Padups

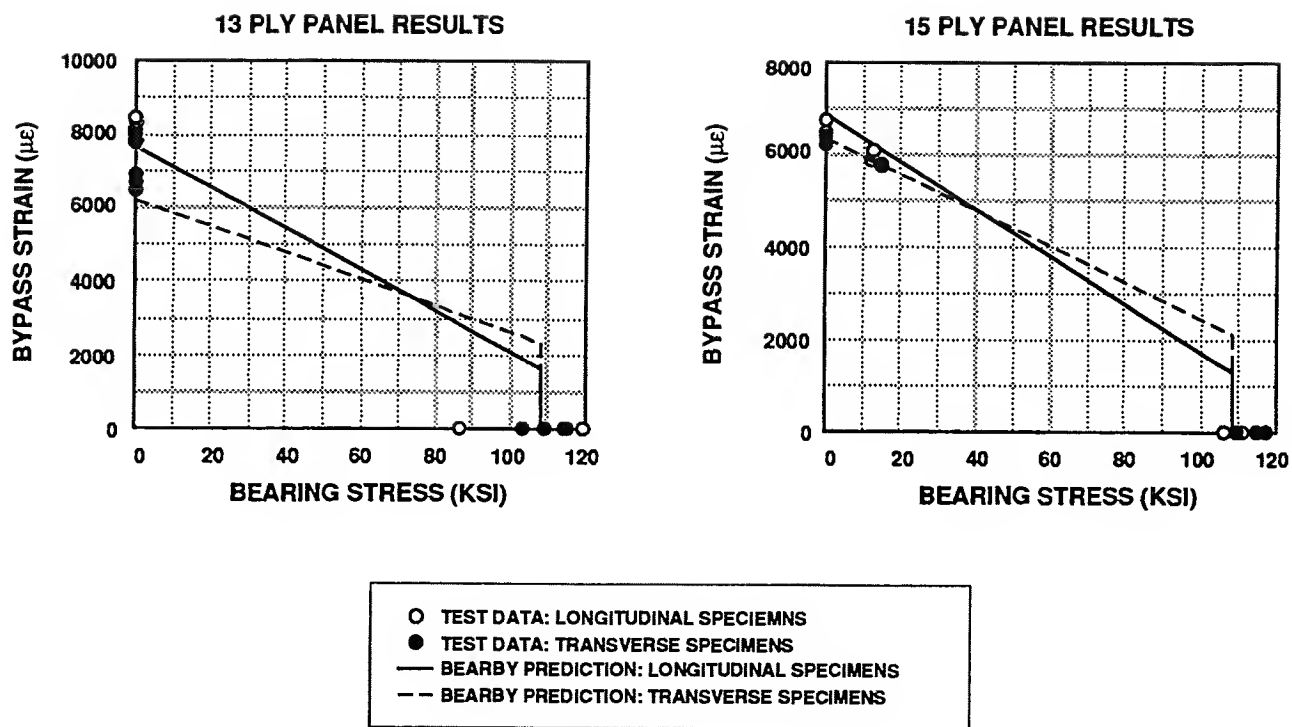


Figure C-11: Bearing-Bypass Interaction Predictions and Test Data for Panels 13 and 15

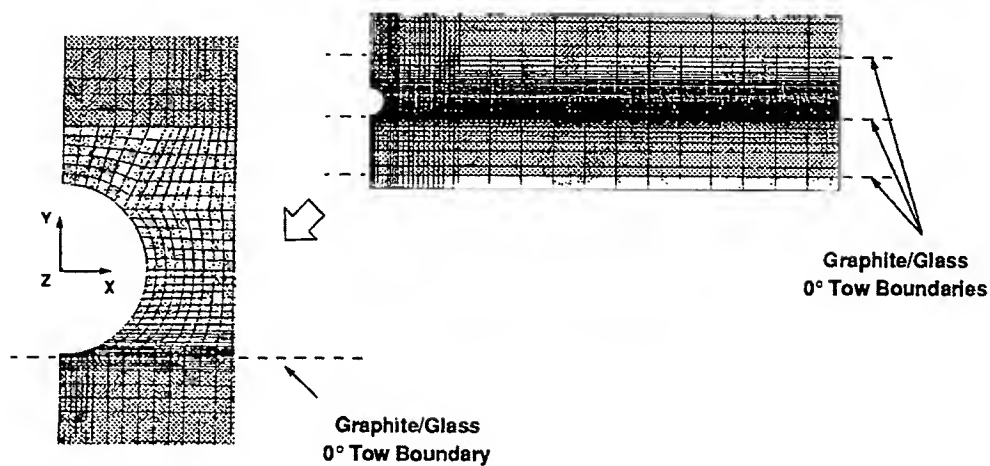


Figure C-12: Typical Finite Element Model for Calculation of Panel 12H Stress Concentrations

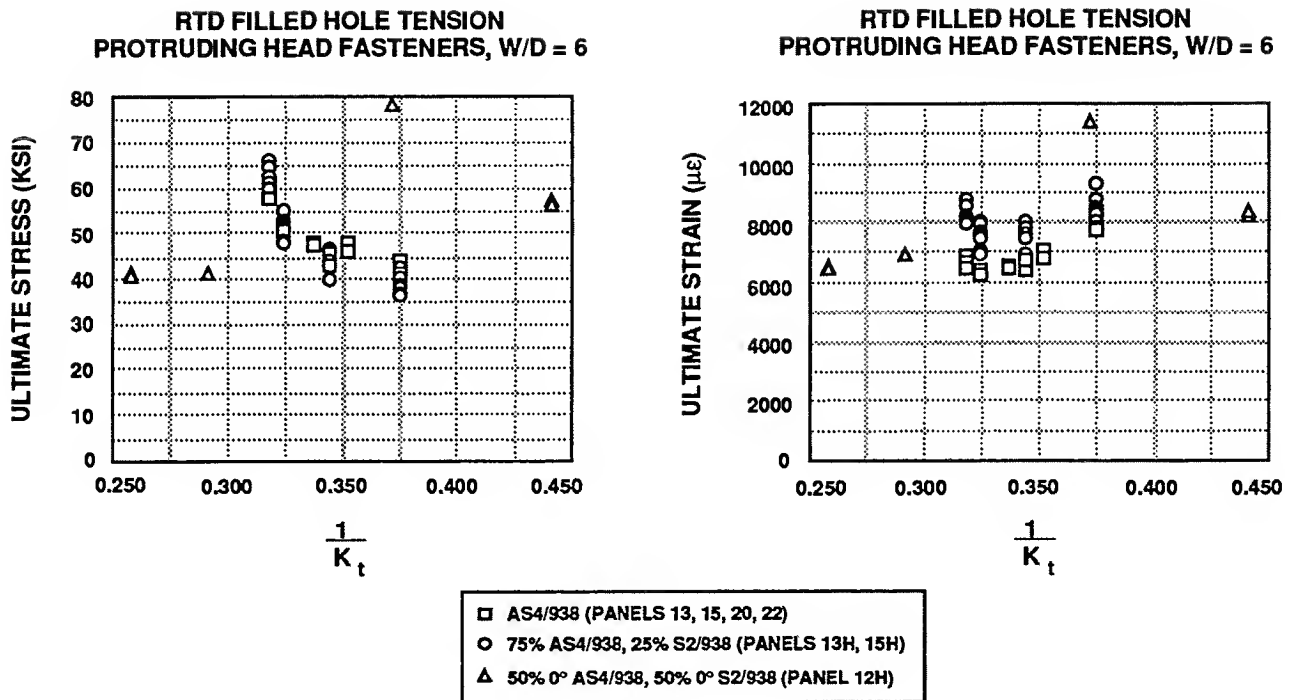


Figure C-13: Relationship Between Failure Stress and Strain and Stress Concentration Factor for AS4/938 and Hybrid Laminates

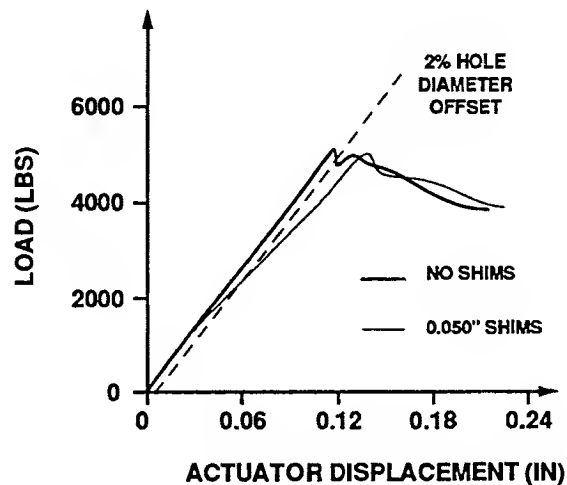


Figure C-14: Typical Load-Deflection Plots for Thermoplastic Rivet Shear

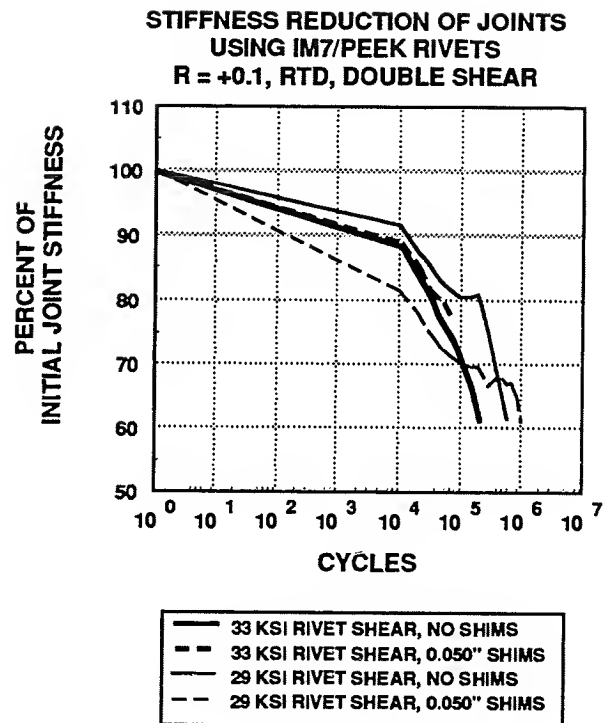
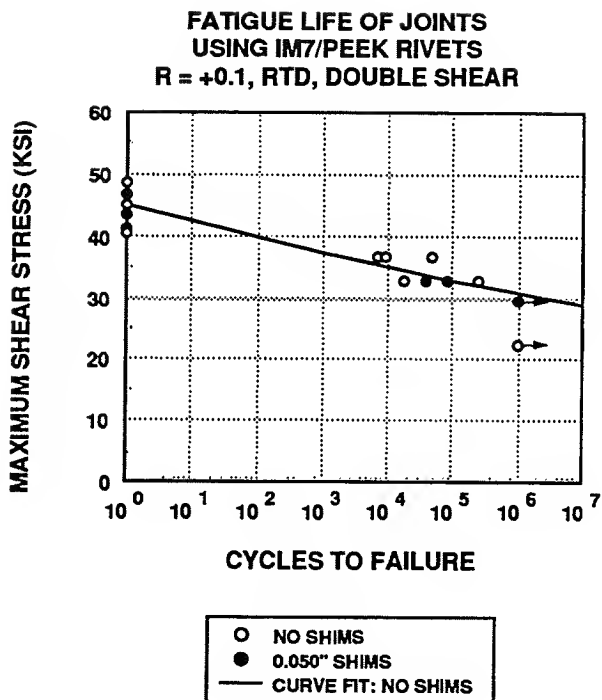


Figure C-15: Fatigue Life and Stiffness Reduction of AS4/1895 Joints Using IM7/PEEK Rivets

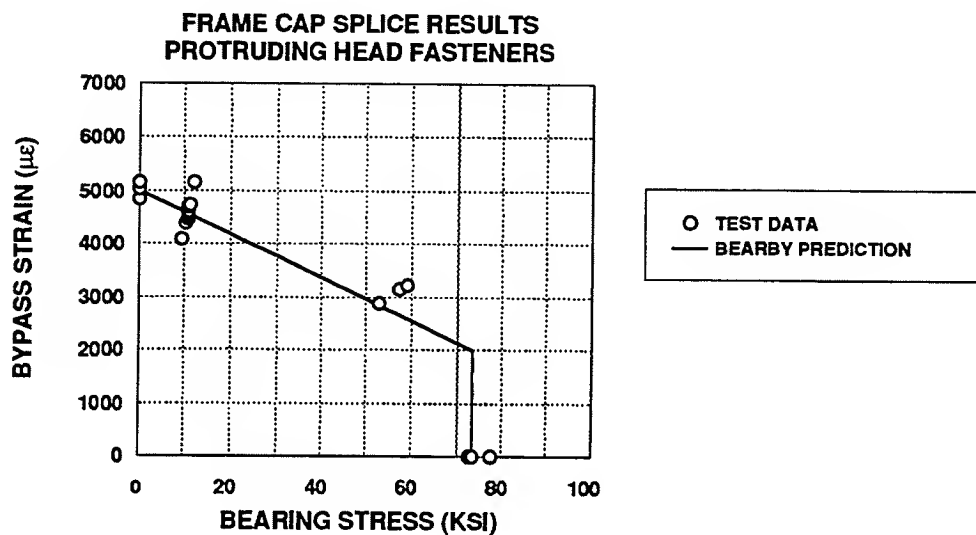


Figure C-16: Bearing-Bypass Interaction in Frame Cap Splice Laminate

APPENDIX D

MDOC Joint Coupon Material Database

Introduction

This report documents the results obtained under Task 2 of the Materials Development Omnibus Contract MDOC program in the development of design values for fuselage keel and side panel laminates and mechanically fastened joints. The report is divided in two sections; the first section documents results of notched tension and compression, bearing, and bearing-bypass interaction tests of keel and side panel laminates, while the second presents the findings of an evaluation of joint performance utilizing thick spacers. The analysis presented in this report is based upon the data contained in project summaries written by Intec [D-1, D-2].

Keel and Side Panel Laminate Design Values

The first phase of this evaluation examined the pure bypass, pure bearing, and bearing-bypass interaction behavior of keel and side panel laminates. A total of 86 tests were conducted in room temperature, cold temperature and elevated temperature environments. The objectives of this set of tests were as follows:

- 1) Examine pure bypass, pure bearing, and bearing-bypass failure modes.
- 2) Develop relationships between notched tension and compression failure strain and laminate configuration (layup).
- 3) Develop design values for keel and side panel laminates using analytical techniques previously used in the ATCAS crown panel material evaluation.

Test Matrix

The matrix of tests performed in this investigation is shown in Table D-1. Emphasis was placed upon generating data using structural configurations critical for given loading conditions, based upon previous research.

In order to span the range of fastener through-thickness clamp-up observed in mechanical assembly, tension bypass tests were conducted using open- and filled-hole specimens fastened with lockbolts. Tests were conducted using both notch types, as previous work has indicated that tape-fabric hybrid laminates are marginally filled-hole critical [D-3 through D-6]. Compression bypass tests were conducted using open-hole specimens, as this condition is known to produce significantly lower notched laminate strengths than does a filled-hole [D-3 through D-6].

Previous experience with tape and fabric angle ply laminates had demonstrated that bearing strength is highly dependent upon fastener clamp-up [D-3 through D-7]. High fastener clamp-up levels increase fastener-laminate friction and inhibit delamination, which increases bearing strength. A reduced fastener clamp-up level must be used to simulate the reduction in fastener clampup over a lifetime of service due to relaxation of laminate through-the-thickness stiffness. For this reason, a clamp-up level equivalent to 40% of normal installation torque (as estimated by Crews and Shivakumar [D-8, D-9] for long term clamp-up relaxation), was used in bearing tests.

Low-load transfer bearing-bypass tests were used to evaluate the effect of small bearing loads upon bypass dominated joints, as larger than expected reductions from pure bypass strength have been observed for certain laminate configurations [D-3 through D-6]. These tests were performed using lockbolt fasteners, as previous testing had demonstrated tension bypass-dominated failures are typically high fastener clamp-up critical.

Biaxial bearing-bypass tests were conducted to examine the compression bypass performance of a typical laminate when subjected to transverse bearing loads. This loading condition can arise in fuselage keel-to-side panel splices during landing. Transverse bearing-tension bypass tests were deemed unnecessary, as previous work had demonstrated that joints subjected to such load cases can be conservatively sized utilizing the ATCAS bearing-bypass analysis methodology [D-10]. Transverse bearing-compression bypass tests were performed using fasteners installed at reduced clamp-up (40% installation torque), as compression bypass-dominated failures were known to be low clamp-up critical [D-3 through D-6].

Testing was conducted at room temperature on specimens nominally dry (RTD), -65°F on specimens nominally dry (CTD), and at 180°F on specimens preconditioned in humid environment (ETW). The majority of tests were performed at RTD conditions; a smaller number of tests were performed at CTD and ETW conditions to develop environmental reduction factors. ETW specimens were preconditioned at 160°F in both 70% and 85% relative humidity to compare moisture absorption rates. Mean moisture contents at the end of 250 days exposure were 0.95% for 70% RH conditioning and 1.20% for 85% RH conditioning, respectively.

Specimen Configurations

The test specimen configurations used in development of the material database are shown in Figures D-1 through D-5. Pure bypass specimens had a width to diameter (w/D) ratio of 6. Pure bearing and bearing-bypass interaction specimens had a width to diameter ratio of 6 and an edge distance to diameter (e/D) ratio of 3.

Test specimens were fabricated from four composite panels manufactured by Hercules Composite Structures under Boeing purchase order #HX1900. Laminates were constructed of 12K AS4/8552 prepreg tow and AS4/8552 plain weave fabric, autoclave cured at 350°F. Tow material was fiber placed using a tow cut and add head. Layups are shown in Table D-2, and nominal laminate properties are shown in Table D-3.

Specimens were machined per BAC5004. Holes were drilled and fasteners installed per BAC5063. Side plates for low load transfer bearing-bypass specimens were instrumented with strain gages as shown in Figure D-4, for use in determining percentage load transfer at the fasteners.

Test Procedures

Uniaxially Loaded Specimens

Pure bypass, bearing, and low-load transfer bearing-bypass tests were conducted at Intec. Specimens were loaded to failure using a servo-hydraulic frame under stroke control, at a

loading rate corresponding to 0.05 inches crosshead deflection per minute. A BSS-7260 anti-buckling fixture was utilized in open-hole compression testing.

Load and actuator displacement data were recorded continuously until ultimate failure. For bearing tests, extensometers were used to measure deflection in the vicinity of the joint. For low-load transfer tests, side plate strain gage data were recorded to monitor load transfer at the fasteners.

Transverse Bearing-Bypass Specimens

Transverse bearing-bypass tests were conducted at Boeing Defense & Space Group, Helicopters Division (HD) using a biaxial loading apparatus. As shown in Figure D-6, the apparatus consisted of clevises to apply bearing loads to the composite specimen, instrumented load links, and attachments to the test machine supports. Longitudinal bypass loads were applied using a 22 kip hydraulic test machine. The transverse loading apparatus, test machine and specimen anti-buckling fixture (based upon the BSS-7260 design) are shown in Figure D-7.

Transverse loads were applied by installing a specimen in the fixture and then torquing the load adjusting bolts. Full and half strain gage bridges were used to record axial and bending strains in the load links (relationships between link strains and applied bearing loads were obtained by calibrating the bridges under tension loading prior to biaxial testing). The specimen ends were then gripped and longitudinal compression loads applied utilizing an MTS hydraulic test machine. Specimens were loaded in compression to failure under stroke control, at a loading rate corresponding to 0.05 inches crosshead deflection per minute. A detailed description of the apparatus and test procedures is provided in Reference D-10.

Load, actuator displacement, and load link strain gage data were recorded continuously until ultimate failure. As transverse bearing loads were applied through a displacement-controlled mechanism, bearing stresses decreased as compression bypass loads were applied (due to Poisson's expansion in the transverse direction) as monitored using the load link gages.

Data Analysis Methodology

Laminate Configuration - Bypass Strain Relationships

Data developed at Boeing have indicated that tension and compression bypass strains vary significantly with laminate configuration. As previously demonstrated in the ATCAS crown panel splice study [D-7], the anisotropic stress concentration factor K_t is a convenient parameter for relating laminate configuration and notched failure strain. For uniaxial loading along a reference axis, x , K_t is related to laminate moduli E_x , E_y , G_{xy} and Poisson's ratio ν_{xy} for symmetric, balanced laminates as follows:

$$K_t = 1 + \sqrt{2 \left(\sqrt{\frac{E_x}{E_y}} - \nu_{xy} \right) + \frac{E_x}{G_{xy}}} \quad (1)$$

For unbalanced laminates (laminates which have unequal percentages of $+\theta$ and $-\theta$ angle plies in regard to the reference axis), a similar calculation is performed using the laminate extensional stiffness matrix to account for extension-shear coupling effects. Research has shown that ultimate tension and compression bypass strain is inversely proportional to K_t for tape, fabric and hybrid laminates.

Failure strains were calculated using failure load P , nominal laminate modulus E_x , nominal laminate thickness, t , and measured specimen width, w , as follows:

$$\epsilon_{byp} = \frac{P}{wtE_x} \quad (2)$$

Gross strains for open- and filled-hole tension and open-hole compression specimens were corrected for finite width effects using the following relationship:

$$\epsilon^\infty = \left[\frac{2 + (1 - D/w)^3}{3(1 - D/w)} \right] \times \epsilon \quad (3)$$

where:

$$\begin{aligned} \epsilon^\infty &= \text{infinite plate gross strain} \\ D &= \text{hole diameter} \\ w &= \text{measured specimen width} \end{aligned}$$

Least squares linear regression analysis was performed using the infinite plate gross strains to obtain a linear relationship between $1/K_t$ and strain:

$$\bar{\epsilon}(K_t) = \bar{\epsilon}(0) + \frac{S}{K_t} \quad (4)$$

where:

$$\begin{aligned} \bar{\epsilon}(K_t) &= \text{mean regression strain for any value of } K_t \\ \bar{\epsilon}(0) &= \text{mean regression strain as } 1/K_t \text{ asymptotically approaches } 0 \\ S &= \text{slope of the mean regression line} \end{aligned}$$

Strains calculated from equation 4 were converted to form an equivalent set of data corresponding to $1/K_t = 0$. This conversion removed the variation in strain due to variances in K_t , creating a univariate data set. The results of this conversion were used to calculate a B-basis

strain design value from the set of data at $1/K_t = 0$. The B-basis design value regression line was then calculated to insure the ratio of B-basis strain to mean regression strain was constant for all values of K_t .

Bearing Strength

Bearing stresses were calculated using failure load P , nominal laminate thickness t and nominal hole diameter D as follows:

$$\sigma_{brg} = \frac{P}{Dt} \quad (5)$$

Two measures of the bearing performance of the laminates were recorded, namely the maximum load carried by the specimen and the linear limit load, which was defined as the load at which joint deflection was offset 2% of the hole diameter from the initial load/deflection slope. These are shown in Figure D-8.

Bearing-Bypass Interaction

Bearing-bypass interaction data were analyzed by calculating the relevant bearing stresses and bypass strains at failure locations using equations 1-3 and 5. Infinite plate corrections were utilized for analyzing tension-loaded joints data, but not for transverse bearing-compression bypass interaction as such corrections are unconservative for the filled-hole compression case. For the low-load transfer specimens, bearing and bypass loads were determined using the side plate strain gage data, which were used to measure the load transferred to the side plates through bearing. A relationship of 1.0585 $\mu\epsilon$ per pound of load transferred to the side plates, as determined by a 2-D finite element analysis using P3/FEA and the pre- and post-processing code PATRAN, was utilized in the load transfer calculations. For the transverse bearing-compression bypass specimens, measurements of bearing and bypass loads were obtained directly using the instrumented load links and the hydraulic test machine data recorder.

Bearing-bypass test results were compared to interaction predictions for the various laminates. Predictions were made using the BEARBY analysis code [D-11], which consists of pre and post processors to the Bolted Joint Stress Field Model (BJSFM) developed by McDonnell Douglas [D-12]. The BEARBY code provides failure predictions of composite laminates under multiaxial bypass and/or off-axis bearing loads, with differing hole sizes and/or differing laminate configurations from baseline test data.

BJSFM determines the stress field around a loaded hole in a homogeneous anisotropic plate under plane stress conditions using a closed form analytic solution based upon the anisotropic theory of elasticity and laminated plate theory. It assumes a cosine radial stress distribution for bearing loads and uses the principle of superposition for combined bearing and bypass loads. The pure bypass stress analysis is based upon infinite plate dimensions; the pure bearing stress analysis includes finite width capability.

The BEARBY methodology predicts bearing-bypass failure loads by applying a point stress failure criterion at the lamina level for the tangential fiber tension, tangential fiber compression, radial fiber tension and radial fiber compression failure modes. For each failure mode, a characteristic dimension is calculated semi-empirically using unnotched uniaxial strength and notched strength data (open- or filled-hole data for tangential fiber tension failure, open-hole data for tangential fiber compression failure, and bearing data for radial fiber tension and compression failure). Lamina failure is assumed to occur when the fiber-direction stress at a characteristic dimension away from the fastener hole, produced by a far-field load equivalent to that at which notched laminate failure occurs, equals to unnotched uniaxial material strength. The characteristic dimension is thus expressed as a function of laminate stress concentration factor. Any inaccuracies created by the neglect of matrix failure modes are accounted for by the semi-empirical nature of the calculation of the characteristic dimension. Lamina strengths used in these analyses, based upon MDOC material qualification and Hercules data normalized to 57% fiber volume, are shown in Table D-4.

The BEARBY methodology has been applied successfully for the prediction of bypass-dominated failures in the design and analysis of bolted structures. Prediction of bearing failure is relatively immature and is hampered by the lack of a true failure definition, as well as complications arising from out-of-plane effects.

Once the required characteristic dimensions have been calculated, BEARBY then calculates the stress field about a loaded hole using BJSFM for multiple bearing-bypass ratios. The point stress criterion is then reapplied for the four fiber failure modes for each lamina, and used to calculate the bearing and bypass load levels at which lamina failure occurs. One essential and useful feature of this methodology is the separation of bearing and bypass-dominated failures, which permits evaluation of environmental and joint configuration effects.

Test Results

Notched Tension

Open- and filled-hole tension specimens failed in typical tension bypass dominated modes, with ultimate failure initiating through fracture of 0° fibers. Matrix splits in $+45^\circ$, -45° and 90° plies were also observed. Little load-deflection nonlinearity was observed prior to ultimate failure.

Failure stresses and strains for open- and filled-hole tension tests are shown in Tables 5 and 6, respectively. Relationships between failure strain and stress concentration factor are shown in Figure D-9 for open-hole tension and in Figure D-10 for filled-hole tension. Mean regression and B-basis lines are plotted for RTD data. Both sets of data demonstrate that failure strain and stress concentration factor are inversely proportional.

Examination of the RTD data indicated that the filled-hole condition was critical only at high K_t , while the open-hole condition was critical as K_t decreased. As shown in Table D-7, little variation from RTD filled-hole failure strains was observed for laminates tested in CTD conditions. A reduction factor of 0.95 was obtained for open-hole failure strains in ETW conditions (based upon ETW results for 160°F , 70% RH conditioning).

B-basis regression lines were calculated for both filled- and open-hole tension failure strains. Tension design values for the range of laminate configurations tested (shown in Figure D-11) were developed using the minimum of the filled- and open-hole B-basis regressions, reduced by a factor of 0.99 and 0.95 respectively to account for critical environment.

Notched Compression

Open-hole compression specimens failed in typical compression bypass dominated modes, with ultimate failure occurring through local compression-shear failure. Little load-deflection nonlinearity was observed prior to ultimate failure.

Failure stresses and strains for open-hole compression tests are shown in Table D-8. Relationships between failure strain and stress concentration factor are shown in Figure D-12. Mean regression lines are plotted for RTD data. As was the case under tension loading, failure strain and stress concentration factor are inversely proportional.

As shown in Table D-7, ETW was the critical environment, with failure strains approximately 80-82% of those observed in RTD conditions. The design values shown in Figure D-12 are based upon the RTD regression but are reduced by a factor of 0.80 to account for critical environment (based upon ETW results for 160°F, 85% RH conditioning).

Pure Bearing

Bearing specimens failed in typical pure bearing-dominated modes, with significant hole elongation and surface ply brooming (local to the fastener head) observed. Load-deflection plots exhibited nonlinearity, as is typical under such loading.

Bearing strengths, shown in Table D-9, were relatively insensitive to laminate configuration. Ultimate bearing strengths in ETW conditions were 90-92% of those observed in RTD conditions for laminate S20. 2% hole diameter offset strengths in ETW conditions were 84-85% of those for RTD conditions.

Utilizing all of the RTD data, a B-basis RTD bearing strength design value of 99.0 ksi was calculated. Accounting for the worst case reduction factor of 0.90 for ETW conditions (160°F, 85% RH conditioning), a bearing strength design value of 89.1 ksi was obtained.

Low Load Transfer Bearing - Bypass Interaction

Low load transfer specimens failed in tension bypass-dominated modes. Some slight hole elongation was observed in both the test laminate and in the aluminum side plates at ultimate failure. Load-deflection behavior was linear to failure.

Typical load-strain data for the side plates up to initial failure are shown in Figure D-13. For laminates S20 and S23, load transfer to the side plates was initially 40-45% but decreased to 25-30% prior to initial failure and then to 20-25% at final failure (not represented in figure). For laminate S22, load transfer to the side plates was initially 25-35% but decreased to 15-20% prior to initial failure and then to 8-15% at final failure. The initial nonlinearity in the load-strain plots may have been caused by friction between the load plates and laminates; as initial friction was overcome, the percentage of load transfer decreased. All specimens exhibited initial failures,

after which the percentage of load transferred to the side plates abruptly decreased. It should be noted that the load transferred to the side plates generally decreases as laminate modulus increases.

Mean bearing strengths and bypass strains are shown in Table D-10. In this table, coefficients of variation are based upon bypass strain at failure. Low load transfer data are plotted versus BEARBY bearing-bypass predictions in Figures D-14 through D-16. In addition to mean strength predictions, the figures also show bearing-bypass design envelopes calculated using the pure tension bypass and bearing design values.

Transverse Bearing - Compression Bypass Interaction

Transverse bearing-bypass specimens exhibited net section compression and local bearing failures, with evidence of a tear-out type mode along the $\pm 45^\circ$ fibers. Load-deflection behavior was slightly nonlinear prior to ultimate failure.

Bearing stress levels observed during test, calculated using load link strain data, are shown in Figure D-17. As longitudinal bypass loads were applied, transverse bearing loads decreased due to Poisson's deformation of the test specimen. Little nonlinearity was observed in the bearing stress vs. bypass strain relationships prior to ultimate failure.

Transverse bearing-compression bypass interaction results are listed in Table D-11. The data are also plotted in comparison to BEARBY predictions and open-hole compression results in Figure D-18. The results plotted utilize the lowest value of bearing stress observed during each test, as estimated using the load link strain data. The transverse bearing-bypass data indicate that the use of open-hole compression data in bearing-compression bypass analysis results in acceptable design envelopes for biaxial load cases.

Discussion of Results

Notched tension and compression performance of the tow-fabric hybrid laminates exhibited behavior consistent with that previously observed for composite laminates. Open- and filled-hole tension failure strains were similar in magnitude, with the open-hole ETW data found to be critical. Open-hole compression failure strains were also ETW critical.

Failure strains for tension and compression are comparable to previously obtained data. As an example, RTD filled-hole tension performance is compared to that exhibited by AS4/938 tow laminates in Figure D-19. A comparison of environmental compensation factors with another thermoset composite system (IM6/3501-6 tape [D-6]) is shown in Table D-12. Open-hole compression strain reductions due to ETW conditions were comparable to those observed for IM6/3501-6 tape, while CTD environmental reduction factors for tension were less severe.

Laminate bearing strengths were also comparable to previously obtained data. Figure D-20 compares mean hybrid bearing strengths to those exhibited by AS4/938 tow laminates of comparable thickness. Bearing-tension bypass strengths were shown to be consistent with predictions generated using the BEARBY analysis code. The use of open-hole compression strains in bearing-compression bypass analysis appears to be an acceptable practice for biaxial load cases.

Joint Performance with Thick Spacers

The second phase of this evaluation compared the performance of typical bolted joints utilizing thick, structural spacers with that of baseline specimens without spacers. These tests were required to help define the configuration of the keel-side panel splice, which must compensate for differences in keel and side panel core thicknesses on the order of 0.20-0.25 inches. Three baseline tests without spacers and three with spacers were conducted. The objectives of this set of tests were as follows:

- 1) Examine failure modes of specimens with and without spacers.
- 2) Determine relative decrease/increase in limit and ultimate bearing-bypass strength for specimens using thick spacers.
- 3) Compare results to bearing-bypass analysis predictions.

Test Matrix & Specimen Configurations

The matrix of tests performed in this phase is shown in Table D-1. All tests were performed in room temperature, nominally dry conditions.

Test laminates were fabricated from panel S20, manufactured using 12K AS4/8552 prepreg tow and AS4/8552 plain weave fabric, autoclave cured at 350°F. Spacers were manufactured using IM6/3501-6 Grade 190 tape, autoclave cured at 350°F. Layups are shown in Table D-2, and nominal laminate properties are shown in Table D-3.

The test specimen configurations used are shown in Figures D-21 and D-22. Specimens had a width to diameter (w/D) ratio of 5 and an edge distance to diameter (e/D) ratio of 2.6. Specimens were machined per BAC5004. Holes were drilled and fasteners installed per BAC5063 except that fasteners were torqued to 70 in-lb nominally, or 40% normal installation torque, to simulate clamp-up relaxation expected during the service lifetime. Laminates were instrumented with strain gages for use in determining percentage load transfer at the fasteners.

Test Procedures

All tests were conducted at Intec. Specimens were loaded to failure using a servo-hydraulic frame under stroke control, at a loading rate corresponding to 0.05 inches crosshead deflection per minute. A stabilization fixture was used to restrict specimen out-of-plane rotation during loading. Load and actuator displacement data, as well as strain gage data, were recorded continuously until ultimate failure.

Data Analysis Methodology

Bearing-bypass interaction data were analyzed by calculating the relevant bearing stresses and bypass strains at failure locations; infinite plate corrections were utilized. Strain gage data were used to measure the load transferred at each fastener through bearing. A 2-D finite element analysis determined that 1.03 $\mu\epsilon$ should be measured by each gage per pound of load transferred at the fastener holes loaded in pure bearing. Equivalent load transfer (50%) was utilized in all

strength calculations, as strain gage readings indicated that any differential loading had been eliminated through hole elongation at failure.

Test Results

Baseline 50% load transfer specimens failed through a bearing-dominated mode, with substantial hole elongation observed. Specimens with spacers exhibited fastener tension failure at the heads. This change in failure mode occurred because the structural spacer increased the bearing load-carrying ability of the joint and also increased the bending moment on the fasteners.

A comparison of joint stiffness is shown in Figure D-23, using load-deflection data. Using load at 0.05 inches actuator displacement as a criterion for comparison, joints with spacers exhibited effective stiffnesses on the order of 70% of that for the baseline joints. This decrease in stiffness is most probably caused by increased fastener bending deformation resulting from the presence of the spacer.

A comparison of load-strain data (up to initial failure) is shown in Figure D-24. For the baseline specimens, load transfer was roughly equivalent between the fasteners, with the greatest differential prior to initial failure being approximately 61%-39% for specimen S2015213. For specimens with spacers, strains were observed to decrease as the spacer began to pick up load (at approximately 20-30 ksi bearing stress). Measured strains were slightly lower than those predicted by finite element analysis due to flexure of the specimen adherends under single shear loading. 50% load transfer was ultimately assumed in bearing-bypass analysis of all specimens, as strain readings fluctuated rapidly after initial failure was observed.

Mean bearing strengths and bypass strains are shown in Table D-13 for both 2% hole diameter offset and ultimate failure. Coefficients of variation are based upon bypass strain. Specimens with spacers exhibited 15% lower load for 2% hole diameter offset, but 12% higher ultimate load. Based upon a 1.5 x 2% offset criterion, effective failure load increased 3% for specimens with spacers.

Baseline failure data are also plotted versus BEARBY bearing-bypass predictions and other data for laminate S20 in Figure D-25. The baseline specimens failed at slightly lower bearing stresses/bypass strains than those predicted. This is partially explained by the use of a 0.25 inch diameter hole in the prediction (actual hole diameter was 0.315 inches) and the use of a smaller specimen edge margin than was used in generating pure bearing data.

Discussion of Results

The presence of a thick structural spacer in a representative keel-side panel splice configuration resulted in a change in failure mode (from laminate bearing to fastener head tensile failure), a 30% reduction in effective joint stiffness, a 15% reduction in 2% hole diameter offset load, a 12% increase in ultimate failure load, and a 3% increase in effective failure load, based upon a 1.5 x 2% offset criterion. Reductions in stiffness and 2% offset load were caused by increased fastener bending due to the presence of the spacer, while the increase in ultimate load apparently was caused by the additional load-carrying capability provided by the spacer. Bearing-bypass

performance of the baseline specimens appeared slightly low in comparison with BEARBY analysis predictions.

Conclusions

The following conclusions were developed during this investigation:

- 1) Relationships between open- and filled-hole strengths and the stress concentration factor at the hole were consistent with those observed for other composite material forms. Failure strain levels were comparable to previously obtained data.
- 2) In RTD tension the filled-hole case was found critical only at high stress concentration values, with the open-hole case being critical for lower stress concentration values. Open-hole tension failure was found to be hot/wet critical. Compression failure was found to be hot/wet critical.
- 3) Bearing strengths were comparable to previously obtained data for tow-placed laminates. Bearing failure modes were found to be hot/wet critical.
- 4) Uniaxial bearing-tension bypass performance was predictable using the BEARBY methodology based upon low load transfer and 50% load transfer specimen results.
- 5) Transverse bearing-compression bypass tests indicated that use of open-hole compression data in bearing-compression bypass analysis is an acceptable procedure for biaxial load cases.
- 6) 50% load transfer specimens representative of the keel-side panel splice changed in failure mode, decreased in stiffness, decreased in 2% hole diameter offset load, and increased in ultimate failure load when thick, structural spacers were utilized. This apparently was due to increased fastener bending and additional bearing load-carrying capability created by the spacer.

References

- D-1. Raj, S., Boeing/ATCAS MDOC AS4/8552 Laminate Physical and Mechanical Properties, Intec Project No. BC0131.
- D-2. Raj, S., Boeing/ATCAS MDOC Joint Material Database, Intec Project No. BC0133.
- D-3. Grant, P. and Sawicki, A., "Development of Design and Analysis Methodology for Composite Bolted Joints," American Helicopter Society National Technical Specialists' Meeting on Rotorcraft Structures, Williamsburg, VA, October 1991.
- D-4. Kesack, W., Stevenson, K. et al, "V-22 Material Substantiating Data and Analysis Report," Contract No. N00019-85-C-0145, Report No. 901-930-022, Revision A, November 1991.
- D-5. Funke, R., Andreshak, D. et al, "F/A-18 E/F Material Substantiating Data and Analysis Report," Contract No. N00019-92-C-0059, Report No. MDC 93B0068, Revision B, March 1994.
- D-6. Grant, P. and Sawicki, A., "Relationship Between Failure Criteria, Allowables Development, and Qualification of Composite Structure," American Helicopter Society National Technical Specialists' Meeting on Rotorcraft Structures, Williamsburg, VA, October 1995.
- D-7. Sawicki, A., Grant, P. and Mabson, G., "Mechanical Assembly of Commercial Transport Fuselage Utilizing Tow-Placed and Textile Composites," AIAA/ASME/ASCE/AHS/ASC 35th Structures, Structural Dynamics, and Materials Conference, Hilton Head, SC, April 1994.
- D-8. Shivakumar, N. and Crews, J., "Bolt Clampup Relaxation in a Graphite/Epoxy Laminate," ASTM STP 813, Philadelphia, PA, 1983, pp. 5-22.
- D-9. Shivakumar, N. and Crews, J., "An Equation for Bolt Clampup Relaxation in Transient Environments," NASA Technical Memorandum 84480, April 1982.
- D-10. Sawicki, A. and Nguyen, N., "The Influence of Transverse Bearing Loads upon the Bypass Strength of Composite Bolted Joints," 6th ASTM Symposium on Composites: Fatigue and Fracture, Denver, CO, May 1995.
- D-11. Sawicki, A. and Mabson, G., "BEARBY Bolted Joints Analysis - Program Description and User's Guide," Boeing Defense & Space Group, Helicopters Division Document # D210-12933-1, April 1993.
- D-12. Garbo, S. and Ogonowski, J., "Effect of Variances and Manufacturing Tolerances on the Design Strength and Life of Mechanically Fastened Composite Joints. Volume 1: Methodology Development and Data Evaluation," Report AFWAL-TR-81-3041, April 1981.

Table D-1. Test matrix.

Test Type	Env.	Panel ID				
		S20 Longitudinal	S21 Longitudinal	S21 Transverse	S22 Longitudinal	S23 Longitudinal
Open-Hole Tension	RTD	3	3	3	3	3
	CTD	3	-	-	-	-
	ETW	4	-	-	-	-
Open-Hole Compression	RTD	3	3	3	3	3
	CTD	3	-	-	-	-
	ETW	4	-	-	-	-
Filled-Hole Tension	RTD	3	3	3	3	3
	CTD	3	-	-	3	-
Bearing	RTD	3	-	-	3	3
	ETW	4	-	-	-	-
Low Load Transfer, Tension	RTD	3	-	-	3	-
Transverse Bearing- Bypass Interaction	RTD	-	-	-	2	-
50% Load Transfer	RTD	6	-	-	-	-

Table D-2. Layups of test panels used in this investigation.

Panel ID	Layup	Material
S20	[F0/+45/0/-45/90/±45/90/-45/0/+45/F0]	AS4/8552 tow and plain weave fabric “F” represents fabric plies
S21	[F0/+45/0/-45/0/+45/90/-45/0/-45/0/+45/F0]	
S22	[F0/+45/0/-45/90/0]S	
S23	[F0/-45/90/+45/0/90]S	
Spacer (50% Load Transfer Tests)	[+45/0/-45/90 ₃ /±45/90 ₃ /±45]2S	IM6/3501-6 Tape

Table D-3. In-plane properties used in this investigation.

Panel ID	Longitudinal Modulus (msi)	Transverse Modulus (msi)	Major Poisson's Ratio	Shear Modulus (msi)	K _t	Nominal Thickness (in)
AS4/8552 tow (tow cut & add head)	17.35	1.36	0.32	0.76	-	0.0071
AS4/8552 plain weave fabric	8.98	8.98	0.046	0.72	-	0.0078
IM6/3501-6 tape	21.00	1.40	0.34	0.80	-	0.0074
S20	6.83	6.83	0.302	2.59	3.01	0.0866
S21	8.71	5.34	0.365	2.45	3.32 (L) 2.82 (T)	0.0937
S22	9.04	6.51	0.244	1.98	3.54	0.0866
S23	6.51	9.04	0.176	1.98	3.15	0.0866
Spacer	4.84	11.70	0.486	2.92	-	0.1924

Table D-4. Lamina strength properties used in BEARBY bearing-bypass analysis.

Material	Property	RTD Strength (ksi)	Design Env. Strength (ksi)
AS4/8552 Tow	0° Lamina Tension Strength	295	266 (-65°F Dry)
	0° Lamina Compression Strength	213	185 (180°F Wet)
AS4/8552 PW Fabric	0° Lamina Tension Strength	115	105 (-65°F Dry)
	0° Lamina Compression Strength	128	103 (180°F Wet)

Table D-5. Results from AS4/8552 open-hole tension tests.

Panel ID	Env.	Number of Tests	Mean Ultimate Tension Stress (ksi)	Mean Nominal Failure Strain (μstrain)	Coefficient of Variation (%)
S20	RTD	3	48.9	7391	3.85
S21 longitudinal		3	59.1	7002	2.03
S21 transverse		3	40.5	7825	5.29
S22		3	65.5	7477	8.93
S23		3	46.0	7288	3.54
S20	CTD	3	49.1	7408	3.20
S20	ETW				
160°F, 70% RH Conditioning		2	46.7	7044	0.48
160°F, 85% RH Conditioning		2	47.8	7222	2.49

Table D-6. Results from AS4/8552 filled-hole tension tests.

Panel ID	Env.	Number of Tests	Mean Ultimate Tension Stress (ksi)	Mean Nominal Failure Strain (μ strain)	Coefficient of Variation (%)
S20	RTD	3	50.3	7588	2.47
S21 longitudinal		3	57.5	6807	2.20
S21 transverse		3	44.0	8502	2.47
S22		3	63.9	7293	3.46
S23		3	46.6	7389	5.01
S20	CTD	3	54.1	8166	0.72
S22		3	63.4	7234	5.43

Table D-7. Environmental compensation factors for various failure modes.

Failure Mode	Laminate Configuration	Environment	Mean Data @ Env.	Mean Data RTD	$\frac{ENV}{RTD}$
Open-Hole Tension	S20 ($K_t = 3.03$)	CTD	7508 $\mu\epsilon$	7391 $\mu\epsilon$	1.00
		ETW	7044 $\mu\epsilon$	7391 $\mu\epsilon$	0.95
Filled-Hole Tension	S20 ($K_t = 3.03$)	CTD	8166 $\mu\epsilon$	7588 $\mu\epsilon$	1.08
	S22 ($K_t = 3.54$)	CTD	7234 $\mu\epsilon$	7293 $\mu\epsilon$	0.99
Open-Hole Compression	S20 ($K_t = 3.03$)	CTD	7586 $\mu\epsilon$	6992 $\mu\epsilon$	1.08
		ETW	5581 $\mu\epsilon$	6992 $\mu\epsilon$	0.80
Laminate Bearing	S20 ($K_t = 3.03$)	ETW	103.1 ksi	114.5 ksi	0.90

Table D-8. Results from AS4/8552 open-hole compression tests.

Panel ID	Env.	Number of Tests	Mean Ultimate Compr. Stress (ksi)	Mean Nominal Failure Strain (μ strain)	Coefficient of Variation (%)
S20	RTD	3	46.3	6992	6.40
S21 longitudinal		3	53.7	6364	2.98
S21 transverse		3	40.7	7867	2.31
S22		3	57.7	6578	3.56
S23		3	44.2	6998	2.38
S20	CTD	3	50.2	7586	3.01
S20	ETW				
160°F, 70% RH Conditioning		2	38.2	5772	3.14
160°F, 85% RH Conditioning		2	37.0	5581	8.88

Table D-9. Results from AS4/8552 bearing tests.

Panel ID	Env.	Number of Tests	Mean Bearing Stress at 2% Hole Diameter Offset (ksi)	Mean Ultimate Bearing Stress (ksi)	Coefficient of Variation (%)
S20	RTD	3	103.8	114.5	4.69
S22		3	101.1	116.0	1.06
S23		3	96.0	106.2	1.43
S20	ETW				
160°F, 70% RH Conditioning		2	88.0	105.3	5.34
160°F, 85% RH Conditioning		2	87.1	103.1	8.12

Table D-10. Results from AS4/8552 low load transfer tests.

Panel ID	Env.	No. of Tests	Mean Load Transfer (%)	Mean Ultimate Bypass Stress (ksi)	Mean Nominal Bypass Strain (μ strain)	Mean Ultimate Bearing Stress (ksi)	Coefficient of Variation (%)
S20	RTD	3	23.0	39.2	5919	70.5	1.83
S22		3	11.4	52.0	5937	40.2	2.76
S23		3	20.7	36.9	5839	57.6	2.27

Table D-11. Results from AS4/8552 transverse bearing-bypass interaction tests.

Panel ID	Env.	No. of Tests	Mean Ultimate Bypass Stress (ksi)	Mean Nominal Bypass Strain (μ strain)	Mean Initial Bearing Stress (ksi)	Mean Ultimate Bearing Stress (ksi)	Coefficient of Variation (%)
S22	RTD	2	-69.9	-7730	91.8	74.6	6.30

Table D-12. Comparison of environmental compensation factors with those observed for IM6/3501-6 tape.

Failure Mode	Material	Environment	<u>ENV</u> RTD
Open-Hole Tension	AS4/8552 Tow/Fabric	CTD (-65°F)	1.00
	IM6/3501-6 Tape		0.79
Filled-Hole Tension	AS4/8552 Tow/Fabric	CTD (-65°F)	0.99
	IM6/3501-6 Tape		0.91
Open-Hole Compression	AS4/8552 Tow/Fabric	ETW (180°F)	0.80
	IM6/3501-6 Tape		0.78
Laminate Bearing	AS4/8552 Tow/Fabric	ETW (180°F)	0.90
	IM6/3501-6 Tape		0.93

Table D-13. Results from AS4/8552 50% load transfer tests.

Panel ID	Env.	No. of Tests	Mean Bypass Stress (ksi)	Mean Nominal Bypass Strain (μ strain)	Mean Bearing Stress (ksi)	Coefficient of Variation (%)
S20 (no spacer) 2% offset data	RTD	3	15.0	2295	74.5	1.38
S20 (spacer) 2% offset data	RTD	3	12.8	1963	64.1	10.1
S20(no spacer) ultimate failure	RTD	3	18.6	2855	92.7	1.87
S20 (spacer) ultimate failure	RTD	3	20.9	3195	104.2	1.60
S20 (spacer) 1.5 x 2% offset	RTD	3	19.2	2945	96.1	10.1

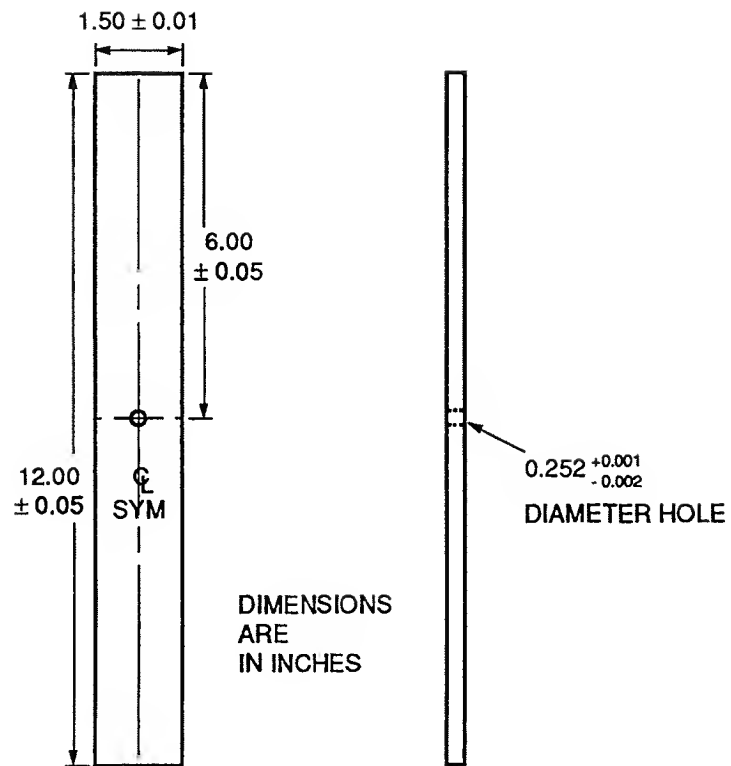


Figure D-1: Open hole tension and compression specimen configuration.

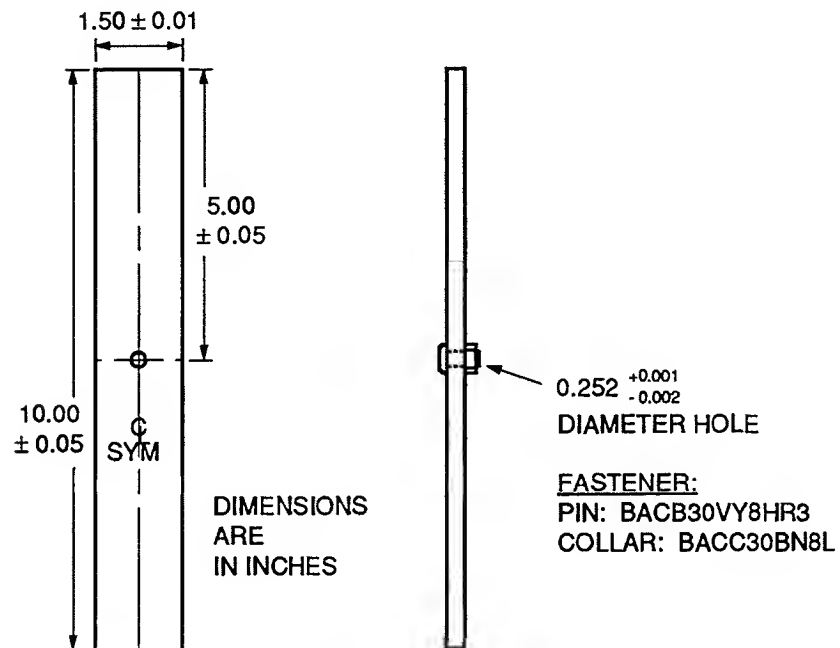


Figure D-2: Filled hole tension specimen configuration.

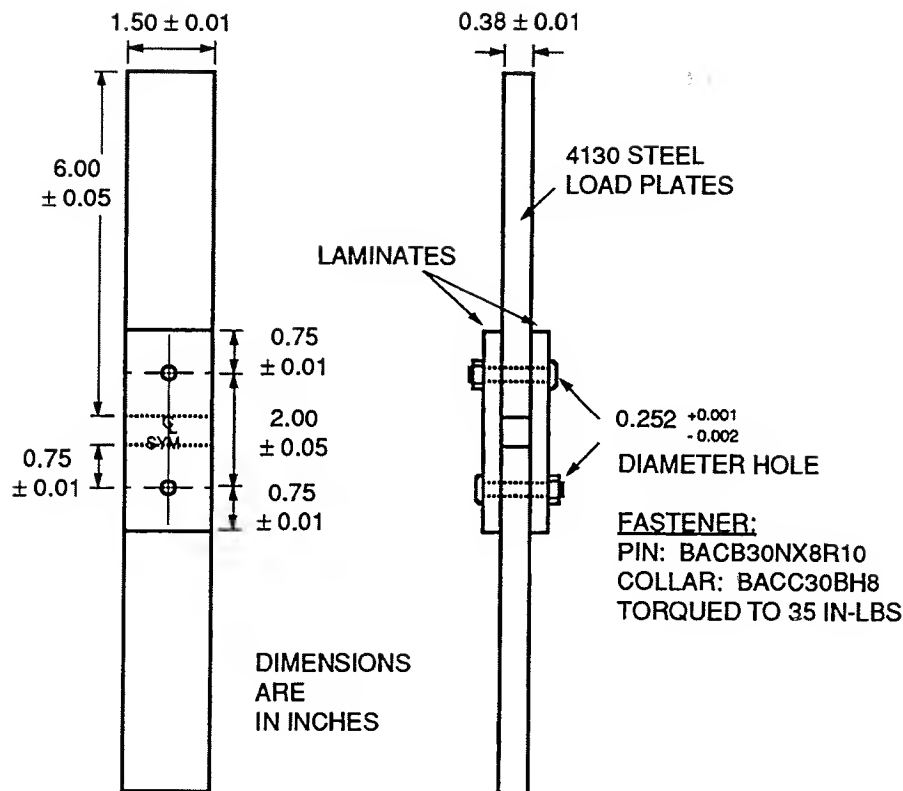


Figure D-3: Bearing specimen configuration.

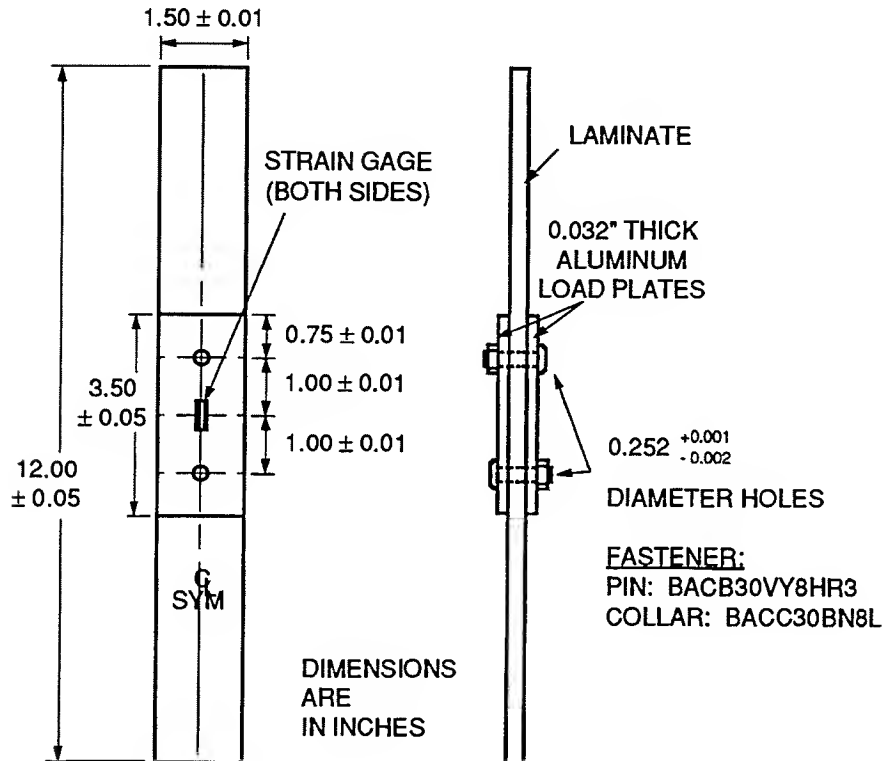


Figure D-4: Low load transfer bearing-bypass specimen configuration.

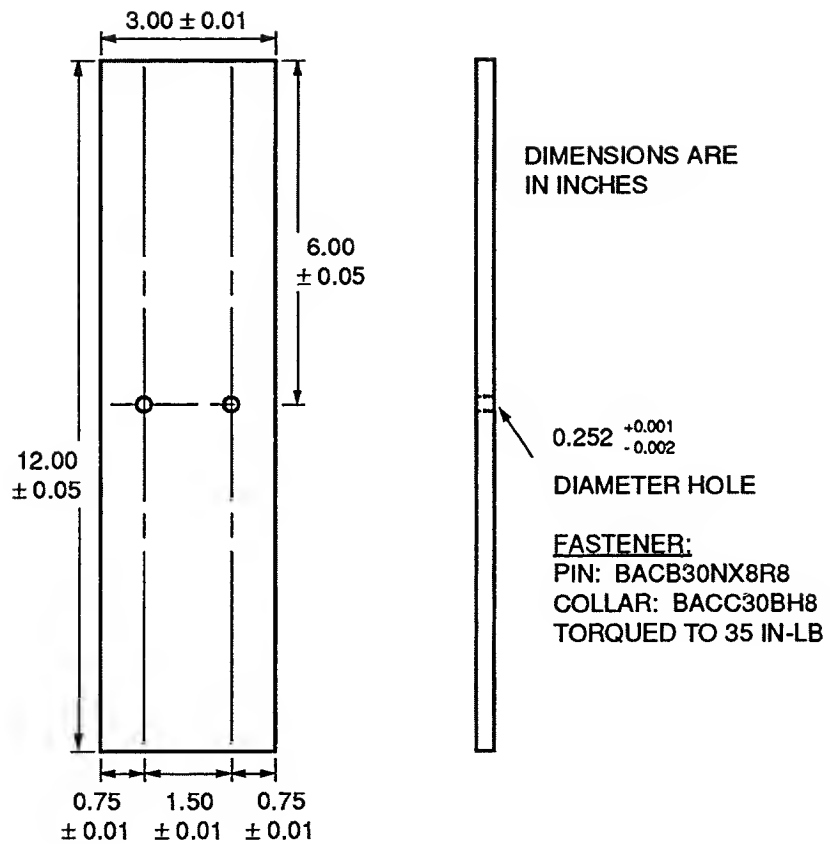


Figure D-5: Transverse bearing-compression bypass specimen configuration.

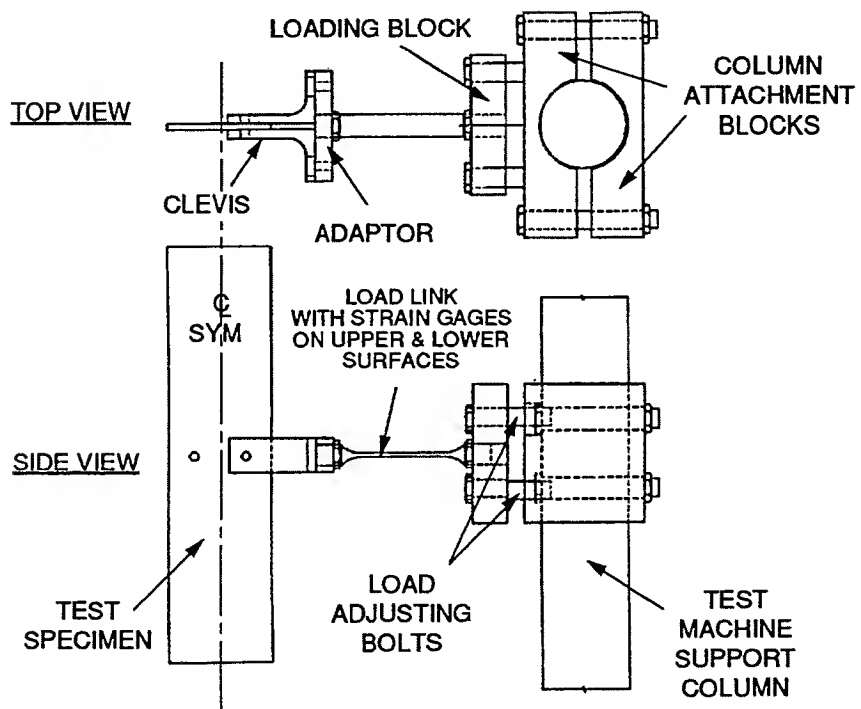


Figure D-6: Transverse loading apparatus.

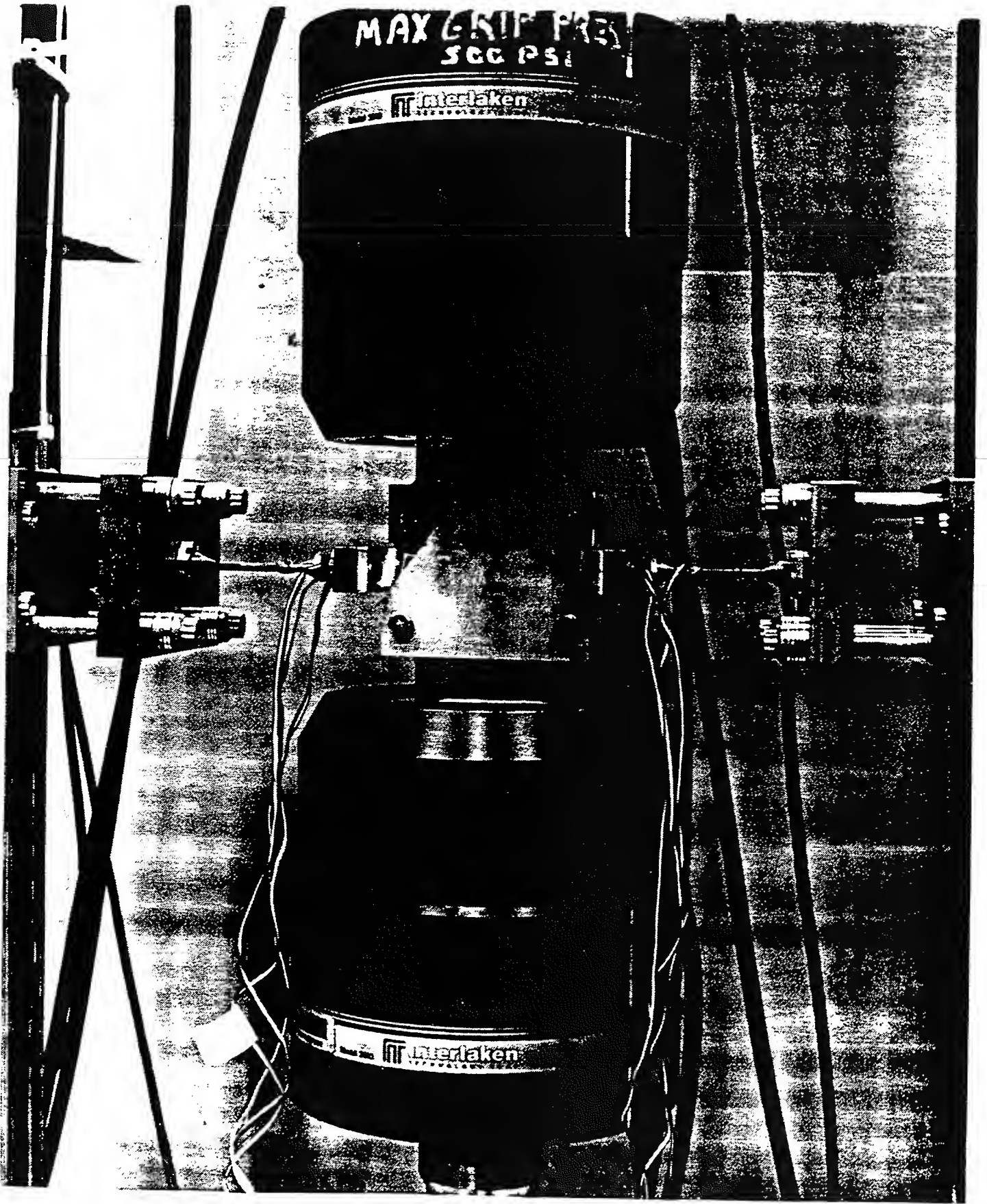


Figure D-7: Transverse bearing-compression bypass test apparatus and stabilization fixture.

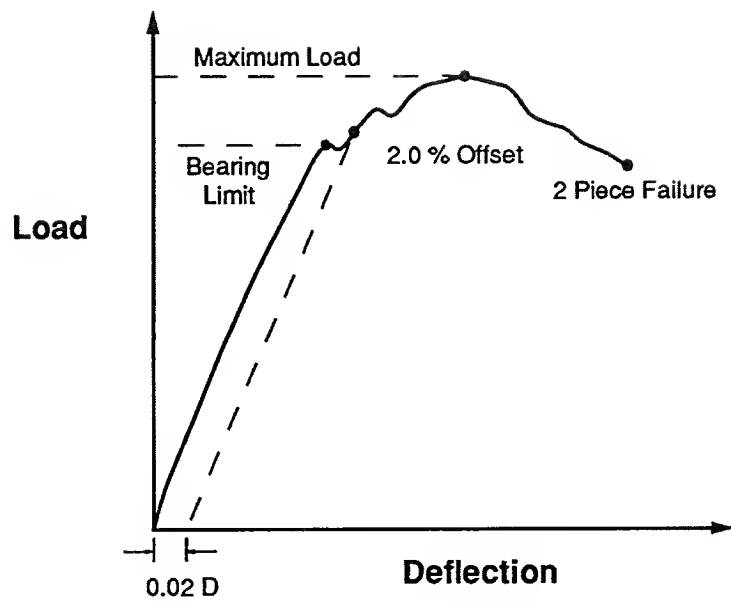


Figure D-8: Typical bearing specimen load-deflection behavior: definitions.

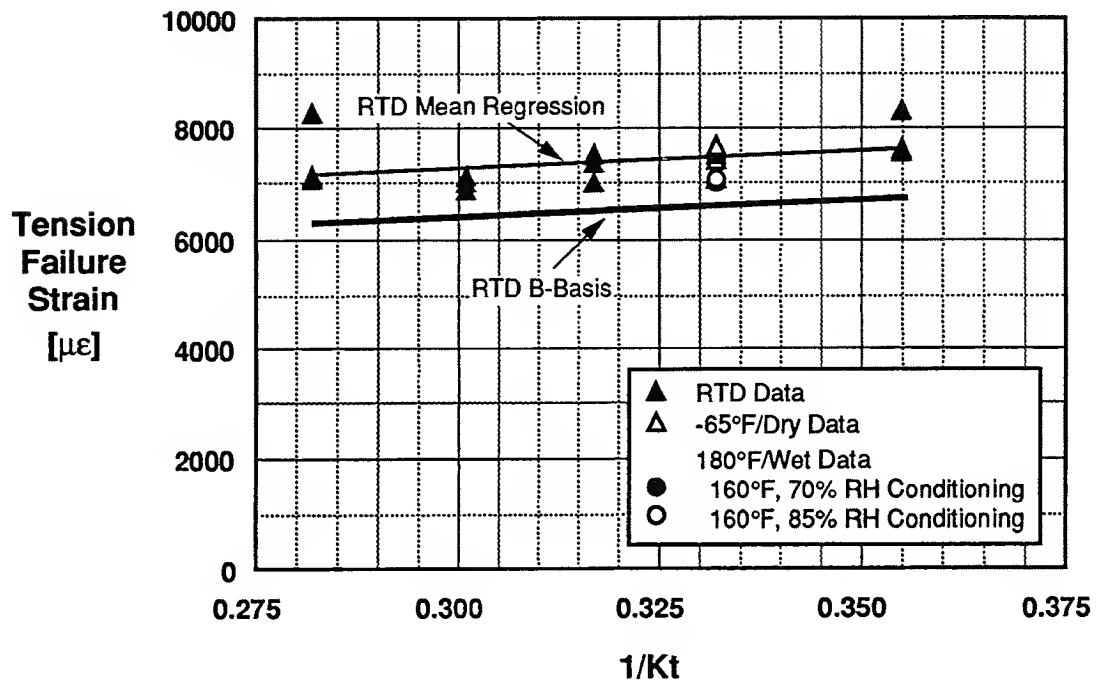


Figure D-9: Open hole tension failure strains vs. inverse of stress concentration factor.

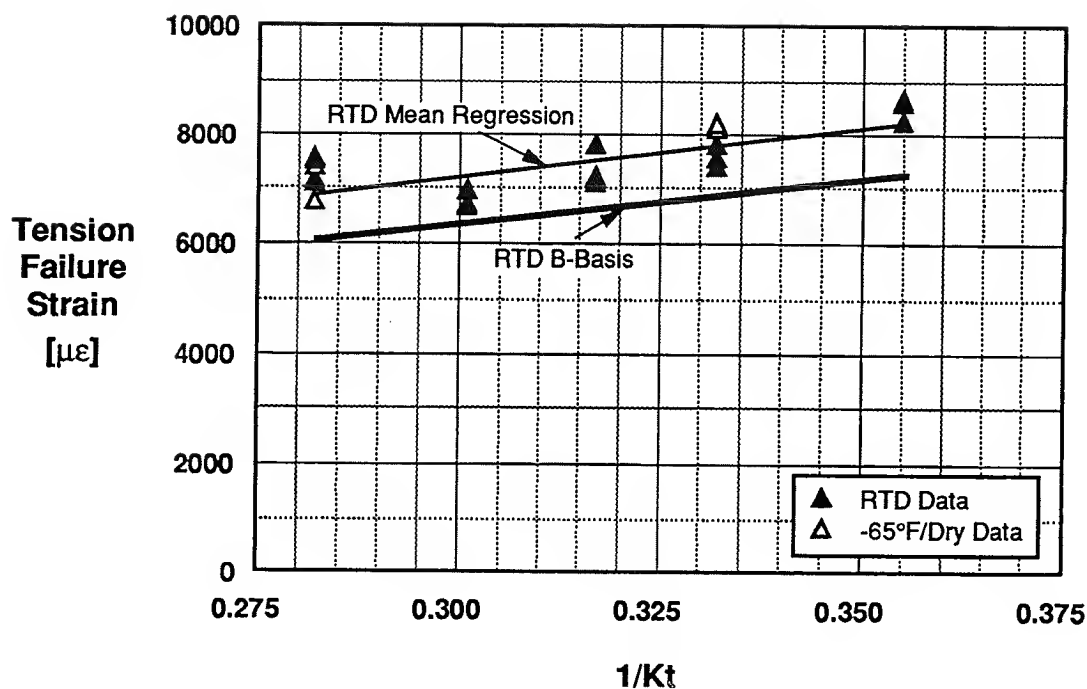


Figure D-10: Filled hole tension failure strains vs. inverse of stress concentration factor.

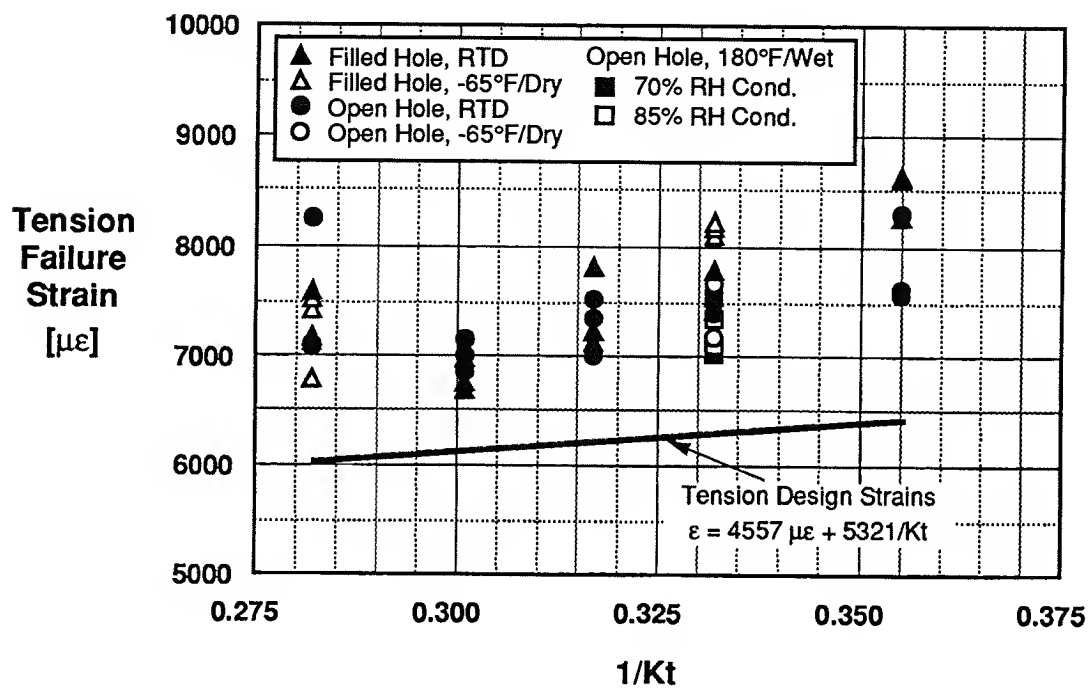


Figure D-11: Filled and open hole tension data versus tension allowable strain.

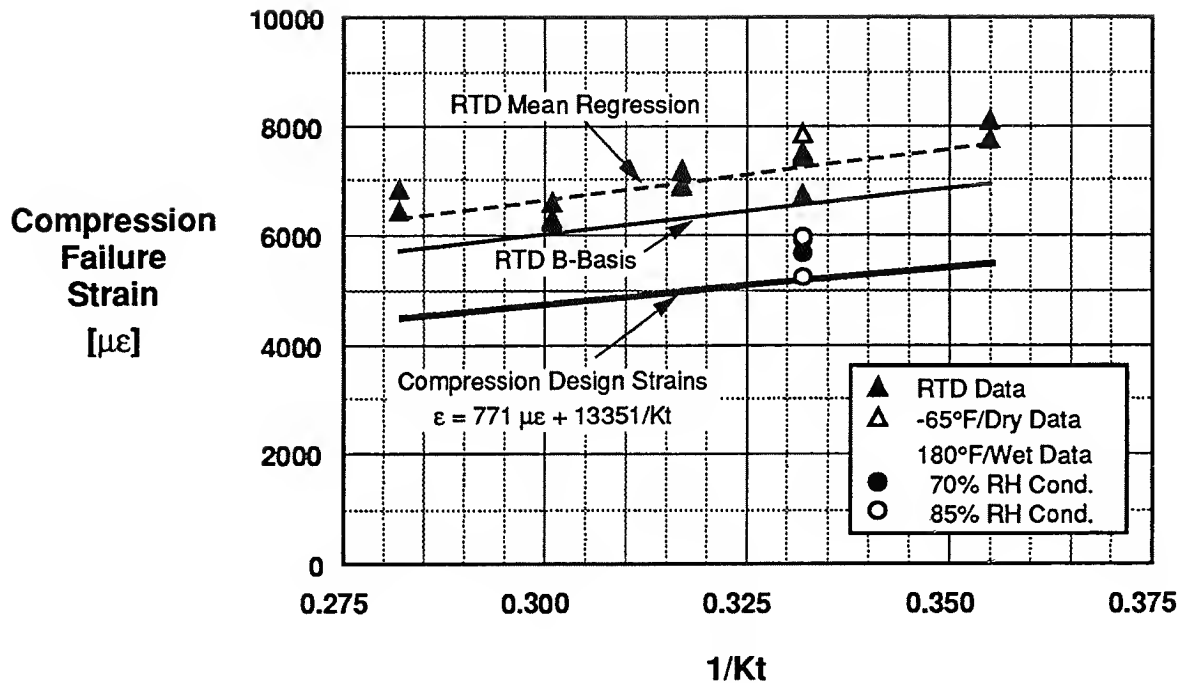


Figure D-12: Open hole failure strains vs. inverse of stress concentration factor and compression allowable strain.

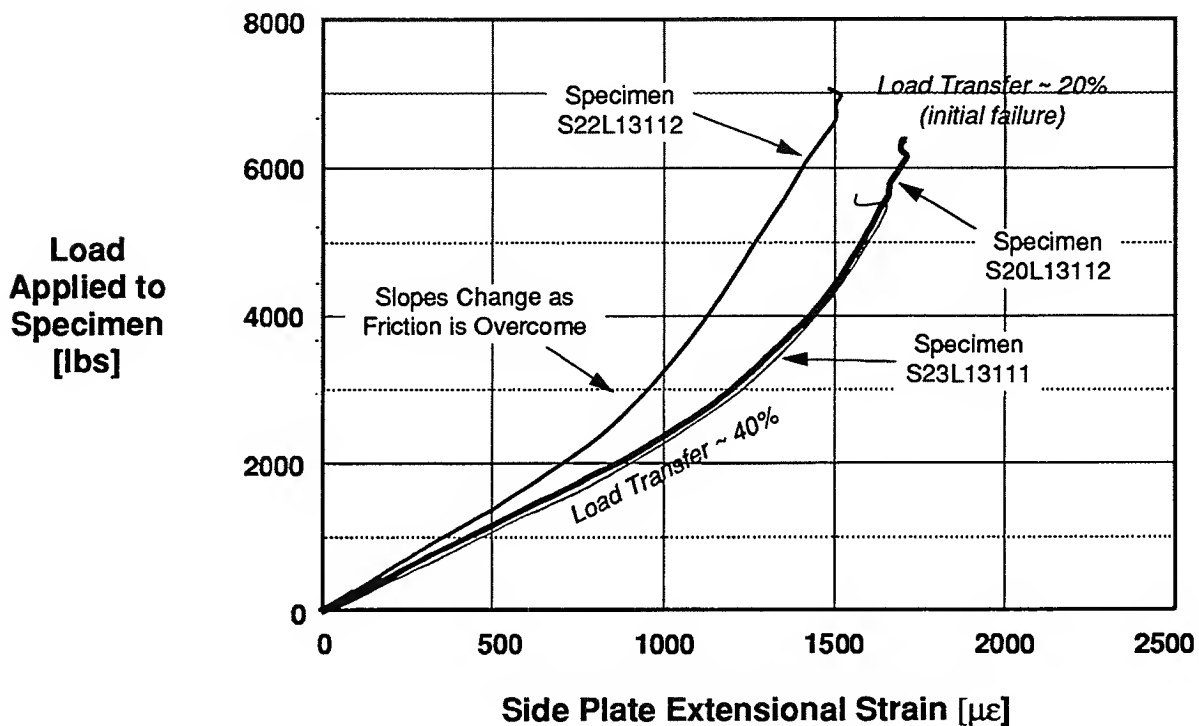


Figure D-13: Comparison of typical load plate strains vs. load applied for low load transfer specimens.

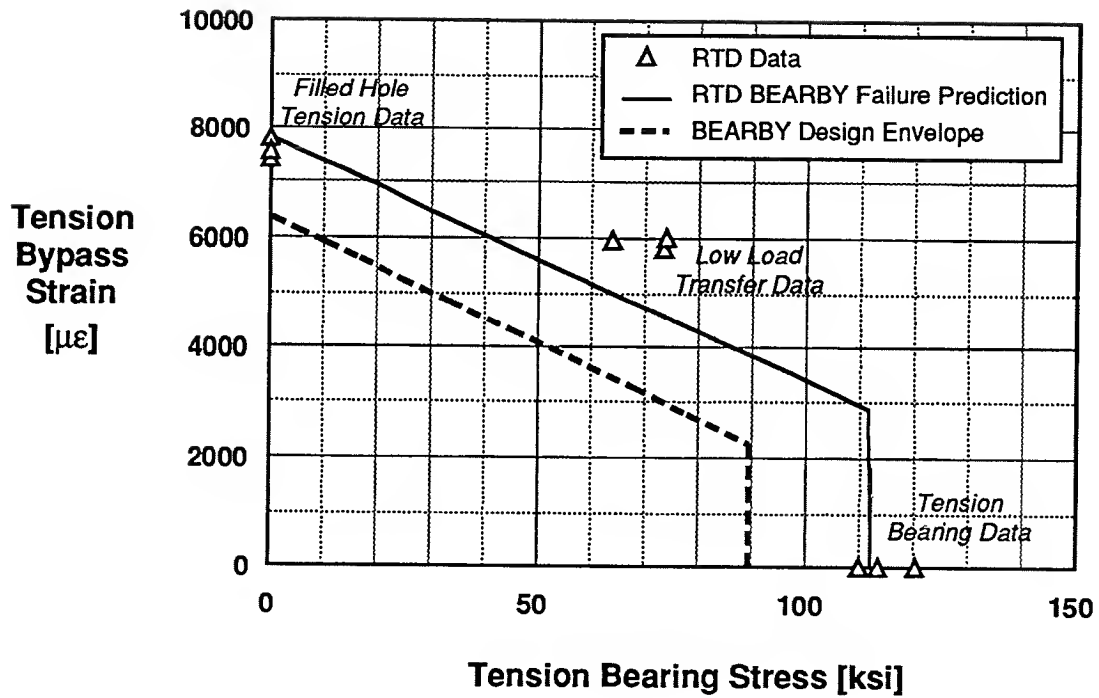


Figure D-14: Bearing-bypass test data, failure predictions and design envelope for laminate S20.

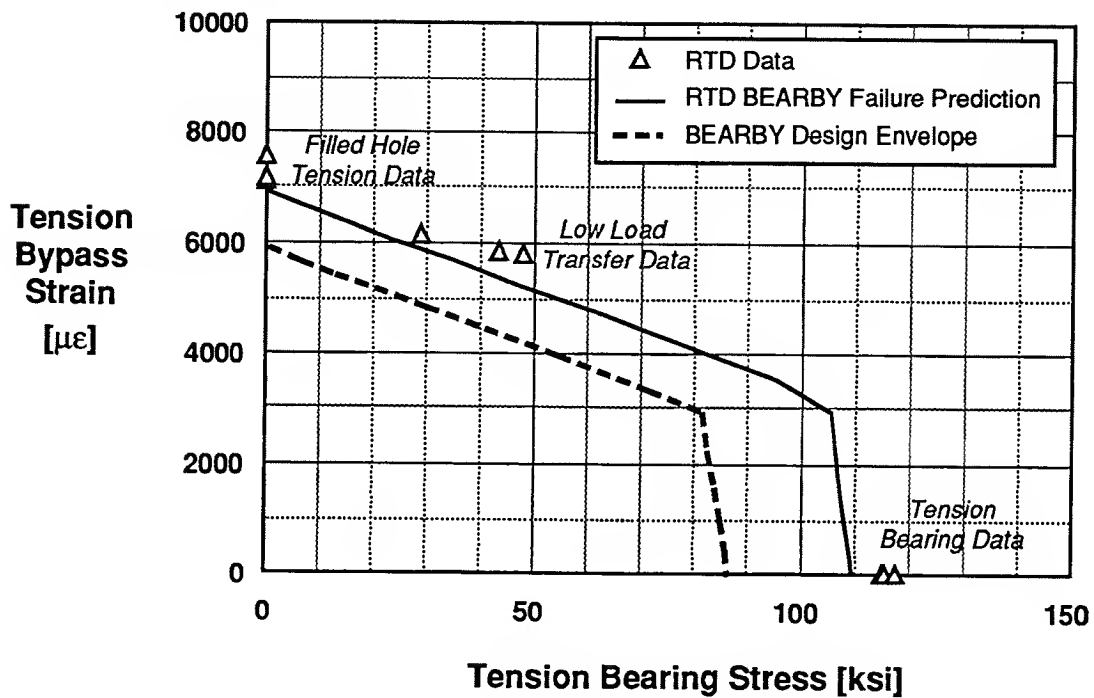


Figure D-15: Bearing-tension bypass test data, failure predictions and design envelope for laminate S22.

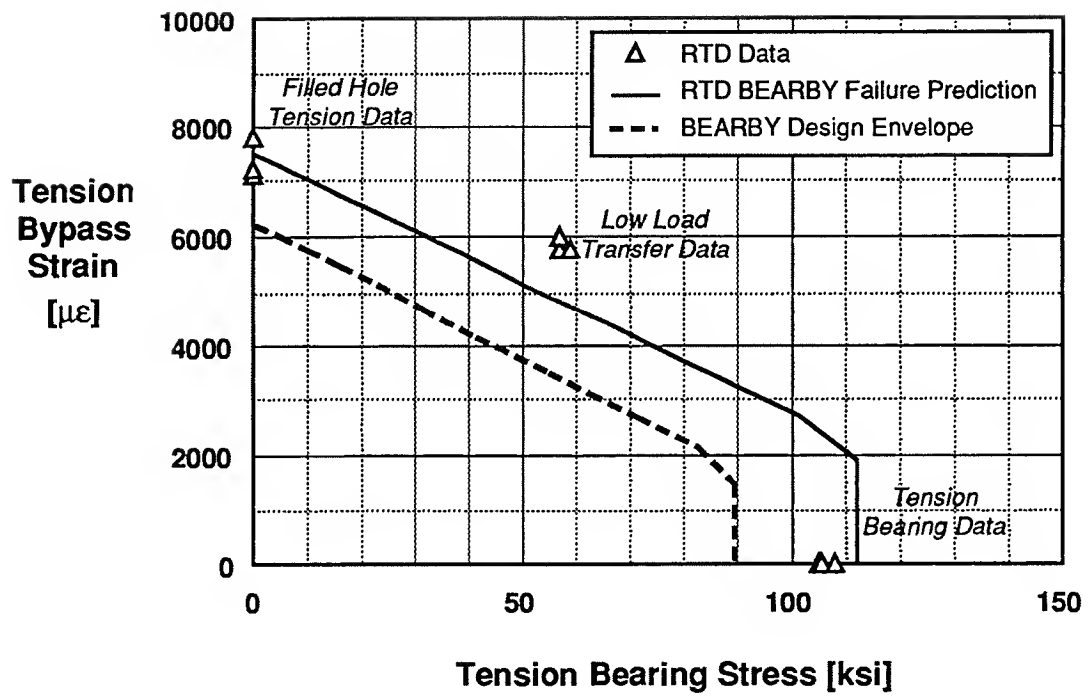


Figure D-16: Bearing-bypass test data, failure predictions and design envelope for laminate S23.

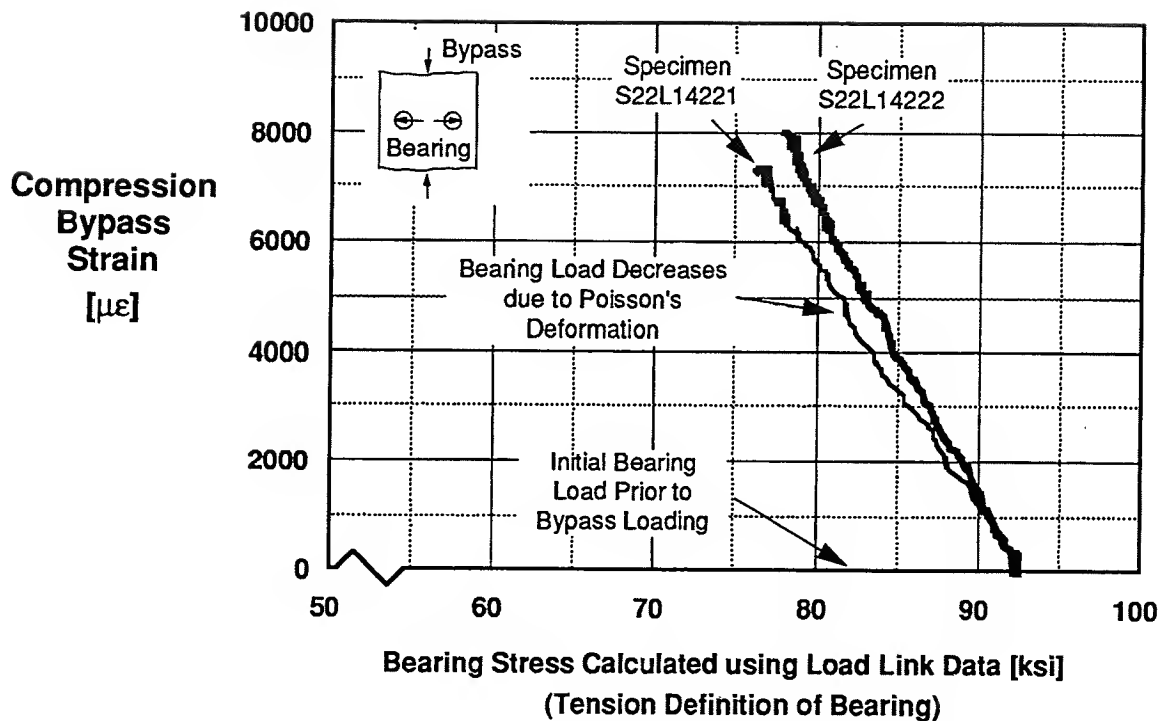


Figure D-17: Typical transverse bearing stress vs. applied bypass strain data obtained using instrumented load links.

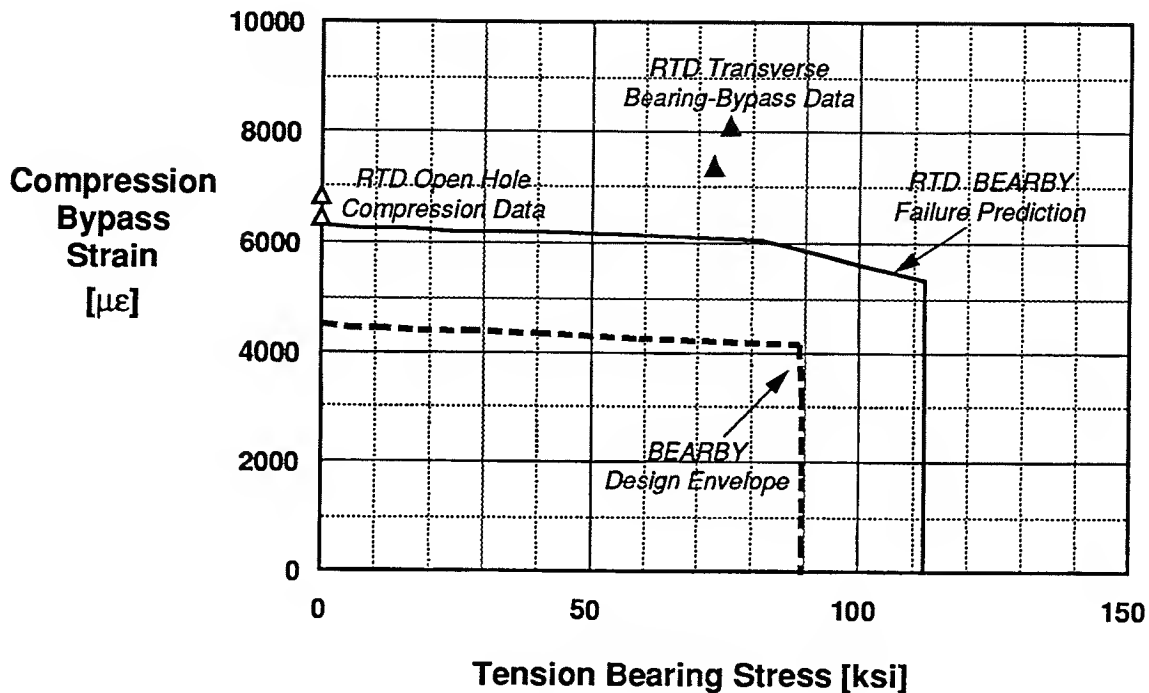


Figure D-18: Comparison of transverse bearing-compression bypass test data with open hole compression data, failure predictions and design envelope for laminate S22. Analysis predictions are based upon open hole compression bypass data.

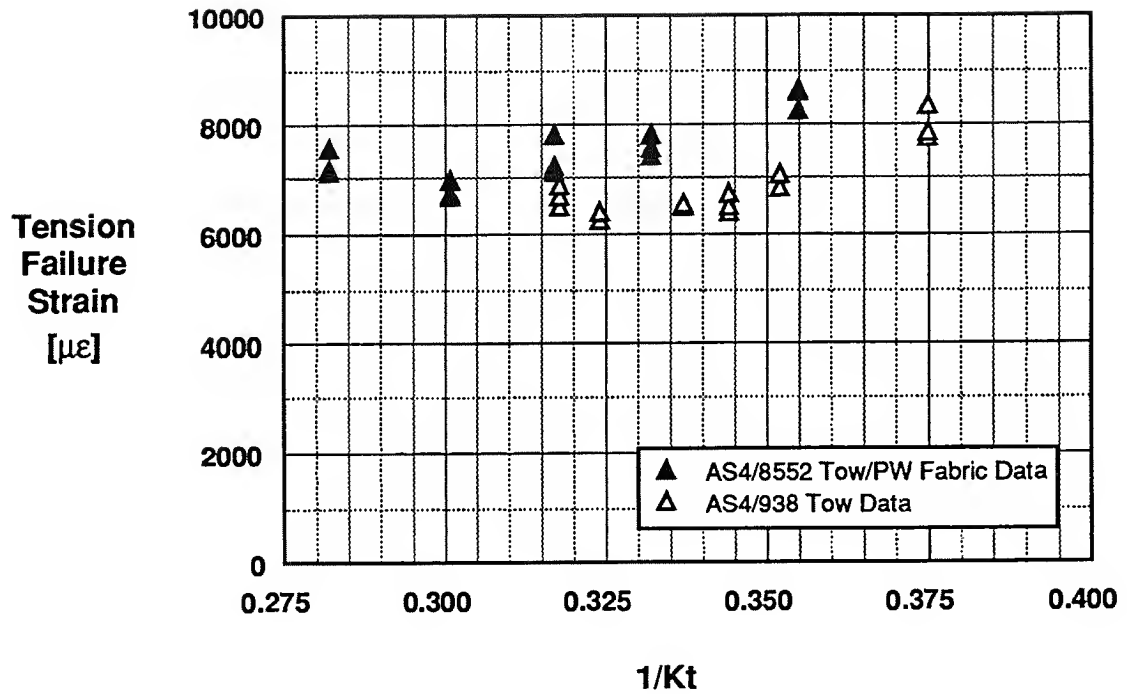


Figure D-19: Comparison of filled hole tension RTD failure strains for AS4/8552 tow/PW fabric hybrid laminates (MDOC keel & side panels) and AS4/938 tow laminates (ATCAS crown panel).

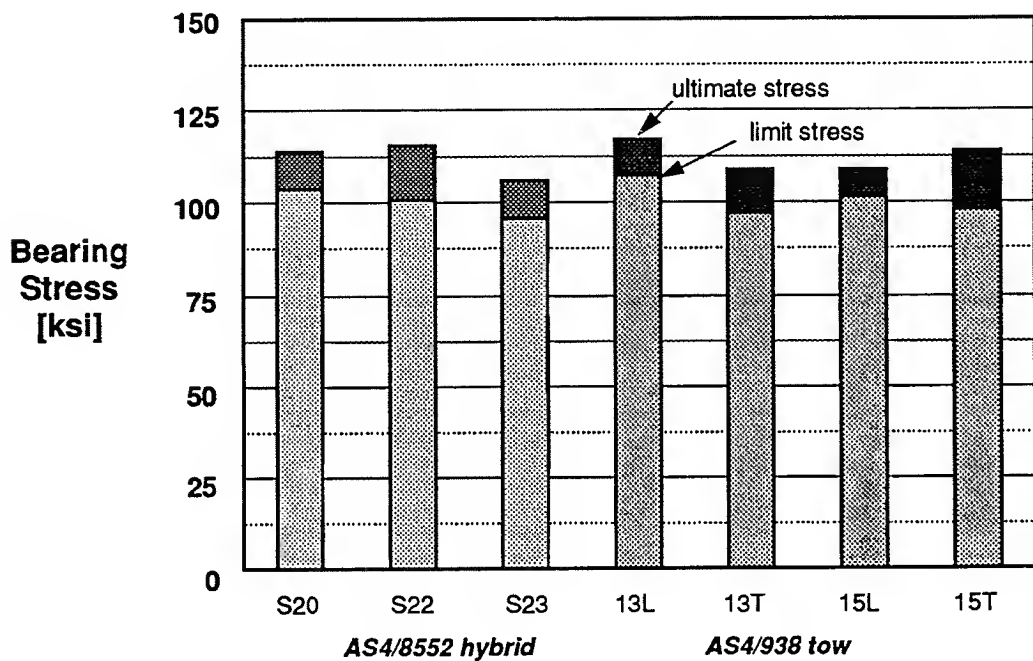


Figure D-20: Comparison of bearing strengths for AS4/8552 hybrid (MDOC keel & side panels) and AS4/938 tow (ATCAS crown panel) laminates.

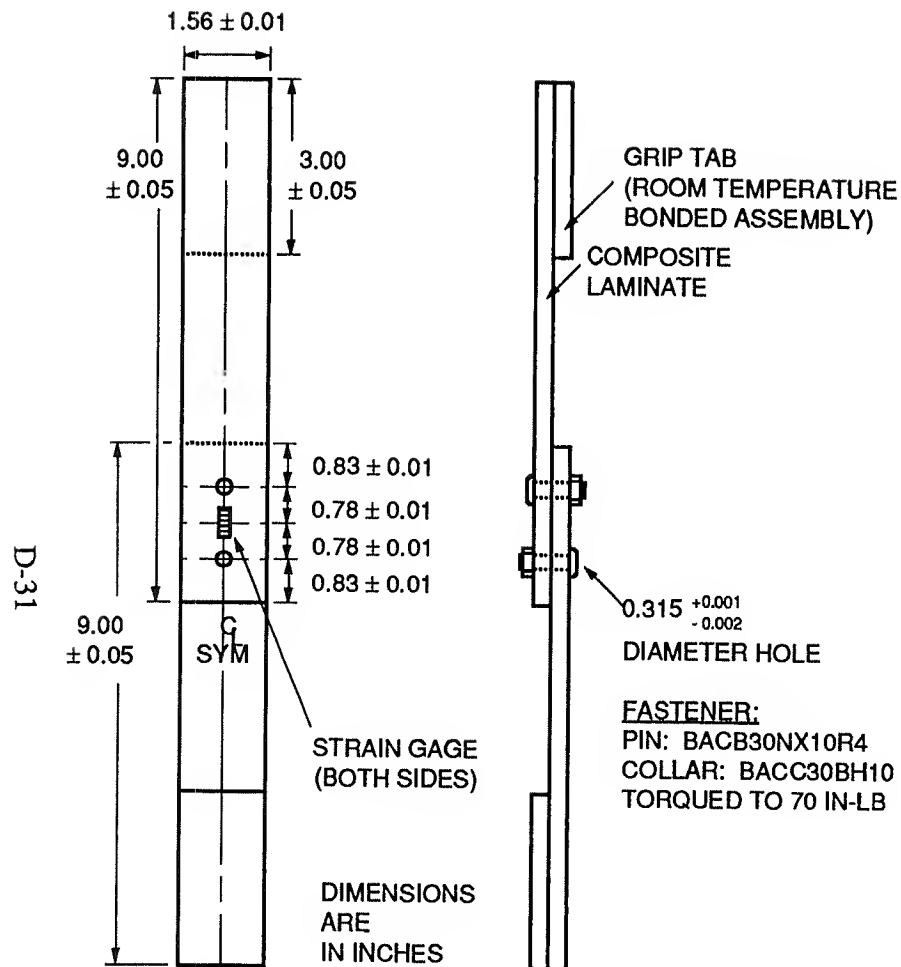


Figure D-21: Baseline 50% load transfer joint for spacer evaluation.

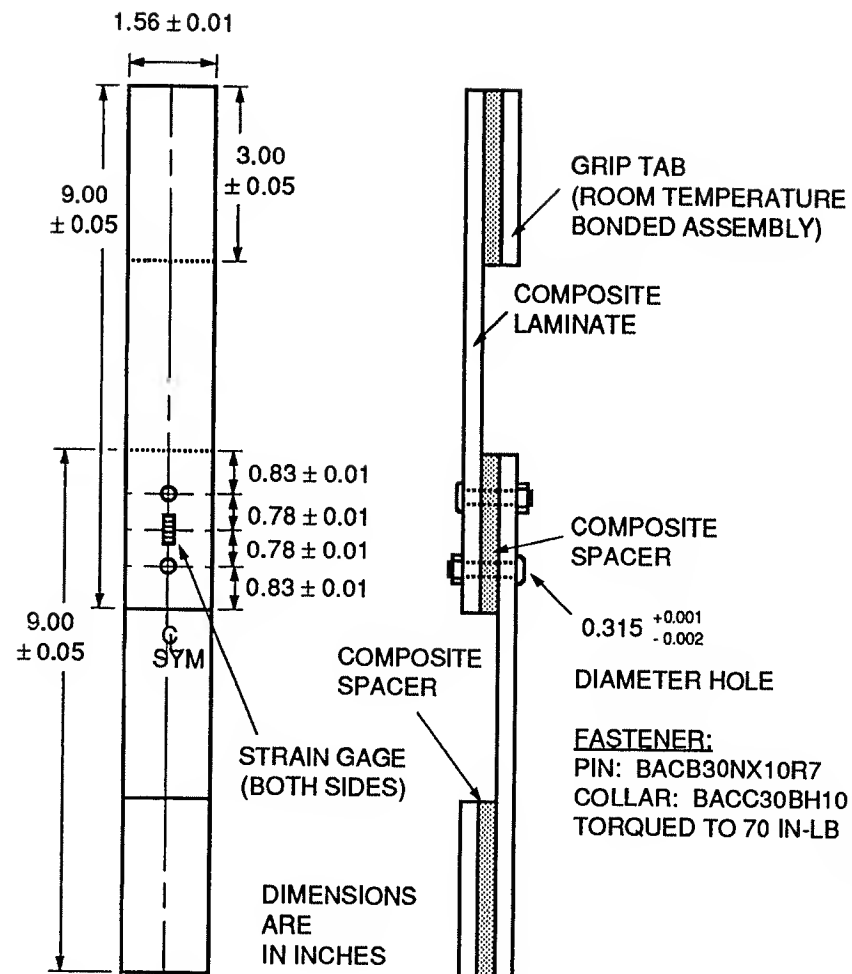


Figure D-22: 50% load transfer joint with structural spacer.

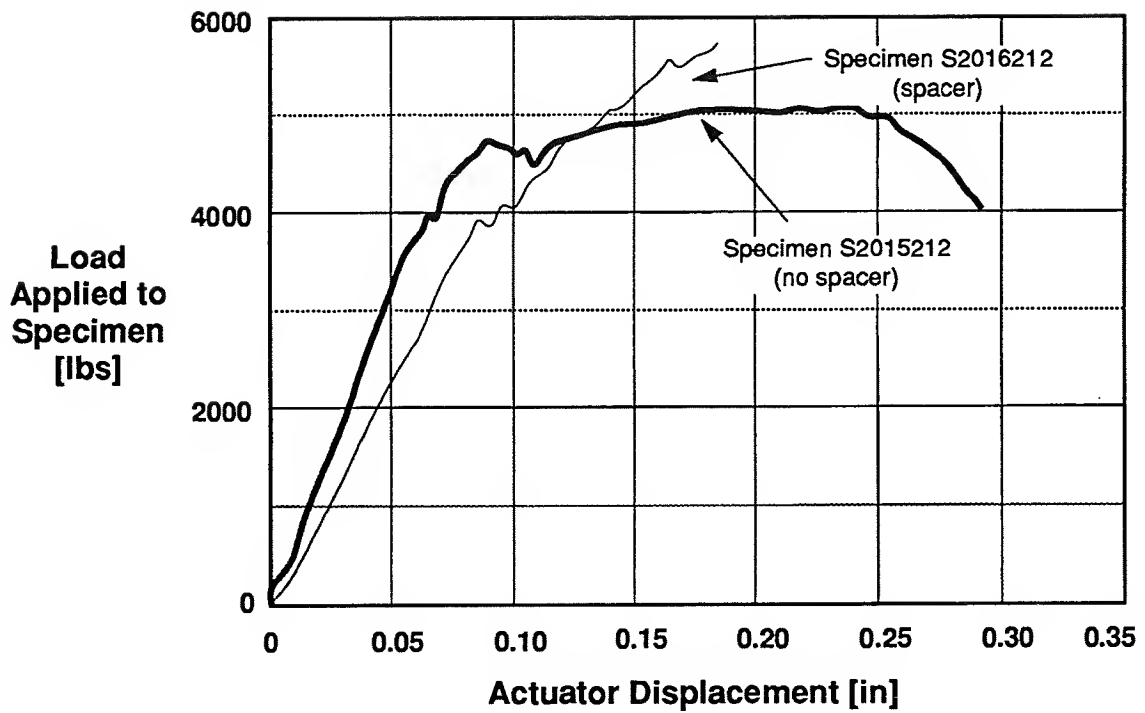


Figure D-23: Comparison of actuator displacement vs. load measurements for specimens with and without spacers.

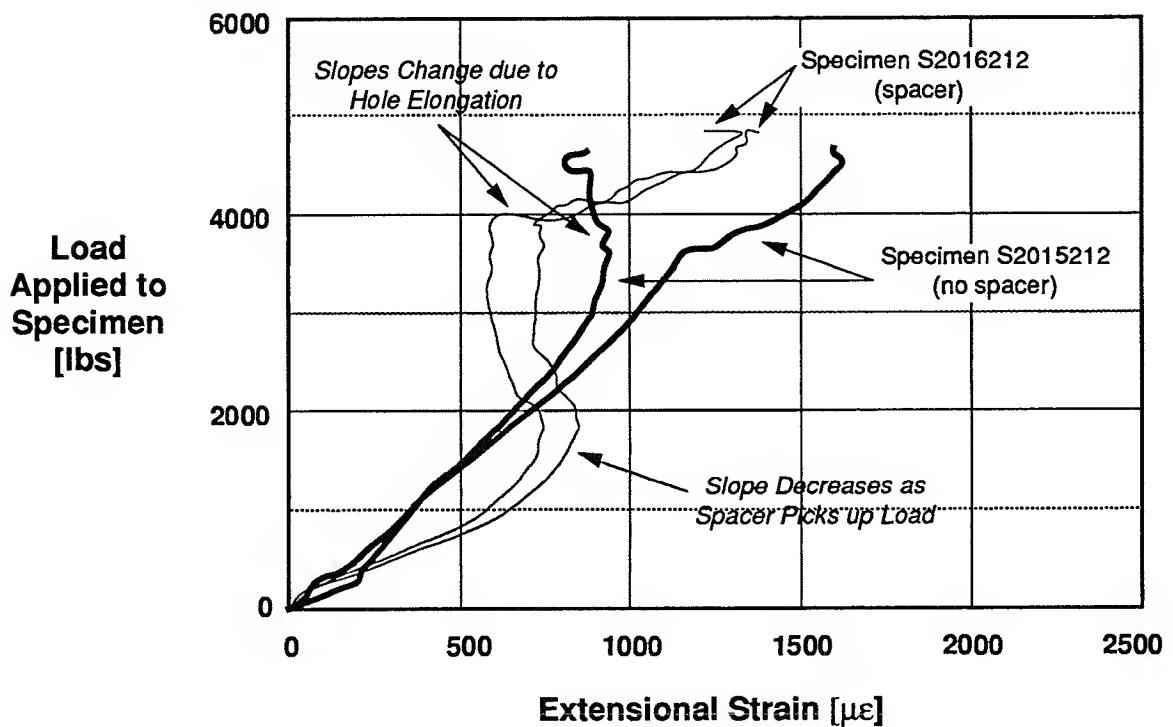


Figure D-24: Comparison of back-to-back strain gage readings strains vs. load specimens with and without spacers.

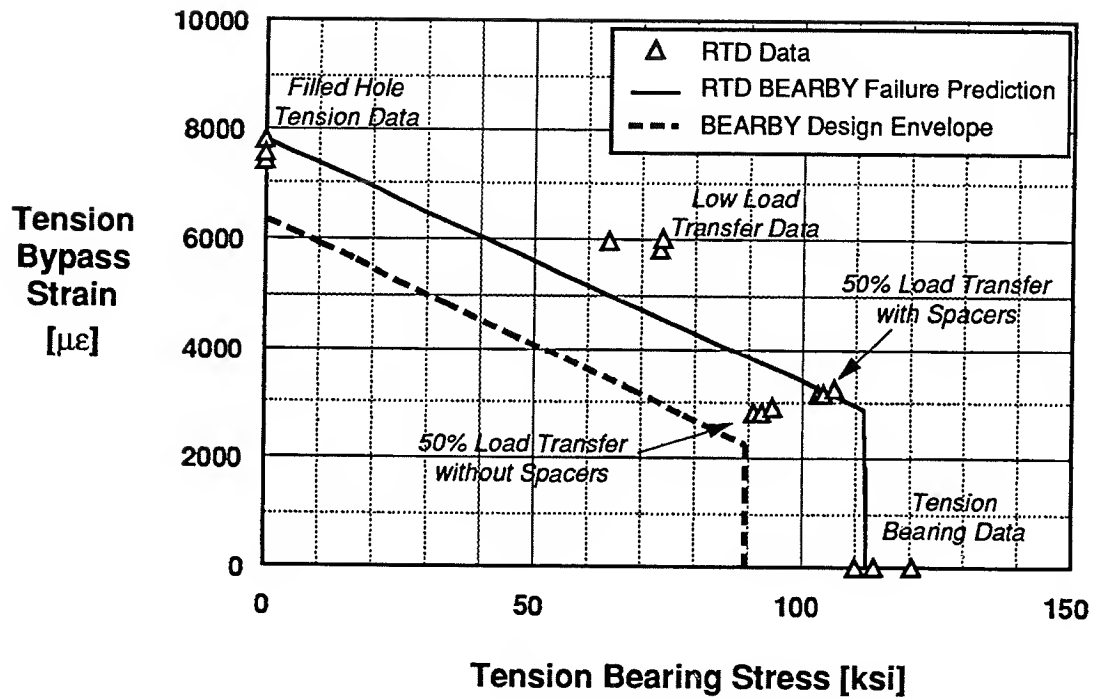


Figure D-25: Comparison of data for joint spacer evaluation specimens with other bearing-bypass data and predictions for laminate S20. 50% load transfer data is for 0.315 inch diameter fasteners.

APPENDIX E

MDOC Sandwich Panel Closeout Evaluation

Introduction

This report documents the results obtained in an evaluation of design concepts for sandwich panel edge closeouts performed under the MDOC program. The report is divided in two sections; the first section documents results obtained for tension and compression tests of sandwich beams tapered locally in thickness, while the second presents findings obtained in an evaluation of the bearing properties of sandwich panel edgebands utilizing open celled braided closeouts to react fastener clamp-up loads. The analysis presented in this report is based upon the data contained in a project summary written by Intec [E-1].

Properties of Sandwich Beams with Locally Tapered Core

The first phase of this evaluation examined the load-deflection behavior and strength of sandwich beams locally tapered in thickness. Six tension and eight compression tests were performed in room temperature dry (RTD) conditions. Two types of locally tapered configurations were examined, one with a solid laminate plug in the tapered, or ramped, region and another with honeycomb core in the tapered region.

The objectives of this set of tests were as follows:

- 1) Examine failure modes associated with locally ramped sandwich structure.
- 2) Examine load distribution in sandwich structure near ramped regions and near solid plugs through comparison of facesheet strains.
- 3) Compare failure modes, stresses, and load distributions for the two configurations.

Specimen Configuration

The test specimen configurations used in the sandwich beam investigation are shown in Figure E-1. These were fabricated from aft core closeout demonstration panels DEMO1 and DEMO2. Facesheets were constructed of AS4/8552 prepreg tape with layup shown in Table E-1. Solid laminate plugs were fabricated using BMS 8-256 plain weave fabric. Nominal laminate properties for the facesheets alone and for the facesheet-solid plug stackups are shown in Table E-2.

Specimens were machined per BAC5004. Holes were drilled and fasteners installed per BAC5063. Glass tabs (0.09 inch thick G-10) were bonded to the specimens to protect the facesheets during hydraulic gripping.

Specimens were instrumented with back-to-back strain gages as shown in Figure E-2. Gages 1-6 were placed in a region where facesheets were supported by honeycomb core. Gages 11-16 were in a region where facesheets were supported by the solid plug. Gages 7-10 were placed at the facesheet radii at the ends of the ramped region, and gages 17 and 18 were placed in the center of the ramped region.

Examination of the specimens after fabrication noted "dimpling" of the bag side facesheets over the unpotted honeycomb core (core cell boundaries were observed on the surface of the

facesheets). Also, the cured thickness of the ramped solid plugs was greater than the thickness of the honeycomb core where they interfaced, resulting in a local through-thickness discontinuity of the bag-side facesheets at those locations.

Test Matrix and Procedure

The matrix of tests performed in this investigation is shown in Table E-3. Specimens were tested in both edgewise tension and compression, under fully clamped end conditions, to evaluate facesheet strains at and around the ramped region.

Specimens were tested to failure using a servo-hydraulic frame under stroke control, at a loading rate corresponding to 0.05 inches crosshead deflection per minute. Load, actuator displacement and strain data were recorded continuously until ultimate failure. When the load carried by the specimen dropped significantly (~10%) during the tests, crosshead displacement was temporarily paused so the specimen could be visually examined for damage. No anti-buckling restraints were utilized in either tension or compression testing.

Static Tension Results

Strain Gage Readings

Typical specimen load-facesheet strain relationships are shown in Figures E-3 through E-6. Extensional and bending strains were calculated as follows:

$$\epsilon_{\text{extensional}} = \frac{(\epsilon_{\text{toolside}} + \epsilon_{\text{bagside}})}{2} \qquad \epsilon_{\text{bending}} = \frac{(\epsilon_{\text{toolside}} - \epsilon_{\text{bagside}})}{2}$$

Positive bending strains shown in Figures E-4 and E-6 indicate the strain magnitude measured in the tool side facesheet was higher than that measured in the bag side facesheet. Extensional and bending strains are relative to the midplane of the specimen local to the gage locations. This implies that bending strains are relative to the midplane of the honeycomb sandwich structure for gages 1 through 8, and relative to the midplane of the plug-facesheet stackup for gages 9-16. It should be noted that the midplane of the plug-facesheet stackup is offset 0.0125 inches from the midplane of the honeycomb sandwich region, due to the difference in ramp depth for bag and tool side facesheets shown in Figure E-1.

Bending and extensional strains were relatively linear until an initial failure, after which bending strain magnitudes increased significantly as the load distribution between the facesheets changed. Specimens loaded in tension were able to carry increased loads after the initial failure, and exhibited several load drops and strain redistributions prior to ultimate failure. For reference, in-plane shear strains measured using rosettes were typically in the 100-300 $\mu\epsilon$ range at initial failure, and were never greater than 700 $\mu\epsilon$ at initial failure.

Prior to the initial failure, strains from gages 7 and 8 were slightly lower than those observed from gages 1 and 2, as flexure in the facesheets at the end of the ramp created local compression

strains. Strains from gages 9 and 10 were equivalent to those from gages 11 and 12 for panel DEMO1 specimens (solid plugs in the ramped region), and were also initially equivalent for all specimens from panel DEMO2 (ramped honeycomb core). At approximately 800-1000 lb/in applied load, DEMO2 strains from gages 9 and 10 were observed to increase until the load-strain relationship was similar to that of gages 1 and 2. It appears that some local failure occurred in the bondline between the facesheets and the solid plug at this load level, and load began to shear from the solid plug into the facesheets farther from the beginning of the ramp. Data from gages 9 and 10 also exhibited nonlinearity of extensional and bending strains prior to initial failure, indicating the local bondline damage was growing.

Comparisons of bag-side and tool-side facesheet strains at initial failure are shown in Figure E-7. Specimens with solid plugs in the ramped region typically demonstrated higher strains in the bag side facesheet due to bending associated with thickness mismatch at the plug-core interface.

Laminate extensional moduli calculated using load-strain data are compared with predicted nominal moduli in Table E-4. Facesheet moduli were compared using extensional strains calculated with data from gages 1 and 2, while moduli for the facesheet-plug stackup were compared using data from gages 11 and 12. At initial failure load, mean facesheet modulus was found to be 76% of nominal modulus for specimens with solid plugs in the ramped regions and 81% of nominal modulus for specimens with ramped honeycomb core. Mean facesheet-plug stackup modulus was 82% of nominal modulus for specimens with ramped solid plugs and 71% of nominal modulus for specimens with ramped honeycomb core. Examination of the specimens indicated local discontinuities of $+45^\circ$ and 0° laminate plies against the honeycomb core ("dimples") in the region of gages 1 and 2. Laminated plate analysis indicated that the observed reductions in modulus were too great to be caused by this distortion alone.

Failure Modes

All tension specimens exhibited ultimate failure through facesheet failure in the radii at both the thick and thin ends of the ramped region, with significant disbonding along the facesheet-solid plug and facesheet-honeycomb core interfaces. Such disbonding was responsible for the numerous load drops and redistributions observed, as this failure mode was noncatastrophic. Specimens from panel DEMO1 also exhibited interlaminar shear failures in the solid plug, between the continuous and discontinuous ply packs in the ramped region. It appears this failure may have precipitated the ultimate facesheet failure by causing unequal facesheet loading and increasing local bending strains.

Failure Stresses

Facesheet stresses at which initial and ultimate tension failure occurred are shown in Table E-5 for individual specimens. Statistical data is shown in Table E-6. Mean initial failure stress for DEMO1 specimens was 69% higher than that of DEMO2 specimens, while ultimate failure stress was 32% higher for DEMO1 specimens than that of DEMO2 specimens. However, the variability associated with both initial and final failure of the DEMO1 specimens was much greater than that of DEMO2 specimens. Therefore, the tensile capability of the DEMO1 configuration may be more sensitive to manufacturing anomalies than that of the DEMO2 configuration. Specimen DEMO1-33 exhibited initial and ultimate failure at load levels similar

to those of the DEMO2 specimens, and thus the modes of failure for this specimen may be similar to those of DEMO2 specimens.

As shown in Figure E-8, DEMO1 specimens demonstrated lower surface ply strains in the ramped regions than did DEMO2 specimens. This results in lower deflections at the radii at the ends of the ramps, and thus produces lower peel and compression stresses in the bondlines at these locations. This is believed to be the primary reason for the higher strengths achieved with the DEMO1 specimens.

The best data available for comparison of ramped specimen facesheet failure and notched laminate performance (used in developing laminate design allowables) was obtained from the MDOC keel and side panel material database [E-2]. As shown in Table E-7, laminates of similar configuration as DEMO1 and DEMO2 facesheets (with fabric outer plies) typically exhibit filled hole tension failure stresses in the 55-65 ksi range. Based upon mean initial failure data and a 1.5 ultimate load factor, facesheet ultimate strength would occur at 70-85% of mean filled hole tension failure stress for the DEMO1 configuration, compared to 40-55% for the DEMO2 configuration. Thus, damage created through modes associated with facesheet ramping (such as disbonding and interlaminar shear) prevented the facesheets from attaining typical in-plane design stresses/strains. Current composite allowables methodologies, which account for stress concentrations about fastener holes, defects and damage with respect to in-plane failure, apparently would not conservatively account for the out-of-plane failure modes which influenced ultimate facesheet failure in these specimens.

Static Compression Results

Strain Gage Readings

Typical load-strain relationships are shown for specimen extension and bending in Figures E-9 through E-12. Extension and bending strains definitions are the same as in the tension loading case. Specimens loaded in compression exhibited linear load-strain behavior until initial failure, after which the load dropped significantly and never again approached the initial failure load. In-plane shear strains measured using rosettes were typically in the 100-300 $\mu\epsilon$ range at initial failure, and were never greater than 400 $\mu\epsilon$ at initial failure.

As was the case under tension loading, strains from gages 7 and 8 were slightly lower in magnitude than those observed from gages 1 and 2 due to local flexure in the facesheets at the end of the ramp. Strains from gages 17 and 18 were equivalent to those from gages 9 and 10 for DEMO1 specimens, but were closer to strains from gages 7 and 8 for DEMO2 specimens. Strains from gages 9 and 10 were slightly higher than those from gages 11 and 12 for the DEMO2 specimens, but did not exhibit the discontinuity observed at low load levels in the tension specimens. As shown in Figure E-7, relationships between bag and tool-side facesheet strains were similar to those observed in tension, although DEMO2 specimens exhibited greater strain magnitudes in the tool side facesheet along the entire length of the ramp.

Laminate extensional moduli calculated using load-strain data are compared with predicted nominal moduli in Table E-4; these were calculated in the same manner as the case of tension loading. At initial failure load, mean facesheet modulus (calculated using data from gages 1 and

2) was found to be 76% of nominal modulus for specimens with ramped solid plug and 75% of nominal modulus for specimens with ramped honeycomb core. Mean facesheet-plug modulus (calculated using data from gages 11 and 12) was 83% of nominal modulus for specimens with ramped solid plugs and 70% of nominal modulus for specimens with ramped honeycomb core.

Failure Modes

All compression specimens exhibited ultimate failure through disbonding along the facesheet-solid plug and facesheet-honeycomb core interfaces. Interlaminar failures in the facesheets were also exhibited. Once facesheets were disbanded, specimens could not be returned to the load level at which initiation of such failure occurred.

Failure Stresses

Facesheet stresses at which ultimate compression failure occurred are shown in Table E-8, with statistics compiled in Table E-9. Mean failure stress for DEMO1 specimens was 27% higher than that of DEMO2 specimens. As was the case in tension, the variability associated with failure of the DEMO1 specimens was greater than that of DEMO2 specimens. Therefore, the compression capability of the DEMO1 configuration may be more sensitive to manufacturing anomalies than that of the DEMO2 configuration.

As shown in Figure E-8, DEMO1 specimens demonstrated lower surface ply strains in the ramped regions than did DEMO2 specimens, and thus exhibited smaller deflections at the radii at the ends of the ramps. As was the case under tension loading, this is believed to be the primary reason for the higher strengths achieved with the DEMO1 specimens.

Ramped specimen failure is compared to notched laminate data in Table E-10. Laminates of similar configuration as DEMO1 and DEMO2 facesheets (with fabric outer plies) typically exhibit RTD open hole compression failure stresses in the 52-60 ksi range. Based upon ultimate compression failure, facesheet ultimate strength would occur at 45-55% of mean open hole compression failure stress for the DEMO1 configuration compared to 35-45% for the DEMO2 configuration. As was the case under tension loading, damage created through modes associated facesheet ramping prevented the facesheets from attaining typical in-plane design stresses/strains.

Discussion of Results

Tension Performance

Under tension loading, initial failures were observed as noncatastrophic disbands at the facesheet- honeycomb core/solid plug interfaces, and were manifested as load drops. Specimens ultimately failed through facesheet fracture initiated by cracking of the innermost ply near the disbanded areas. Ultimate failure of specimens with solid plugs in the ramped region appears to have been initiated by interlaminar failure in the ramped region of the solid plugs.

Mean initial and ultimate failure stresses were significantly higher for specimens with solid plugs in the ramped regions; however, the data exhibited high coefficients of variation, as local failures similar to those observed in the specimens with honeycomb core ramps were observed.

It is believed that this variance was created by thickness mismatch between the plugs and the honeycomb core. If this mismatch can be minimized, it is believed the DEMO1 configuration can provide significantly superior performance compared to the DEMO2 configuration, since facesheet strains and deflections are lowered in the ramped region due to the presence of the load-carrying solid plug.

Facesheet failure stresses (based on initial failure and a 1.5 load factor) were found to be on the order of 75-85% of typical notched laminate tension failure stresses obtained in RTD environmental conditions for the DEMO1 configuration and 40-55% for the DEMO2 configuration. Current composite allowables methodologies apparently would not conservatively account for the out-of-plane failure modes which influenced ultimate facesheet failure in these specimens.

Compression Performance

Under compression loading, failures were observed as catastrophic disbonds at the facesheet-honeycomb core/solid plug interfaces. Mean failure stresses were higher for specimens with solid plugs in the ramped regions; however, the data exhibited higher coefficients of variation. Again, this variance was probably created by thickness mismatch between the plugs and the honeycomb core. As was the case for tension loading, it is believed the DEMO1 configuration is superior to the DEMO2 configuration due to the lower facesheet strains and deflections in the ramped region.

Facesheet failure stresses were found to be on the order of 45-55% of typical notched laminate compression failure stresses obtained in RTD environmental conditions for the DEMO1 configuration and 35-45% for the DEMO2 configuration. Current composite allowables methodologies apparently would not conservatively account for the out-of-plane failure modes which influenced ultimate facesheet failure in these specimens.

Bearing Properties of Composite Facesheets Supported by Open Celled Braided Closeouts

The second phase of this evaluation examined the load-deflection behavior and bearing strength of sandwich panel edgebands utilizing open celled braided closeouts to support the facesheets. In this manner, the facesheets remain flat at the panel edge as the closeouts are equivalent in thickness to the honeycomb core in the rest of the panel. The closeouts contribute to edgeband bearing strength by providing through-thickness clamp-up loads in the facesheet when fasteners are installed, as well as by carrying bearing loads themselves.

Six static and six $R = +0.1$ fatigue bearing tests were performed in room temperature dry (RTD) conditions. Tests were performed utilizing both composite and steel load introduction plates to impart bearing loads to the edgebands.

The objectives of this set of tests were as follows:

- 1) Examine bearing failure modes of edgebands utilizing the braided closeout concept.
- 2) Compare static and fatigue strengths obtained with typical laminate bearing strengths.

Specimen Configuration

The test specimen configurations used in the edgeband investigation are shown in Figure E-13. These were fabricated from demonstration panel AK25. Facesheets were constructed of 12K AS4/8552 prepreg tow, using a band head fiber placement machine, with layup shown in Table E-1. Closeouts were braided AS4 fiber, resin transfer molded with RSL 1895 resin. Load introduction plates were either composite, of the same layup as the AK25 facesheets, or 4130 steel. Nominal laminate properties for the facesheets and closeouts are shown in Table E-2.

Specimens were machined per BAC5004. Holes were drilled and fasteners installed per BAC5063. Fasteners were installed at 60 in-lb torque, or 40% of normal installation torque for a 0.3125 inch diameter titanium fastener. This torque level simulates the reduction in fastener clampup over a lifetime of service due to relaxation of laminate through-the-thickness stiffness, as estimated in work by Crews and Shivakumar [E-3, E-4]. Low fastener torque has previously been demonstrated to be critical for bearing-dominated load cases [E-5].

Composite load plates were match assembled to the closeout specimens to insure that the direction of panel curvature remained the same. Spacer shims (for installation in hydraulic grips) were made by filling scrap closeout pieces with high temperature potting compound (Epocast 1636-A). When steel load plates were used, the plates and specimens were assembled using Hysol 9394 epoxy to match the panel curvature. Flat spacer shims fabricated from A2 tool steel were machined to the nominal thickness of the closeouts with facesheets and used for installation in hydraulic grips.

Test Matrix and Procedure

The matrix of tests performed in this investigation is shown in Table E-3. Specimens were tested in both static and $R = +0.1$ fatigue bearing, utilizing both composite and steel load introduction plates. The results obtained using steel plates provide greater insight into failure modes and strengths of the edgebands with braided closeouts by themselves, while the results with composite plates provide information on the comparative performance of the edgeband facesheets alone versus that of the facesheet-closeout combination.

Static specimens were tested to failure using a servo-hydraulic frame under stroke control, in tension at a loading rate corresponding to 0.05 inches crosshead deflection per minute. Load and actuator displacement data were recorded continuously until ultimate failure. Data acquired included the maximum load achieved, the 2% hole diameter offset load, and load versus deflection plots.

Fatigue tests were performed under $R = +0.1$ (tension-tension) loading, at a frequency of 5 Hz when composite load plates were used and at 10 Hz when steel load plates were used. This maintained specimen temperature below 120°F. Load-deflection hysteresis loops were obtained as shown in Figure E-14, before fatigue cycling and after 10,000, 20,000, 30,000, 40,000, 50,000, 75,000, 100,000, 150,000, 200,000, and every 100,000 cycles thereafter, and at 0.1" hole elongation or runout. During the measurement of the hysteresis loop, the maximum load achieved and the deflection each time zero load was crossed were recorded. This permitted measurement of joint hole elongation and stiffness.

Criteria for failure were as follows:

- 1) Inability to carry prescribed load.
- 2) 0.1" hole deformation (32% of initial hole diameter) based on load deflection plots. Hole elongation was measured by subtracting the initial hole clearance from the hole clearance after N cycles.

No residual strength tests were performed for specimens at 1.0 million cycles, after taking a final hysteresis loop.

Static Results

Failure Modes

All static specimens failed in a bearing-dominated mode, with hole elongation observed in both the facesheets and in the closeouts. Significant brooming was observed on the interior surfaces of the braided closeouts, similar to that observed in pin bearing tests where no through-thickness restraint is applied. Hole deformation was equivalent on both facesheet surfaces, indicating load distribution was fairly equivalent throughout the tests. For specimens utilizing composite load introduction plates, significant hole elongation and brooming in front of the fastener head and collar were observed. No geometry-induced ultimate failures were observed.

Failure Stresses

Static bearing strengths observed in testing of the edgeband specimens are shown in Table E-11, with statistical analysis provided in Table E-12. Bearing strengths presented for calculations using both the nominal thickness of the facesheets and closeouts, as well as using the facesheet thickness alone. This is provided for additional insight when comparing bearing stresses at initial and final failure in the edgeband specimens with typical laminate data.

Examination of the mean data demonstrate that 2% offset bearing stress and ultimate bearing stress were 36% and 12% higher using steel in lieu of composite load plates, respectively. These differences were caused by the reduced fastener flexure observed utilizing steel load plates; when composite load plates were used, fastener flexure was greater due to bearing deformation of the load plates. Mean 2% percent offset bearing stress was 87% of mean ultimate bearing stress using steel load plates.

Comparative static bearing data are shown in Table E-13 for laminates tested with 40% nominal fastener torque in RTD conditions. AS4/8552 tow data were obtained during the MDOC keel & side panel database study [E-2], while AS4/938 tow and AS4/1895 braid results are from the ATCAS crown panel database study [E-6, E-7]. 0.3125 inch diameter hole strengths were estimated from 0.25 inch hole data using a 0.944 correction factor, per the V-22 Analysis Guide [E-8]. Edgeband bearing strengths are approximately 65-70% of those obtained for AS4/938 and AS4/8552 tow/hybrid laminates, but are roughly equivalent to those previously obtained for AS4/1895 braided laminates. Thus, the effective bearing strength exhibited by the combined facesheets and closeouts is lower than is typical for conventional graphite/epoxy composites.

It is hypothesized that edgeband bearing strengths were lower than typical laminate bearing strengths because of the relatively lower through-thickness clamp-up loads obtained when using the closeout design configuration. Also, the contribution of the braided closeout to edgeband bearing strength is limited, due to the relatively low bearing strengths characteristic of such architectures [E-6]. However, it is notable that if edgeband bearing strengths are calculated assuming the facesheet carries bearing loads alone, the effective bearing strength is nearly equivalent to that exhibited by typical laminates. Thus, the reduction in facesheet bearing capability caused by reduced clamp-up is offset by the additional bearing capability the closeouts provide.

Fatigue Results

Hole Elongation and Joint Stiffness Measurements

Hole elongation and joint stiffness measurements calculated using load-deflection plots are shown in Figures E-15 and E-16. The hole elongation data demonstrate decreasing levels of elongation for a given number of cycles. It is notable that after approximately 2% hole elongation is achieved, further elongation proceeds rapidly (based upon a logarithmic scale), until elongation greater than 32% (per the test stoppage criterion) is passed. The joint stiffness data indicate that for relatively high maximum bearing stresses (≥ 49 ksi), joint stiffness declines continuously and falls off rapidly once the fastener holes begin elongating. For lower bearing stress levels, joint stiffness actually increases initially but then falls off once the holes elongate. This may be caused by some slight elongation of the holes, which results in a more even load distribution between the fasteners.

Failure Modes

Fatigue specimens failed in a bearing-dominated mode, with hole elongation observed in both the facesheets and in the closeouts, in a similar fashion as was exhibited in static testing. Significant brooming of the braided closeouts was observed. The only geometry-induced ultimate failure mode observed was shear-out, caused by elongation of the fastener holes.

Failure Stresses

R = +0.1 fatigue S-N data (based upon bearing stresses calculated using the nominal thickness of the facesheets and closeouts) are shown in Figure E-17, along with static data at 10^0 cycles. Runouts to 10^6 cycles were observed for specimens under maximum bearing stresses of less than 47 ksi, as calculated using nominal thickness of the facesheets and closeouts. Data are plotted for hole elongation $\leq 3\%$, as well as for hole elongation $\geq 32\%$ per the test stoppage criterion. S-N data at test stoppage are also shown in Table E-14. Examination of the data indicates that runout to 10^6 cycles should occur at approximately 43 ksi bearing stress in the facesheets and closeouts. There also appears to be a roughly linear relationship (on a logarithmic scale) between fatigue cycles and maximum bearing stress levels at which rapid hole elongation occurs.

Comparative R = +0.1 bearing fatigue data are shown in Figure E-18 for laminates tested with 40% nominal fastener torque in RTD conditions. The comparative AS4/3501-6 plain weave fabric data were obtained during the V-22 FSD allowables program [E-9]. 0.3125 inch diameter

hole strengths were estimated from 0.25 inch hole data using a 0.944 correction factor, as in the static case. Edgeband bearing strengths (for $\geq 20\%$ hole elongation) at 10^6 cycles appear to be about 60-70% of those obtained for AS4/3501-6 laminates, as calculated using the combined facesheet and closeout thicknesses. When it is assumed that the facesheets alone carry bearing loads, bearing strengths were 85-95% of those obtained for AS4/3501-6 laminates. Thus, effective facesheet bearing fatigue capability is lower than typical laminate capability. It is hypothesized that this is caused by the lower clamp-up loads attainable using the closeout design concept.

Discussion of Results

Static Performance

Sandwich panel edgebands failed in a bearing-dominated mode, with significant hole elongation observed in the facesheets and closeouts and brooming observed on the unsupported side of the closeouts. Ultimate bearing strength of the edgebands appeared to be on the order of 60-75% of that observed for typical graphite/epoxy laminates. However, when the facesheets alone were assumed to carry bearing loads, effective facesheet bearing capability was nearly equivalent to typical laminates.

Fatigue Performance

Sandwich panel edgebands exhibited modes similar to those observed under static loading. Edgeband bearing strengths (for $\geq 20\%$ hole elongation) at 10^6 cycles under $R = +0.1$ loading appear to be about 60-70% of those obtained for typical graphite/epoxy laminates. When the facesheets alone were assumed to carry bearing loads, effective facesheet bearing capability was 85-95% of that observed for typical laminates.

Conclusions

The following are significant conclusions based upon the results of this investigation:

- 1) Failure of tapered sandwich beams initiates as local bondline damage between the facesheets and the core or plug material. In tension, this local failure is noncatastrophic, and final failure occurs through facesheet fracture after the local damage grows. In compression, local failure rapidly grows, and the peak load at which the local damage was created can never be attained again.
- 2) Manufacturing anomalies and local damage can cause significant differences in facesheet strains.
- 3) Use of solid plug in the ramped region reduces facesheet strains in the radii, as some load is carried within the plug. Consequently, the facesheet deforms less than when honeycomb core is used in the ramped region, so local bondline failures initiate at higher far-field load levels.

- 4) Laminate moduli based upon strain gage readings were lower than those calculated using nominal properties. The reasons for this discrepancy is unclear. One potential reason is the facesheet "dimpling" observed over the honeycomb core.
- 5) Facesheet tension failure stresses were found to be on the order of 75-85% of typical notched laminate failure stresses obtained in RTD environmental conditions for the DEMO1 configuration and 40-55% for the DEMO2 configuration. Compression failure stresses were 45-55% of typical notched laminate stresses for the DEMO1 configuration and 35-45% for the DEMO2 configuration. Current composite allowables methodologies apparently would not conservatively account for the out-of-plane failure modes which influenced ultimate facesheet failure in these specimens.
- 6) Sandwich panel edgebands using the braided closeout concept had static and fatigue bearing strengths on the order of 60-75% of that typical of graphite/epoxy laminates. It is hypothesized this is due to lower clamp-up loads obtained using the closeout design concept, and subsequent "brooming" on the unsupported side of the braided closeout, similar to that observed in pure pin bearing tests. When the facesheets alone were assumed to carry bearing loads, effective facesheet bearing capability was nearly equivalent to that of typical laminates.
- 7) Hole elongation progresses rapidly under fatigue loading after approximately 2-3% hole elongation is achieved.
- 8) Edgeband $R = +0.1$ fatigue bearing strengths appear to be about 60-70% of those obtained for typical graphite/epoxy laminates. When the facesheets alone were assumed to carry bearing loads, effective facesheet bearing capability was 85-95% of that observed for typical laminates.

References

- E-1. Raj, S., *Boeing/ATCAS MDOC Sandwich Panel Closeout Evaluation*, Intec Project No. BC0142, June 1995.
- E-2. Sawicki, A., "MDOC Joint Coupon Material Database," MDOC program internal report, November 1995.
- E-3. Shivakumar, N. and Crews, J., "Bolt Clampup Relaxation in a Graphite/Epoxy Laminate," ASTM STP 813, Philadelphia, PA, 1983, pp. 5-22.
- E-4. Shivakumar, N. and Crews, J., "An Equation for Bolt Clampup Relaxation in Transient Environments," NASA Technical Memorandum 84480, April 1982.
- E-5. Grant, P. and Sawicki, A., "Development of Design and Analysis Methodology for Composite Bolted Joints," American Helicopter Society National Technical Specialists' Meeting on Rotorcraft Structures, Williamsburg, VA, October 1991.
- E-6. Sawicki, A., "Mechanical Assembly of Commercial Transport Fuselage Utilizing Tow-Placed and Textile Composites," ATCAS program internal report, Revision A, November 1995.
- E-7. Sawicki, A., Grant, P. and Mabson, G., "Mechanical Assembly of Commercial Transport Fuselage Utilizing Tow-Placed and Textile Composites," AIAA/ASME/ASCE/AHS/ASC 35th Structures, Structural Dynamics, and Materials Conference, Hilton Head, SC, April 1994.
- E-8. Grant, P., Magiso, A. H. and LaMon, S., "V-22 Engineering and Manufacturing Development Allowables," Bell-Boeing interoffice memo 8-7487-1-926, February 1993.
- E-9. Grant, P., Nguyen, N. and Sawicki, A., "Bearing Fatigue and Hole Elongation in Composite Bolted Joints," American Helicopter Society 49th Annual Forum, May 1993.

Table E-1. Layups of sandwich panel facesheets, closeouts and solid laminate plugs.

Panel ID	Layup	Material
DEMO 1, 2 Facesheets	[+45/0/-45/90/0/-45/+45/0/90/-45/0/+45]	AS4/8552 tape
DEMO 1, 2 Solid Plugs:		
minimum thickness	$[(45/0)_5/0/(45/0)_5/\overline{45}]_s$	BMS 8-256 PW Fabric
maximum thickness	$[(45/0)_5/0/(45/0)_{11}/0/(45/0)_5]_s$	BMS 8-256 PW Fabric
AK25 Facesheets	[+45/0/-45/90/0/-45/+45/0/90/-45/0/+45]	AS4/8552 tow
AK25 Braided Closeouts	33% 6K longitudinal, 67% $\pm 60^\circ$ 3K braid, 2 plies	AS4/1895

Table E-2. In-plane properties used in this investigation.

Panel ID	Longitudinal Modulus (msi)	Transverse Modulus (msi)	Major Poisson's Ratio	Shear Modulus (msi)	Nominal Thickness (in)
unidirectional AS4/8552 tow & tape (band head for fiber placement)	17.35	1.36	0.32	0.76	0.0073
0/90 BMS 8-256 PW Fabric	8.1	8.1	0.06	0.70	0.0085
DEMO 1, 2 Facesheets	7.98	5.53	0.353	2.53	0.0876
DEMO 1, 2 Facesheets & Solid Plugs combined:					
minimum thickness	6.67	5.88	0.325	2.35	0.5407
maximum thickness	6.44	5.97	0.311	2.27	0.9232
AK25 Facesheets	7.98	5.53	0.353	2.53	0.0876
AK25 Braided Closeouts	-	-	-	-	0.0400

Table E-3. Test matrix.

Panel ID	Sandwich Tension	Sandwich Edgewise Compression	Static Bearing	R = +0.1 Bearing Fatigue
DEMO1	3	4	-	-
DEMO 2	3	4	-	-
AK25 (composite load plates)	-	-	3	2
AK25 (steel load plates)	-	-	3	4

Table E-4. Sandwich laminate secant modulus at limit of linearity.

Specimen ID	Nominal Facesheet Modulus, E11 (msi)	Measured Modulus (Gages 1&2) (msi)	Nominal Facesheet & Plug Modulus, E11 (msi)	Measured Modulus (Gages 11&12) (msi)
DEMO1-31	7.98	6.20	6.67	5.51
DEMO1-32		5.75		4.85
DEMO1-33		6.22		5.97
DEMO2-31	7.98	6.58	6.67	4.60
DEMO2-32		6.59		4.70
DEMO2-33		6.19		4.93
DEMO1-42	7.98	6.45	6.67	5.98
DEMO1-43		5.71		5.29
DEMO1-44		6.09		5.28
DEMO2-42	7.98	6.05	6.67	4.91
DEMO2-43		6.34		4.92
DEMO2-44		5.63		4.27

Table E-5. Individual specimen results for tapered sandwich beam tension tests.

Specimen ID	Plug Type in Ramp-Up	Facesheet Stress at Initial Load Drop (ksi)	Ultimate Facesheet Stress (ksi)
DEMO1-31	Solid Laminate	34.9	63.3
DEMO1-32		36.1	48.5
DEMO1-33		21.4	38.1
DEMO2-31	Honeycomb Core	17.2	38.8
DEMO2-32		19.0	38.5
DEMO2-33		18.8	36.4

Table E-6. Statistical analysis of tapered sandwich beam tension tests.

Test Type	Facesheet Stress at Initial Load Drop (ksi)	Coefficient of Variation	Ultimate Facesheet Stress (ksi)	Coefficient of Variation
DEMO1 (solid ramp)	30.8	26.6%	50.0	25.3%
DEMO2 (honeycomb ramp)	18.3	5.22%	37.9	3.42%

Table E-7. Comparison of facesheet tension strengths with filled hole tension data.

Panel ID	Layup	Material	Longitudinal Modulus (msi)	Ultimate Tension Strength (ksi) (1)
DEMO1	[+45/0/-45/90/0/-45/+45/0/90/-45/0/+45]	AS4/8552 tow	7.98	46.2
DEMO2	[+45/0/-45/90/0/-45/+45/0/90/-45/0/+45]	AS4/8552 tow	7.98	27.5
S21 (2)	[F0/+45/0/-45/0/+45/90/-45/0/-45/0/+45/F0]	AS4/8552 tow & PW fabric	8.71	57.5
S22 (2)	[F0/+45/0/-45/90/0 ₂ /90/-45/0/+45/F0]		9.04	63.9

Notes: 1) Strengths based upon 1.5 x initial load drop stresses.

2) Data obtained from Reference E-2.

Table E-8. Individual specimen results for tapered sandwich beam compression tests.

Specimen ID	Plug Type in Ramp-Up	Ultimate Facesheet Stress (ksi)
DEMO1-41	Solid Laminate	25.4
DEMO1-42		28.6
DEMO1-43		30.9
DEMO1-44		26.0
DEMO2-41	Honeycomb Core	22.5
DEMO2-42		20.5
DEMO2-43		20.5
DEMO2-44		23.5

Table E-9. Statistical analysis of tapered sandwich beam compression tests.

Specimen Type	Ultimate Facesheet Stress (ksi)	Coefficient of Variation
DEMO1 (solid ramp)	27.7	9.08%
DEMO2 (honeycomb ramp)	21.8	6.88%

Table E-10. Comparison of facesheet compression strengths with open hole compression data.

Panel ID	Layup	Material	Longitudinal Modulus (msi)	Ultimate Comp. Strength (ksi)
DEMO1	[+45/0/-45/90/0/-45/+45/0/90/-45/0/+45]	AS4/8552 tow	7.98	27.7
DEMO2	[+45/0/-45/90/0/-45/+45/0/90/-45/0/+45]	AS4/8552 tow	7.98	21.8
S21 (1)	[F0/+45/0/-45/0/+45/90/-45/0/-45/0/+45/F0]	AS4/8552 tow & PW fabric	8.71	53.7
S22 (1)	[F0/+45/0/-45/90/0 ₂ /90/-45/0/+45/F0]		9.04	57.7

Notes: 1) Data obtained from Reference 2.

Table E-11. Individual specimen results from static closeout bearing tests.

Specimen ID	Load Introduction Plate Type	Bearing Stresses calculated using Facesheet Thickness only (ksi)		Bearing Stresses calculated using Facesheet & Closeout Thickness (ksi)	
		2% Offset	Ultimate	2% Offset	Ultimate
AK25-11	Composite	70.7	86.2	48.5	59.2
AK25-12		65.0	90.2	44.6	61.9
AK25-13		63.5	94.5	43.6	64.9
AK25-14	Steel	93.5	108.2	64.2	74.3
AK25-15		90.8	106.5	62.3	73.1
AK25-16		95.1	97.8	65.3	67.1

Table E-12. Statistical analysis of static closeout bearing data.

Load Introduction Plate Type	Bearing Stress Definition	Mean 2% Offset Bearing Stress (ksi)	Coefficient of Variation	Mean Ultimate Bearing Stress (ksi)	Coefficient of Variation
Composite	Facesheets & Closeouts (1)	45.6	5.69%	62.0	4.60%
	Facesheets Only (2)	66.4		90.3	
Steel	Facesheets & Closeouts (1)	63.9	2.33%	71.5	5.36%
	Facesheets Only (2)	93.1		104.2	

Notes: 1) Bearing stresses calculated assuming load is carried by both the facesheets and the braided closeouts.

2) Bearing stresses calculated assuming load is carried by the facesheets only.

Table E-13. Comparison of static closeout bearing strengths with typical laminate data.

Material	Laminate Thickness (in)	Fastener Diameter (in)	Ultimate Bearing Strength (ksi)	Calculated Bearing Strength for 5/16" Diameter Hole (1) (ksi)
AS4/8552 tow & AS4/1895 braid:			(steel load plates)	
facesheets & closeouts (2)	0.1276	0.3125	71.5	71.5
facesheets only (3)	0.0876		104.2	104.2
AS4/8552 tow & PW fabric (4)	0.0866	0.25	114.5 116.0 106.2	108.1 109.5 100.3
AS4/938 tow (5)	0.0962 0.0962 0.111 0.111 0.148 0.1628	0.25	117.3 108.9 108.9 113.9 97.6 113.2	110.7 102.8 102.8 107.5 92.1 106.9
AS4/1895 (5) 37.4% 18K longitudinal, 62.6% 66.5° 6K braid, 5 plies	0.131	0.25	74.8	70.6

Notes: 1) Calculated strengths for 5/16" diameter holes assume a 0.944 conversion factor from 1/4" data per Reference 8.

2) Bearing stresses calculated assuming load is carried by both the facesheets and the braided closeouts.

3) Bearing stresses calculated assuming load is carried by the facesheets only.

4) Data obtained from Reference 2.

5) Data obtained from Reference 6.

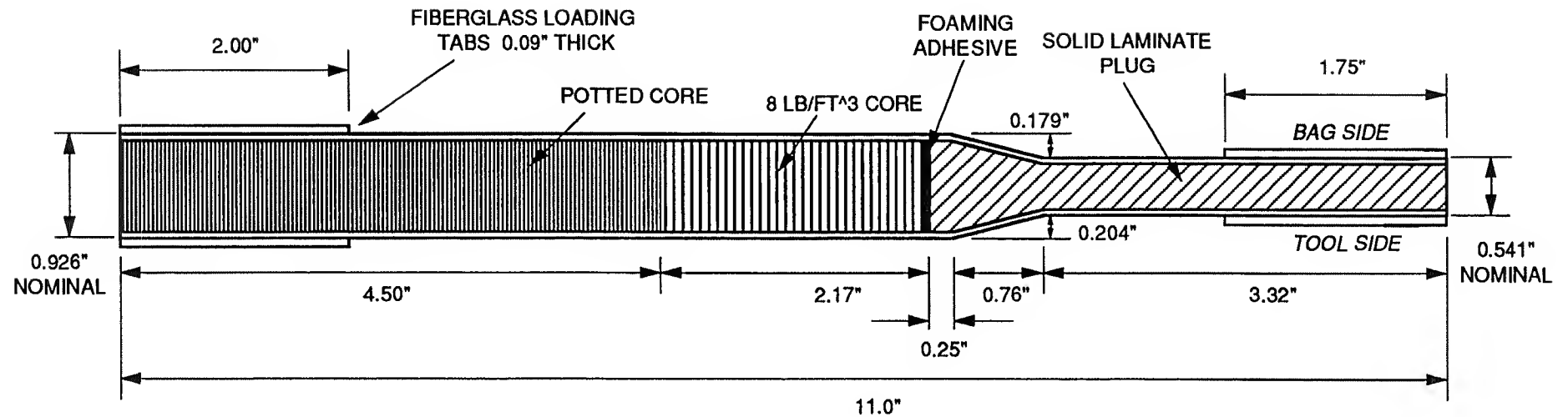
Table E-14. Hole elongation results from closeout bearing $R = +0.1$ fatigue tests.

Specimen ID	Load Introduction Plate Type	Maximum Bearing Fatigue Stress (facesheets & closeout) (ksi) (1)	Maximum Bearing Fatigue Stress (facesheets only) (ksi) (2)	Cycles to 0.01" (~3%) Hole Elongation	Cycles to Failure
AK25-21	Composite	20.4	29.7	>1,000,000	>1,000,000
AK25-21A		31.4	45.7	>1,000,000	>1,000,000
AK25-22	Steel	33.9	49.3	>1,000,000	>1,000,000
AK25-22A		48.3	70.3	700,000	800,000
AK25-23		54.6	79.5	10,000	14,796
AK25-24		50.2	73.1	300,000	340,651

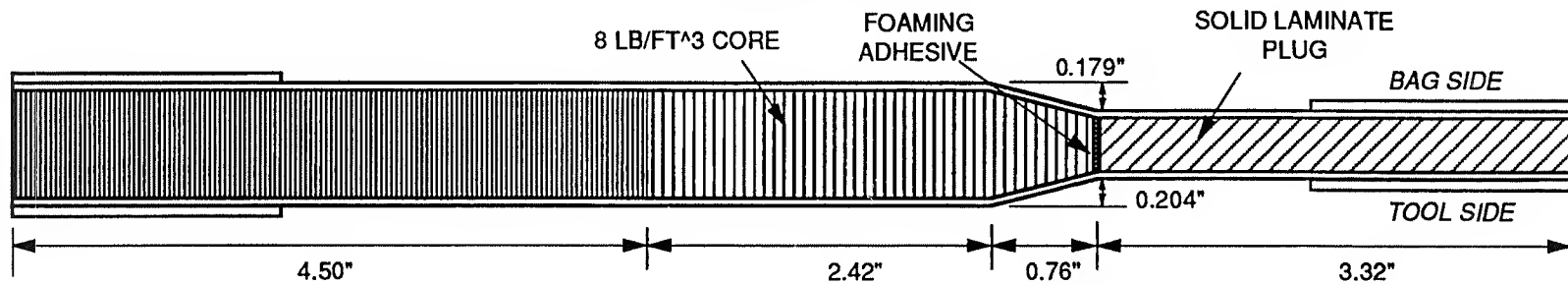
Notes: 1) Bearing stresses calculated assuming load is carried by both the facesheets and the braided closeouts.

2) Bearing stresses calculated assuming load is carried by the facesheets only.

DEMO1 PANEL

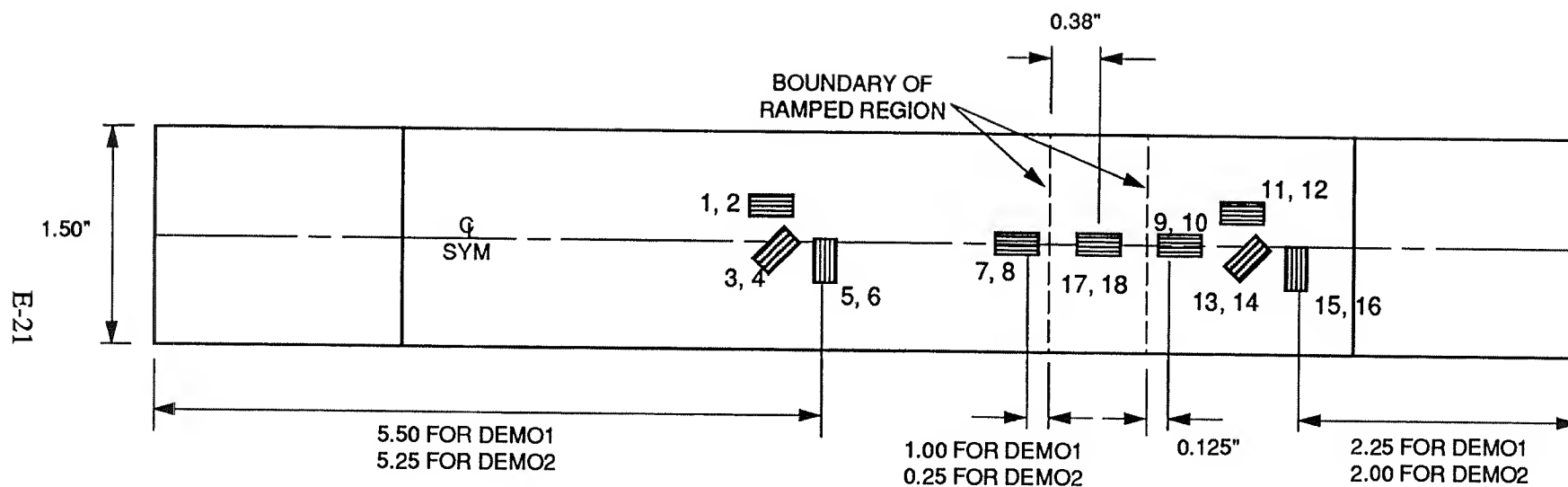


DEMO2 PANEL



ALL OTHER DIMENSIONS AND MATERIALS EQUIVALENT TO DEMO1

Figure E-1: Tapered sandwich specimen configurations.



ODD NUMBERED GAGES ON TOOL SIDE FACESHEET
EVEN NUMBERED GAGES ON BAG SIDE FACESHEET

UNIAXIAL GAGES: MEASUREMENTS GROUP CEA-06-250AE-350
ROSETTES: MEASUREMENTS GROUP CEA-06-250UR-350

Figure E-2: Sandwich specimen instrumentation.

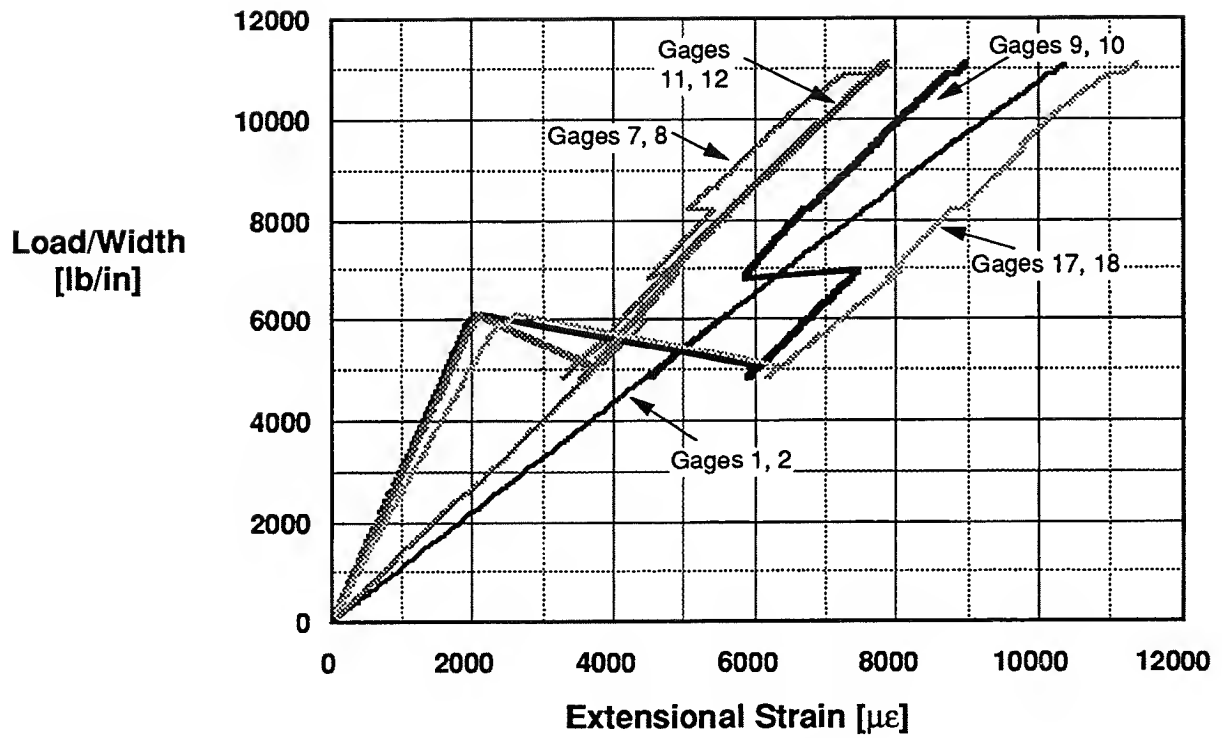


Figure E-3: Load-extensional strain behavior for specimen DEMO1-31 (solid plug in ramp, tension).

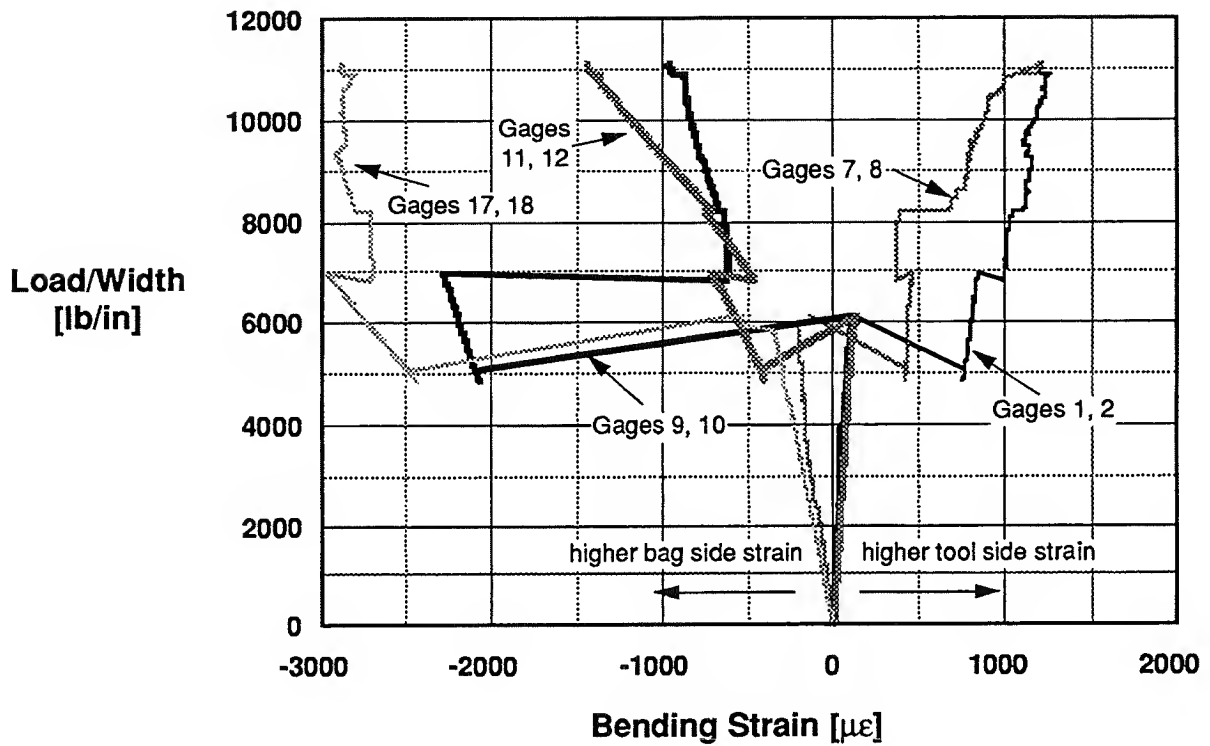


Figure E-4: Load-bending strain behavior for specimen DEMO1-31 (solid plug in ramp, tension).

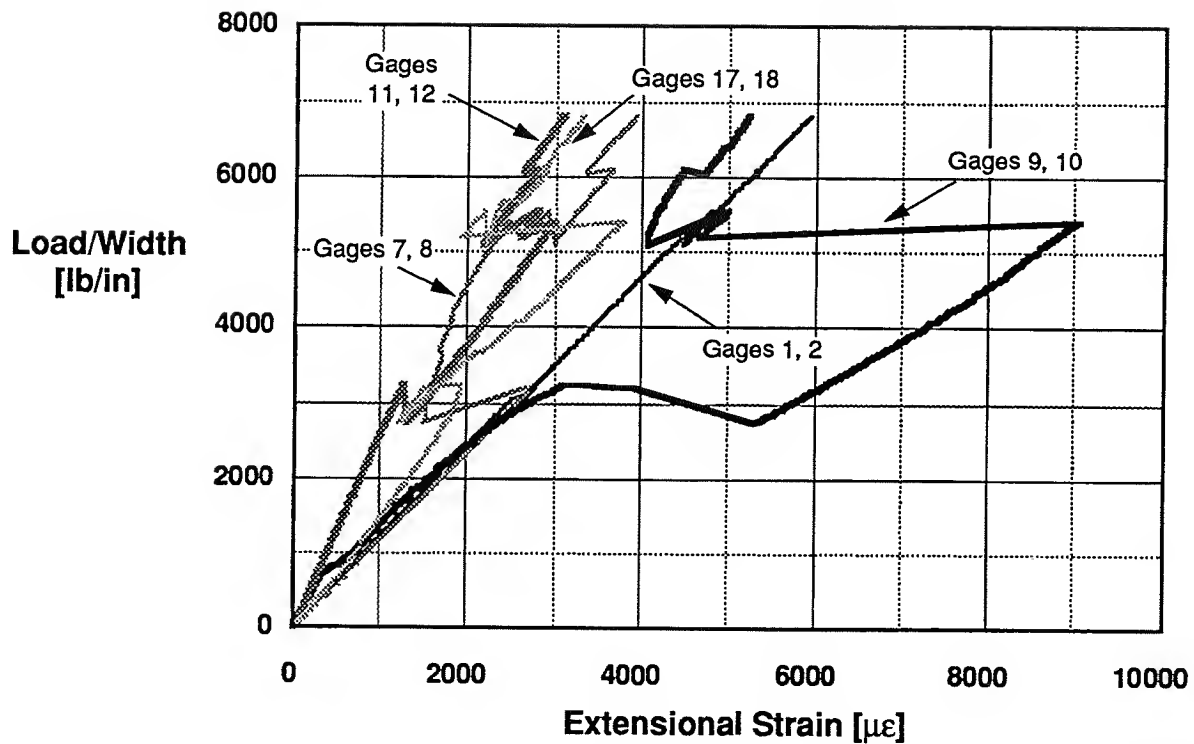


Figure E-5: Load-extensional strain behavior for specimen DEMO2-31 (honeycomb core in ramp, tension).

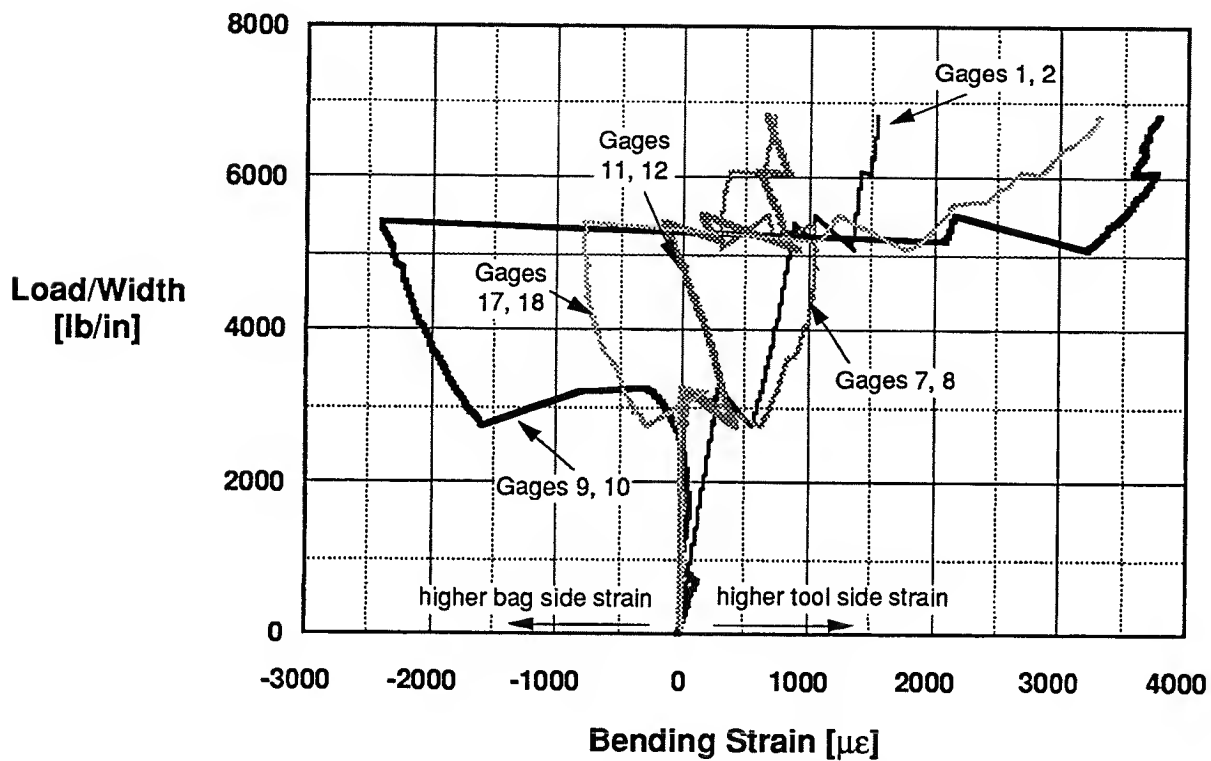


Figure E-6: Load-bending strain behavior for specimen DEMO2-31 (honeycomb core in ramp, tension).

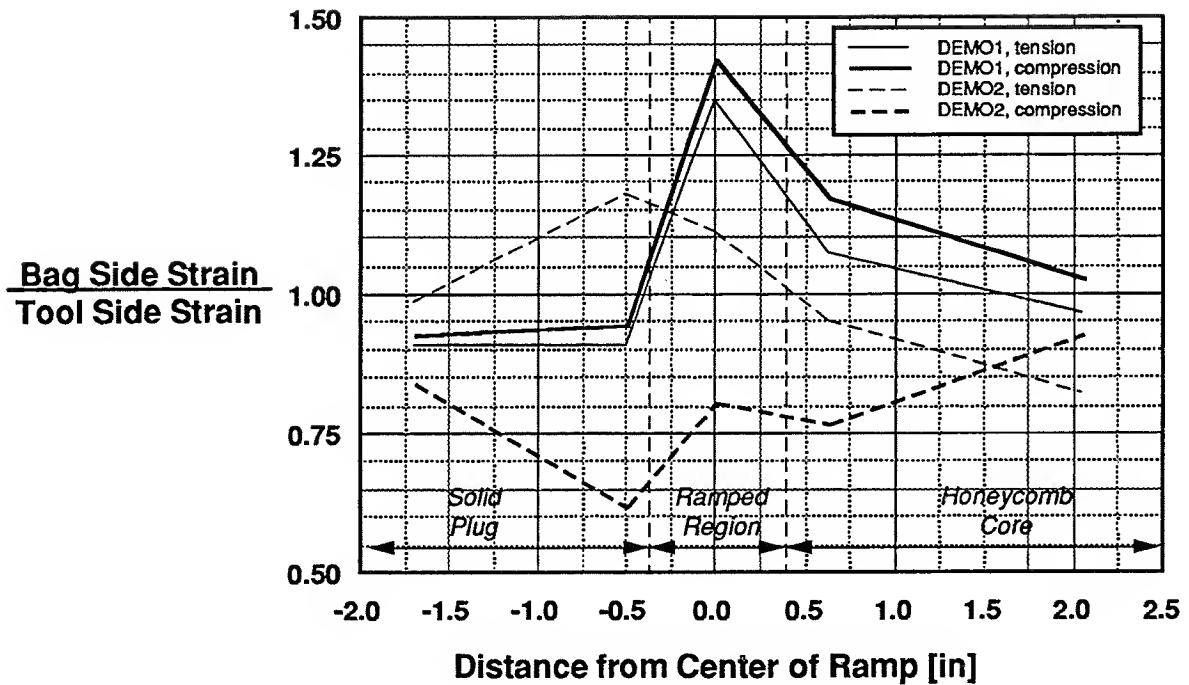


Figure E-7: Averaged ratio of bag side extensional strain to tool side extensional strain for tapered core specimens at initial failure.

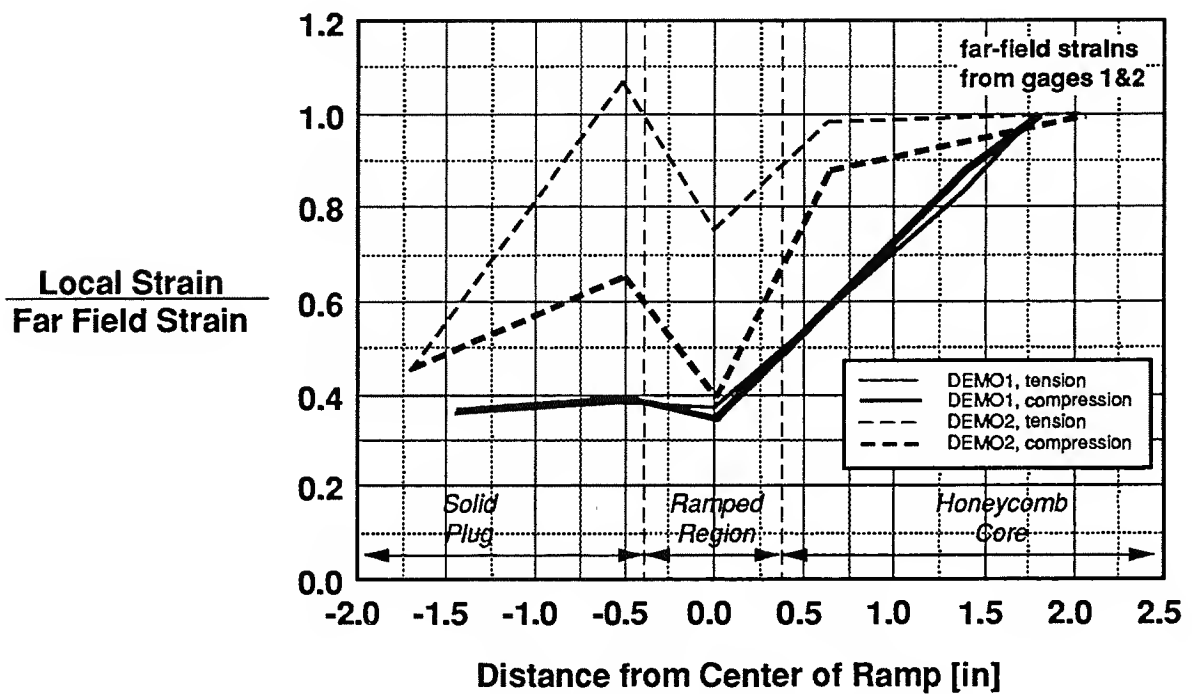


Figure E-8: Averaged ratio of local extensional strain to far field extensional strain (facesheets over honeycomb core) at initial failure.

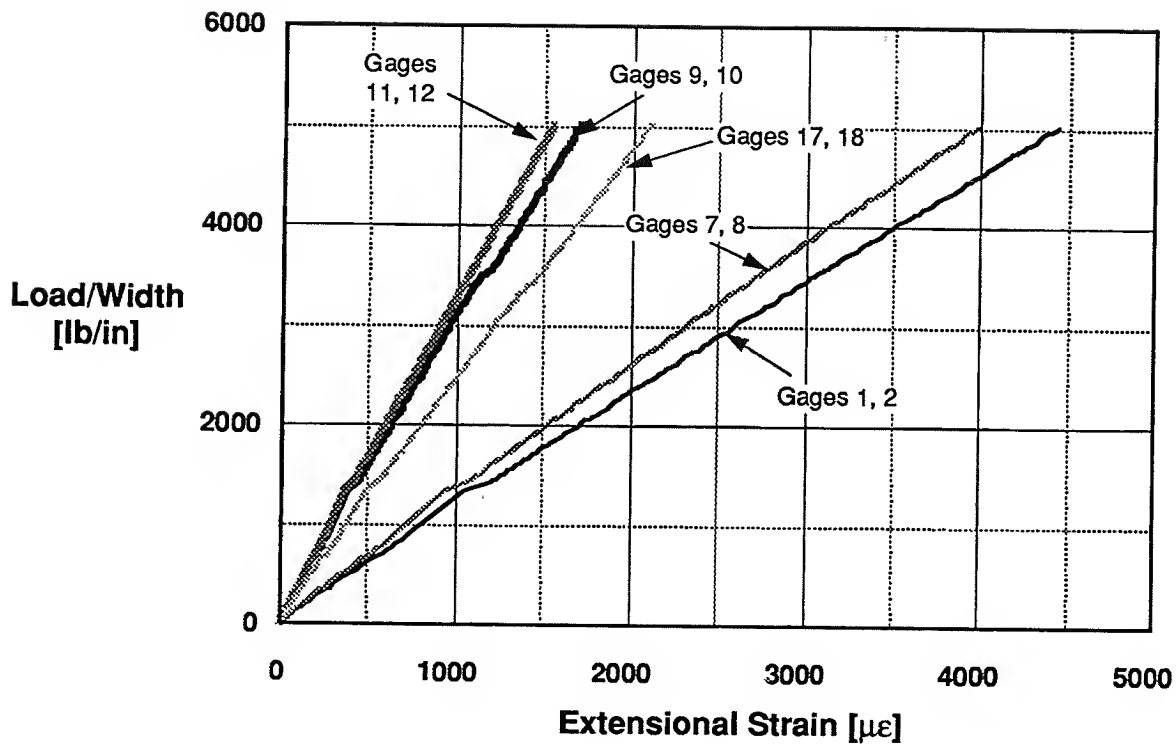


Figure E-9: Load-extensional strain behavior for specimen DEMO1-42 (solid plug in ramp, compression).

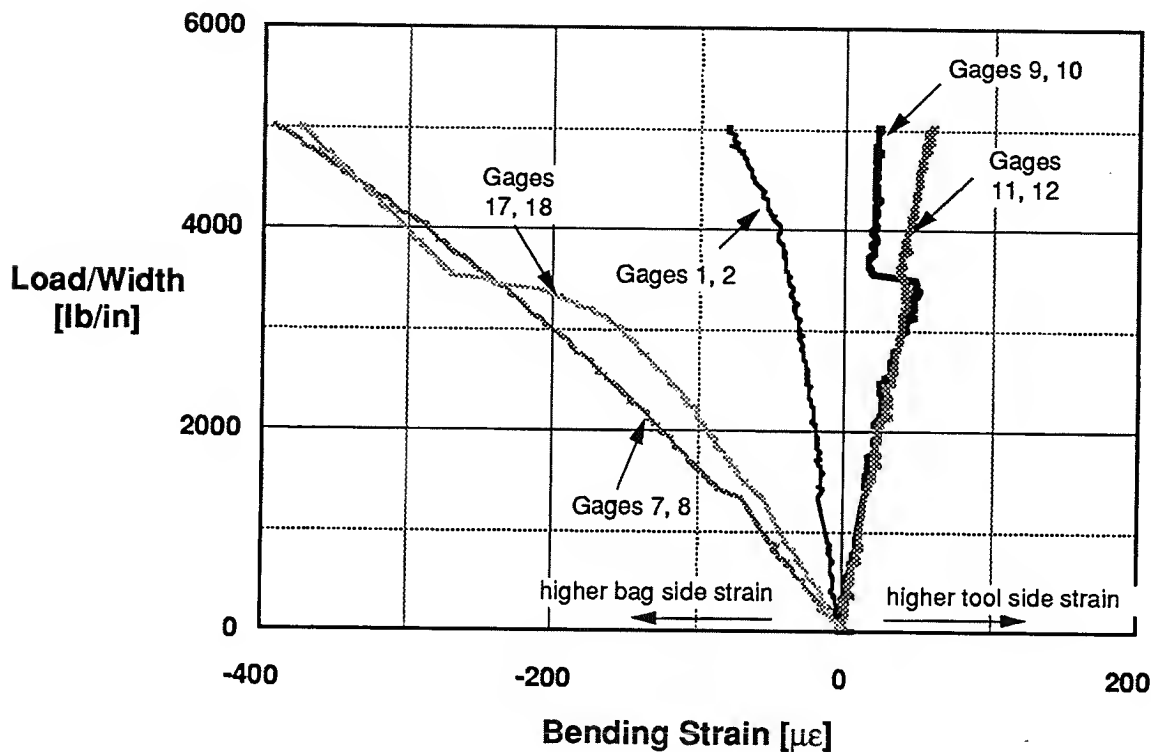


Figure E-10: Load-bending strain behavior for specimen DEMO1-42 (solid plug in ramp, compression).

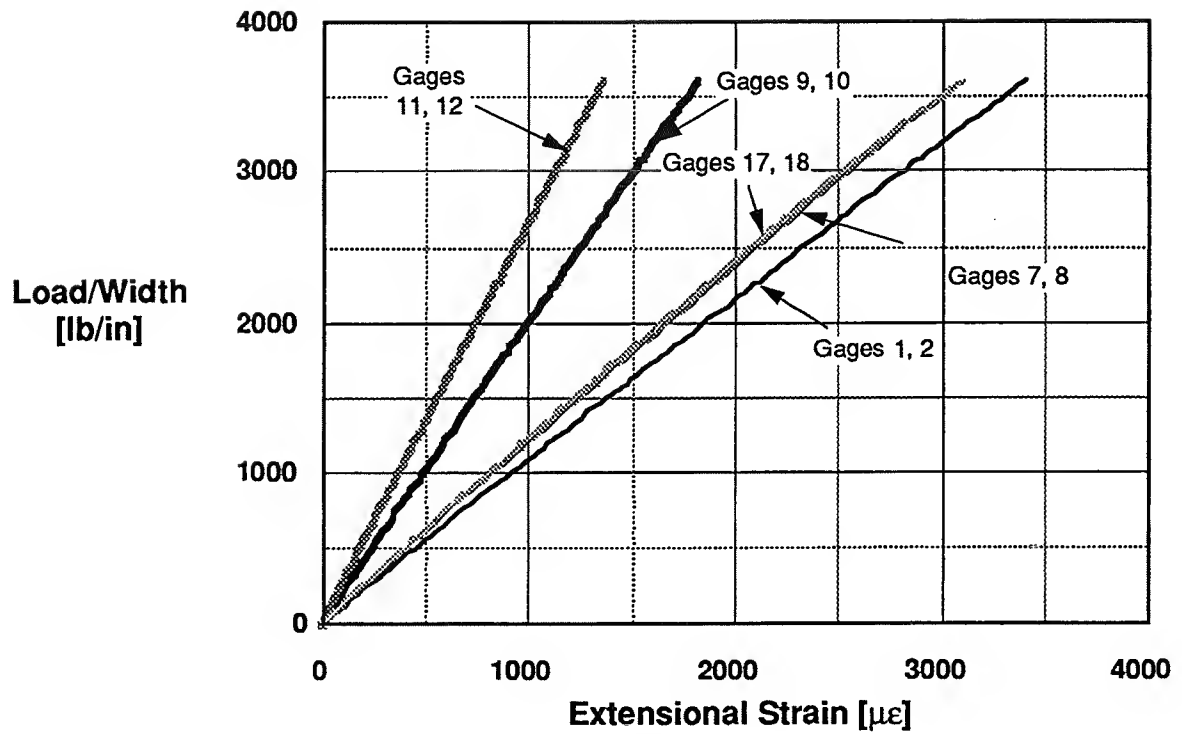


Figure E-11: Load-extensional strain behavior for specimen DEMO2-42 (honeycomb core in ramp, compression).

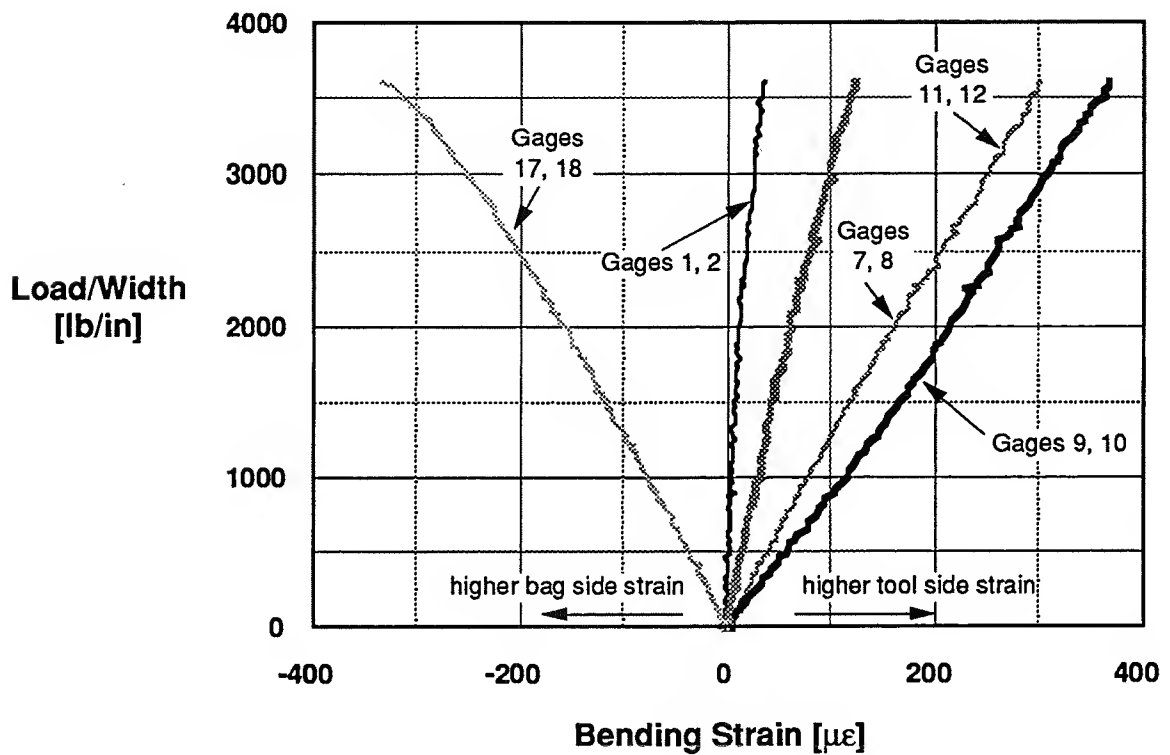
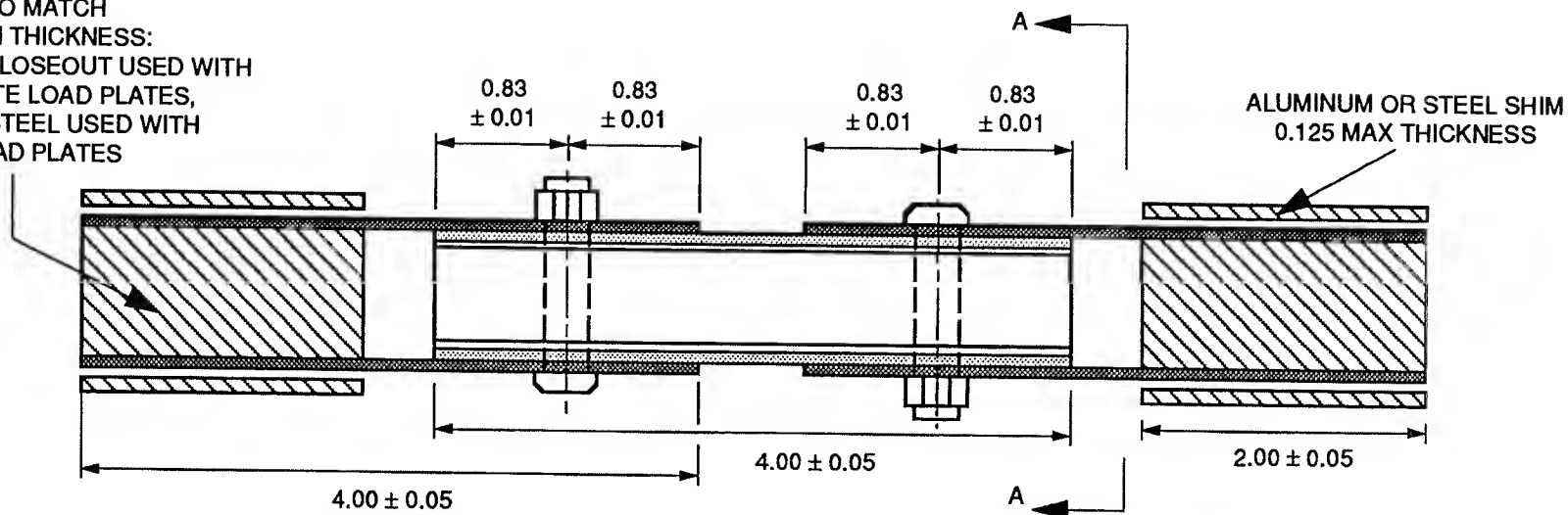


Figure E-12: Load-bending strain behavior for specimen DEMO2-42 (honeycomb core in ramp, compression).

SPACER TO MATCH
SPECIMEN THICKNESS:
POTTED CLOSEOUT USED WITH
COMPOSITE LOAD PLATES,
A2 TOOL STEEL USED WITH
STEEL LOAD PLATES



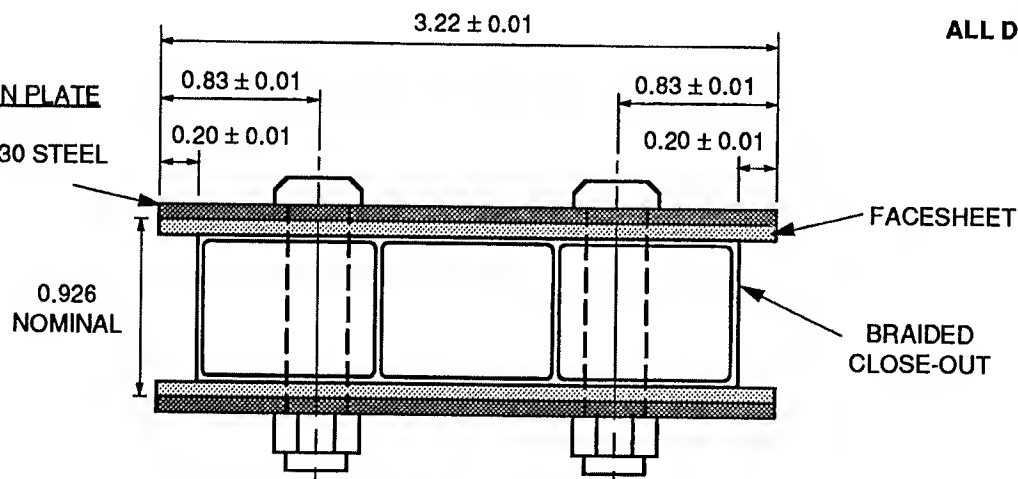
VIEW A-A

SPECIMENS ARE MANUFACTURED FROM A CURVED PANEL,
WITH A 122 INCH RADIUS OF CURVATURE

HYSOL 9394 LIQUID SHIM USED TO MATCH PANEL CURVATURE

ALL DIMENSIONS IN INCHES

LOAD INTRODUCTION PLATE
COMPOSITE OR
0.125 INCH THICK 4130 STEEL



FASTENERS:
PIN: BACB30NX10R18
COLLAR: BACC30BH10
(5/16 DIAMETER)

INSTALLED PER BAC5063
EXCEPT AT 60 IN-LB
TORQUE

Figure E-13: Edgeband bearing test specimens.

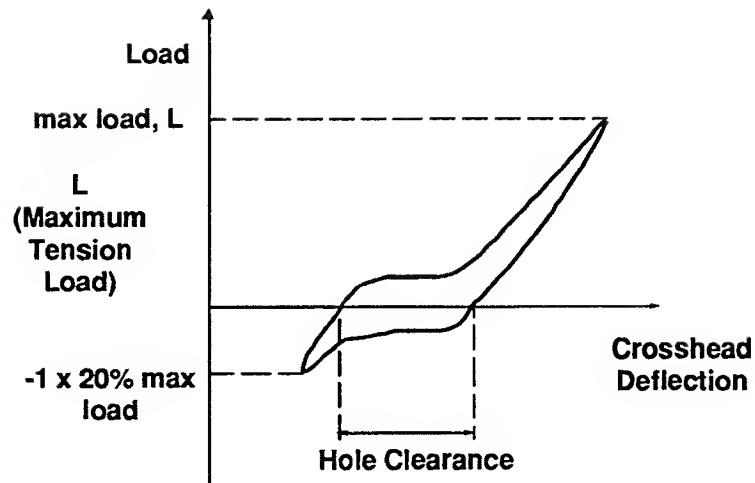


Figure E-14: Load-deflection hysteresis loop used in measurement of hole elongation and joint stiffness.

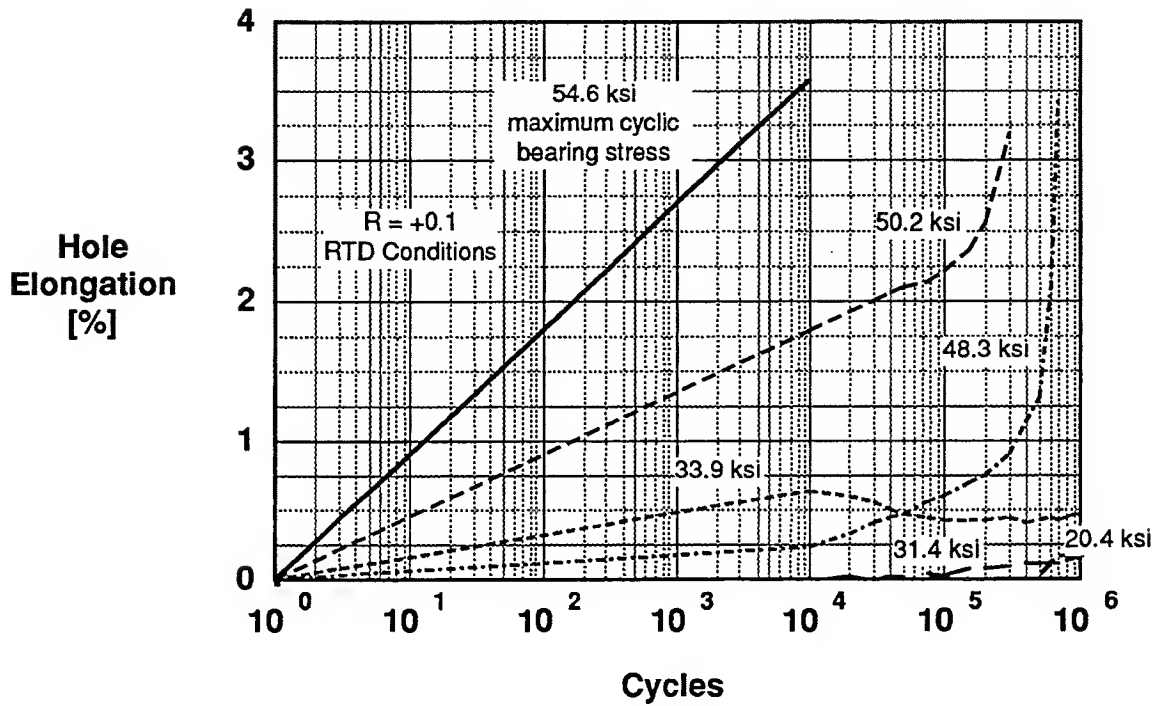


Figure E-15: Hole elongation versus load cycles for edgeband bearing specimens (bearing stresses calculated for combined facesheet and closeout thickness).

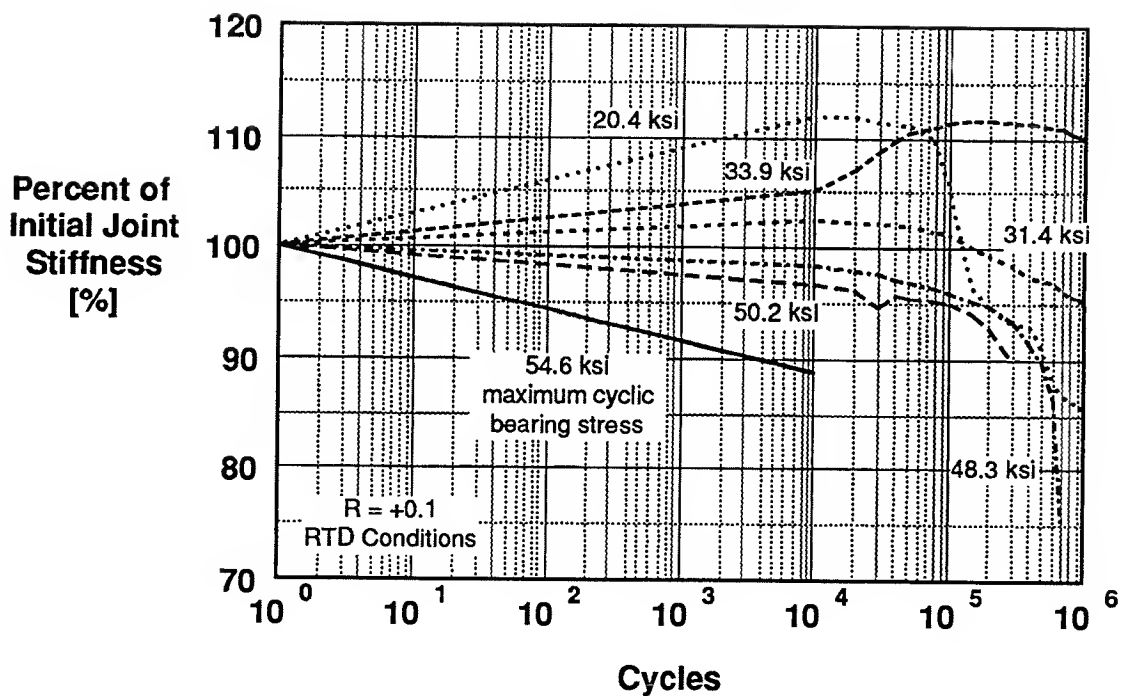


Figure E-16: Change in joint stiffness versus load cycles for edgeband bearing specimens (bearing stresses calculated for combined facesheet and closeout thickness).

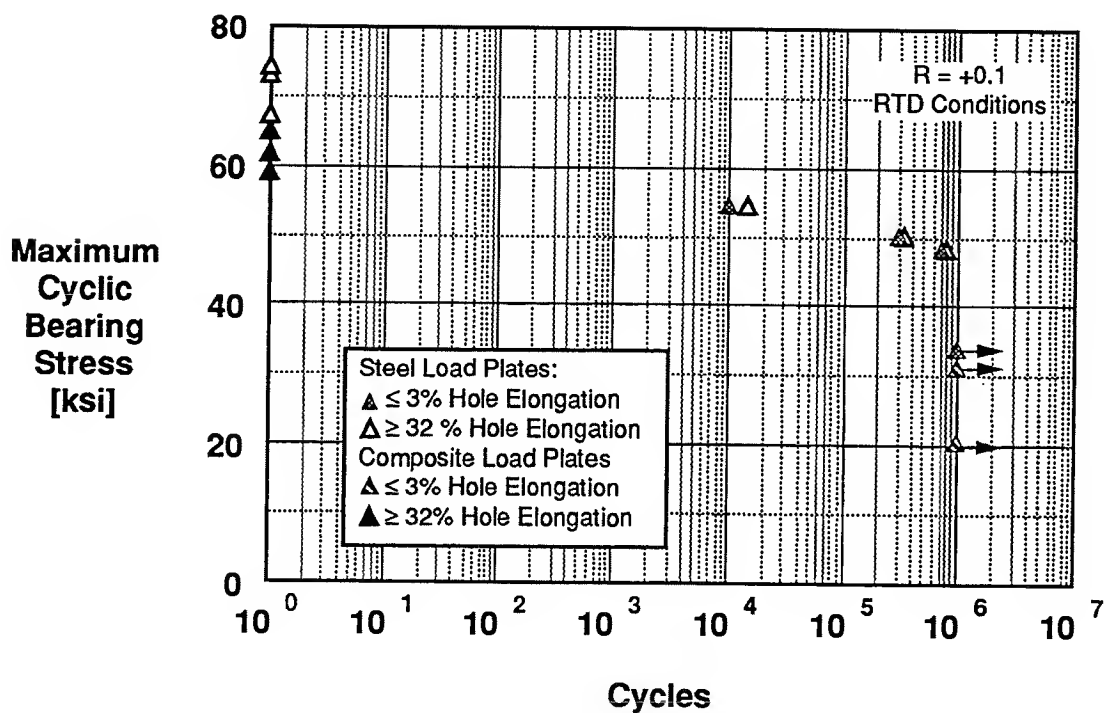


Figure E-17: S-N data for edgeband bearing failure (bearing stresses calculated for combined facesheet and closeout thickness).

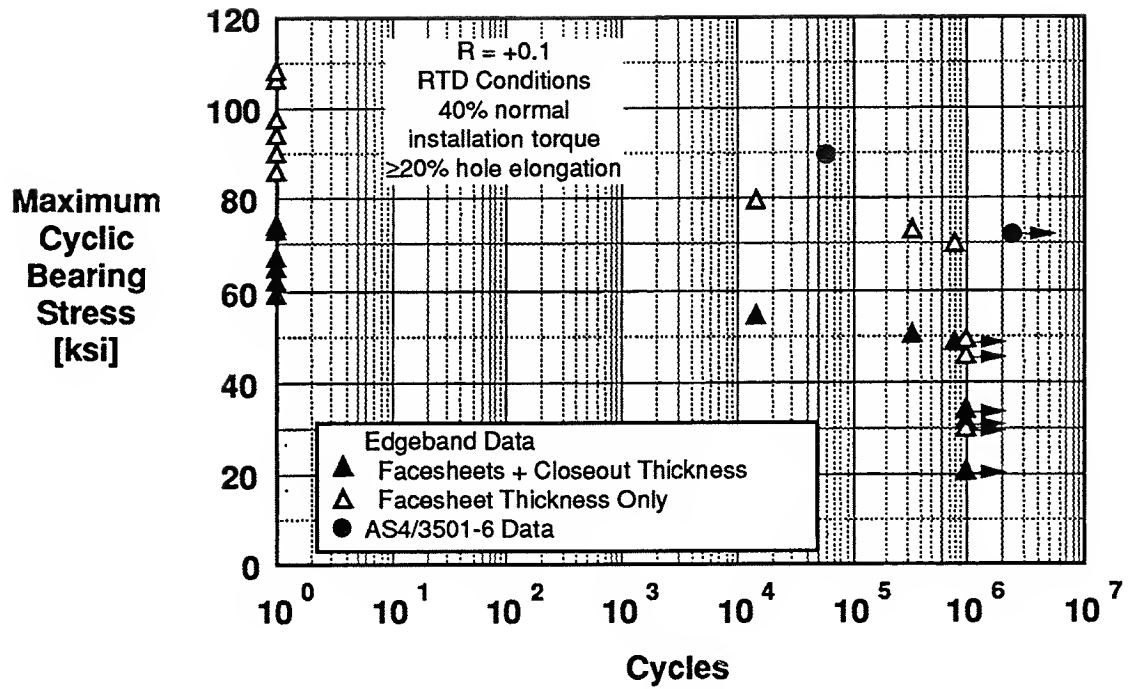


Figure E-18: Comparison of S-N data for edgebands with braided closeouts and AS4/3501-6 plain weave fabric laminates.

APPENDIX F

Impact Damage Resistance and Tolerance of Sandwich Structures with Various Core Materials

Summary

The impact damage resistance and CAI strength of sandwich panels representative of minimum gage fuselage structure with a variety of honeycomb core materials were characterized to aid core material selection.

Test Matrix and Procedures

Impact survey coupons were constructed of 8 ply quasi-isotropic AS4/8553-40 facesheets and 0.5 inch thick core of seven types. Candidate core materials were Hexcel products listed in Table F-1. The fraction in Hexcel's core material designation denotes honeycomb cell size in inches and the decimal number denotes the honeycomb density in pounds per cubic foot. K foam is a cyanate ester foam which has been combined with two of the low cost honeycomb materials in an attempt to improve their impact damage resistance and tolerance. The K foam adds 6 pounds per cubic foot to the density of the core material. The core material matrix was based mainly on availability but offers one to one comparisons of fiber type, fiber architecture and resin type. Honeycomb density was held constant. The AS4/8553-40 facesheet material had fiber areal weight of 190 g/m² and 40% resin content. CYTEC'S Metalbond 1515 film adhesive was used for cocuring the facesheets to the core materials.

Table F-1. Candidate Core Materials for Impact Damage Resistance Testing.

Material Designation	Description
HRP-3/16-5.5	0/90 glass/phenolic honeycomb
HFT-1/8-5.5	±45 glass/phenolic honeycomb
TPC-3/16-5.5	±45 glass/polyamide-imide honeycomb
HFT-G-3/16-6.0	±45 carbon/polyimide honeycomb
HRH-10-1/8-5.0	aramid paper/phenolic honeycomb
HRP-3/16-5.5 K foam	0/90 glass/phenolic honeycomb cyanate-ester foam
HRH-10-1/8-5.0 K foam	aramid paper/phenolic honeycomb cyanate-ester foam

Coupons were impacted on the toolside surface over a 4 x 4 inch simple support with a one inch diameter steel impactor at impact energies of 80, 100, 200 and 500 inch-pounds. The coupons were then photographed, inspected with through transmission ultrasonic (TTU) C-scan, and sectioned through the center of the impact.

CAI (compression-after-impact) tests were performed on 5 x 10 inch coupons cut from the same panels used for impact surveys. The coupons were supported for compression

testing in a manner consistent with NASA's ST-1 method for laminate CAI tests (rigid end constraints and simple supports along coupon edges).

Test Results and Discussion

Impact Damage Resistance

Impact dent depth was found to be essentially unaffected by core material type at low impact energies (≤ 200 inch-pounds) as shown in Figure F-1. None of the panels sustained visible damage (dent depth ≥ 0.05 inches) from impacts of ≤ 100 inch-pounds. 200 inch-pound impacts resulted in visible damage in all cases. 500 inch-pound impacts resulted in perforation of the first facesheet in all cases and subsequent impact of the farside facesheet in most cases (as determined by the impact load plots). A significant amount of variation was observed in replicate tests.

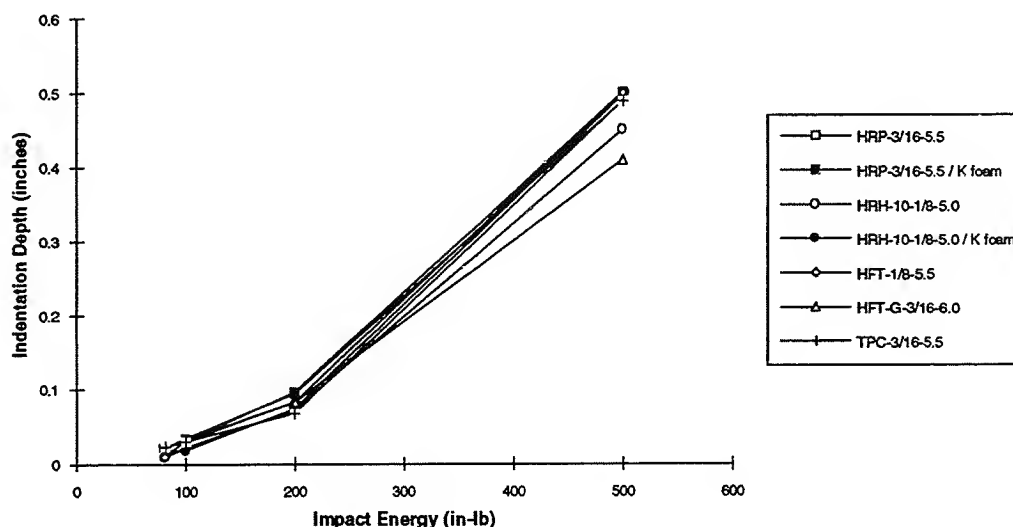


Figure F-1. Indentation Depth Following Impact of Representative Minimum Gage Sandwich Structure with Candidate Honeycomb Core Materials.

TTU inspection results for the coupons with unfilled honeycomb were representative of facesheet and core damage as determined by cross-sectioning. Figure F-2 is a plot of impact damage area (as determined by TTU) vs. impact energy. The best impact damage resistance was observed for the TPC (± 45 glass/thermoplastic) core. The HFT-G (± 45 carbon/polyimide) and HRH-10 (aramid paper/phenolic) materials also performed well. The greatest effect of any material variable was that of resin matrix type. The thermoplastic matrix honeycomb (TPC) exhibited the best impact damage resistance while the thermoset matrix core with similar fiber type and architecture (HFT) exhibited the worst. Fiber type also had a significant effect on impact damage resistance. The carbon fiber reinforced honeycomb (HFT-G) performed better than the glass reinforced

(HFT). 0/90 fiber orientation (HRP) was observed to provide better impact damage resistance than the bias weave (HFT). Some variation was observed in replicate tests.

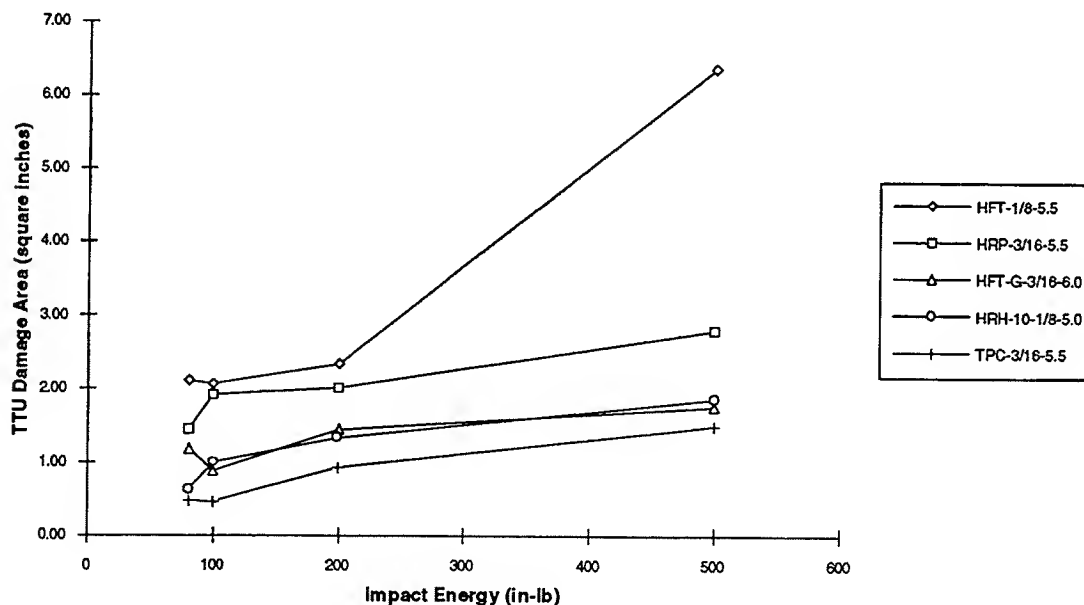


Figure F-2. Impact Damage Resistance of Representative Minimum Gage Sandwich Structure with Candidate Honeycomb Core Materials.

The extent of damage in coupons with filled honeycomb was difficult to determine by sectioning although TTU inspection provided results similar to those for unfilled honeycomb. Figure F-3 shows damage area as a function of impact energy for the filled honeycomb core materials and their unfilled counterparts. In most cases the damage area of filled honeycomb was greater than that of unfilled. The 500 inch-pound impact of the coupon with filled HRP core resulted in disbond of the far side facesheet from the core. The disbond was caused by the impactor penetrating the first facesheet and core and striking the farside facesheet. Disbond in the filled core coupon was most likely a result of the lack of adhesive fillets to the honeycomb cell walls and corresponding low flatwise tensile strength.

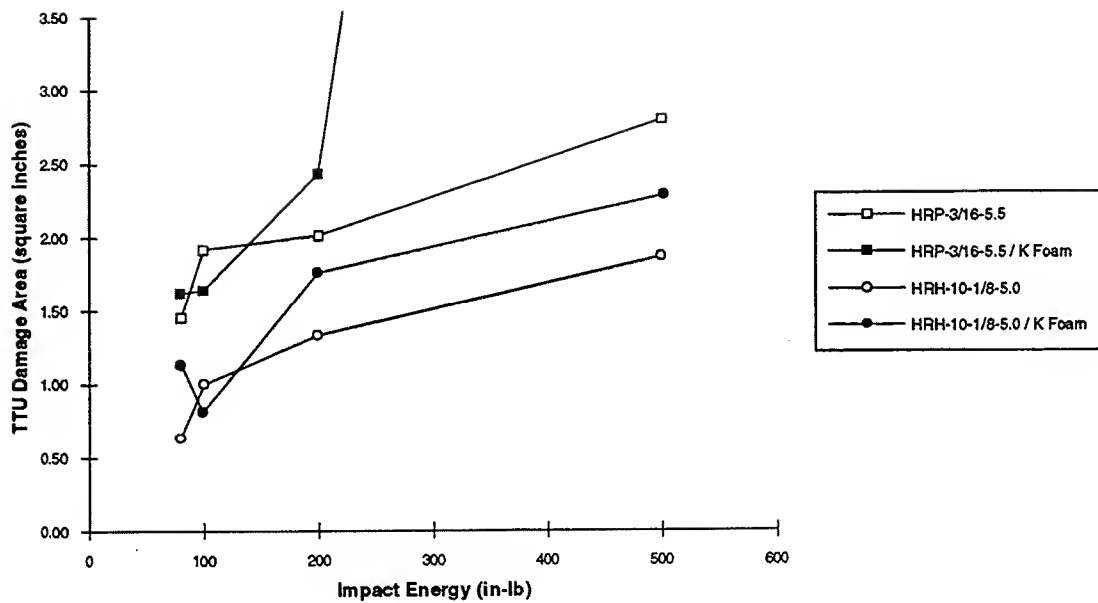


Figure F-3. Impact Damage Resistance of Representative Minimum Gage Sandwich Structure with Foam-Filled Honeycomb Core Materials.

One coupon of each type was impacted on the bagside with a one inch diameter impactor at 200 inch-pounds. The bagside impact appears to result in greater indentation depth in several cases (Figure F-4). Damage area appears to be slightly less extreme for bagside impacts (Figure F-5). However, the large amount of variation observed in replicate tests for toolside impacts make these conclusions unreliable.

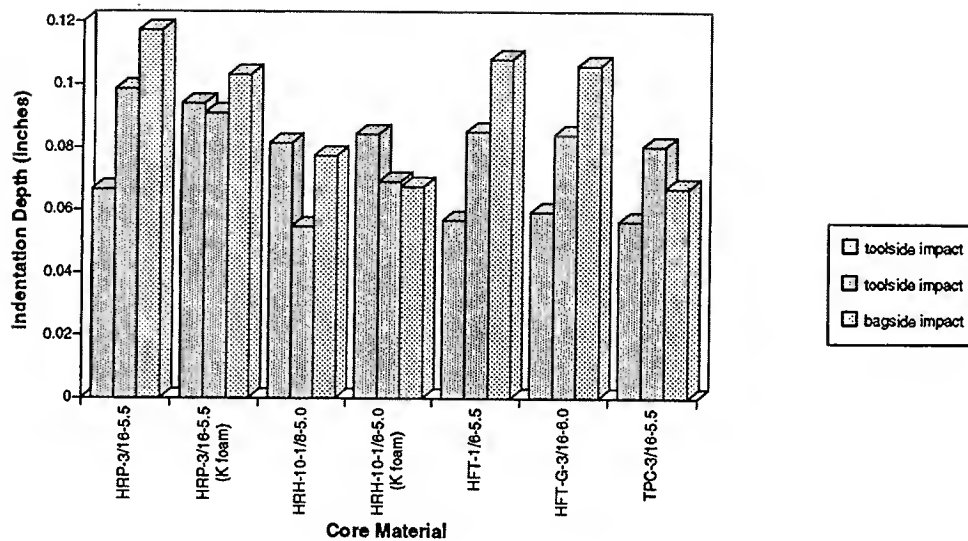


Figure F-4. Bagside and Toolside Impact Damage Resistance of Representative Minimum Gage Sandwich Structure (Indentation Depth).

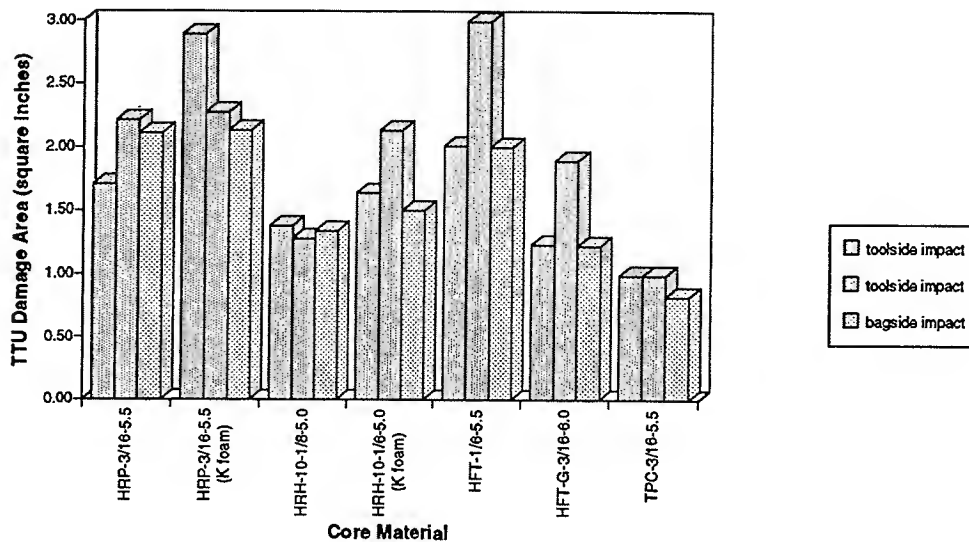


Figure F-5. Bagside and Toolside Impact Damage Resistance of Representative Minimum Gage Sandwich Structure (Damage Area).

One coupon of each type was impacted at 80 inch pounds with a two inch diameter impactor. Indentations were much less severe for impact with the larger impactor in most cases (Figure F-6). Exceptions to this trend are the HRH-10 and HFT materials.

The greater impactor diameter caused damage over a larger area in the glass reinforced phenolic core materials as shown in Figure F-7.

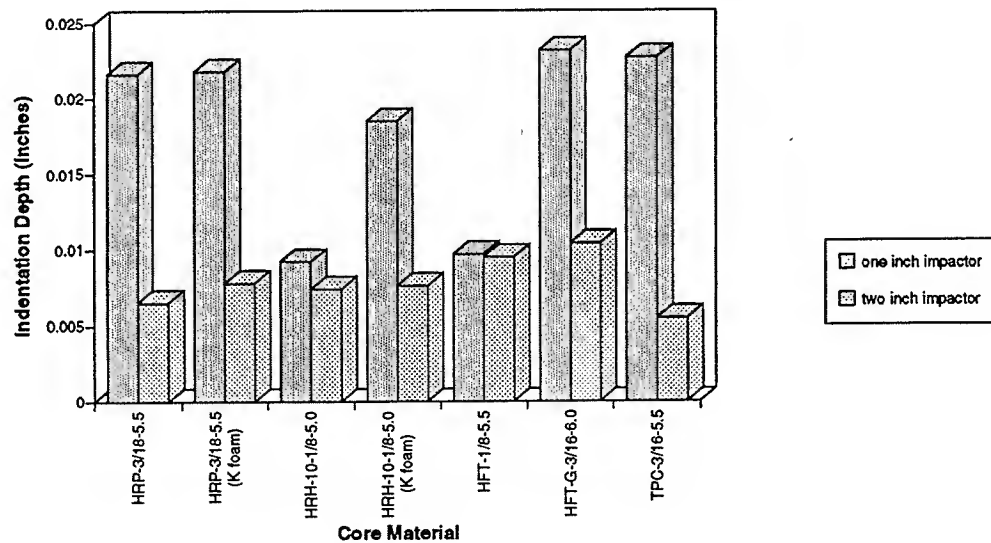


Figure F-6. Effect of Impactor Diameter on Indentation Depth.

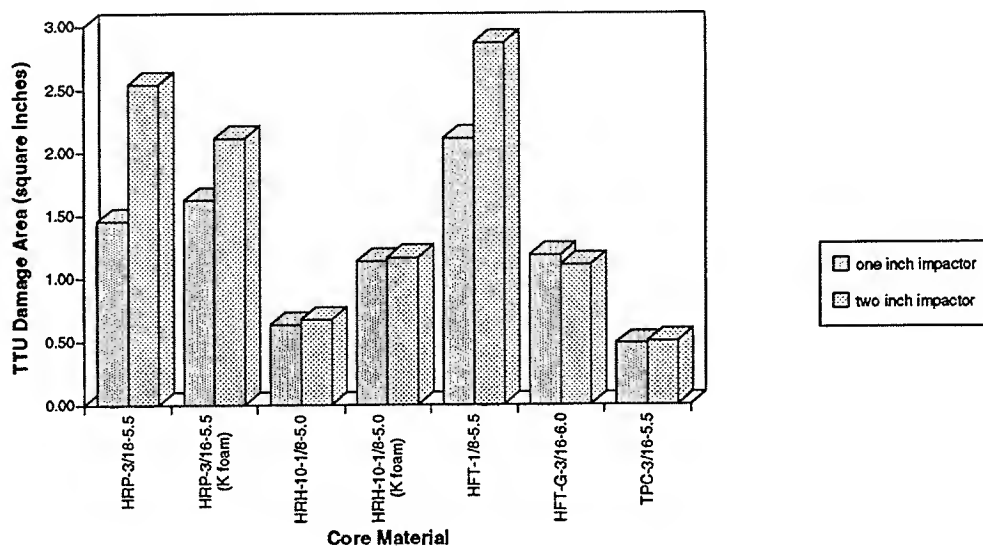


Figure F-7. Effect of Impactor Diameter on Damage Area.

Compression Strength After Impact

CAI strain at failure results are presented in Figure F-8 as a function of impact energy. The TPC thermoplastic core which exhibited the best damage resistance also provided

the highest CAI strengths. The HFT-G carbon fiber reinforced core also performed well in both tests. However, the CAI strengths for the HRH-10 aramid paper reinforced core were low even though the material exhibited good damage resistance. The HFT glass reinforced phenolic core performed better than would have been expected considering the poor damage resistance of this material. CAI coupons with foam filled HRP and foam filled HRH-10 honeycomb cores were tested after 200 inch pound impacts only. The performance of coupons with foam filled core materials was equal to or slightly inferior to their unfilled counterparts. These results are consistent with damage resistance tests for the foam filled honeycomb.

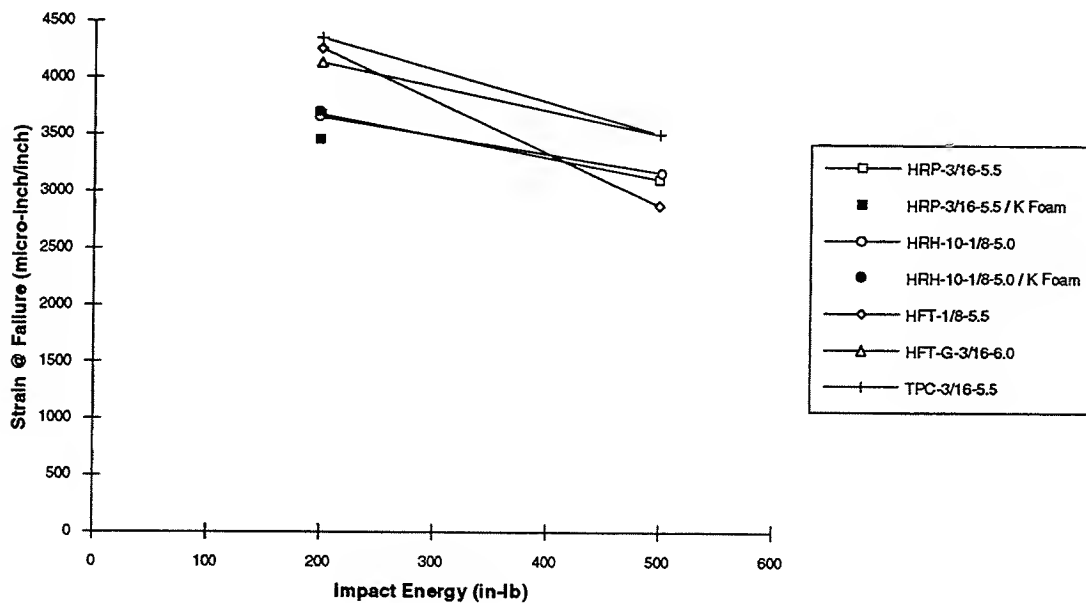


Figure F-8. CAI Strain at Failure of Representative Minimum Gage Sandwich Panels with Candidate Honeycomb Core Materials.

A strong correlation has been found between CAI strength and impact damage area in laminate coupons with damage area greater than approximately one square inch. This relationship is believed to be a result of instability in sublaminates created during the impact event. This relationship was not observed in AS4/8553-40 coupons with differing core materials as shown in Figure F-9.

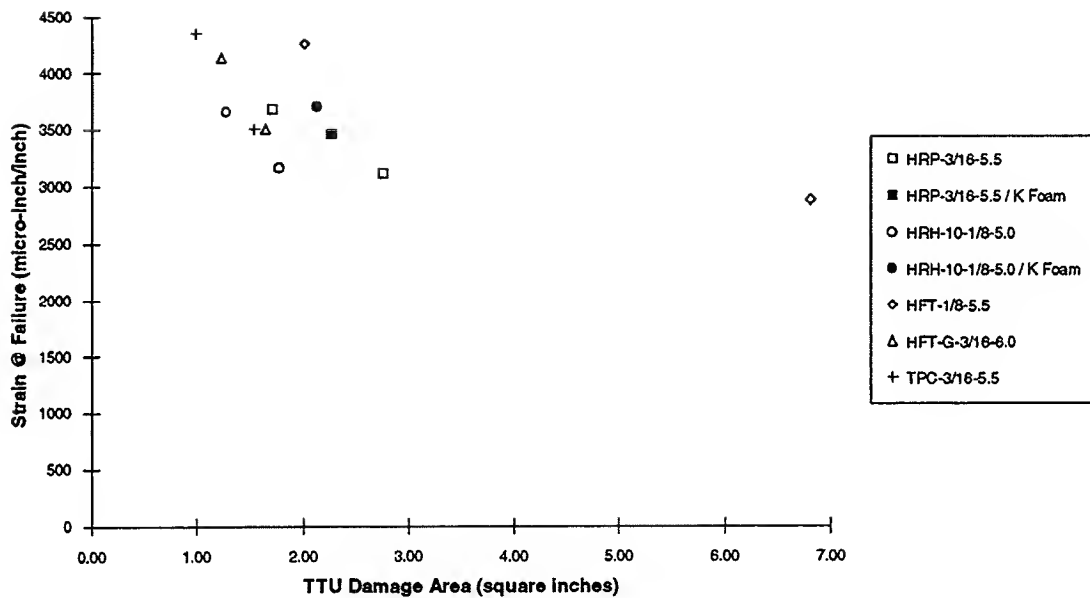


Figure F-9. Correlation of CAI Strain at Failure with Impact Damage Area.

Shadow Moiré results for CAI tests indicate complex failure modes which vary as a function of core type. Local buckling was evident in most of the CAI coupons as growth of the original indentation. All of the coupons which were impacted at 200 inch-pounds exhibited local buckling. In most cases the buckled area became slightly larger than the original area of damaged material. In some cases the growth of the dent was accompanied by propagation of an existing crack from the edge of the impact damage. Of the coupons impacted at 500 inch-pounds, only those with HRP and HFT cores exhibited local buckling. A simple correlation between the amount of local buckling and compression strength is not evident. This may be due to a competing failure mode driven by the stress concentration resulting from damage created during the impact event which is not related to facesheet or sublaminate stability.

APPENDIX G

The Influence of Material, Structural, and Extrinsic Variables on the Impact Damage Resistance and Tolerance of Composite Sandwich Structure

Summary

The influence of several material, structural and extrinsic variables on the impact damage resistance and tolerance of composite sandwich structures was investigated. Core material type and density, facesheet thickness, impact event support type, impactor size, and impact energy were considered.

Test Matrix and Procedures

Five test panels were constructed of AS4/8553-40 facesheets and 0.9 inch thick honeycomb core as shown in Table G-1. The AS4/8553-40 facesheet material had fiber areal weight of 190 g/m² and 40% resin content. Core materials were Hexcel products. The fraction in Hexcel's core material designation denotes honeycomb cell size in inches and the decimal number denotes the honeycomb density in pounds per cubic foot. The core ribbon direction was oriented parallel to the facesheet 0° fiber direction in all cases. CYTEC's Metalbond 1515 film adhesive was used for cocuring the facesheets to the core materials.

Table G-1: Test Panel Construction.

Facesheet Layup	Facesheet Thickness (inches)	Core Material	Description
[45/90/0/-45/0] _S	0.078	HRP-3/16-5.5	0/90 glass/phenolic
		HRP-3/16-12.0	0/90 glass/phenolic
		TPC-3/16-5.5	+/-45 glass/polyamide-imide
[45/90/0/-45/0] _{S3}	0.234	HRP-3/16-5.5	0/90 glass/phenolic
		HRP-3/16-12.0	0/90 glass/phenolic

The panels were impacted with one and two inch diameter steel tups at various impact energies over simple and rigid supports as shown in the summary test matrix in Table G-2. Simple and rigid supports were intended to simulate impact over and between stiffeners. "Simple support" was provided over an eight inch square opening. A greater span was desired but was limited by panel size. Rigid support was not provided for some of the impacts as intended. Slight curvature caused the panels to lose contact with the anvil when supported over a large area. Shims were used to correct the problem for the remainder of the tests. The influence of support type was not pursued in panels with thick facesheets because of the high flexural stiffness of these panels. The depth of the resulting indentation was measured for each impact and the panels were inspected by TTU to determine the planar extent of core damage. Coupons not intended for CAI testing were sectioned to characterize the internal damage state.

Table G-2: Impact Survey Test Matrix.

	Support Type:	rigid				simple					
	Impactor Diam. (in):	1.0		2.0		1.0				2.0	
	Impact Energy (in-lb):	200	500	200	500	200	500	750	1000	200	500
Facesheet Layup	Core Material										
[45/90/0/-45/0] _S	HRP-3/16-5.5	1*	1	1	1	2**	1			1	2**
	HRP-3/16-12.0	1*	1	1	1	1	1			1	2**
	TPC-3/16-5.5	1*	1	1	1	1	1			1	2**
[45/90/0/-45/0] _{S3}	HRP-3/16-5.5					1	1	1	1		
	HRP-3/16-12.0					1	1	1	1		

* rigid support was not provided for these tests as discussed above.

** includes one CAI coupon.

CAI (compression after impact) tests were performed on coupons cut from the same panels used for impact surveys as noted in Table G-2. CAI coupons were twelve inches wide by eighteen inches long. The coupons were impacted in the center on the tool side with one and two inch diameter steel tups at impact energy levels indicated in Table G-3. The two inch diameter tup was chosen to inflict internal damage over a large area while causing little indentation. Impact levels were chosen to cause visible impact damage (greater than 0.050 inch dent depth). The coupons were inspected by TTU following impact to determine core damage area. The coupons were instrumented with strain gages to verify uniform loading of the test coupons. Additional strain gages were used to characterize the response of the facesheet material next to the impact dent over damaged core material, just outside the damaged core material, and along the width of the coupon. A gage was also placed on the bagside of each coupon behind the impact location to characterize local buckling and through thickness load transfer around the impact damage. The shadow Moire' technique was used on the both sides of the coupons to characterize out-of-plane displacements.

Table G-3: Compression-After-Impact Test Matrix.

	Support Type:	simple	
	Impactor Diameter (in):	1.0	2.0
	Impact Energy (in-lb):	200	500
Facesheet Layup	Core Material		
[45/90/0/-45/0] _S	HRP-3/16-5.5	1	1
	HRP-3/16-12.0		1
	TPC-3/16-5.5		1

Test Results and Discussion

Impact Damage Resistance

Results for the impact surveys are presented in Table G-4. Impact support type had a minor influence on damage resistance. Impact over a rigid support resulted in greater dent depth than impact over simple support in most cases (Figure G-1). Visible damage was expected to occur at a lower impact energy for rigidly supported panels because the panel cannot bend to absorb energy. Notable exceptions are the 200 inch-pound impacts with a one inch diameter tup where rigid support was not really provided as described above. In this case the panel may have been able to bend even more than during the "simply supported" tests. The effect of support type on damage area was more complex (Figure G-2). Rigid support generally resulted in greater damage at low impact energy, but less damage at high energy. Greater damage at low energy may be a result of the inability of the panel to absorb energy through flexure. The same inability to bend may have resulted in earlier perforation of the impacted facesheet and therefore less planar damage propagation at high energy. The magnitude of the effects of support type may be greater when a greater span length between simple supports is used.

Table G-4: Impact Survey Test Results [Indentation depth (inches) and damage area (square inches)].

	Support Type:	rigid				simple					
	Impactor Diameter:	1.0		2.0		1.0				2.0	
	Impact Energy:	200*	500	200	500	200	500	750	100	200	500
Facesheet Layup	Core Material										
[45/90/0/-45/0] _S	HRP-3/16-5.5	.054 1.96	** 2.39	.027 3.87	.089 5.15	.140 2.36	** 2.48			.012 3.16	.084 6.32
	HRP-3/16-12.0	.030 0.87	.177 1.64	.016 1.47	.090 2.08	.046 0.88	.145 1.68			.013 1.05	.054 2.67
	TPC-3/16-5.5	.024 0.68	.260 1.55	.020 1.11	.095 2.56	.045 0.90	** 1.53			.013 0.82	.056 2.15
[45/90/0/-45/0] _{S3}	HRP-3/16-5.5					.007 0.65	.021 2.28	.046 3.14	.096 3.60		
	HRP-3/16-12.0					.007 0.35	.012 1.13	.042 1.42	.091 1.82		

* Rigid support was not provided for these tests as discussed above.

** Dent depth could not be measured because the impacted facesheet was perforated.

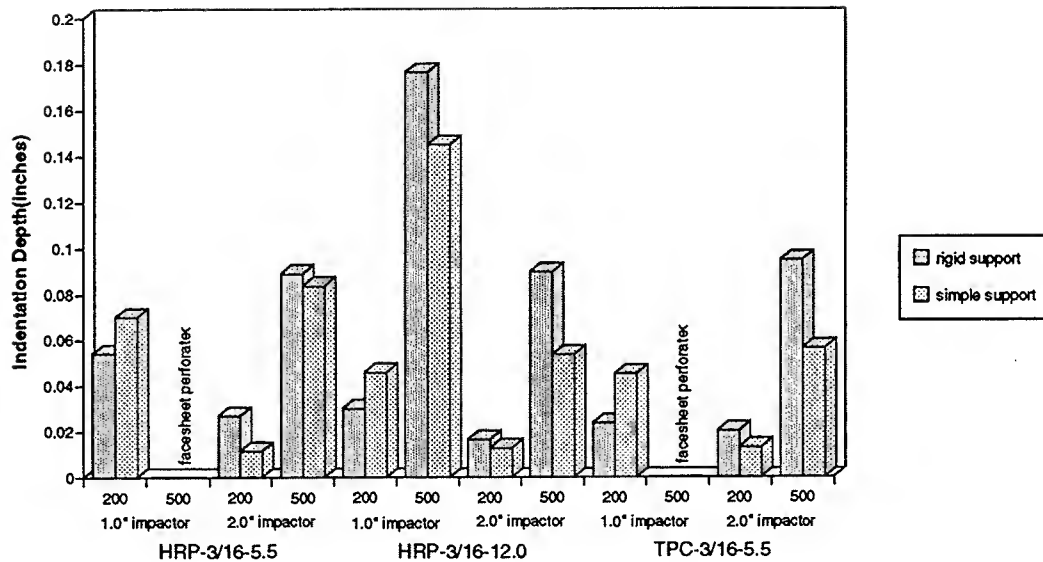


Figure G-1: Effect of Impact Support Type on Indentation Depth in Composite Sandwich Structures.

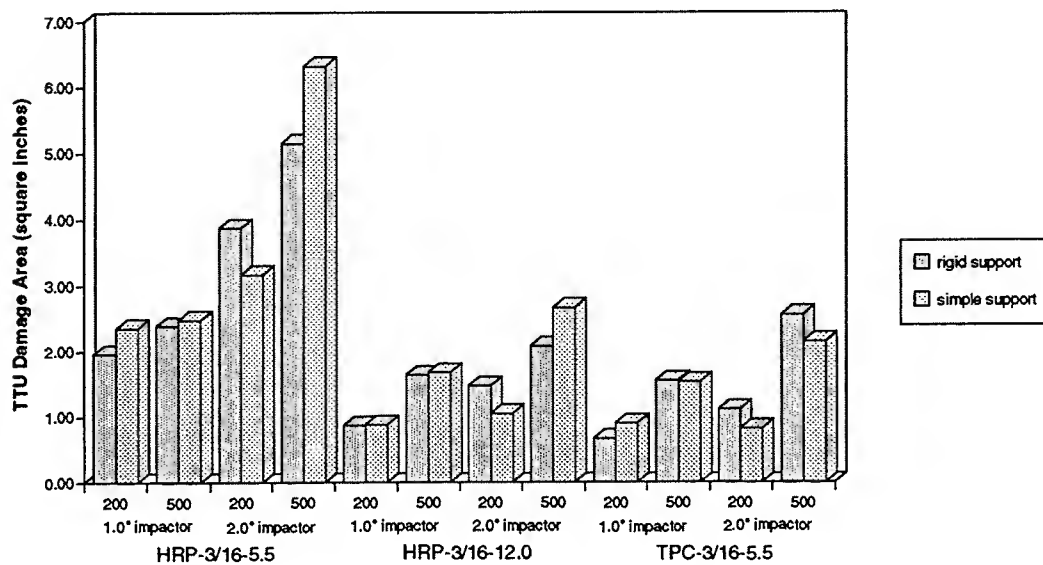


Figure G-2: Effect of Impact Support Type on Damage Area in Composite Sandwich Structures.

Impactor diameter had a significant influence on both indentation depth (Figure G-3) and damage area (Figure G-4). Impact with the larger tup resulted in a smaller indentation and greater damage area in nearly every case.

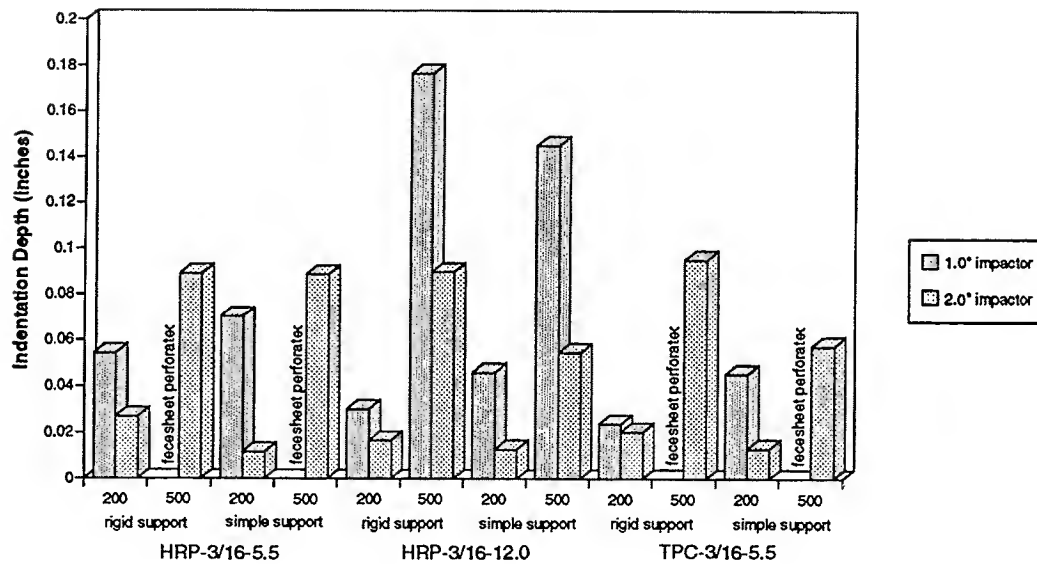


Figure G-3: Effect of Impactor Diameter on Indentation Depth in Composite Sandwich Structures.

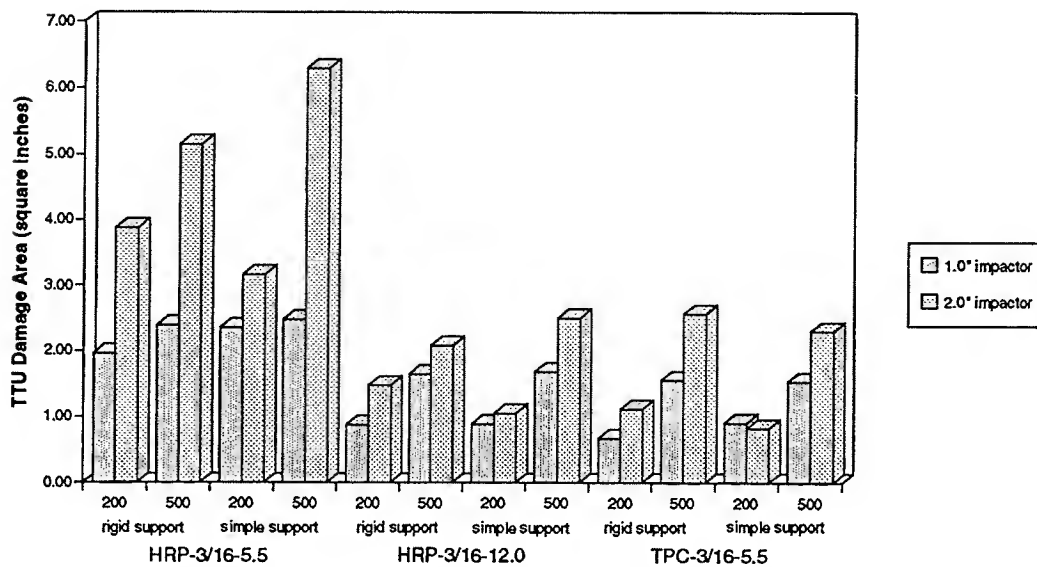


Figure G-4: Effect of Impactor Diameter on Damage Area in Composite Sandwich Structures.

Core type and density also proved to have a significant influence on impact damage resistance (Figures G-5 and G-6). The panel with 12.0 pcf HRP sustained less indentation than the panel with 5.5 pcf HRP in most cases and less damage area in all cases. The 12.0 pcf HRP core sustained less damage than 5.5 pcf HRP even when

impacted at levels high enough to cause comparable indentation depths. Performance of the 5.5 pcf TPC thermoplastic core was comparable to that of the 12.0 pcf HRP in most cases.

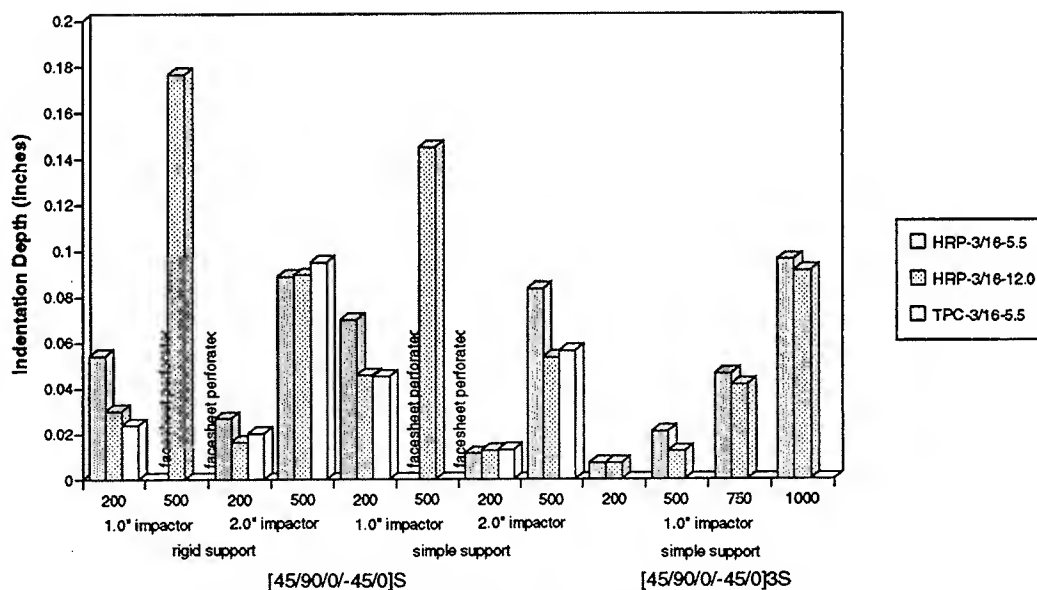


Figure G-5: Effect of Core Material Type and Density on Indentation Depth in Composite Sandwich Structures.

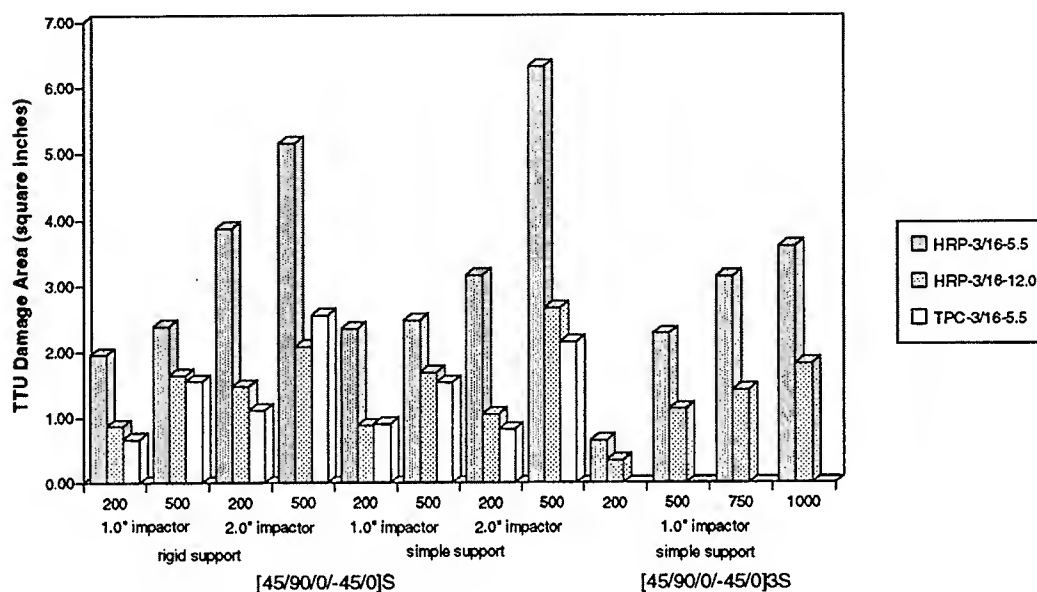


Figure G-6: Effect of Impactor Diameter on Damage Area in Composite Sandwich Structures.

Panels with thicker facesheets sustained smaller indentations and damage over a smaller area than those with thin facesheets for a given energy level (Figures G-7 and G-8). However, damage area appears to be approaching a higher asymptote with increasing impact energy for panels with thicker facesheets.

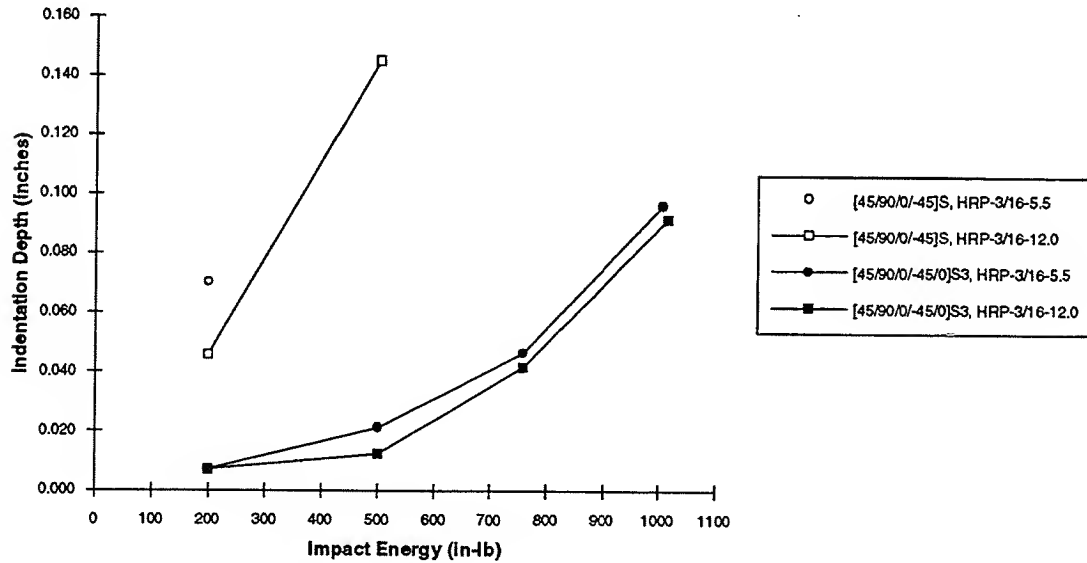


Figure G-7: *Effect of Facesheet Thickness on Indentation Depth in Composite Sandwich Structures.*

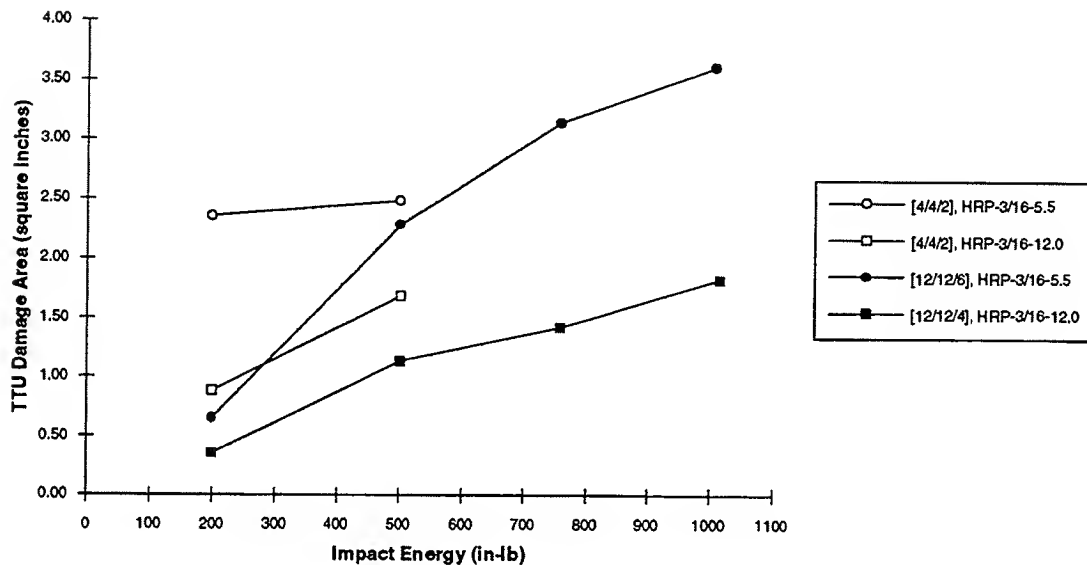


Figure G-8: *Effect of Facesheet Thickness on Damage Area in Composite Sandwich Structures.*

Compression Strength After Impact

Results of CAI tests are presented in Table G-5. The low energy impact with the small impactor (200 in-lbs, 1.0") resulted in lower residual strength than the high energy impact with the large impactor (500 in-lbs, 2.0") in panels with 5.5 pcf HRP even though the apparent damage was less severe. Shadow Moire' results for the 5.5 pcf HRP coupon impacted at low energy with small impactor indicated no significant out-of-plane displacement. Local buckling was indicated by shadow Moire' results for the 5.5 pcf HRP coupon impacted at high energy with the large impactor. Buckling was manifested as growth of the original impact dent to a size slightly wider and slightly shorter than the area of impact damaged material prior to failure. The buckled material may have acted to soften the stress concentration created by impact damage and provide higher strain at failure.

Local buckling was also observed in the panel with 12.0 pcf HRP. The buckled region again grew to the edge of the impact damaged material. This panel achieved higher strain at failure than the panel with 5.5 pcf HRP impacted at low energy with the small impactor even though comparable damage states were sustained.

Shadow Moire' results for the 5.5 pcf TPC panel indicate facesheet wrinkling combined with extension of an existing crack from the impact dent. This failure mode resulted in low strength relative to the 12.0 pcf HRP panel with similar damage state.

Load vs. strain plots exhibited typical stress concentrations due to load redistribution around the impact dent for all of the coupons. High compression strains were measured inside the buckled regions.

Table G-5: Compression-After-Impact Test Results.

	Support Type:	simple	
		1.0	2.0
	Impactor Diameter (in.):	1.0	2.0
	Impact Energy (in-lb):	200	500
Facesheet Layup	Core Material		
[45/90/0/-45/0] _S	HRP-3/16-5.5		
	dent depth (in.):	0.059	0.079
	damage area (in. ²):	2.32	6.34
	failure strain (μ-in./in.):	3250	3800
	HRP-3/16-12.0		
	dent depth (in.):		0.056
	damage area (in. ²):		2.83
	failure strain (μ-in./in.):		4400
	TPC-3/16-5.5		
	dent depth (in.):		0.053
	damage area (in. ²):		2.00
	failure strain (μ-in./in.):		3600

REPORT DOCUMENTATION PAGE			Form Approved OMB No. 0704-0188	
<small>Public reporting burden for this collection of information is estimated to average 1 hour per response, including the time for reviewing instructions, searching existing data sources, gathering and maintaining the data needed, and completing and reviewing the collection of information. Send comments regarding this burden estimate or any other aspect of this collection of information, including suggestions for reducing this burden, to Washington Headquarters Services, Directorate for Information Operations and Reports, 1215 Jefferson Davis Highway, Suite 1204, Arlington, VA 22202-4302, and to the Office of Management and Budget, Paperwork Reduction Project (0704-0188), Washington DC 20503</small>				
1. AGENCY USE ONLY (Leave Blank)	2. REPORT DATE April 1997	3. REPORT TYPE AND DATES COVERED Contractor Report		
4. TITLE AND SUBTITLE Advanced Technology Composite Fuselage - Materials and Processes		5. FUNDING NUMBERS C NAS1-18889 C NAS1-20013 (Task 2) WU 510-02-13-01		
6. AUTHOR(S) D.B. Scholz, E.F. Dost, B.W. Flynn, L.B. Ilcawicz, K. M. Nelson, A. J. Sawicki, T. H. Walker, and R. S. Lakes				
7. PERFORMING ORGANIZATION NAME(S) AND ADDRESS(ES) The Boeing Company P.O. Box 3707 Seattle, WA 98124-2207		8. PERFORMING ORGANIZATION REPORT NUMBER		
9. SPONSORING / MONITORING AGENCY NAME(S) AND ADDRESS(ES) National Aeronautics and Space Administration Langley Research Center Hampton, VA 23681-0001		10. SPONSORING / MONITORING AGENCY REPORT NUMBER NASA CR-4731		
11. SUPPLEMENTARY NOTES Langley Technical Monitor: W.T. Freeman, Jr.				
12a. DISTRIBUTION / AVAILABILITY STATEMENT FOUO Publicly Available Subject Category 24		12b. DISTRIBUTION CODE		
13. ABSTRACT (Maximum 200 words) <p>The goal of Boeing's Advanced Technology Composite Aircraft Structures (ATCAS) program was to develop the technology required for cost and weight efficient use of composite materials in transport fuselage structure. This contractor report describes results of material and process selection, development, and characterization activities. Carbon fiber reinforced epoxy was chosen for fuselage skins and stiffening elements and for passenger and cargo floor structures. The automated fiber placement (AFP) process was selected for fabrication of monolithic and sandwich skin panels. Circumferential frames and window frames were braided and resin transfer molded (RTM'd). Pultrusion was selected for fabrication of floor beams and constant section stiffening elements. Drap forming was chosen for stringers and other stiffening elements. Significant development efforts were expended on the AFP, braiding, and RTM processes. Sandwich core materials and core edge close-out design concepts were evaluated. Autoclave cure processes were developed for stiffened skin and sandwich structures.</p> <p>The stiffness, strength, notch sensitivity, and bearing/bypass properties of fiber-placed skin materials and braided/RTM'd circumferential frame materials were characterized. The strength and durability of cocured and cobonded joints were evaluated. Impact damage resistance of stiffened skin and sandwich structures typical of fuselage panels was investigated. Fluid penetration and migration mechanisms for sandwich panels were studied.</p>				
14. SUBJECT TERMS Advanced Composite Technology Program; Materials and process developments; Automated fiber placement; Sandwich core; Core close-outs; Braiding; Resin transfer molding; Mechanical performance; Braided textile; Bonded joints; Impact damage; Environmental durability; Test results		15. NUMBER OF PAGES 250		
		16. PRICE CODE		
17. SECURITY CLASSIFICATION OF REPORT Unclassified	18. SECURITY CLASSIFICATION OF THIS PAGE Unclassified	19. SECURITY CLASSIFICATION OF ABSTRACT Unclassified	20. LIMITATION OF ABSTRACT	